Benefits from a multi-receiver architecture for GNSS precise positioning and attitude determination

Xiao Hu

THÈSE

En vue de l'obtention du

DOCTORAT DE L'UNIVERSITÉ DE TOULOUSE

Délivré par :

Institut National Polytechnique de Toulouse (Toulouse INP)

Discipline ou spécialité :

Informatique et Télécommunication

Présentée et soutenue par :

M. XIAO HU

le vendredi 1 octobre 2021

Titre :

Benefits from a multi-receiver architecture for GNSS precise positioning

---

Ecole doctorale :

Mathématiques, Informatique, Télécommunications de Toulouse (MITT)

Unité de recherche :

Laboratoire d'Informatique Interactive (LII-ENAC)

Directeur(s) de Thèse :

M. CHRISTOPHE MACABIAU

M. PAUL THEVENON

Rapporteurs :

M. HONGLEI QIN, Université de Beihang

MME VALERIE RENAUDIN, UNIVERSITE GUSTAVE EIFFEL

Membre(s) du jury :

M. DAVID BÉTAILLE, UNIVERSITE GUSTAVE EIFFEL, Président

M. CHRISTOPHE MACABIAU, ECOLE NATIONALE DE L'AVIATION CIVILE, Membre

MME SANDRA VERHAGEN, UNIVERSITE DE DELFT, Membre

M. PAUL THEVENON, ECOLE NATIONALE DE L'AVIATION CIVILE, Membre

Benefits from a multi-receiver architecture for GNSS RTK positioning and attitude determination

Ph.D. Thesis

Xiao HU

Abstract

Precise positioning with a stand-alone GPS receiver or using differential corrections is known to be strongly degraded in an urban or sub-urban environment due to frequent signal masking, strong multipath effect, frequent cycle slips on carrier phase, etc. The objective of this Ph.D. thesis is to explore the possibility of achieving precise positioning with a low-cost architecture using multiple installed low-cost single-frequency receivers with known geometry whose one of them is RTK positioned w.r.t an external reference receiver. This setup is thought to enable vehicle attitude determination and RTK performance amelioration. In this thesis, we firstly proposed a method that includes an array of receivers with known geometry to enhance the performance of the RTK in different environments. Taking advantage of the attitude information and the known geometry of the installed array of receivers, the improvement of some internal steps of RTK w.r.t an external reference receiver can be achieved. The navigation module to be implemented in this work is an Extended Kalman Filter (EKF). The performance of a proposed two-receiver navigation architecture is then studied to quantify the improvements brought by the measurement redundancy.

This concept is firstly tested on a simulator in order to validate the proposed algorithm and to give a reference result of our multi-receiver system's performance. The pseudo-range measurements and carrier phase measurements mathematical models are implemented in a realistic simulator. Different scenarios are conducted, including varying the distance between the 2 antennas of the receiver array, the satellite constellation geometry, and the amplitude of the noise measurement, in order to determine the influence of the use of an array of receivers. The simulation results show that our multi-receiver RTK system w.r.t an external reference receiver is more robust to noise and degraded satellite geometry, in terms of ambiguity fixing rate, and gets a better position accuracy under the same conditions when compared with the single receiver system. Additionally, our method achieves a relatively accurate estimation of the attitude of the vehicle which provides additional information beyond the positioning.

In order to optimize our processing, the correlation of the measurement errors affecting observations taken by our array of receivers has been determined. Then, the performance of our real-time single frequency cycle-slip detection and repair algorithm has been assessed. These two investigations yielded important information so as to tune our Kalman Filter.

The results obtained from the simulation made us eager to use actual data to verify and improve our multi-receiver RTK and attitude system. Tests based on real data collected around Toulouse, France, are used to test the performance of the whole methodology, where different scenarios are conducted, including varying the distance between the 2 antennas of the receiver array as well as the environmental conditions (open sky, suburban, and constrained urban environments). The thesis also tried to take advantage of a dual GNSS constellation, GPS and Galileo, to further strengthen the position solution and the reliable use of carrier phase measurements. The results show that our multi-receiver RTK system is more robust to degraded GNSS environments. Our experiments correlate favorably with our previous simulation results and further support the idea of using an array of receivers with known geometry to improve the RTK performance.

Résumé

Le positionnement précis avec un récepteur GPS autonome ou utilisant des corrections différentielles est connu pour être fortement dégradé dans un environnement contraint (conditions urbaines ou suburbaines) en raison d'un masquage fréquent du signal, d'un fort effet de trajets multiples, de fréquents sauts de cycles sur la mesure de phase, etc. L'objectif de cette thèse est alors d'explorer la possibilité de réaliser un positionnement précis avec une architecture à faible coût : en utilisant plusieurs récepteurs monofréquence à faible coût avec une géométrie connue pour permettre la détermination de l'attitude du véhicule et l'amélioration des performances RTK. Dans cette thèse, nous avons premièrement proposé une méthode qui comprend un réseau de récepteurs à géométrie connue pour améliorer les performances du RTK dans différents environnements. En tirant parti des informations d'attitude et de la géométrie connue du réseau de récepteurs, l'amélioration de certaines étapes internes de positionnement précis RTK peut être réalisée. Le module de navigation à implémenter dans ce travail est un filtre de Kalman étendu (EKF). Les performances de notre proposition d'architecture de navigation à deux récepteurs sont ensuite étudiées pour quantifier les améliorations apportées par la redondance de mesures, dont le nombre est doublé.

Ce concept est d'abord testé sur un simulateur pour valider l'algorithme proposé et donner une référence des performances de notre système multi-récepteurs. Les modèles mathématiques des mesures de pseudodistance et des mesures de phase sont implémentés dans un simulateur réaliste. Différents scénarios sont conduits dont la variation de la distance entre les 2 antennes du réseau de récepteurs, la géométrie de la constellation de satellites et l'amplitude de la mesure du bruit pour valider l'influence de l'utilisation d'un réseau de récepteurs. Les résultats de la simulation montrent que notre système RTK multi-récepteurs est plus robuste au bruit et à une dégradation de la géométrie de satellites, en termes de taux de fixation d'ambiguïté, et obtient une meilleure précision de positionnement dans les mêmes conditions par rapport au système à récepteur unique. De plus, notre méthode permet d'obtenir une estimation relativement précise de l'attitude du véhicule qui fournit des informations supplémentaires au-delà du positionnement.

Afin d'optimiser notre traitement, la corrélation des erreurs de mesure affectant les observations effectuées par notre réseau de récepteurs a été déterminée. Ensuite, les performances de notre algorithme de détection et de réparation de sauts de cycle mono-fréquence en temps réel ont été évaluées. Ces deux études ont fourni des informations importantes afin d'ajuster notre filtre de Kalman.

Les résultats obtenus à partir de la simulation nous incitent à utiliser des données réelles pour vérifier et améliorer notre modèle multi-récepteur. Des tests basés sur des données réelles collectées autour de Toulouse, en France, sont utilisés pour tester les performances de l'ensemble de la méthodologie, où différents scénarios sont menés, notamment en faisant varier la distance entre les 2 antennes du réseau de récepteurs et les conditions environnementales (ciel ouvert, suburbain et urbain contraint). La thèse a également tenté de tirer parti d'une double constellation de GNSS, GPS et Galileo, pour renforcer davantage la solution de position et l'utilisation fiable des mesures de phase de porteuse. Les résultats montrent que notre système RTK multi-récepteurs est plus robuste aux environnements GNSS dégradés. Nos expériences sont en corrélation favorable avec nos résultats de simulation précédents et soutiennent en outre l'idée d'utiliser un réseau de récepteurs avec une géométrie connue pour améliorer les performances RTK.

Acknowledgments

This PhD research work was carried out in the Signal Processing and Navigation (SIGNAV) Group of the TELECOM Lab at the École Nationale de l'Aviation Civile (ENAC). It has been a wonderful experience pursuing my study at ENAC. I remember myself as an ambitious and aspiring young man when I first stepped into ENAC in 2015, I had the feeling that I was going to make a big difference. Six years have passed so fast, on this beautiful campus, I got my master's and engineer's degree in 2017 and now there comes the graduation of my Ph.D. It's my great honor to take this opportunity to express my special thanks to a variety of people who have helped me a lot along this journey.

My deepest gratitude goes first and foremost to my thesis supervisors, Prof. Christophe MACABIAU and Dr. Paul THEVENON. Thank you so much for your constant help, encouragement, and guidance during the past four years, it's definitely a pleasure and I'm so lucky to be able to work with you guys. Without your patient instruction, insightful advice and expert guidance, the completion of this thesis would not have been possible. I could not have imagined having better advisors, mentors but also friends for my PhD study and my career.

In addition, this PhD is conducted with the financial support of the China Scholarship Council (CSC), I'm extremely grateful to CSC for choosing me and giving me this opportunity to realize my dream.

I want also to express my gratitude for the great jury committee, formed by my thesis reviewers Prof. Valérie RENAUDIN and Prof. Honglei QIN, the examiner Prof. Sandra VERHAGEN, and the jury chairman Prof. David BÉTAILLE. Thanks for accepting to be part of the jury and attending to my oral defense. Your precious advice, suggestions and questions helped me a lot to improve my thesis and my research.

My sincere thanks also go to the following staffs and friends in ENAC and Telecom lab: Jérémy, Hasna, Hélène, and Serge, thanks for your continuous help for all the technical and administrative things; Yu Wang and Olivier, who shared their code with me in the very beginning of my PhD which let me get started faster; Anne-Marie, Capucine, Anthony, David, and Bruno, who shared the same office with me during my PhD; Ikhlas, my best partner for my first international conference in my life; Heekwon, Junesol, and Jan, who helped me to collect the data and gave me great advice for my oral defense; and all the labmates that I have met in SIGNAV group: Antoine, Anaïs, Alexandre, Anne-Christine, Axel, Carl, Christophe, Roberto, Rémi, Sara, Eugene, Florian, Thomas, Maxandre and all the others that I forget to mention, thank you for making the time spent that memorable and happy.

I would like also to thank all my friends in France: Fan, Xizhe, Chengdan, my best homies, and brothers; Ruohao and Shangrong, our double date group; Dr.Liang, Alex, Jiayi, and Ziqing, my game and tennis partners; Yuyao, who came from afar to participate in my oral defense; and also Frédéric, Guoyan, Gilles, Zhengyi, Ji Ma, Mahfoud, Xin Tu, Sana, Hang, Hasan, Tengfei, Weibin and all the other friends for all the fun and great memories we had during the vacations, week-ends and even lunch breaks.

Finally, I would like to express my sincere and deepest gratitude to my dear parents, Xu LI and Yingqi HU, no matter what difficulties I come across, I know that you are always there for me, you are the best parents in my heart.

Especially, thanks to my girlfriend Ying HUO, thanks for your support and love, meeting you in this beautiful country is the luckiest thing ever in my life, nothing is important without you.

Table of contents

List of Figures

List of Tables

List of Acronyms

ABAS	Aircraft Based Augmentation System
AFM	Ambiguity Function Method
ARCE	Ambiguity Resolution using Constraint Equation
ARNS	Aeronautical Radio Navigation Services
A-S	Anti-Spoofing
BDS	BeiDou Navigation System
BOC	Binary Offset Carrier
BPSK	Binary Phase Shift Keying
C/A	Coarse/Acquisition
CBOC	Composite Binary Offset Carrier
CDMA	Code Division Multiple Access
CMC	Code-Minus-Carrier
CNS/ATM	Communications, Navigation, Surveillance / Air Traffic Management
CORS	Continuously Operating global Reference Stations
CS-DR	Cycle Silp Detection and Repair
CW	Carrier Wave
D8PSK	Differentially encoded 8 Phase Shift Key
DCM	Direction Cosine Matrix
DD	Double Differencing
DGPS	Differential GPS
DGNSS	Differential GNSS
DIAS	Direct Integer Ambiguity Search
DLL	Delay Locked Loop
DOP	Dilution Of Precision
DSSS	Direct Sequence Spread Spectrum
ECEF	Earth Centered Earth Fixed
EGNOS	European Geostationary Navigation Overlay Service
EKF	Extended Kalman Filter
ENAC	École Nationale de l'Aviation Civile
ENU	East-North-Up
ERIS	External Regional Integrity Services
EUROCAE	European Organization for Civil Aviation Equipment
FARA	Fast Ambiguity Resolution Approach
FASF	Fast Ambiguity Search Filter
FDMA	Frequency Division Multiple Access
FEC	Forward Error Correction
FT-RT	Fixed Threshold Ratio Test
GAGAN	GPS Aided GEO Augmented Navigation
GBAS	Ground Based Augmentation System
GDOP	Geometric Dilution of Precision
GEO	Geostationary Orbit

GLONASS	GLObal NAvigation System
GNSS	Global Navigation Satellite System
GPS	Global Positioning System
GRAPHIC	GRoup And Phase Ionospheric Correction
GSS	Galileo Sensor Stations
GST	Galileo System Time
HAL	Horizontal Alert Limit
HDOP	Horizontal DOP
IAR	Integer Ambiguity Resolution
ICAO	International Civil Aviation Organization
ICD	Interface Control Document
IF	Intermediate Frequency
ILS	Integer Least Square
IMU	Inertial Measurement Unit
INS	Inertial Navigation System
IGSO	Inclined Geosynchronous Orbits
IRNSS	Indian Regional Navigation Satellite System
ITRS	International Terrestrial Reference System
KF	Kalman Filter
LAAS	Local Area Augmentation System
LAMBDA	Least-Squares Ambiguity Decorrelation Adjustment
LDGNSS	Local Area DGNSS
LIDAR	Light Detection and Ranging
LIMS	LIDAR Imaging and Measurement System
LOS	Line-Of-Sight
LSAST	Least Squares Ambiguity Search Technique
MAPAS	Maximum A Posteriori Ambiguity Search
MCS	Master Control Station
MCLAMBDA	Multivariate Constrained LAMBDA method
MEMS	Micro-Machined Electromechanical System
MEO	Medium Earth Orbit
MIDS	Multifunctional Information Distribution System
MLAMBDA	Modified LAMBDA method
MOPS	Minimum Operational Performance Standards
MS	Monitor Stations
NH	Neuman-Hofman
NAVSTAR	Navigation by Satellite Ranging and Timing
NAVIC	Navigation with Indian Constellation
NED	North-East-Down
NLOS	Non-Line-Of-Sight
NSE	Navigation System Error
OPP	Orthogonal Procrustes Problem
P	Precision
PDOP	Position Dilution Of Precision
PEE	Position Estimation Error

PF	Particle Filter
PNT	Position, navigation, and timing
PPS	Precise Positioning Service
PPP	Precise Point Positioning
PRN	Pseudo Range Noise
PSD	Power Spectral Density
PVT	Position, Velocity, and Time
QZSS	Quasi-Zenith Satellite System
RAIM	Receiver Autonomous Integrity Monitoring
RDGNSS	Region-Area DGNSS
RGP	Reseau GNSS Permanent
RF	Radio Frequency
RMS	Root Mean Square
RNSS	Radio Navigation Satellite Services
RTK	Real Time Kinematic
QZSS	Quasi-Zenith Satellite System
QZO	Quasi-Zenith Orbits
SA	Selective Availability
SAR	Search-and-Rescue
SARP	Standards And Recommended Practices
SBAS	Satellite Based Augmentation System
SD	Single Differencing
SDCM	System for Differential Correction and Monitoring
SIS	Signal-In-Space
SPP	Single Point Positioning
SPS	Standard Positioning Service
TEC	Total Electron Content
TMBOC	Time Multiplexed Binary Offset Carrier
TOI	Time Of Interval
TOW	Time Of Week
TTF	Time-To-Fix
TTC	Telemetry, Tracking and Command
UDRA	User Differential Range Accuracy
UERE	User Differential Range Error
UHF	Utra High Frequency
UIRE	User Ionospheric Range Error
UKF	Unscented Kalman Filter
ULS	Uplink Stations
UNB	University of New Brunswick
URA	User Range Accuracy
UTC	Universal Time Coordinated
VC	Variance-Covariance
VHF	Very High Frequency
VRS	Virtual Reference Station
VTEC	Vertical Total Electron Content

WAAS	Wide Area Augmentation System
WDGNSS	Wide-Area DGNSS
WOPP	Weighted Orthogonal Procrustes Problem

Chapter 1. Introduction

1.1. Background and Motivation

Over the past decades, the universal Global Navigation and Satellite System (GNSS) has been increasingly utilized in various domains, such as aviation, marine, precise agriculture, geodesy, surveying, and automotive. Most current positioning systems rely on the stand-alone GNSS. However, the accuracy, availability, or integrity that a low-cost standard stand-alone GNSS receiver can provide in a constrained urban or indoor environment is far from satisfactory. Especially for specific application scenarios like autonomous driving of vehicles or precise mobile mapping, where decimeter or centimeter accuracy and additional vehicle attitude information are mostly envisioned and required. To reach this level of accuracy, the use of GNSS carrier phase measurements appears compulsory. The impact of noise and multipath on carrier phase measurements is lower than on code measurements by a factor of a hundred [1]. Techniques using raw carrier phase measurements have then been developed like the differential Real-time Kinematic (RTK) based GNSS positioning.

Nevertheless, carrier phase measurements are also less robust and include a so-called integer ambiguity that requires implementing a specific integer ambiguity resolution (IAR) process to use them for positioning. In some harsh environments, severe multipath and losses of lock of the receiver tracking loops create carrier cycle slips, which result in sudden changes of these ambiguities. If not detected, the cycle slips will create a bias on the carrier phase measurement resulting in a degradation of position accuracy when considering a wrong ambiguity determination. Even if detected, the IAR process must be, at least partially, re-initialized, leading also to a loss of positioning accuracy. To increase confidence and accelerate the IAR process by limiting the search space, restrictions can be established from the use of an array of two or more receivers installed on a vehicle, with prior known and fixed geometry. That geometry includes the length of the baseline vectors between the antennas of the receiver array and the orientation of the vectors.

In recent years, several studies have focused on the use of a vehicle-installed array of receivers for attitude determination [2], GNSS positioning accuracy amelioration [3], or even calibration of magnetic field sensors to help the GNSS [4]. Gabrielle et al.[5] studies the viability of attitude determination by using a new ambiguity-attitude estimator which improves the probability of successful integer ambiguity resolution. Nonetheless, the improvement of RTK positioning performance was not studied. Medina et al. [6] developed a method for the recursive estimation of the positioning and attitude problems using GNSS carrier phase observations from an array of installed receivers taking advantage of the known geometric constraints between receivers. Farhad et al. [7] [8] used an adaptive KF for 3-dimensional attitude determination and position estimation of a mobile robot by fusing the information from a system of two RTK GPSs and an IMU. However, they also did not consider the known geometry of the receiver as a constraint to help improve the positioning performance. Zheng et al. [9] presented a methodology for integrating carrier phase attitude determination and positioning systems by considering that one of the receivers in the pair used for the attitude determination system is also used as the rover for the relative positioning system. Nevertheless, their proposed attitude determination and positioning systems remained independent which did not much ameliorate the

success rate of IAR for the RTK. Nandakumar et al. [10] provided a numerical insight into the role taken by the multi-GNSS integration in delivering high-precision solutions, however, they focused on the PPP solution rather than the RTK processing, and this requires a long convergence time to reach cm-level accuracy. Khodabandeh et al. [11], [12] introduced a concept of array-based between-satellite single difference satellite phase biases determination to accelerate the single-receiver IAR, but they did not take into consideration the attitude information of the vehicle thus cannot analyze the influence with attitude consideration. Peirong et al.[13] proposed a dual-antenna constraint RTK algorithm to improve the system AR success rate, which combines GNSS measurements of both antennas by making use of the baseline vector constraint between them. However, the attitude information of the vehicle is still not taken into account.

In fact, the use of multiple installed antennas/receivers configuration allows involving more information in the estimation process. The redundant measurements from an additional antenna may alleviate the effects of the environment, thus can improve the GNSS positioning performance in constrained areas. Unfortunately, very few publications can be found that address the use of an installed array of receivers to improve the accuracy of the array position or for some internal steps of precise position computation for RTK processing such as cycle slip detection or integer ambiguity resolution, with vehicle attitude determination at the same time.

In this dissertation, the possibility of applying the precise positioning technique RTK to GNSS measurements collected from multiple installed low-cost single-frequency multi-constellation receivers is investigated. Taking advantage of the known geometric constraints between the array rover receivers, the feasibility of the vehicle attitude determination is also studied. The performance of the algorithm is further tested using the simulation data and the real data collections, in both the GNSS-favorable environment and the GNSS-denied environment.

1.2. Thesis Objectives and Contributions

The objective of this Ph.D. thesis is to explore the possibility of achieving precise positioning with a low-cost architecture using multiple low-cost, single-frequency installed receivers with known geometry to enable the vehicle attitude determination as well as RTK performance amelioration w.r.t an external reference receiver. In this thesis, we firstly propose a method that includes an array of installed receivers with known geometry to enhance the performance of the RTK in different environments. Taking advantage of the attitude information and the known geometry of the array of receivers, the improvement of some internal steps of RTK precise positioning can be achieved. The navigation module implemented in this work is an Extended Kalman Filter (EKF). The performances of our proposed two-receiver navigation architecture are then studied to quantify the improvements brought by the doubled measurement redundancy.

This concept is first tested on a simulator. This is mainly used for validation of the algorithm implementation and gives a reference indication of our multi-receiver system's performance. The pseudo-range measurements and carrier phase measurements mathematical models are implemented in a realistic simulator. Different scenarios are conducted, including varying the distance between the 2 antennas of the installed receiver array, the satellite geometry, and the amplitude of the noise measurement, in order to validate the influence of the using of an array of receivers. The simulation results show that our multi-receiver RTK system is more robust to noise and degraded satellite geometry, in terms of ambiguity fixing rate, and gets a better position accuracy under the

same conditions when compared with the single receiver system. Additionally, our method achieves a relatively accurate estimation of the attitude of the vehicle which provides additional information beyond the positioning.

In order to optimize our processing, the correlation of the measurement errors affecting observations taken by our array of receivers has been determined. Then, the performance of our real-time single frequency cycle-slip detection and repair algorithm has been assessed. The improvement of cycle-slip detection and repair for RTK processing by using multi-receivers with known geometry is also studied using both the simulated data and real data. These two investigations yielded important information so as to tune our Kalman Filter.

The results obtained from the simulation made us eager to use actual data to verify and improve our multi-receiver model. Tests based on real data collected around Toulouse, France, are used to test the performance of the whole methodology, where different scenarios are conducted, including varying the distance between the 2 antennas of the receiver array and the environmental conditions (open sky, suburban, and constrained urban environments). The thesis also tried to take advantage of a dual GNSS constellation, GPS and Galileo, to further strengthen the position solution and the reliable use of carrier phase measurements. The results show that our multi-receiver RTK system is more robust to degraded GNSS environments. Our experiments correlate favorably with our previous simulation results and further support the idea of using an installed array of receivers with known geometry to improve the RTK performance.

The results obtained from this Ph.D. has yielded one journal paper and five communications in international conferences which are listed as follows:

- **Journal paper:**

Xiao Hu, Paul Thevenon, Christophe Macabiau. “Attitude Determination and RTK Positioning Using Multiple Low-Cost Receivers with Known Geometry”. *GPS World*, Aster Pub. Corp., May 2021, 32 (5), pp.35-41. ⟨hal-03243925⟩

- **Conference papers:**

Xiao Hu, Paul Thevenon, Christophe Macabiau. “Attitude Determination and RTK Performances Amelioration Using Multiple Low-Cost Receivers with Known Geometry”. *ION ITM 2021, International Technical Meeting*, Jan 2021, Virtual event, France. pp. 439-453, ⟨10.33012/2021.17841⟩. ⟨hal-02984329v2⟩

Xiao Hu, Paul Thevenon, Christophe Macabiau. “Improving reliability and efficiency of RTK ambiguity resolution using multiple rover receivers connected to the same antenna”. *ENC 2020 European Navigation Conference*, ⟨10.23919/ENC48637.2020.9317367⟩. Nov 2020, Dresden (Virtual event), Germany. ⟨hal-03147591⟩

Xiao Hu, Paul Thevenon, Christophe Macabiau. “Cycle Slip Detection and Repair Using an Array of Receivers with Known Geometry for RTK Positioning”. *PLANS 2020 IEEE/ION Position, Location and Navigation Symposium*, Apr 2020, Portland, United States. pp.1123-1134 / ISBN: 978-1-7281-9446-2, ⟨10.1109/PLANS46316.2020.9109871⟩. ⟨hal-02866389⟩

Xiao Hu, Paul Thevenon, Christophe Macabiau. "Improvement of RTK performances using an array of receivers with known geometry". *ION ITM 2020, International Technical Meeting*, Jan 2020, San Diego, United States. ⟨10.33012/2020.17154⟩. ⟨hal-02549028⟩

Arnau Ochoa Banuelos, Jan Bolting, **Xiao Hu**, Paul Thevenon, Bryan Cazabonne, Matthieu Pascaud and Arnaud Ginestet, "Centralized Processing of Multiple Smartphone Raw Measurements with Fixed and Known Position Onboard a Vehicle", *ION GNSS+ 2021*, Sep 2021, St. Louis, United States

1.3. Thesis Outline

This thesis is composed of seven chapters, the detailed structure is as follows:

Chapter 2 first presents the state of the art of the GNSS systems. Different GNSS constellations are introduced, then a review of the GNSS receiver processing including the signal processing leading to the production of the GNSS raw measurements is given. The GNSS code and phase observations including all nominal errors sources and their impact are described.

Chapter 3 provides the description of the GNSS precise positioning techniques, which includes DGNSS (Differential GNSS), PPP (Precise Point Positioning), and RTK (Real-Time Kinematic). The challenges of GNSS precise positioning in highly constrained environments like the urban environment are revealed. An overview and classification of current mathematical algorithms and techniques utilized in the process of GNSS-based attitude estimation are described as well at the end.

Chapter 4 is devoted to giving the detailed implementations of our proposed multi-receiver architecture for GNSS RTK precise positioning and vehicle attitude estimation adapted to the constrained environment. This includes our RTK measurement model, state vector, system configuration and geometry, signal pre-processing module, integer ambiguity resolution techniques, as well as the expected benefits of the proposed multi-receiver architecture.

Chapter 5 focuses on the experimental validation of the proposed multi-receiver method based on the simulated data. The tests carried out are described, as well as the details about the experimental procedures of the proposed algorithm using simulated GNSS measurements. Different scenarios are considered in order to analyze the benefits of the proposed architecture in various environmental situations. The performance of the developed RTK navigation solutions (position and attitude determination) is assessed based on these tests. Performance indicators such as fix success rate, position estimation accuracy, and attitude estimation accuracy are analyzed.

Chapter 6 presents the performance of the proposed algorithm using real data. To reflect different environmental situations, 3 different GNSS collections campaigns under various satellite visibility conditions are conducted. First, the environmental conditions of these 3 data collection scenarios are reviewed, as well as the details about the data collection set-ups. The availability statistics of the GNSS measurements in different scenarios are also presented. The performance of our proposed multi-receiver RTK navigation solution (position estimation and attitude determination accuracy) is then assessed based on the test results using the collected real GNSS data in all the considered environmental conditions. The impact of the distance between the 2 antennas of the installed receiver array and the advantage brought by the GPS/Galileo dual constellation are also analyzed and presented.

Chapter 7 synthesizes the main results of the Ph.D. study and draws conclusions based on the results obtained. Recommendations for future work are finally presented.

Chapter 2. GNSS Functional and Stochastic Model

The Global Navigation Satellite Systems (GNSS) are satellite-based systems that are generally used for positioning, navigation, and precise timing purposes. GNSS has been defined by the International Civil Aviation Organization (ICAO) as a worldwide position and time determination system that includes one or more satellite constellations, aircraft receivers, and system integrity monitoring, augmented as necessary to support the required navigation performance for the intended operation [14].

This chapter presents the state of the art of the GNSS functional and stochastic model. The content is organized as follows:

- Section 2.1 gives an overview of the different GNSSs and presents the signals transmitted by the American, European, Russian, and Chinese constellations. Other regional GNSS systems are also presented briefly.
- Section 2.2 focuses on the review of the GNSS Receiver including the Signal Processing process that how the receiver will respectively give the code pseudorange and the carrier phase measurements as by-products.
- Section 2.3 aims at describing the GNSS code and carrier phase observations including all nominal errors sources.
- Section 2.4 finally concludes this chapter.

2.1. Global Navigation Satellite Systems Overview

2.1.1. Introduction

Global navigation satellite system is the collective term for those navigation systems that provide the user with a 3-D positioning solution by passive ranging using radio signals transmitted by orbiting satellites. GNSS is thus a self-positioning system; the position solution is calculated by the user equipment, which does not transmit any signals for positioning purposes.

A number of systems aim to provide global coverage. The most well-known is the Navigation by Satellite Ranging and Timing (NAVSTAR) Global Positioning System [15], owned and operated by the United States government and usually known simply as GPS. GLObal NAvigation System (GLONASS) is a navigation system owned by the Russian Federation Government and used to provide positioning, navigation, and timing services globally, it is also fully operational [16]. China has expanded its regional BeiDou Navigation Satellite System into the global BeiDou-3 GNSS and has declared globally operational in 2020 [17]. The European Union's Galileo is a global GNSS that consists of 24 operational satellites and up to 6 active spares, positioned in three circular Medium Earth Orbit planes, providing a highly accurate and global positioning service under civilian control [18]. India currently has a satellite-based augmentation system, GPS Aided GEO Augmented Navigation (GAGAN), which enhances the accuracy of NAVSTAR GPS and GLONASS positions. India has already launched the IRNSS, with an operational name NAVIC (Navigation with Indian Constellation), a constellation of satellites for navigation in and around the Indian Subcontinent [19]. Japan is in the process of developing regional

navigation systems Quasi-Zenith Satellite System (QZSS) as well [20], QZSS composed mainly of satellites in quasi-zenith orbits (QZO).

For each GNSS constellation, Table 2-1 provides the status, the number of GNSS satellites that have been already launched and that are currently operational, the targeted number of GNSS satellites, and the coverage of the GNSS constellation.

Table 2-1 Current and future GNSS constellations

GNSS constellation	Status	Number of operational satellites	Targeted number of operational satellites	Coverage
GPS (American system)	Operational	31 (US Air Force ensures availability of at least 24 satellites 95% of the time) [15], [21]	At least 24 satellites 95% of the time	Worldwide
Galileo (European system)	Operational	24 [18]	24+6 from 2021 [18]	Worldwide
GLONASS (Russian system)	Operational	23 [16], [22]	24 [16]	Worldwide
BeiDou/Com-pass (Chinese system)	Operational	8 GEO, 10 IGSO, 26 MEO [17]	5 GEO, 3 IGSO, 27 MEO [17]	China and the neighboring regions in 2012 (BDS-2), worldwide from 2020 (BDS-3)
QZSS (Japanese system)	Under development	4 (1 geostationary and 3 quasi-zenith orbit satellites) [20]	7 (geostationary and quasi-zenith orbit satellites) [20]	East Asia, and Oceania
IRNSS (Indian system)	Under development	3 GEO (2+1 spare), 4 IGSO [19]	7 (geostationary and non-geostationary satellites) [19]	India and the neighboring areas

This document focuses on GPS and Galileo systems since they both are currently operational and are used in the thesis. BeiDou and GLONASS systems are also introduced briefly because of their global nature. QZSS and IRNSS are not detailed in this document since they will only cover East Asia/Oceania and India, respectively.

2.1.2. Global Positioning System (GPS): General Presentation and Signals

2.1.2.1. GPS Services

The Global Positioning System (GPS) is a space-based radio-positioning and time transfer system. GPS provides accurate position, velocity, and time information to an unlimited number of suitably equipped ground, sea, air, and space users. Two levels of service are provided by GPS [23]:

- The Precise Positioning Service (PPS). The PPS is an accurate positioning velocity and timing service which is available only to authorized users. The PPS is primarily intended for military purposes. Authorization to use the PPS is determined by the U.S. Department of Defense. Access to the PPS is controlled by two features using cryptographic techniques, Selective Availability (SA) and Anti-Spoofing (A-S). SA is used to reduce GPS position, velocity, and time accuracy for unauthorized users. SA operates by introducing pseudorandom errors into the satellite signals. In May 2000, at the direction of President Bill Clinton, the U.S government discontinued its use of Selective Availability to make GPS more responsive to civil and commercial users worldwide. In September 2007, the U.S. government announced its decision to procure the future generation of GPS satellites, known as GPS III, without the SA feature. Doing this will make the policy decision of 2000 permanent and eliminate a source of uncertainty in GPS performance that had been of concern to civil GPS users worldwide.
- The Standard Positioning Service (SPS). The SPS is a less accurate positioning and timing service which is available to all GPS users. The SPS is primarily intended for civilian purposes.

In order to provide SPS and PPS, GPS consists of three different segments: a space segment, a control segment, and a user segment. These segments are presented in the next paragraph.

2.1.2.2. GPS Infrastructure

Space segment [23]

The space segment consists of a nominal constellation of 24 satellites in semi-synchronous (approximately 11 hours and 58 minutes) orbits. The extra satellites may increase GPS performance but are not considered part of the core constellation [21]. The satellites are arranged in six orbital planes with four satellites in each plane. The orbital planes have an inclination angle of 55 degrees relative to the earth's equator. The satellites have an average orbit altitude of 20200 kilometers above the surface of the earth. The operational satellites are designated Block II, Block IIA, Block IIR, Block IIR-M, and Block IIR-F. The future generation of satellites is designated Block III satellites.

The United States is committed to maintaining the availability of at least 24 operational GPS satellites, 95% of the time. To ensure this commitment, the U.S. Space Force has been flying more than 30 operational GPS satellites for well over a decade. As of June 15, 2021, there were a total of **31 operational satellites** in the GPS constellation [21], not including the decommissioned, on-orbit spares.

The GPS constellation is a mix of old and new satellites [21]. The following Figure 2-1 summarizes the features of the current and future generations of GPS satellites, including Block IIA (2nd generation, "Advanced"), Block IIR ("Replenishment"), Block IIR-M ("Modernized"), Block IIF ("Follow-on"), GPS III, and GPS IIIF ("Follow-on"). in 2021.

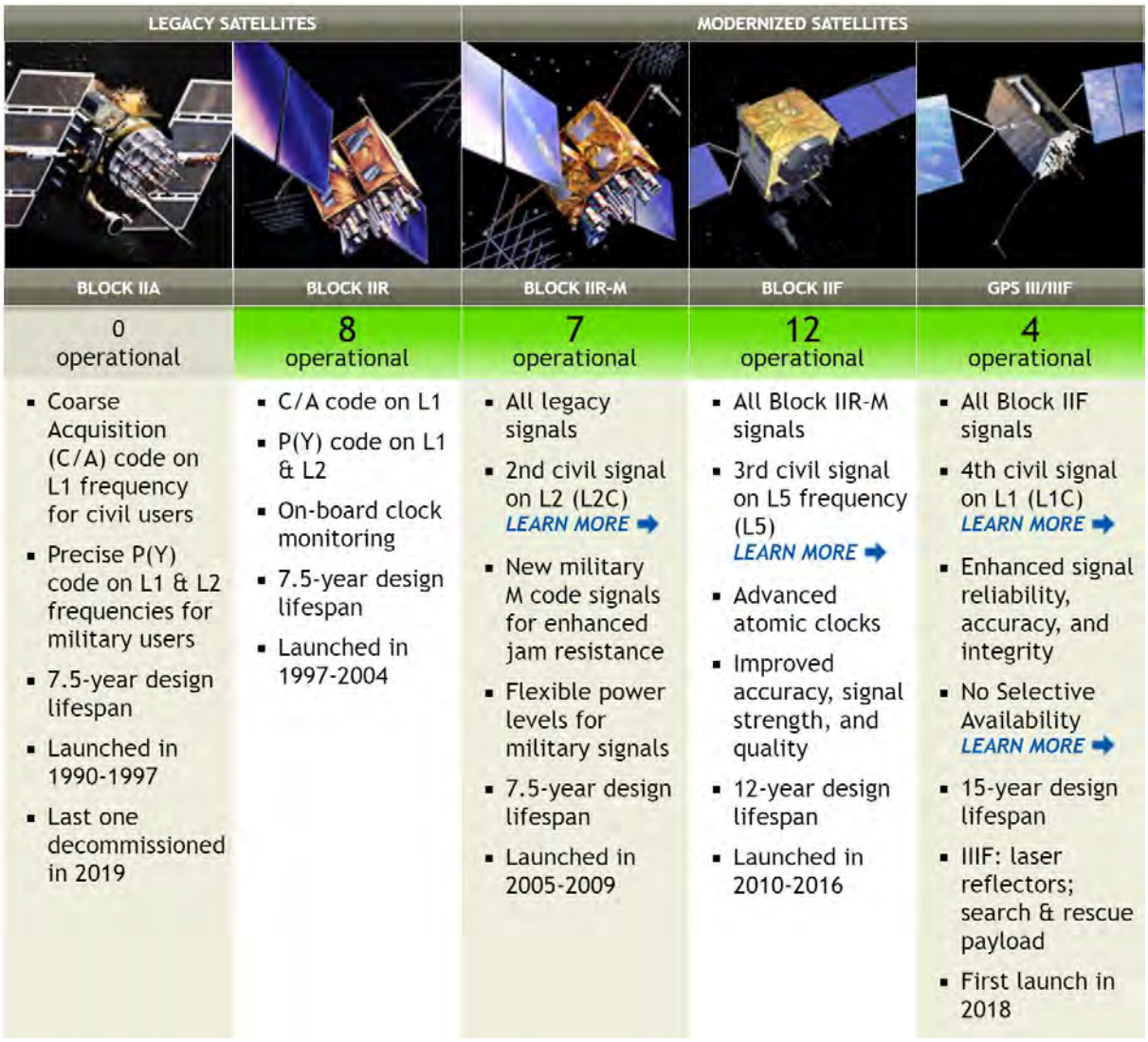

Figure 2-1 GPS Constellation Status in 2021 (Figure from [21])

Control segment [23]

The Control Segment primarily consists of a Master Control Station (MCS), at Falcon Air Force Base in Colorado Springs, USA, plus Monitor Stations (MS) and ground antennas at various locations around the world.

The MCS is the central processing facility for the Control Segment and is responsible for monitoring and managing the satellite constellation. The MCS functions include:

- control of satellite station-keeping maneuvers,
- regularly updating the navigation messages transmitted by the satellites,
- satellite health monitoring,
- maintenance activities.

The MS passively tracks all GPS satellites in view, collecting ranging data from each satellite. This information is transmitted to the MCS where the satellite ephemeris and clock parameters are estimated and predicted. The MCS uses the ground antennas to periodically upload the ephemeris and clock data to each satellite for retransmission in the navigation message. Communications between

the MCS the MS and ground antennas are typically accomplished via the U.S. Defense Satellite Communication System.

User segment [23]
The user segment consists of receivers specifically designed to receive, decode, and process the GPS satellite signals. Receivers can be stand-alone, integrated with, or embedded into other systems. GPS receivers can vary significantly in design and function, depending on their application for navigation, accurate positioning, time transfer, surveying, and attitude reference.

The following paragraph aims at describing the GPS navigation signals transmitted by the GPS satellites.

2.1.2.3. GPS Signals

The first part of this section aims at presenting several concepts which have been used to design GPS and Galileo signals. The second part provides an overview of the GPS frequency plan. Finally, GPS signals that can be used in civil aviation are described.

2.1.2.3.1. Background

Binary Phase Shift Keying (BPSK) modulation
The modulation of GPS and Galileo signals is based on the BPSK modulation technique. In the BPSK signals case, a data waveform, and a Radio Frequency (RF) carrier are combined by multiplication. The data waveform takes on a value of either +1 or -1 for each successive interval of $T_d = 1/f_d$ seconds, where f_d is the data rate in bits per second (bps) or Hertz (Hz). The RF carrier is transmitted with or without a 180° phase shift over successive intervals of time depending on the value of the data waveform. The data waveform is a baseband signal since its Power Spectral Density (PSD) is concentrated around 0 Hz. In the BPSK signals case, the data waveform is modulated by the RF carrier, leading to center the PSD of the BPSK signal about the carrier frequency. Hence, BPSK signals are bandpass signals.

Direct Sequence Spread Spectrum (DSSS) signals and Code Division Multiple Access (CDMA) concepts
DSSS is an extension of the BPSK modulation technique. All GNSS signals are DSSS signals. In the DSSS signals case, two waveforms are combined by multiplication and the resulting signal is multiplied by the RF carrier. These waveforms are:

- the data waveform or navigation message that contains the different types of data needed to perform positioning [24]. More specifically, the following data are provided. Almanac data are needed to indicate the position of all the satellites in the constellation with reduced accuracy. Ephemeris data are needed to indicate the position of the satellite to the user receiver. Ionospheric model parameters are needed to correct partially the ionospheric delay that affects the travel time between the transmission of the signal by the satellite and the reception of the signal by the receiver. Time and clock correction parameters are needed to compute the offset of the physical satellite signal time of transmission relative to the satellite signal time of transmission in the appropriate system time. The signal heath status, the navigation data validity and signal-in-space (SIS) accuracy information provide information about the accuracy and validity of the signal and of its content. Time parameters are needed to derive time in the appropriate system time and in the Universal Time Coordinated (UTC). Indeed, ICAO mentions

that "the time data provided by the GNSS to the user shall be expressed in a time scale that takes the Universal Time Coordinated (UTC) as reference" [14].

- the spreading or Pseudo Range Noise (PRN) waveform, which is similar to the data waveform, but with a much higher symbol rate. The symbol rate of the spreading waveform is called chip rate and is referred to as f_c in the following. A chip is the basic duration over which the spreading waveform assumes a constant value. The duration of each chip is $T_c = 1/f_c$, where T_c is called chip period. The spreading waveform is periodic, and the finite sequence of bits needed to generate the spreading waveform is referred to as PRN code.

Moreover, the data symbols and PRN codes broadcast by GPS and Galileo satellites are modeled as coin-flip sequences. Coin-flip sequences are defined as "sequences that randomly assume values of either +1 or -1 with each outcome occurring with equal probability and with each value being independent of other values". As PRN codes are assumed to be coin-flip sequences, the autocorrelation function of the PRN signal c(.) is given by [25]:

$$R(\tau) = \int_{-\infty}^{+\infty} g(t)g^*(t-\tau)dt \tag{2-1}$$

where:

- * denotes complex conjugation,
- g(.) corresponds to the materialization of the PRN sequence $\{c_k\}$ resulting in the PRN signal c(.):

$$c(t) = \sum_{k=-\infty}^{+\infty} c_k g(t - kTc) \tag{2-2}$$

The Power Spectral Density (PSD) function is defined as the Fourier transform of the autocorrelation function [25]:

$$G(f) = \int_{-\infty}^{+\infty} R(\tau)exp\,(-j2\pi f\tau)d\tau \tag{2-3}$$

where:

- R(.) is the autocorrelation function of the PRN signal c(.). The mathematical expression of R(.) is provided by **Equation (2-1)**.

In addition, the cross-correlation function does not present any significant peak, so any PRN code is almost uncorrelated with any other PRN code.

In GPS and Galileo systems, each satellite has its own PRN code, and each PRN code is considered as a coin-flip sequence. This enables multiple satellites to transmit signals simultaneously and at the same frequency. The transmission of multiple DSSS signals having different spreading sequences on a common carrier frequency is referred to as Code Division Multiple Access.

BPSK-R signals

BPSK-R signals are a category of DSSS signals that employ rectangular shapes for the spreading sequence and data navigation message sequence materialization. The mathematical expression of the spreading waveform corresponding to BPSK-R signals is given by [25]:

$$C_{BPSK-R}(t) = \sum_{k=-\infty}^{+\infty} c_k \frac{1}{\sqrt{T_c}} rect_{T_c}(t - kT_c) \tag{2-4}$$

where:

- $\{c_k\}$ is the PRN sequence,
- T_c is the chip duration,
- $rect_{T_c}(.)$ is the rectangular function defined as:

$$rect_{Tc}(t) = \begin{cases} 1, & 0 \le t \le T_c \\ 0, & elsewhere \end{cases}$$

Using **Equations (2-1), (2-3)**, and **(2-4)**, the auto-correlation function and power spectral density function for unit-power BPSK-R signals are:

$$R_{BPSK-R}(\tau) = \begin{cases} 1 - \frac{|\tau|}{T_c}, & |\tau| \le T_c \\ 0, & elsewhere \end{cases} \tag{2-5}$$

$$G_{BPSK-R}(f) = T_c sinc^2(\pi f T_c)$$

It is noted that the notation BPSK-R(n) is often used to denote a BPSK-R signal with a chip rate equal to: $R_{c,BPSK-R(n)} = n \times 1.023\ MHz.$

Binary Offset Carrier (BOC) signals

BOC signals are a category of DSSS signals that are the product of a BPSK-R signal with a square wave subcarrier for the spreading sequence and data navigation message sequence materialization. The sub-carrier is the sign of a sine or a cosine waveform, and the resulting signal is a sine-phased or a cosine-phased BOC signal respectively. **Equation (2-6)** provides the mathematical expression of a spreading waveform modulated by a BOC sine-phased and cosine-phased signal respectively:

$$\begin{aligned} C_{BOC}(t) &= C_{BPSK-R}(t) sign[sin(2\pi f_s t)] \\ C_{BOC}(t) &= C_{BPSK-R}(t) sign[cos(2\pi f_s t)] \end{aligned} \tag{2-6}$$

where:

- $C_{BPSK-R}(.)$ is the spreading waveform corresponding to BPSK-R signals. The mathematical expression of $C_{BPSK-R}(.)$*is* given by **Equation** (**2-4**),
- f_s is the sub-carrier frequency.

It is noted that the notation BOC(m,n) is often used to denote a BOC signal with a chip rate and a sub-carrier frequency provided by respectively:

$$\begin{aligned} f_{c,BOC(m,n)} &= n \times 1.023\ MHz \\ f_{s,BOC(m,n)} &= m \times 1.023\ MHz \end{aligned} \tag{2-7}$$

The autocorrelation functions for unit-power sine-phased and cosine-phased BOC signals are given in [25]. The power spectral density functions for unit-power sine-phased and cosine-phased BOC signals are given by respectively [26]:

$$\begin{aligned} G^{sin}_{BOC(m,n)}(f) &= f_c \left[\frac{sin\left(\frac{\pi f}{f_{c,BOC(m,n)}}\right) sin\left(\frac{\pi f}{2f_{s,BOC(m,n)}}\right)}{\pi f cos\left(\frac{\pi f}{2f_{s,BOC(m,n)}}\right)} \right]^2 \\ G^{cos}_{BOC(m,n)}(f) &= f_c \left[\frac{2sin\left(\frac{\pi f}{f_{c,BOC(m,n)}}\right) sin^2\left(\frac{\pi f}{4f_{s,BOC(m,n)}}\right)}{\pi f cos\left(\frac{\pi f}{2f_{s,BOC(m,n)}}\right)} \right]^2 \end{aligned} \tag{2-8}$$

2.1.2.3.2. Frequency bands

In the first years of GPS, two RF carriers have been used to modulate the GPS spreading codes and navigation messages: L1 and L2 carriers that are characterized by the carrier frequencies f_{L1} and f_{L2} equal to 1575.42 MHz and 1227.60 MHz respectively. The civilian spreading code referred to as Coarse/Acquisition (C/A) code is modulated by GPS-L1 carrier and the military spreading code referred to as Precision (P) code is modulated by both GPS-L1 and GPS-L2 carriers. In the following, the GPS-L1 signal component that carries the C/A code and that can be used by civil users is referred to as the GPS-L1 C/A signal.

In recent years, the satellite constellation has been upgraded. Indeed, a civil code has been added on GPS-L2 signal, referred to as GPS-L2C, and a new military spreading code called Military (M) code has been added on both GPS-L1 and GPS-L2 signals. In addition, Block IIR-M and Block II-F satellites emit a new civil signal. This signal is a GPS-L5 signal and is characterized by the carrier frequency f_{L5} equal to 1176.45 MHz. The first launch of a block II-F satellite was in 2009 [27]. The full operation of the GPS-L5 signal is planned for 2027, as of Jan 2020 [28]. Finally, the current Block III satellites emit a third civil signal referred to as the GPS-L1C signal on the L1 carrier. In 2010, the first launch of a GPS block-III satellite was done in 2018. As of Jan 2020, it is broadcast by 4 satellites, and the full operation of the GPS-L1C signal is planned for the end of the decade.

Figure 2-2 depicts the current and future GPS frequency plan. In Figure 2-2, ARNS stands for Aeronautical Radio Navigation Services and RNSS stands for Radio Navigation Satellite Services.

As shown in Figure 2-2, the L2 frequency band does not belong to the ARNS band. As a conclusion, the GPS-L2 signal cannot be used by civil aviation users and is not described in this document. The following

paragraphs aim at presenting the structure of the GPS civil signals that can be used in civil aviation: GPS-L1 C/A, GPS-L1C, and GPS-L5 signals.

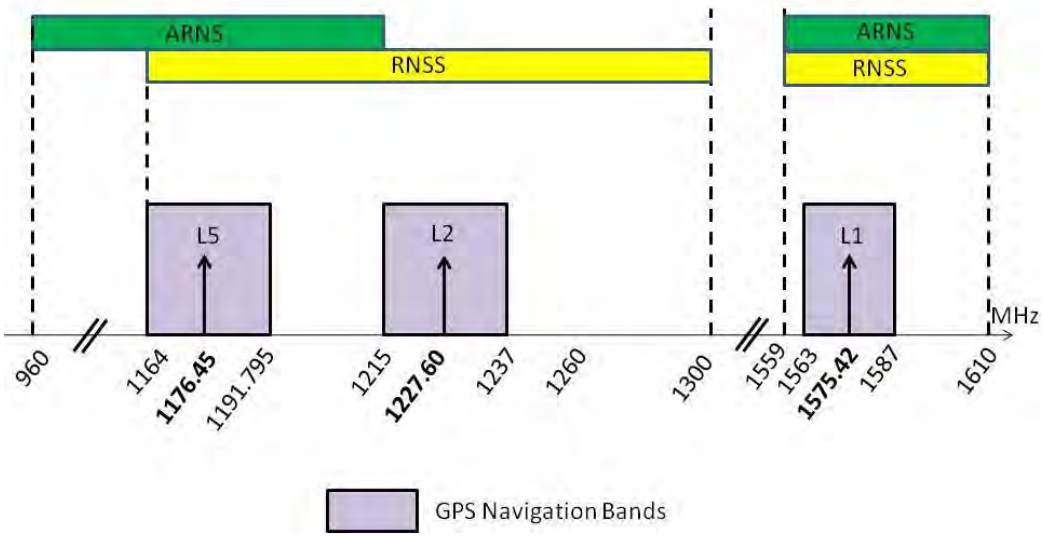

Figure 2-2 GPS current and future frequency plan [15]

2.1.2.3.3. GPS-L1 C/A signal

GPS-L1 C/A signal: temporal characteristics

The GPS-L1 signal consists of two carrier components which are in phase quadrature with each other. Each carrier component is multiplied by the combination of two waveforms. The resulting signal is a DSSS signal. One carrier component is multiplied by the modulo-2 sum of the C/A code and the GPS navigation message. The other carrier component is multiplied by the modulo-2 sum of the P-code and the GPS navigation message [15]. The mathematical expression of GPS-L1 signal broadcast by a GPS satellite i is given by [29]:

$$s_{L1}^{i}(t) = \sqrt{\frac{P}{2}} c_{C/A,i}(t) d_i(t) \cos(2\pi f_{L1} t + \theta) + \sqrt{\frac{P}{2}} c_{P,i}(t) d_i(t) \sin(2\pi f_{L1} t + \theta) \quad (2\text{-}9)$$

where:

- P is the mean radiated power,
- $c_{C/A,i}(.)$ is the PRN signal emitted by the i-th satellite corresponding to the rectangular materialization of the i-th satellite C/A code,
- $d_i(.)$ is the navigation signal emitted by the i-th satellite corresponding to the rectangular materialization of the i-th satellite navigation message,
- f_{L1} is the carrier frequency of GPS-L1 signals, $f_{L1} = 1575.42$ MHz
- θ is the phase on L1,
- $c_{P,i}(t)$ is the PRN signal emitted by the i-th satellite corresponding to the rectangular materialization of the i-th satellite P-code,
- t is the time in seconds expressed in the satellite generated time scale:

$$t = t_{GPS} - \Delta t_S^i \quad (2\text{-}10)$$

where:

- t_{GPS} is the time expressed in GPS time,
- Δt_S^i is the i-th satellite clock offset.

It is noted that civilian users can only track the C/A component of the GPS-L1 signal since they have no knowledge about the military P-code. In the following, GPS-L1 C/A denotes the C/A component of the GPS-L1 signal. The mathematical expression of the GPS-L1 C/A signal emitted by the i-th GPS satellite is as follows:

$$s_{L1\,C/A}^i(t) = \sqrt{\frac{P}{2}} c_{C/A,i}(t) d_i(t)\, cos(2\pi f_{L1} t + \theta) \tag{2-11}$$

The structures of the C/A code and the data navigation message are detailed below.

Description of the GPS-L1 C/A spreading code

The C/A code consists of a 1023-bit PRN code with a clock rate of 1.023MHz. Thus, the C/A code repeats every 1 millisecond. A different PRN is assigned to each GPS satellite and selected from a set of codes called Gold codes. The Gold codes are designed to minimize the probability that a receiver will mistake one code for another (minimize the cross-correlation).

Description of the GPS-L1 C/A navigation message

The navigation message consists of 25 frames of data, each frame consisting of 1,500 bits. Each frame is divided into 5 sub-frames of 300 bits each. At the 50 Hz transmission rate, it takes 12.5 minutes to receive all 25 frames [23].

The navigation message includes data unique to the transmitting satellite and data common to all satellites. Sub-frames 1, 2, and 3 have the same data format for all 25 frames. This allows the receiver to obtain critical satellite-specific data within 30 seconds. More specifically [23]:

- Sub-frame 1 contains the clock correction for the transmitting satellite, as well as parameters describing the accuracy and health of the broadcast signal.
- Sub-frames 2 and 3 contain ephemeris (precise orbital) parameters used to compute the location of the satellite for the positioning equations.
- Sub-frames 4 and 5 have data that cycle through the 25 data frames. They contain data that is common to all satellites and less critical for a receiver to acquire quickly. Sub-frames 4 and 5 contain almanac (coarse orbital) data and low-precision clock corrections, simplified health and configuration status for every satellite, user text messages, and the coefficients for the ionospheric model and UTC calculation.

GPS-L1 C/A signal: spectral characteristics

As the C/A codes are assumed to be coin-flip sequences and as a rectangular materialization is used to transmit the C/A codes, the mathematical expression for the autocorrelation function of the unit-power C/A spreading signal is as follows:

$$R_{L1\,C/A}(\tau) = \begin{cases} 1 - \dfrac{|\tau|}{Tc}, |\tau| \le Tc \\ 0, elsewhere \end{cases} \tag{2-12}$$

By computing the Fourier transform of Equation (2-12), the PSD of the unit-power GPS-L1 C/A baseband signal is as follows:

$$G_{L1\,C/A}(f) = T_c sinc^2(\pi f T_c) \tag{2-13}$$

As explained before, only the GPS-L1 data channel can be used by civil users. It implies that the coherent integration time for the correlation process in a GPS receiver is limited by the length of a data bit. To avoid this problem, new civil signals such as GPS-L1C and GPS-L5 signals have a data-free channel, allowing extending the integration time. This leads to an increase in accuracy, tracking sensitivity, and robustness. The following sections aim at presenting the GPS-L1C and GPS-L5 signals.

2.1.2.3.4. GPS-L1C signal

Several reasons have motivated the design of a new civil GPS signal on L1. Firstly, the GPS-L1C signal has been designed to overcome the deficiencies of the GPS-L1 C/CA signal (this signal has no pilot carrier, and the C/A PRN code is relatively short and has poor correlation performance). Secondly, the United States / European Union agreement in 2004 requires a new civil GPS signal interoperable with the future civil Galileo signal called Galileo E1 signal. GPS-L1C and Galileo E1 signals use the same carrier frequency (L1 frequency) and have the same spectral characteristics.

GPS-L1C signal will be emitted by all Block III satellites. The launch of the first Block III satellite is planned for 2013, and GPS-L1C should be fully operational by 2026 [28]. The GPS-L1C signal structure is specified in [23] and summarized below.

GPS-L1C signal: temporal characteristics

The GPS-L1C signal consists of two main components:

- the pilot component is modulated by the modulo-2 sum of a spreading code and an overlay code,
- the data component is modulated by the modulo-2 sum of another spreading code and a data navigation message.

The mathematical expression of the GPS-L1C signal emitted by the i-th GPS satellite is given by:

$$\begin{aligned} s^i_{GPS-L1C}(t) = &\sqrt{\frac{P}{4}} c_{LIC-D,i}(t) d_{L1C,i}(t)\, cos(2\pi f_{L1} t + \theta) \\ &+ \sqrt{\frac{P}{4}} c_{L1C-P,i}(t) c_{overlay,i}(t) sin(2\pi f_{L1} t + \theta \end{aligned} \tag{2-14}$$

Where:

- $c_{\mathrm{LIC-D,i}}(.)$ is the PRN signal emitted by the i-th satellite on the data channel,
- P is the mean radiated power,
- $d_{\mathrm{L1C,i}}(.)$ is the data navigation waveform emitted by the i-th satellite,
- $c_{\mathrm{L1C-P,i}}(.)$ is the PRN signal emitted by the i-th satellite on the pilot channel,
- $c_{\mathrm{overlay,i}}(.)$ is the overlay signal emitted by the i-th satellite on the pilot channel,
- f_{L1} is the carrier frequency of GPS-L1C signals, $f_{L1} = 1575.42$ MHz,
- θ is the phase on L1.

Equation (2-14) shows that 75% of the total power is allocated to the pilot channel and 25% to the data channel. The structures of the PRN codes, the overlay code, and the data navigation message are detailed below.

Description of GPS-L1C spreading codes

The PRN sequences $\{c_{LIC-D,i,k}\}$ and $\{c_{LIC-P,i,k}\}$ (Weil codes) emitted by the i-th satellite on the data and pilot channels respectively are independent and time-synchronized. The chip rate of the PRN codes is equal to 1.023 MHz and the PRN code length is 10,230 chips. The period of each PRN code is equal to 10 ms. The design of Weil codes based on Legendre sequences is detailed in [23].

The overlay codes are independent, time-synchronized, and 18 seconds in length at a rate of 100 bps, for a total length of 1800 bits. The functional description of overlay codes is given in [23].

Description of the GPS-L1C navigation message

The GPS-L1C data navigation message is called Civil Navigation 2 (CNAV2) message. The data navigation message consists of a frame and 3 sub-frames. A frame is 883 bits long and it takes 18 seconds to transmit a frame. The structure and content of each sub-frame are detailed below:

- Sub-frame 1 is 9 bits long and consists of the Time Of Interval (TOI) data. The TOI data correspond to the time epoch at the start of the next following frame.
- Sub-frame 2 is 600 bits long and consists of non-variable clock and ephemeris data with Cyclic Redundancy Check (CRC) bits. CRC bits aim at protecting against burst and random errors in the transmission of navigation data. The content of sub-frame 2 does not vary over 15 minutes. The satellite position computation from the ephemeris parameters is provided in [30].
- Sub-frame 3 is 274 bits long. The content of sub-frame 3 varies from one frame to the next one and is identified by a page number. Hence, multiple frames are required to broadcast the complete data navigation message.

Sub-frames 2 and 3 are encoded using Forward Error Correction (FEC) code.

GPS-L1C signal modulation

The bit stream of the data component, L1C-D, consists of the modulo-2 sum of the data PRN code and of the navigation message. This bit stream is modulated using BOC(1,1) modulation. The bit stream of the pilot component, L1C-P, consists of the modulo-2 sum of the pilot PRN code and of the overlay code. This bit stream is modulated using a Time Multiplexed Binary Offset Carrier (TMBOC) modulation technique. TMBOC technique uses a mixture of BOC(1,1) symbols and BOC(6,1) symbols. All the bits of the pilot component are modulated using BOC(1,1) modulation, except 4 bits every 33 bit sequences which are modulated using BOC(6,1) modulation technique.

GPS-L1C signal: spectral characteristics

As 75% of the total power is allocated to the pilot component and 25% to the data component, the normalized PSD of the baseband signal is given by:

$$G_{GPS-L1C}(f) = \frac{3}{4}G_{pilot}(f) + \frac{1}{4}G_{data}(f) \quad (2\text{-}15)$$

where:

- $\mathrm{G}_{\mathrm{pilot}}(.)$ is normalized the PSD function of the pilot channel:

$$G_{pilot}(f) = \frac{29}{33} G_{BOC(1,1)}(f) + \frac{4}{33} G_{BOC(6,1)}(f)$$

- $\mathrm{G}_{\mathrm{data}}(.)$ is normalized the PSD function of the data channel:

$$G_{data}(f) = G_{BOC(1,1)}(f)$$

Hence, **Equation (2-15)** leads to:

$$G_{GPS-L1C}(f) = \frac{10}{11} G_{BOC(1,1)}(f) + \frac{1}{11} G_{BOC(6,1)}(f) \quad (2\text{-}16)$$

By using **Equation (2-9)**, **Equation (2-16)** becomes:

$$G_{GPS-L1C}(f) = \frac{f_c}{11\pi^2 f^2} sin^2\left(\frac{\pi f}{f_c}\right)\left[10tan^2\left(\frac{\pi f}{2f_c}\right) + tan^2\left(\frac{\pi f}{12f_c}\right)\right] \quad (2\text{-}17)$$

GPS-L1C signal: advantages

The structure of the GPS-L1C signal leads to improve the performance of this signal in comparison with the current civil GPS-L1 C/A signal. Some examples of the improvements brought by the GPS-L1C signal are listed below, and an exhaustive listing of improvements is provided in [31] and [32].

Firstly, the overlay code and the longer spreading codes allow a better protection against narrow band interference and cross satellite interference. Moreover, the Weil codes approach ideal correlation properties, and that leads to a decrease in the probability to confuse the secondary lobes with the main lobe during acquisition.

Secondly, the new message structure and the FEC coding allow demodulation of navigation message data at the lowest signal tracking threshold.

Finally, the signal power is unequally split between data and pilot parts allowing a better code and carrier tracking threshold.

2.1.2.3.5. GPS-L5 signal

Several reasons have motivated the design of a third and more powerful civil GPS signal. For civil aviation users, GPS-L5 signal is the second ARNS signal. The utilization of two frequency bands, L1 and L5 bands, will enable airborne estimation of the dispersive ionospheric delay [33]. It is important to estimate the additional delays on the travel times between the satellites and the receiver caused by the ionosphere since it is one of the main error that affect the pseudo-range estimates. In addition, the Receiver Autonomous Integrity Monitoring (RAIM) will be more efficient if both GPS-L1 and GPS-L5 signals are used [33]. Finally, GPS-L5 signals are more powerful than the other GPS signals and will enable aircrafts to make precision landings in high multipath environments.

The first satellite of the new Block IIR-M capable of broadcasting GPS-L5 signal was launched in March 2010 and began to broadcast GPS-L5 signal in April 2010. Until May 2021, 16 GPS satellites are broadcasting L5 signals, and the signals are considered pre-operational, scheduled to reach 24 fully

operational satellites by approximately by 2027, [28] specifies the GPS-L5 signal structure. This structure is summarized below.

GPS-L5 signal: temporal characteristics

The GPS-L5 signal consists of two main components:

- the pilot (quadrature phase) component is modulated by the modulo-2 sum of a spreading code and a synchronization sequence,
- the data (in-phase) component is modulated by the modulo-2 sum of another spreading code, another synchronization sequence, and a data navigation message.

The mathematical expression of the GPS-L5 signal emitted by the i-th GPS satellite is given by:

$$s^{i}_{GPS-L5}(t) = \sqrt{\frac{P}{2}} c_{L5-D,i}(t) d_{L5,i}(t) NH_{10}(t)\, cos(2\pi f_{L5} t + \theta) + \sqrt{\frac{P}{2}} c_{L5-P,i}(t) NH_{20}(t) sin\,(2\pi f_{L5} t + \theta) \quad (2\text{-}18)$$

where:

- $c_{L5-D,i}(.)$ is the PRN signal emitted by the i-th satellite on the data channel,
- P is the mean radiated power,
- $d_{L5,i}(.)$ is the data navigation waveform emitted by the i-th satellite,
- $c_{L5-P,i}(.)$ is the PRN signal emitted by the i-th satellite on the pilot channel,
- $NH_{10}(.)$ is the synchronization signal on the data channel,
- $NH_{20}(.)$ is the synchronization signal on the pilot channel,
- f_{L5} is the carrier frequency of GPS-L5 signals, $f_{L5} = 1176.45$ MHz,
- θ is the phase on L5.

The structures of the PRN codes, the synchronization sequences, and the data navigation message are detailed below.

Description of GPS-L1C spreading codes

The PRN sequences $\{c_{L5-D,i,k}\}$ and $\{c_{L5-P,i,k}\}$ emitted by the i-th satellite on the data and pilot channels respectively are independent and time-synchronized. The chip rate of the PRN codes is equal to 10.23 MHz and the PRN code length is 10,230 chips. The period of each PRN code is equal to 1ms. The sequences generation is detailed in [15].

The synchronization sequences are referred to as Neuman-Hofman (NH) codes and are clocked at 1 kHz. Hence, the duration of the 10-bit NH code on the data channel and of the 20-bit NH code on the pilot channel is 10ms and 20 ms respectively. The 10-bit NH code serves to extend the length of the in-phase PRN code from 10 230 to 102 300 chips. The 20 bit NH code serves to extend the length of the quadrature-phase PRN code from 10,230 to 204,600 chips [33].

Description of the GPS-L5 navigation message

The GPS-L5 data navigation message is called Civil Navigation (CNAV) message. The data navigation message consists of 6 seconds and 300 bits long messages. The data stream is generated at 50 bps and

is encoded using FEC code allowing the receiver to correct errors introduced in the transmission due to noise and interference. Each message contains:

- a CRC parity block covering the entire 300-bit message,
- the Time Of Week (TOW) count,
- an alert flag that indicates to the users that the User Range Accuracy (URA) and/or the User Differential Range Accuracy (UDRA) may be worse than indicated in the navigation message.

The navigation data also contain the ephemeris, the clock, ionospheric and group delay, the almanac, and the clock and differential correction. [15] provides the equations needed to compute the satellite position, the satellite clock error, the ionospheric and group delay correction, the UDRA estimate, and the GPS to UTC conversion from the parameters broadcast in the navigation message.

GPS-L5 signal modulation

The bit streams of the data and pilot components are modulated using a BPSK-R modulation.

GPS-L5 signal: advantages

The new GPS-L5 signal has several advantages in comparison with the current GPS-L1 C/A signal. These advantages are presented in [33] and summarized below.

Firstly, the PRN code rate on L5 is ten times faster than the C/A code rate. This leads to improving the noise performance of the GPS receiver and reducing the tracking error. These yields also mitigate the effects of multipath relatively easily and decrease the vulnerability of the GPS-L5 signals to interference.

Secondly, the PRN codes on L5 are longer than the C/A code. This means that the auto-correlation and cross-correlation side lobes are lower than those for the C/A code. Hence, the probability of a false lock during signal acquisition is reduced.

Thirdly, the utilization of a new coding algorithm to modulate navigation message data decreases the probability of bit errors while demodulating the navigation message.

Finally, the data-free channel will decrease the signal-to-noise ratio required to acquire the signal.

2.1.3. Galileo System: General Presentation and Signals

2.1.3.1. Galileo Services

Galileo is the European global navigation satellite system providing a highly accurate, guaranteed, and global positioning service under civilian control. It is interoperable with GPS and GLONASS, the two other popular global satellite navigation systems [18]. The main missions of the Galileo are:

- Implementation of an independent GNSS that operates alongside existing and planned navigation and communication systems to provide enhancement and redundancy
- Improve European infrastructure (e.g., multi-modal transport) with global high-quality PVT
- Support of safety-of-life and critical applications, anticipate value-added supply, and create new markets

In order to provide these services, Galileo consists of three different segments: a space segment, a control segment, and a user segment. These segments are presented in the next paragraph.

2.1.3.2. Galileo Infrastructure

Space segment

The fully deployed Galileo system consists of 30 satellites (27 operational satellites and 3 in-orbit spare satellites), positioned in three circular Medium Earth Orbit planes at a nominal average orbit semi-major axis of 29,601.297 km, and at an inclination of the orbital planes of 56 degrees (55 degrees for GPS) with reference to the equatorial plane. Each satellite has an average altitude of 23,222 kilometers above the surface of the earth. Each operational satellite broadcasts a set of navigation signals carrying clock synchronization, ephemeris, integrity, and other data, depending on the particular signal.

Control segment

The Galileo Control Center controls the complete Galileo constellation, monitors the satellite health, and up-loads data for subsequent broadcast to users via the mission Uplink Stations (ULS) [18]. The key elements of this data such as clock synchronization, ephemeris, and integrity information are derived from measurements made by a worldwide network of Galileo Sensor Stations (GSS).

User segment

The user segment is the aggregate of all Galileo military or civilian receivers equipped capable to receive around 11 Galileo satellite signals to determine their positions within a few meters [18].

The following paragraph aims at describing the Galileo navigation signals transmitted by the Galileo satellites.

2.1.3.3. Galileo Signals

2.1.3.3.1. Frequency bands

Three independent CDMA signals, named E5, E6, and E1, are permanently transmitted by all Galileo satellites. The E5 signal is further sub-divided into two signals denoted E5a and E5b. The Galileo navigation Signals are transmitted in the four frequency bands indicated in Figure 3.1. These four frequency bands are the E5a, E5b, E6, and E1 bands. Figure 2-3 depicts the Galileo frequency plan.

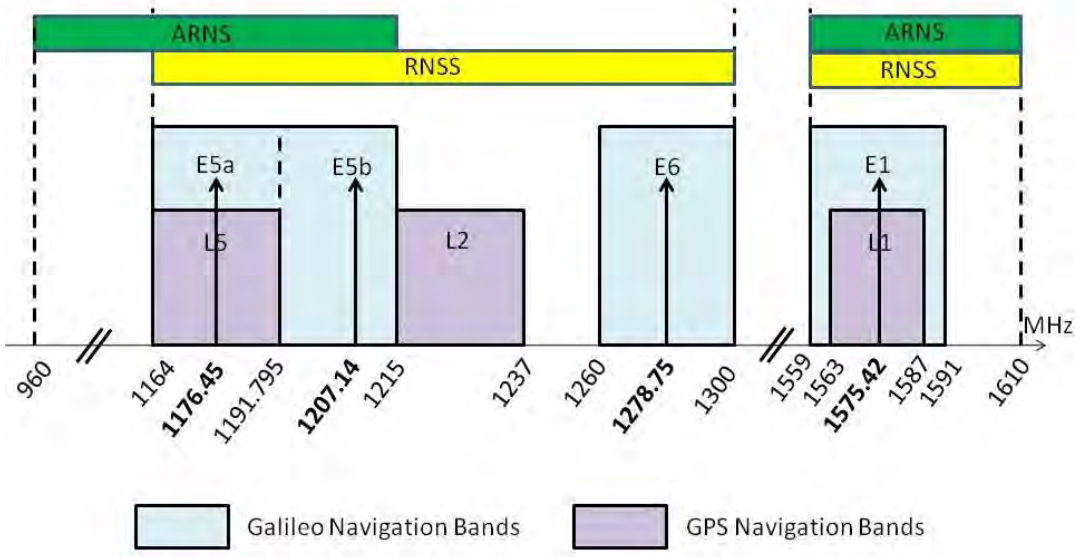

Figure 2-3 Galileo Frequency Plan [18]

As shown in Figure 2-3, the Galileo frequency bands have been selected in the allocated spectrum for RNSS and in addition to that, E5a, E5b, and E1 bands are included in the allocated spectrum for ARNS, employed by civil-aviation users [18]. E6 Galileo signal is not included in the ARNS band. Thus, this signal cannot be utilized in civil aviation and this document focuses only on E1, E5a, and E5b Galileo signals. [18] defines E1, E5a, and E5b Galileo signals as follows:

- The civil E1 Galileo signal consists of the E1-B and E1-C components. E1-B and E1-C are respectively data and pilot channels and are in phase with each other. It is noted that the military E1 Galileo signal consists of the E1-A component. As the E1-A component cannot be used by civil aviation users, this document does not take into account this component.
- The E5 Galileo signal consists of two signals E5a and E5b. Each E5a and E5b signal consists of a data channel transmitted in the in-phase component and a pilot channel transmitted in the quadrature component.

E1-B, E1-C, E5a, and E5b Galileo signal components will be used to provide one or more Galileo services [26]. Hence, the structure, temporal and spectral characteristics of E1-B, E1-C, E5a, and E5b Galileo signals are studied and developed in the next paragraphs.

2.1.3.3.2. Galileo E1 signal

Galileo E1 signal: temporal characteristics

The E1 Galileo signal modulation has been proposed in such a way that the Power Spectral Density (PSD) of the proposed solution would be identical for GPS L1C and Galileo E1 when the pilot and data components are computed together [26]. This allows high interoperability between both signals. The proposed modulation is a Composite Binary Offset Carrier (CBOC) modulation. The Galileo E1 signal consists of two main components:

- The pilot component which is modulated by a spreading code,
- The data component which is modulated by the modulo-2 sum of another spreading code and a data navigation message.

The mathematical expression of the Galileo E1 signal emitted by the i-th satellite is given by:

$$s_{E1}^{i}(t) = \sqrt{\frac{P}{2}} c_{E1-B,i}(t) d_{I/NAV,i}(t) CBOC\left(6,1,\frac{1}{11},'+'\right)(t)\, cos(2\pi f_{E1} t + \theta) + \sqrt{\frac{P}{2}} c_{E1-C,i}(t) CBOC(6,1,\frac{1}{11},'-')(t) sin\,(2\pi f_{E1} t + \theta) \quad (2\text{-}19)$$

where:

- $c_{E1-B,i}(.)$ is the materialization of the PRN code on the data component corresponding to the BPSK-R modulation,
- P is the mean radiated power,
- $d_{I/NAV,i}(.)$ is the materialization of the I/NAV data navigation message corresponding to the BPSK-R modulation,
- $CBOC\left(6,1,\frac{1}{11},'+'\right)(.)$ is the waveform that modulates the data stream on the data component,
- f_{E1} is the carrier frequency of Galileo E1 signals, $f_{E1} = 1575.42$ MHz
- θ is the phase

- $c_{E1-C,i}(.)$ is the materialization of the PRN code on the pilot component corresponding to the BPSK-R modulation,
- $\mathrm{CBOC}(6,1,\frac{1}{11},'-')(.)$ is the waveform that modulates the data stream on the pilot component.

Galileo E1 signal modulation

The bit streams of the data component E1-B and of the pilot component E1-C are modulated using a CBOC modulation or $MBOC\left(6,1,\frac{1}{11}\right)$ modulation, which is a particular implementation of the MBOC modulation technique. CBOC linearly combines BOC(1,1) and BOC(6,1) sub-carriers [Macabiau and al, 2007]. The bit streams of the data and pilot components are modulated by respectively:

$$\begin{aligned} CBOC\left(6,1,\frac{1}{11},'+'\right) &= \alpha.sc_{E1,BOC(1,1)}(t) + \beta.sc_{E1,OC(6,1)}(t) \\ CBOC\left(6,1,\frac{1}{11},'-'\right) &= \alpha.sc_{E1,BOC(1,1)}(t) - \beta.sc_{E1,BOC(6,1)}(t) \end{aligned} \quad (2\text{-}20)$$

where:

- $sc_{E1,BOC(1,1)}(t) = sgn\left(sin\left(2\pi fs_{E1-BOC(1,1)}t\right)\right)$
- $sc_{E1,BOC(6,1)}(t) = sgn\left(sin\left(2\pi fs_{E1-BOC(6,1)}t\right)\right)$
- $fs_{E1-BOC(1,1)}$ and $fs_{E1-BOC(6,1)}$ are the sub-carrier rates of the sub-carriers $sc_{E1-BOC(1,1)}$ and $sc_{E1-BOC(6,1)}$, respectively. From the presentation of the BOC modulation provided in Section 2.1.2.3.1, the values of $fs_{E1-BOC(1,1)}$ and $fs_{E1-BOC(6,1)}$ are, respectively:

$$fs_{E1-BOC(1,1)} = 1 \times 1.023\ MHz$$

$$fs_{E1-BOC(6,1)} = 6 \times 1.023 = 6.138\ MHz$$

- Parameters α and β are given by:

$$\begin{cases} \alpha = \sqrt{\frac{10}{11}} \\ \beta = \sqrt{\frac{1}{11}} \end{cases}$$

Galileo E1 signal: spectral characteristics

The normalized PSD (specified without the effect of band-limiting filters and payload imperfections) of the E1 Galileo baseband signal has the same expression as the normalized PSD of the GPS-L1C baseband signal. This expression is given by [26]:

$$G_{MBOC\left(6,1,\frac{1}{11}\right)}(f) = \frac{10}{11}G_{BOC(1,1)}(f) + \frac{1}{11}G_{BOC(6,1)}(f) \quad (2\text{-}21)$$

where:

- $G_{BOC(1,1)}$ is the PSD of the BOC(1,1) frequency component:

$$G_{BOC(1,1)}(f) = f_c \left[\frac{sin\left(\frac{\pi f}{f_c}\right) sin\left(\frac{\pi f}{2f_c}\right)}{\pi f cos\left(\frac{\pi f}{2f_c}\right)} \right]^2$$

- $G_{BOC(6,1)}$ is the PSD of the BOC(6,1) frequency component:

$$G_{BOC(6,1)}(f) = f_c \left[\frac{sin\left(\frac{\pi f}{f_c}\right) sin\left(\frac{\pi f}{12f_c}\right)}{\pi f cos\left(\frac{\pi f}{12f_c}\right)} \right]^2$$

- f_c = 1.023MHz is the spreading code chip rate of the E1-B and E1-C Galileo signals.

Hence**, Equation (2-21)** leads to:

$$G_{MBOC\left(6,1,\frac{1}{11}\right)}(f) = \frac{f_c}{11\pi^2 f^2} sin^2\left(\frac{\pi f}{f_c}\right)\left[10tan^2\left(\frac{\pi f}{2f_c}\right) + tan^2\left(\frac{\pi f}{12f_c}\right)\right] \quad (2\text{-}22)$$

2.1.3.3.3. E5 Galileo signals

E5 Galileo signal: temporal characteristics

The proposed modulation is the Alternative Binary Offset Carrier (AltBOC) modulation which is a modified version of a BOC modulation. The mathematical expression of the Galileo E5 signal emitted by the i-th satellite is given by [Understanding the signal structure]:

$$s^i_{E5}(t) = Re(s^i_{E5,baseband}(t) exp\,(j2\pi f_{E5} t)) \quad (2\text{-}23)$$

where:

- Re(.) denotes the real part,
- $s^i_{E5,baseband}(.)$ is the Galileo E5 baseband signal,
- f_{E5} is the Galileo E5 center frequency, $f_{E5} = 1191.795\ MHz.$

E5 Galileo signal modulation

The spreading codes and navigation messages carried on E5a and E5b are modulated using an AltBOC(15,10) modulation technique. For this kind of modulation, the spreading code chip rate and the frequency of the sub-carrier used to modulate the bit streams are given by respectively:

$$f_{c,E5} = 10 \times 1.023 = 10.23\ MHz$$
$$f_{s,E5} = 15 \times 1.023 = 15.345\ MHz$$

The sub-carrier used to modulate the bit streams by the AltBOC modulation technique is the complex sum of the rectangular cosine and the rectangular sine. The following equation provides the expression of the complex sub-carrier which modulates the E5a and E5b bit streams:

$$c_s(t) = sign\left[cos\left(2\pi f_{S,E5} t\right)\right] + jsign\left[sin\left(2\pi f_{S,E5} t\right)\right] \quad (2\text{-}24)$$

The mathematical expression of the E5 Galileo baseband signal is provided by:

$$s^i_{E5,baseband}(t) = \left[e_{E5a-I,i}(t) + je_{E5a-Q,i}(t)\right]c_s(t) + \left[e_{E5b-I,i}(t) + je_{E5b-Q,i}(t)\right]c_s{}^*(t) \quad (2\text{-}25)$$

where:

- * denotes the complex conjugate.
- $c_s(.)$ is the sub-carrier used to modulate the PRN codes and data navigation messages.
- $e_{E5a-I,i}(.)$, $e_{E5a-Q,i}(.)$, $e_{E5b-I,i}(.)$ and $e_{E5b-Q,i}(.)$ are the waveforms corresponding to the materialization of the bit streams of the E5a data channel, E5a pilot channel, E5b data channel, and E5b pilot channel respectively:

$$e_{E5a-I,i}(t) = c_{E5a-I,i}(t)d_{F/NAV,i}(t)$$
$$e_{E5a-Q,i}(t) = c_{E5a-Q,i}(t)$$
$$e_{E5b-I,i}(t) = c_{E5b-I,i}(t)d_{I/NAV,i}(t)$$
$$e_{E5b-Q,i}(t) = c_{E5b-Q,i}(t)$$

- $c_{E5a-I,i}(.)$, $c_{E5a-Q,i}(.)$,$c_{E5b-I,i}(.)$and $c_{E5b-Q,i}(.)$ are the materializations of the PRN codes on the E5a data and pilot components and the E5b data and pilot components, respectively.
- $d_{F/NAV,i}(.)$ and $d_{I/NAV,i}(.)$ are the materializations of the F/NAV and I/NAV data navigation messages, respectively.

The structures of the spreading codes on the E5a and E5b data and pilot components and of the I/NAV and F/NAV data navigation messages are detailed in Sections 2.1.3.3.4

E5 Galileo signal: spectral characteristics

The normalized PSD of the E5 Galileo signal modulated by the AltBOC(m,n) modulation technique depends on the parity of the parameter $\varphi = 2 \times \frac{m}{n}$ which is odd for AltBOC(15,10) modulation. The normalized PSD of the constant envelope E5 baseband signal modulated by the AltBOC(15,10) modulation is provided by [26]:

$$G_{AltBOC(15,10)}(f) = \frac{4f_{C,E5}}{\pi^2 f^2} \times \frac{cos^2\left(\frac{\pi f}{f_{C,E5}}\right)}{cos^2\left(\frac{\pi f}{2f_{S,E5}}\right)} \times \left[cos^2\left(\frac{\pi f}{2f_{S,E5}}\right) - cos\left(\frac{\pi f}{2f_{S,E5}}\right) - 2cos\left(\frac{\pi f}{2f_{S,E5}}\right)cos\left(\frac{\pi f}{4f_{S,E5}}\right) + 2\right] \quad (2\text{-}26)$$

2.1.3.3.4. Galileo spreading codes

The Galileo spreading codes are built from so-called primary and secondary codes by using the construction of a tiered code described as follows. Spreading codes are generated by a tiered code construction, whereby a secondary code sequence is used to modify successive repetitions of a primary code period.

2.1.3.3.5. Galileo navigation message

As depicted in Table 2-2, the data channels of E1, E5a, and E5b Galileo signals [18], which are E1-B, E5a-I, and E5b-I respectively, transmit two types of navigation message: F/NAV and I/NAV.

Table 2-2 Navigation messages allocation to Galileo signal components [18]

Message type	Component
F/NAV	E5a-I
I/NAV	E5b-I and E1-B

The complete navigation message data are transmitted on each data component as a sequence of frames. A frame is composed of several sub-frames, and a sub-frame in turn is composed of several pages. The page is the basic structure for building the navigation message. The general structure of the F/NAV and I/NAV navigation messages are depicted in Figure 2-4 and Figure 2-5, respectively.

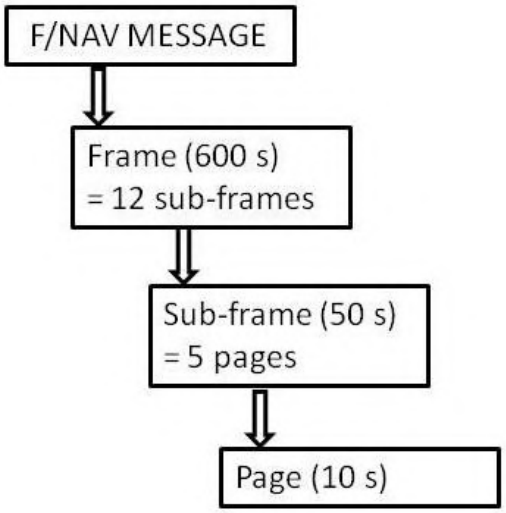

Figure 2-4: F/NAV message structure [18]

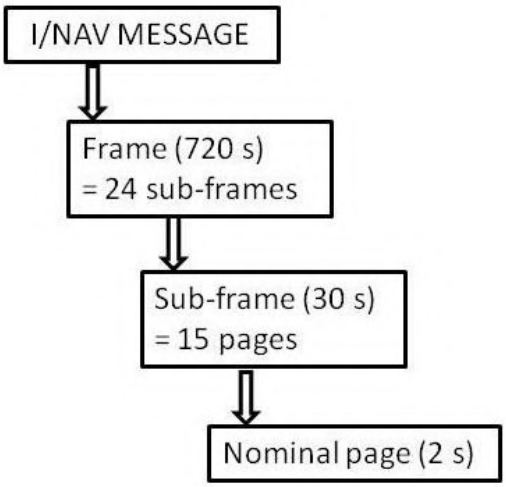

Figure 2-5: I/NAV message structure [18]

The navigation messages F/NAV and I/NAV contain all the parameters that enable the user to perform positioning service. They are stored on board each satellite with validity duration and broadcast worldwide by all the satellites of the Galileo constellation. The different types of data needed to perform positioning [18]:

- The Galileo System Time (GST) is composed of 2 parameters as follows:

  - The Week Number (WN) is an integer counter that gives the sequential week number from the origin of the Galileo time. This parameter is coded on 12 bits, which covers 4096 weeks (about 78 years). Then the counter is reset to zero to cover the additional period modulo 4096.

- The Time Of Week (TOW) is defined as the number of seconds that have occurred since the transition from the previous week. The TOW covers an entire week from 0 to 604799 seconds and is reset to zero at the end of each week.

- GST - Universal Time Coordinated (UTC) conversion parameters. GST is estimated by the user through its GST determination algorithm and has to be converted into UTC. The equations leading to performing the GST-UTC conversion algorithm from the GST-UTC parameters are provided in [18].

- GPS time - GST conversion parameters that are needed to convert GST into GPS time. This can be useful for double constellation GPS-Galileo receivers. The equations leading to perform the GPS time-GST conversion algorithm from the GPS time-GST parameters are provided in [18].

- Time and clock correction parameters are needed to compute pseudo-range. Each navigation message type broadcasts 4 satellite time correction model parameters relative to the dual-frequency (f_1,f_2) used for the clock model. F/Nav message type uses the dual-frequency (E1, E5a) for the clock model. I/NAV message type uses the dual-frequency (E1, E5b) for the clock model. The offset of the physical satellite signal time of transmission relative to the satellite signal time of transmission in GST is known as “satellite time correction” and is computed for the signal combination (f_1, f_2) by means of the 4-satellite time correction model parameters from the navigation message. The equations leading to computing the Galileo satellite time correction from the satellite time correction model parameters are provided in [18].

- Ephemeris is needed to indicate the position of the satellite to the user receiver. The ephemeris for each Galileo satellite is composed of 16 parameters. The user can compute the Earth Centered Earth Fixed (ECEF) coordinates of the antenna phase center position of the Galileo satellites at GST time t utilizing the 16 parameters contained in the ephemeris data. The equations leading to computing the Galileo satellites' positions from the ephemeris parameters are provided in [18].

- Ionospheric model parameters are needed to correct partially the ionospheric. It is assumed that the ionospheric model corrects 70% of the ionosphere when operating on E5a, E5b, and E1 frequencies.

- Service parameters that are needed to identify:
  - the satellites by means of the satellite Identification (ID) parameter,
  - the navigation data batches by means of the Issue of Data (IOD) parameter. In nominal operation, the navigation data have limited validity duration depending on the data type. The identification of each batch by an IOD value enables to indicate to the user receiver the validity of the data (which must be updated using the new issue of navigation data),

  -the signal heath status and the navigation data validity. The checksum, which employs a CRC technique, is used to detect the reception of corrupted data.

- Almanac is needed to indicate the position of all the satellites in the constellation with reduced accuracy. The almanac data is a reduced-precision subset of the clock and ephemeris parameters of the active satellites in orbit. Additionally, a predicted satellite health status is provided for each of these satellites, giving indications on the satellite's signal components health and navigation data health. Finally, the almanac IOD allows identifying without ambiguity an almanac batch.

2.1.3.3.6. Spreading codes and navigation messages: synthesis

[34] provides the values of the spreading code chip rate, primary and secondary length, and navigation message data rate. These values are presented in Table 2-3:

Table 2-3 Main characteristics of E1 and E5 Galileo spreading codes and navigation messages [32]

Signal	Spreading code chip rate (Mchip.s^{-1} or MHz) (f_c)	Primary code length	Secondary code length	Navigation message data rate (bits.s^{-1})
E1-B (data)	1.023	4092 (4ms)	No	125
E1-C (pilot)	1.023	4092 (4ms)	Primary x 25 (100 ms)	No data
E5a-I (data)	10.23	10230 (1ms)	Primary x 20 (20 ms)	25
E5a-Q (pilot)	10.23	10230 (1ms)	Primary x 100 (100 ms)	No data
E5b-I (data)	10.23	10230 (1ms)	Primary x 4 (4 ms)	125
E5b-Q (pilot)	10.23	10230 (1ms)	Primary x 100 (100 ms)	No data

2.1.4. GLONASS System: Brief Introduction and Signals Presentation

2.1.4.1. GLONASS Services

GLONASS is a Russian global satellite navigation system aiming at providing users with real-time three-dimensional position and velocity estimates for military and civilian users. GLONASS delivers a standard precision service which is an open-access service and a high precision service for military purposes. To provide standard and high precision services, GLONASS consists of three different segments: a space segment, a control segment, and a user segment. These segments are presented in the next paragraph.

2.1.4.2. GLONASS Infrastructures

Space segment

The GLONASS space segment consists of a constellation of 27 satellites in roughly 11 hours and 16 minutes orbits. **23 satellites** are currently operational, 1 spare, 1 in maintenance, and 2 in the testing phase as of June 2021 [22]. The satellites are arranged in 3 orbital planes. The orbital planes have an

inclination angle of 64.8 degrees relative to the earth's equator [16]. The satellites have an average orbit altitude of 19 100 kilometers above the surface of the earth [35].

The GLONASS space segment is currently rebuilding since satellites are launched at regular intervals. The objective is to reach the final constellation of 30 satellites. The GLONASS satellites are designated GLONASS, GLONASS-M and GLONASS-K satellites. The first GLONASS-M and GLONASS-K satellites were launched in 2003 and 2009, respectively.

To this day, the first generation GLONASS satellites (developed in the 1980s) are not launched anymore, the developed generations GLONASS-M, GLONASS-M+, GLONASS-K1, GLONASS-K1+, and GLONASS-K2 were subsequently launched in following decades [35].

Control segment

The GLONASS control segment consists of 4 Telemetry, Tracking and Command (TTC) stations located in Russia and a System Control Center. The Control Center provides monitoring of GLONASS constellation status, correction to the orbital parameters, and navigation data uploading [35]. TTC stations monitor the quality of GLONASS space segment performance. However, because of the location of the TTC stations, the system integrity is difficult to maintain [36].

User segment

The user segment consists of processors receiving and processing the GLONASS navigation signals and allows computing the position and velocity of the users. All current GLONASS receivers combine GPS and GLONASS constellations. The advantage provided by these double constellation receivers is that it leads to an increase in the number of satellites in view and more specifically it leads to an increase in the number of satellites in view at high elevation. Hence, the precision and the performance of the double constellation receiver in obstructed areas are improved. The disadvantage of GPS/GLONASS receivers is that GLONASS and GPS time and reference systems do not match, and increases the complexity of double constellation GPS/GLONASS receivers [36]. Indeed, both GLONASS and GPS clock errors must be evaluated and the deviation between the position of the user in the GPS reference system and the GLONASS reference system (International Terrestrial Reference System (ITRS)) is up to 15 meters.

The following paragraph aims at describing the GLONASS navigation signals transmitted by the GLONASS satellites.

2.1.4.3. GLONASS signals

GLONASS signals are DSSS signals. The main difference between GLONASS signals and GPS/Galileo signals is that the Frequency Division Multiple Access (FDMA) concept is used to design GLONASS signals while the CDMA technique is utilized for GPS/Galileo. The spreading codes broadcast by GLONASS satellites are common to all GLONASS satellites and each satellite transmits the unique spreading code on different carrier frequencies. As each satellite uses a different carrier frequency, the receiver can differentiate the signals coming from the satellites. The transmission of multiple DSSS signals having a common spreading code on different carrier frequencies is referred to as the FDMA technique.

As explained in the previous paragraph, different carrier frequencies are used to modulate the spreading code and the navigation messages. These carrier frequencies are particular frequencies of

L1 and L2 frequency bands. The carrier frequencies on L1 and L2 frequency bands are given by respectively [35]:

$$f_{GLONASS-L1,K} = f_{01} + K\Delta f_{01}$$
$$f_{GLONASS-L2,K} = f_{02} + K\Delta f_{02} \quad (2\text{-}27)$$

where:

- $f_{01} = 1602$ MHz
- $\Delta f_{01} = 562.5$ kHz
- $f_{02} = 1246$ MHz
- $\Delta f_{02} = 437.5$ kHz
- K is a frequency number, $K \in [\![0,24]\!]$ for satellites launched before 2005 and $K \in [\![-7,6]\!]$ for satellites launched after 2005.

All current GLONASS signals are based on the FDMA technique resulting in some difficulties to determine phase ambiguities when computing the user position by the carrier phase measurements as explained in [37]. Moreover, the spreading code used by GLONASS signals has a lower chip rate than GPS and Galileo chip rates, and that results in a lower precision for the pseudo-range estimates.

The utilization of the GLONASS system in civil aviation has not been developed. SARP (Standards And Recommended Practices) and MOPS (Minimum Operational Performance Standards) about the utilization of GLONASS signals in civil aviation do not exist. For these reasons, the structure, and main characteristics of current GLONASS signals are not described in this document, but they can be found in [35].

2.1.5. BeiDou System

Beidou (called COMPASS; in English, BeiDou Navigation Satellite System or BDS) is a Chinese satellite navigation and positioning system, comprising about thirty satellites and covering the whole of the Earth. In the late 20th century, China started to explore a path to develop a navigation satellite system suitable for its national conditions, and gradually formulated a three-step development strategy [38]:

1. By 2000, the construction of BDS-1 was completed to provide services to China.
2. By 2012, the construction of BDS-2 was completed to provide services to the Asia-Pacific region.
3. By 2020, the construction of BDS-3 was completed to provide services worldwide.

The first version of BeiDou, renamed BeiDou-1, comprising three satellites, two operational plus one as a backup, began to be deployed in 2000 and will be declared operational in 2003. This regional system made it possible to determine its position only in China and in the surrounding areas with an accuracy of about 100 meters or 20 meters with a two-way transmission system. This phase started in 1994 and ended in 2003.

The second generation of the system, BeiDou-2, which started in 2007, provides RNSS (Radio Navigation Satellite Service) over China and Asia-Pacific region with an accuracy of 10 meters in its civilian version. This is provided by three types of satellites: 5 satellites in geostationary orbit, three in inclined geosynchronous orbit (55 °), and 27 in medium orbit. Beidou-2 has been operational since the end of 2012 with coverage including China and surrounding countries. The performance of Beidou-2 over time must be comparable to the three other operational global systems (GPS, GLONASS, and

Galileo). All BeiDou satellites are equipped with laser retroreflector arrays for Satellite Laser Ranging and the verification of the orbit quality.

The BeiDou-3 generation, started in March 2015, was finalized by the last satellite put into orbit on June 23, 2020 [39]. The constellation comprises thirty-five satellites, of which thirty are operational: 3 satellites in geostationary orbit, 3 in a geosynchronous orbit inclined to 55 °, and 24 in medium orbit (On 3 planes). BeiDou-3 satellites are fitted with high-performance B1C and B2a systems [40], which are interoperable with the other existing global navigation satellite systems (GNSS). It also provides satellite-based augmentation system (SBAS) and search-and-rescue (SAR) services. The BDS-3 global service system offers horizontal/vertical positioning accuracy of 10m with velocity and time accuracies of 0.2 meters per second and 20 nanoseconds, respectively. It offers a global service availability of more than 95%. In the Asia-Pacific region, the positioning accuracies are 5m horizontal and 5m vertical.

2.1.6. Other Regional Systems

2.1.6.1. QZSS System

Japan's Quasi-Zenith Satellite System (QZSS) is a regional space-based positioning, navigation, and timing system that provides interoperable signals for GPS (L1, L2, and L5), a wide-area differential GPS augmentation signal. QZSS provides navigation services for East Asia, including Japan, and Oceania. QZSS is still under development and its first satellite was launched in 2010 [27].

The QZSS system is based on the use of the signal emitted by three satellites which circulate in an orbit constantly over the region centered on Japan. GPS receivers that pick up the signal from these satellites can benefit from increased accuracy. Furthermore, signal losses are significantly reduced in mountainous areas and urban areas (signals usually reverberated or blocked by buildings). The satellites are placed in an elliptical geosynchronous orbit that allows them to be visible from Japan at a significant elevation for part of their orbit. Three satellites circulating in the same orbit, including one launched in 2010, to which is added a satellite in geostationary orbit, should allow the start of this service from 2018. The Japanese government approved in April 2016 the project to launch three other satellites in 2023 to improve the quality of service.

2.1.6.2. IRNSS System

Indian Regional Navigation Satellite System (IRNSS) The Indian Regional Navigation Satellite System or IRNSS is an Indian satellite positioning system whose current deployment should be completed at the end of 2016. Its coverage is regional: the receivers can operate in India and its periphery up to a distance of 1,500 to 2,000 km from its borders [19]. The terminals in the basic service provide a position with an accuracy of 20 meters. The IRNSS system is compatible with the GPS and Galileo systems. [27].

2.2. GNSS Receiver Review

Between transmitter and receiver, the signal passes through a transmission channel. Consequently, the receiver antenna recovers signals which are different from the transmitted signals. Indeed, the received signal is mainly affected by:

- a delay corresponding to the propagation time,
- a phase offset,

- a carrier frequency offset due to the relative motion of the satellite with respect to the receiver (Doppler effect),
- Additive noise.

Hence, the analytical expression of the signal recovered at the receiver antenna is:

$$\begin{aligned} s_{rec}(t) &= \sum_i s_{rec}^i(t) \\ &= \sum_i \sqrt{C_{data,i}} h_{data,i}(t-\tau_i) d_i(t-\tau_i)\, cos\big(2\pi(f_c + f_{D,i})t + \varphi_i\big) \\ &\quad + \sqrt{C_{pilot,i}} h_{pilot,i}(t-\tau_i)\, sin\big(2\pi(f_c + f_{D,i})t + \varphi_i\big) + \eta(t) \end{aligned} \tag{2-28}$$

Where:

- $s_{rec}^i(.)$ is the received signal from the i-th satellite. For more information about GNSS signals structure,
- $d_i(.)$ is the navigation message emitted by the i-th satellite,
- $h_{data,i}(.)$ is the spreading signal emitted by the i-th satellite on the data channel,
- $h_{pilot,i}(.)$ is the spreading signal emitted by the i-th satellite on the pilot channel,
- f_c is the carrier frequency,
- $f_{D,i}$ is the Doppler frequency of the i-th satellite signal,
- φ_i is the phase offset of the i-th satellite signal,
- τ_i is the delay introduced by the transmission channel on the i-th satellite signal (code delay),
- $\eta(.)$ is the noise component,
- $C_{data,i}$ is the received signal power from the i-th satellite on the data channel,
- $C_{pilot,i}$ is the received signal power from the i-th satellite on the pilot channel.

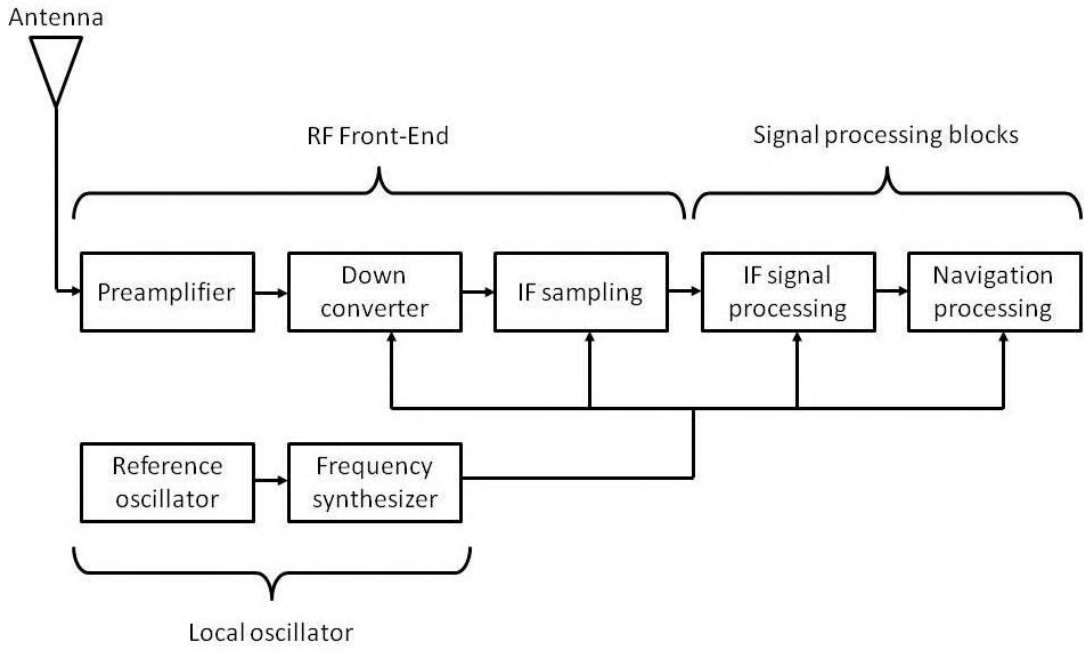

Figure 2-6: GNSS receiver signal processing architecture

To determine its position, a GNSS receiver needs to precisely estimate the parameters of the signals transmitted by the different GNSS satellites. Indeed, the signal parameters are then converted to distances. Next, the position is estimated by trilateration based on the estimated distances. The parameters of the signals are:

- The propagation time or code delay,
- The Doppler frequency,
- The carrier phase or phase offset.

A generic GNSS receiver block diagram is provided in Figure 2-6. As most modern GNSS receivers are digital receivers, a generic GNSS receiver is used to represent GNSS receiver architecture. The signal parameters estimation is performed by the RF front-end and by the Intermediate Frequency (IF) signal processing block. The position estimation is performed by the navigation processing block. Figure 2-6 shows that the recovered signals are at first pre-amplified, down-converted, and sampled by the RF front-end before entering in the IF signal block processing block and in the navigation processing block.

2.3. The GNSS code and phase observations

To compute the position, velocity, and time estimate, the navigation processing block uses the outputs of the tracking loops to obtain two types of measurements as shown in Figure 2-7:

- the code pseudorange measurements which are deduced from the code delay estimated by the **DLL** (Delay Locked Loop),
- the carrier phase measurements which are deduced from the phase estimated by the **PLL** (Phase Locked Loop).

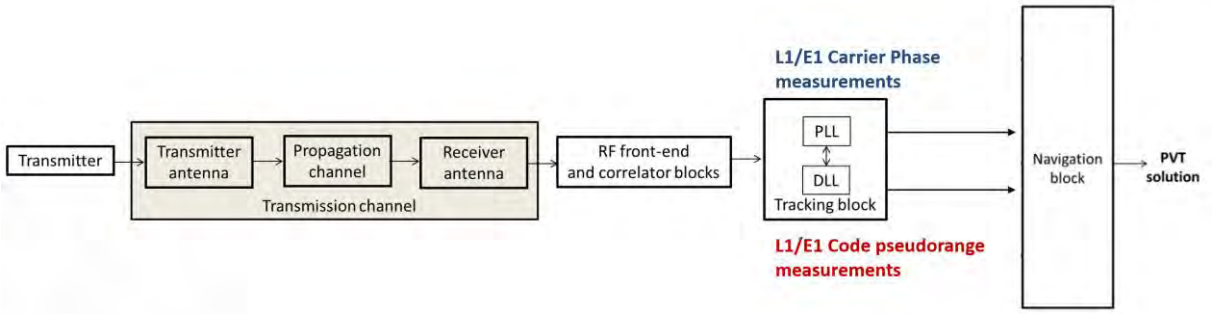

Figure 2-7 GNSS receiver architecture (Single-frequency)

The following paragraphs aim at presenting the models of the code pseudorange and carrier phase measurements.

2.3.1. Code Pseudorange Measurements

The pseudorange (code) measurement between satellite "k" and the receiver "r" is obtained by multiplying the output of the DLL (estimated time travel time from the satellite "k" to the receiver denoted as $\hat{\tau}_r^k$ in the following) by the speed of light c:

$$P_r^k = c\hat{t}_r^k \tag{2-29}$$

The code pseudorange measurement model is given by:

$$P_r^k = \left(\boldsymbol{e}_r^k\right)^T \cdot \left(\boldsymbol{r}_r - \boldsymbol{r}^k\right) + c\left(dt_r - dt^k\right) + \gamma I_r^k + T_r^k + b_{P,r} + b_P^k + m_{P,r}^k + n_{P,r}^k$$
$$= \rho_r^k + c\left(dt_r - dt^k\right) + \gamma I_r^k + T_r^k + b_{P,r} + b_P^k + m_{P,r}^k + n_{P,r}^k \quad (2\text{-}30)$$

where:

- $\boldsymbol{e}_r^k$ is the Line-of-Sight vector of satellite k towards the receiver r
- $\boldsymbol{r}_r$ is the position vector of the receiver r at the time of reception
- $\boldsymbol{r}^k$ is the position vector of the satellite k at the time of transmission
- $\rho_r^k = \left\|\boldsymbol{r}_r - \boldsymbol{r}^k\right\|$ is the topocentric distance between the receiver at the time of reception and the satellite at the time of transmission.
- dt_r is the receiver clock bias of receiver r
- dt^k is the satellite clock bias of satellite k
- γ is the ionospheric dispersion factor and depends on the frequency, and:
  - $\gamma = 1$ for L1 or E1,
  - $\gamma = {f_{L1}}^2/{f_{L5}}^2$ for L5 or E5a,
  - $\gamma = {f_{L1}}^2/{f_{E5b}}^2$ for E5b.
- I_r^k is the ionospheric delay on L1 in meters
- T_r^k is the tropospheric delay in meters
- $b_{P,r}$ is the receiver hardware bias for the code measurement of receiver r
- b_P^k is the satellite hardware bias for the code measurement of satellite k
- $m_{P,r}^k$ is the code pseudorange measurement error due to multipath propagation
- $n_{P,r}^k$ is the residual noise for the code measurement
- c is the speed of light

It should be noted that the:

- The index 'r' designates the receiver (necessary in the differential case) and the exponent 'k' designates the satellite. Errors may only depend on satellite, receiver, or k/r pair
- Some errors are also specific to code measurements or common to phase measurements. It is therefore sometimes necessary to specify which measures are affected by the term in question.
- In addition, to be complete, it would also be necessary to add an indicator of the time corresponding to the measurement.

2.3.2. Carrier Phase Pseudorange Measurements

The PLL tracks the difference between the signal received from the satellite and the local copy. The receiver also keeps track of the number of "zero-crossings" of the phase difference, which when added to the fractional phase gives the integrated carrier beat phase observable between satellite "k" and receiver "r" denoted as $\widehat{\varphi}_r^k$ [cycles]. The phase pseudorange measurement [meters] between satellite "k" and the receiver "r" is obtained by multiplying the output of the PLL ($\widehat{\varphi}_r^k$) by the carrier wavelength λ_c:

$$\phi_r^k = \lambda_c \hat{\varphi}_r^k \quad (2\text{-}31)$$

The phase measurement model is given by:

$$\begin{aligned}\lambda\phi_r^k &= (\boldsymbol{e}_r^k)^T \cdot (\boldsymbol{r}_r - \boldsymbol{r}^k) + c(dt_r - dt^k) - \gamma I_r^k + T_r^k + b_{\phi,r} + b_\phi^k + \lambda N_r^k + m_{\phi,r}^k + n_{\phi,r}^k \\ &= \rho_r^k + c(dt_r - dt^k) - \gamma I_r^k + T_r^k + b_{\phi,r} + b_\phi^k + \lambda N_r^k + m_{\phi,r}^k + n_{\phi,r}^k\end{aligned} \quad (2\text{-}32)$$

where:

- $b_{\phi,r}$ is the receiver hardware bias for the carrier phase measurement of receiver r
- b_ϕ^k is the satellite hardware bias for the carrier phase measurement of satellite k
- $m_{\phi,r}^k$ is the carrier phase measurement error due to multipath propagation
- $n_{\phi,r}^k$ is the residual noise for the carrier phase measurement
- N_r^k is the phase ambiguity term (real value, in principle constant and integer)
- λ is the wavelength of the RF carrier

One can notice that for the carrier phase measurement:

- Some errors are strictly identical to code measurements: distance, receiver/sat clock bias, tropospheric delay.
- Note that the ionospheric error is the same as for the code measurement, except for the opposite sign.
- The other big difference is the presence of a phase ambiguity term.

2.4. Chapter Summary

In this chapter, we provided a global overview of GNSS systems and presented the signal processing techniques adopted in the receiver to obtain the required measurements. The state of the art of GNSS functional and stochastic models are illustrated. Different GNSS constellations are introduced, including the American (GPS), European (Galileo), Russian (GLONASS), and Chinese (BeiDou) constellations and other regional navigation systems. As presented, there is a wide variety of GNSS systems, nevertheless, since this Ph.D. thesis emphasizes only on 2 specific signals: GPS L1 C/A and Galileo E1 OS, only these two systems are presented in detail.

In addition, a review of the GNSS receiver including the signal processing process and the production of the GNSS raw measurements is given. Finally, the GNSS code and phase observations including all nominal errors sources are described, these measurements are used to allow the user to calculate its PVT solution. In the next chapter, the GNSS-based precise positioning technique which is the focus of this Ph.D. will be further introduced in detail.

Chapter 3. GNSS-based Precise Positioning and Attitude Estimation

A precise position and attitude information is significantly required for specific application scenarios like autonomous driving of vehicles or precise mobile mapping. However, standard stand-alone Global Navigation Satellite System (GNSS) positioning accuracy is not capable to satisfy the sub-meter or even centimeter-level need for this kind of requirement. Therefore, the realization of GNSS precise positioning has become a hot topic in recent years.

Navigation with GNSS is ultimately the process of determining the 3D position coordinate of the rover in a specific coordinate system. The level of accuracy of the state solution is a key indicator of navigation performance. To achieve greater accuracy, a lot of effort has been put, for example, both on the GNSS constellation side (i.e., new modernization methods of GNSS signals and satellites, etc.) and the receiver side. In precise position applications, the user position is estimated with carrier phase measurements because this technique leads to achieving position estimates with a precision of a few centimeters routinely. That is why to achieve a more accurate positioning estimation, the GNSS carrier phase measurements appear mandatory.

In this section, precise positioning techniques are first introduced to show the procedures implemented on the receiver side to improve navigation performance, including the carrier phase integer ambiguity resolution techniques.

The environment has also a significant impact on the positioning results, the environment in which the mobile is located is never a negligible factor. The problems that can arise from the urban environment, a space common to most users of daily life, are also presented in this section.

What is more, attitude determination using GNSS signals is one of the many applications of satellite-based navigation. In fact, multiple GNSS antennas installed on a given platform can be used to provide orientation estimates, thus adding attitude information to the standard positioning service. The purpose of this Ph.D. contribution is to present, analyze and test a novel RTK performance amelioration and attitude determination method, thus an overview and classification of current mathematical algorithms and techniques utilized in the process of GNSS-based attitude estimation are described as well at the end.

The structure of this chapter is as follows:

- Section 3.1 is an overview of the current GNSS precise positioning algorithms which includes DGNSS (Differential GNSS), PPP (Precise Point Positioning), and RTK (Real-Time Kinematic). The GNSS Single Differencing (SD) and Double Differencing (DD) Models, for long baselines and short baselines, are also presented, respectively.
- Section 3.2 describes the integer ambiguity resolution (IAR) which is a necessary step when using the GNSS carrier phase observations.
- Section 3.3 illustrates the challenges of GNSS precise positioning in highly constrained environments like the urban environment.

- Section 3.4 gives a review and classification of the existing attitude representation methods and introduces the GNSS-based attitude determination problem. A literature review of GNSS-based attitude estimation is also given.
- Section 3.5 finally summary this chapter.

3.1. GNSS Precise Positioning Principles and techniques

Standalone GNSS signals enable the calculation of the receiver's position, however, given the impact of the errors on the satellite position and clock, atmospheric effects, local environmental effects (such as multipath or satellite masking), and limited signal tracking accuracy, these positions have limited accuracy (~4m). [41] Emerging applications such as drones, and augmented reality are driving the demand for high accuracy (<1m) and high precision real-time positioning in the mass market. Besides, for fully autonomous driving to become reality, a number of technologies have to reach maturity and be rolled out in concert. One of the most important technologies among them is affordable, scalable, and reliable high GNSS precision positioning. Unfortunately, until now, significant challenges remain in obtaining high-accuracy (cm/dm level) position data using low-cost GNSS receivers due to their tendency to obtain poor quality measurements [42].

Precise positioning by GNSS generally combines the fact to use additional corrections or to use the phase measurements (accurate to a few cm, but with integer ambiguity to be corrected). To achieve real-time high accuracy positioning using GNSS, several signal augmentation techniques such as DGNSS, RTK, PPP have been developed [41]. These technologies can deliver cm/dm level accuracy but have traditionally been implemented using sophisticated, high-performance hardware (e.g., multi-frequency receivers, geodetic antenna) which are not available in mass-market devices such as low-cost receivers. Given the potential benefit of bringing high accuracy and precision positioning to mass-market devices, there is a need to review the current market situation of these services.

3.1.1. Differential GNSS

A commonly used technique for improving GNSS performance is Differential GNSS (DGNSS), the basic innovation idea of DGNSS is to benefit from the spatial or time correlation characteristics of most errors contaminating the positioning accuracy for users separated by tens or even hundreds of kilometers away. Thus, one or multiple reference station receivers are involved in DGNSS to provide corrections for these sources of errors to the user. The distance between the user and the reference station is referred to as the baseline [42].

In differential GNSS, the position of a fixed GNSS receiver referred to as a base station, is determined to a high degree of accuracy using conventional surveying techniques. Then, the base station determines ranges to the GNSS satellites in view using:

- The code-based or phase-based tracking technique.
- The location of the satellites is determined from the precisely known orbit ephemerides and satellite time.

The base station compares the surveyed position to the position calculated from the satellite ranges. Differences between the positions can be attributed to satellite ephemeris and clock errors, and mostly to errors associated with atmospheric delay. The base station sends these errors to other nearby receivers (rovers), which incorporate the corrections into their position calculations.

Differential positioning requires a data link between the base station and rovers if corrections need to be applied in real-time, and at least four GNSS satellites are in view at both the base station and the rovers. The absolute accuracy of the rover's computed position will depend on the absolute accuracy of the base station's position.

A typical DGNSS process is illustrated in Figure 3-1.

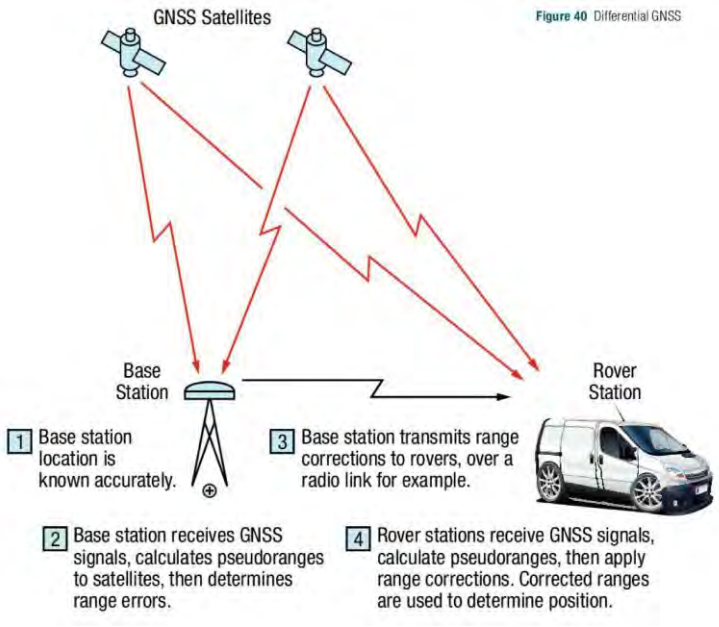

Figure 3-1 Differential GNSS(DGNSS) [43].

DGNSS techniques can be classified in different ways depending on specific consideration aspects. Depending on the type of GNSS measurements involved, the code-based DGNSS, when only pseudo-range measurements are processed, is separated from the carrier phase-based DGNSS when the pseudo-range and carrier phase measurements are considered.

Considering the geographic size, the basic categories of DGNSS techniques are [1], [42], [44].

- local area DGNSS (LDGNSS),
- region-area DGNSS (RDGNSS), and
- wide-area DGNSS (WDGNSS).

The LDGNSS system is expected to serve a region of less than 10-100 km from a reference station, while an area up to 1000 km and a larger service area are respectively concerned with the RDGNSS system and the WDGNSS system [2].

Within each DGNSS category, the number of reference stations involved and the type of correction data that the reference station provides are also different. In the case of LDGNSS, majorities of the space-correlated errors can be mitigated by using the pseudorange/carrier phase domain correction of a reference station, while three or more reference stations are required along the RDGNSS coverage perimeter to provide satisfying performance. DGNSS positioning performance is highly dependent on the length of the baseline because the residual errors after correction increase with the baseline. Meter-level or a decimeter-level accuracy when under better conditions can be achieved with code-based LDGNSS / WDGNSS [2].

When more precise positioning is desired, it is essential to take the carrier phase observations [13] into account. In fact, the carrier phase measurements are very interesting because they contain a very small tracking jitter (compared to pseudo-range measurements), generally less than 1 cm (1 sigma). As a result, once ionosphere and troposphere errors are effectively mitigated, they could be used to target positioning down to the centimeter. However, there are many obstacles to achieving this goal. First, the phase measurements of the carrier are ambiguous and therefore cannot be used directly for absolute positioning. There is therefore a necessary step to correctly estimate the entire ambiguity of each measure. This is very difficult because the frequency L1 creates a carrier wavelength of the order of less than 20 cm. Second, it is known that the PLL used to generate carrier phase measurements is not very robust. As a result, carrier phase measurements may be unavailable for a period of time (under high dynamic or low C/N0 conditions), and when they become available again, the ambiguity will change, requiring a new ambiguity estimation. These 2 obstacles partly explain why such methods have mainly been used by applications that take place in fairly open environments.

In the next 2 sections, two types of well-known precise positioning techniques are described: Precise Point Positioning (PPP) and Real-Time Kinematic (RTK). The advantages and drawbacks of each technique will be exposed. The PPP technique does not require surrounding reference stations, while the RTK does. These methods will be looked at in the context of this PhD which only tackles single-frequency GPS/Galileo receivers to represent the exact limitation of most low-cost GNSS receivers.

3.1.2. Precise Point Positioning

As mentioned earlier, the main biases preventing the isolation of carrier phase ambiguity as a constant are ionospheric delay, orbit error, satellite clock, and tropospheric delay.

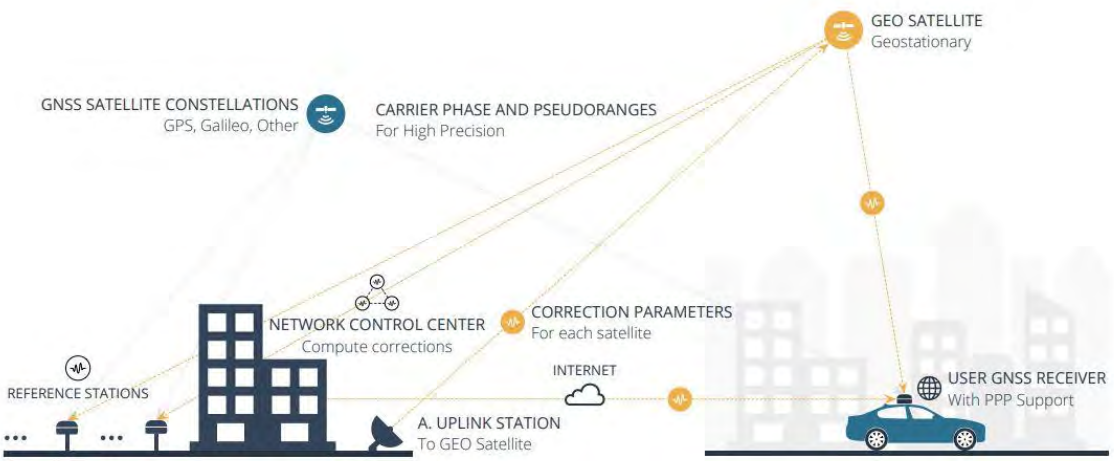

Figure 3-2 Precise Point Positioning [47]

The concept of PPP was firstly proposed in 1997 to achieve precise point positioning using undifferenced, dual-frequency, carrier phase, and pseudorange measurements, as well as precise satellite orbit and clock products [42], [45], [46]. PPP is a signal augmentation technique that removes errors from the GNSS system to provide high precision positioning using a single receiver and has become an attractive alternative to RTK. PPP solutions are based on GNSS satellite clock and orbit corrections, generated from a network of continuously operating global reference stations (CORS). Once the corrections have been calculated, they are provided to the user via satellite or the Internet, which makes it possible to obtain dm level positioning or better positioning in real-time without the

need for a local base station. PPP solutions typically require a convergence period of 5 to 30 minutes to resolve local biases such as atmospheric conditions, multipath, and satellite geometry. A typical PPP system is shown in Figure 3-2.

The main sources of error for PPP are mitigated in the following ways [1], [45], [46], [48]:

Dual-frequency operation: The first-order ionospheric delay is proportional to the frequency of the carrier wave. Therefore, the first-order ionospheric delay can be completely eliminated by using the combinations of dual-frequency GNSS measurements to get iono-free measurements. It consists in removing the first order of the ionospheric delay while keeping the other effects unchanged. For dual-frequency L1/L2 code measurements. The mathematical form is provided in (**3-1**)

$$P_{\mathrm{IF}} = \alpha P_1 - \beta P_2 = \rho + c(\mathrm{dt} - \mathrm{dT}) + T + b_{r,P_{\mathrm{IF}}} - b^{s}_{P_{\mathrm{IF}}} + \varepsilon_{P_{\mathrm{IF}}} \tag{3-1}$$

Where $a = \frac{f_1^2}{f_1^2 - f_2^2} = 2.546$, and $\beta = \frac{f_2^2}{f_1^2 - f_2^2} = 1.546$.

The same combination can be formed with carrier-phase observables in (**3-2**):

$$\Phi_{\mathrm{IF}} = \alpha\phi_1 - \beta\phi_2 = \rho + c(\mathrm{dt} - \mathrm{dT}) + T + \alpha N_1\lambda_1 - \beta N_2\lambda_2 + b_{r,\phi_{\mathrm{IF}}} - b^{s}_{\phi_{\mathrm{IF}}} + \varepsilon_{\phi_{\mathrm{IF}}} \tag{3-2}$$

Satellite Orbit and Clock Correction Data: This includes satellite orbit and clock corrections. The ephemeris of the broadcast navigation data is not precise enough to correct these errors, because the network used to estimate the broadcast corrections is made up of only a few stations in the world. However, a number of organizations including the IGS [49] provide more precise estimated corrections using a larger network of stations, in real-time or for post-processing purposes. These corrections have the advantage of requiring very low data exchange and can be applied regardless of the distance between the user and the nearest reference station. Figure 3-3 gives the different types of IGS products for the GPS Satellite Ephemerides/Satellite & Station Clocks corrections.

Type		Accuracy	Latency	Updates	Sample Interval
Broadcast	orbits	~100 cm	real time	–	daily
	Sat. clocks	~5 ns RMS ~2.5 ns SDev			
Ultra-Rapid (predicted half)	orbits	~5 cm	real time	at 03, 09, 15, 21 UTC	15 min
	Sat. clocks	~3 ns RMS ~1.5 ns SDev			
Ultra-Rapid (observed half)	orbits	~3 cm	3 - 9 hours	at 03, 09, 15, 21 UTC	15 min
	Sat. clocks	~150 ps RMS ~50 ps SDev			
Rapid	orbits	~2.5 cm	17 - 41 hours	at 17 UTC daily	15 min
	Sat. & Stn. clocks	~75 ps RMS ~25 ps SDev			5 min
Final	orbits	~2.5 cm	12 - 18 days	every Thursday	15 min
	Sat. & Stn. clocks	~75 ps RMS ~20 ps SDev			Sat.: 30s Stn.: 5 min

Figure 3-3 Product correction IGS for GPS [form igs.org]

Modeling: The tropospheric delay is corrected using a model, e.g., the UNB model developed by the University of New Brunswick. However, the wet part of the tropospheric delay is very variable and cannot be modeled with sufficient precision. Thus, the residual tropospheric delay is estimated as an additional state in addition to the position, receiver clock, and carrier phase ambiguities. Modeling can also be used in the PPP receiver to correct for the effect of solid earth tides [43].

PPP filter algorithms: An extended Kalman filter (EKF) is mostly used for PPP estimation. Position, receiver clock error, the zenith tropospheric delay, and carrier phase float ambiguities are estimated EKF states. EKF minimizes the noise in the system and makes it possible to estimate the position with centimeter precision. Estimates of EKF states are improved with successive GNSS measurements until they converge to stable and accurate values. The typical convergence time of PPP to a horizontal error of less than 10 cm is between 20 and 40 minutes, but it depends on the number of satellites available, the geometry of the satellites, the quality of the correction products, the environment multipath of the receiver and atmospheric conditions.

There are several PPP service providers, including VERIPOS, TerraStar, OmniSTAR, and StarFire [43]. PPP service providers operate a network of ground reference stations to collect correction data for the different signals broadcast by each satellite. The corrections calculated from these data are broadcast from the geostationary satellites to the receivers of the subscribed users.

In the case of a single-frequency user, ionospheric delay can be partially or totally mitigated using 3 methods:

- The so-called **GRAPHIC** (GRoup And Phase Ionospheric Correction) **combination**, usually performed on L1 measurements:

$$P_{1,GRAPHIC} = \frac{P_1 + \Phi_1}{2} = \rho + c(dt - dT) + T + N_1 \frac{\lambda_1}{2} + b_{r,\frac{P_1+\phi_1}{2}} - b^S_{\frac{P_1+\phi_1}{2}} + \varepsilon_{\frac{P_1+\phi_1}{2}} \qquad (3\text{-}3)$$

- **Use of ionospheric TEC maps**. Ionospheric TEC maps are a time-stamped geographic grid of vertical TEC values that can be interpolated to determine the vertical ionospheric delay at the desired location. For example, the IGS provides a grid, spaced by 2.5 degrees in latitude and 5 degrees in longitude of Vertical Total Electron Content (VTEC) values every 2 hours. SBAS systems, such as WAAS and EGNOS are also providing ionospheric grids in real-time, with precision allowing to obtain decimeter-level position [50].
- **Using empirical models** such as the Klobuchar model or NeQuick model. However empirical model has currently too low accuracy to be used for PPP.

Currently, PPP has drawbacks. One of the most persistent is the time it takes to resolve cycle ambiguity. The time required to go from a float to a fixed solution is prolonged because the ambiguity cannot be assumed to be an integer as it is in a differentiated solution. This leads to a long initialization time, which requires a full reset if the signal is lost, and the convergence can take 20 minutes or more. Also, dual-frequency receivers are required in PPP to attenuate the ionospheric delay, which makes this method more difficult to implement on low-cost single-frequency receivers.

The benefit provided by the fact that the integer-nature ambiguities are resolved or fixed, i.e., Integer Ambiguity Resolution (IAR), is not only improving the accuracy of the system but also reducing system

convergence times. This is the reason why multi-frequency PPP users strive to come up with new techniques (PPP-AR techniques) to achieve correct integer ambiguity resolution [45]. This emerging technique requires additional corrections to remove satellite biases that must be estimated by the global reference network.

Such satellite biases are removed when considering differential carrier-based positioning techniques, allowing the estimation of carrier integer ambiguities. Thus, the Real-Time Kinematic (RTK) methodology, is discussed in the next section.

3.1.3. Real-Time Kinematic

With the rapid development of satellite positioning technology, people's demand for fast and high-precision location information is becoming more and more strong. High-precision GPS measurements must use carrier phase observations. Currently, the most widely used high-precision positioning technology is RTK (Real-Time Kinematic). RTK positioning technology is a real-time dynamic positioning technology based on carrier phase observations. It can provide real-time three-dimensional positioning results of the survey site in a specified coordinate system and achieve centimeter-level accuracy [41], [43].

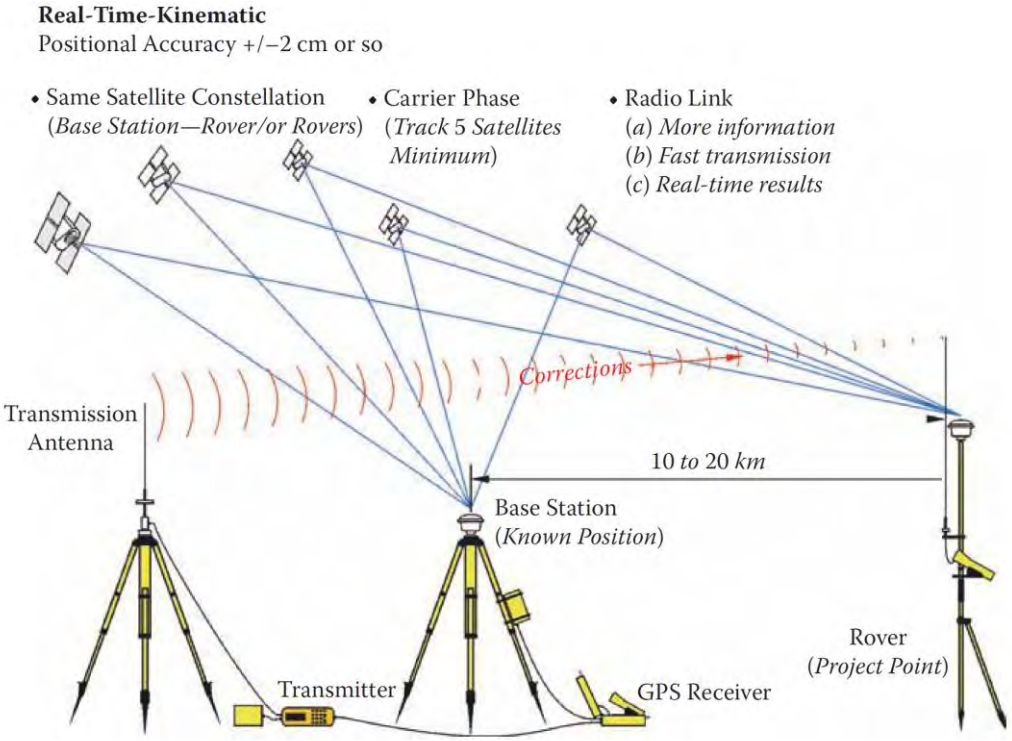

Figure 3-4 RTK Principles [51]

In fact, most errors affecting GNSS measurements are correlated in space or in time. Atmospheric errors (ionospheric and tropospheric errors), satellite hardware bias, satellite orbit error, or satellite clock offset error are spatially and temporally correlated errors. This means that 2 closely spaced receivers tracking the same signals at the same time experience approximately the same error. By simply differentiating the measurements of 2 nearby and synchronized receivers, spatially correlated errors are eliminated or reduced. This is the basic principle of Differential GNSS and the RTK methodology. The key of RTK technology lies in the use of GNSS carrier phase observations and the

use of observation errors between the reference base station and the mobile rover pair station, as illustrated in Figure 3-4.

RTK is the gold standard for high precision applications and is based on the use of carrier phase measurements and the transmission of corrections from a base station (whose location is precisely known) to the rover (potentially in motion, the position of which is being determined) so that the main positioning errors can be eliminated [41]. The base receiver takes measurements from satellites in view and then broadcasts them, together with its location, to the rover receiver(s). The rover not only receives data from the reference station through the data link, but also collects GPS observation data, and composes differential observations in the system for real-time processing. The rover then estimates its location relative to the base station (referred to as the "**baseline**").

The spatial correlation removes most of the errors in the observation data of the mobile station by difference, so as to obtain a high precision positioning (decimeter or even centimeter level). An RTK base station typically covers a service area of 30-50 km and requires a real-time communication channel to connect the base station and the rover. As long as the tracking of the phase observations of more than four satellites and the necessary geometric figures can be maintained, the rover can provide centimeter-level positioning results at any time.

The biggest problem encountered in the application of RTK technology is the effective range of reference station correction data. The spatial correlation of GPS errors gradually loses linearity as the distance between the reference station and the mobile station increases. Therefore, at a longer distance (single frequency>10km, dual frequency>30km), the user data after differential processing still contains a lot of observation error, which leads to the decrease of positioning accuracy and the inability to resolve the ambiguity of the carrier phase. Therefore, to ensure satisfactory positioning accuracy, the operating distance of the traditional stand-alone RTK is very limited.

To overcome the shortcomings of traditional RTK technology, in the mid-1990s, people proposed network RTK technology. In the network RTK technology, the linearly attenuated single-point GPS error model is replaced by the regional GPS network error model, that is, the GPS network composed of multiple reference stations is used to estimate the GPS error model of an area, and the GPS error model for the network coverage area provides correction data to the user. And what the user receives is not the observation data of an actual reference station, but the data of a virtual reference station, and the correction data of a reference grid that is closer to its own location, so the network RTK technology is also called virtual Reference station technology (Virtual Reference) [52].

3.1.3.1. RTK Process

As discussed before, the key to achieving centimeter-level positioning accuracy with RTK is the use of the GNSS carrier phase signals. Carrier phase measurements are like precise tape measures from the base and rover antennas to the satellites. In the receiver, carrier phase measurements are made with millimeter precision. Although carrier phase measurements are highly precise, they contain an unknown bias, termed the integer cycle ambiguity, or carrier phase ambiguity, that prevents them to be used directly for positioning [41], [42]. The rover must resolve, or initialize, the carrier phase ambiguities at power-up and every time that the satellite signals are interrupted. Figure 3-5 Illustrates the typical RTK algorithm calculation steps:

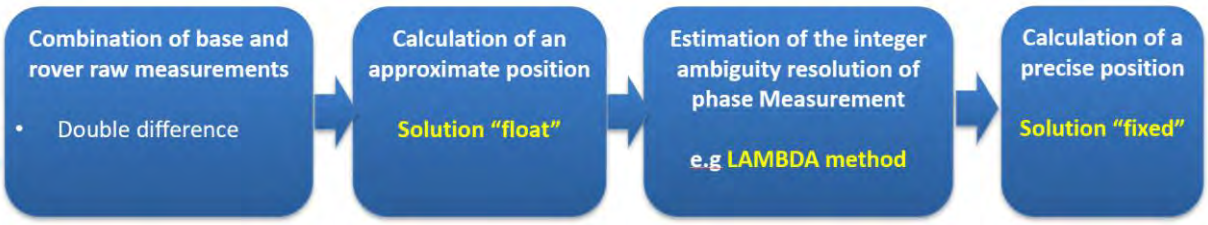

Figure 3-5 RTK Calculation Process

- The float solution estimates phase ambiguities as real numbers.
- The fixed solution estimates phase ambiguities as integer numbers.
- The fixed solution is much more precise than the float solution.
- The float solution benefits from better accuracy than a traditional stand-alone GNSS solution (code-based weighted least squares without differential corrections, aka Single Point Positioning, or SPP, solution) thanks to the use of differential corrections and carrier observables.

The ability to resolve the integer ambiguity quickly and correctly is one of the key performance indicators of the RTK methodology and a strong differentiator from PPP. In the following sections, the formation of GNSS differential measurements will firstly be reviewed (Single Difference, SD, and Double Difference, DD, Measurements), followed by the introduction of the core part of the RTK methodology, namely the integer ambiguity resolution (IAR).

3.1.3.2. Single Difference measurements

As described above, raw GNSS measurements are broadcast by the reference station to the rover receiver. These measurements are then used by the rover receiver to form so-called difference measurements. Two basic forms of differential observations are generally used: Single Differencing and Double Differencing.

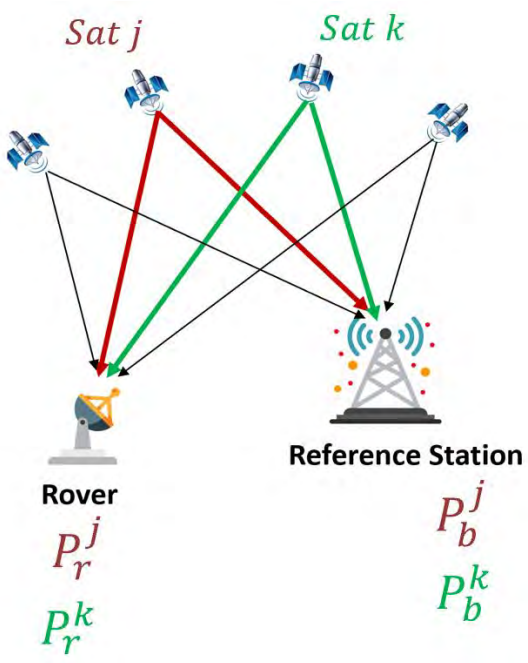

Figure 3-6 SD and DD illustrations

By differentiating the measurements made by the rover and the base station on the same satellite, the common errors of satellite origin are canceled: sat clock, ephemeris error, and satellite hardware bias.

- **SD**: "Single–differencing between receivers" refers to the difference of measurements between a pair of receivers, i.e., the rover's receiver and the reference station's receiver, while keeping the same satellites.

Considering only the L1 signal, the full mathematical formulations of SD measurements are:

SD of Code measurement

$$\begin{aligned} P_{rb}^{j} &= P_{r}^{j} - P_{b}^{j} \\ &= \rho_{r}^{j} + c\left(dt_r - dt^{j}\right) + I_{r}^{j} + T_{r}^{j} + b_{P,r} + b_{p}^{j} + m_{P,r}^{j} + n_{P,r}^{j} \\ &-\left(\rho_{b}^{j} + c\left(dt_b - dt^{j}\right) + I_{b}^{j} + T_{b}^{j} + b_{P,b} + b_{P}^{j} + m_{P,b}^{j} + n_{P,b}^{j}\right) \\ &= \rho_{rb}^{j} + cdt_{rb} + I_{rb}^{j} + T_{rb}^{j} + b_{P,rb} + m_{P,rb}^{j} + n_{P,rb}^{j} \end{aligned} \tag{3-4}$$

SD of Carrier Phase measurement

$$\begin{aligned} \phi_{rb}^{j} &= \phi_{r}^{j} - \phi_{b}^{j} \\ &= \rho_{rb}^{j} + cdt_{rb} - I_{rb}^{j} + T_{rb}^{j} + b_{\phi,rb} + \lambda N_{rb}^{j} + m_{\phi,rb}^{j} + n_{\phi,rb}^{j} \end{aligned} \tag{3-5}$$

where:

- P_{rb}^{j} refers to the single-difference code phase measurement from satellite j of receiver pair rb
- $\lambda\phi_{rb}^{j}$ refers to the single-difference carrier phase measurement from satellite j of receiver pair rb
- ρ_{rb}^{j} refers to the single-difference geometry distance between the receiver pair rb and the satellite j
- cdt_{rb} refers to the single-difference receiver clock bias of receiver pair rb
- I_{rb}^{j}, T_{rb}^{j} refer to the single-difference ionospheric delay and tropospheric delay on the path to satellite j of receiver pair rb respectively.
- $b_{P,rb}$, $b_{\phi,rb}$ refer to single-difference receiver hardware bias
- $m_{P,rb}^{j}$, $m_{\phi,rb}^{j}$ refer to the single-difference multipath error of the code and phase measurement respectively on the path to satellite j of receiver pair rb
- N_{rb}^{j} refers to the SD integer ambiguity of receiver pair rb for satellite j
- $n_{P,rb}^{j}, n_{\phi,rb}^{j}$ refer to the noise measurement of the SD code and phase measurement of receiver pair rb for satellite j respectively.

3.1.3.3. Double Difference measurements

The receiver clock errors and receiver hardware delays in the single difference equations (**3-4**) (**3-5**) are common for all the satellites tracked at the same frequency. Therefore, these terms can be eliminated by forming a double difference (DD) combination, obtained by subtracting two SD measurements of type (**3-4**) (**3-5**) from two different satellites:

- **DD**: Double differencing is the difference between two SD measurements collected from two different satellites, but with the same pair of receivers.

DD of GPS Code measurement

$$\begin{aligned} P_{rb}^{jk} &= P_{rb}^{j} - P_{rb}^{k} \\ &= \rho_{rb}^{j} + cdt_{rb} + I_{rb}^{j} + T_{rb}^{j} + b_{P,rb} + m_{P,rb}^{j} + n_{P,rb}^{j} \\ &-\left(\rho_{rb}^{k} + cdt_{rb} + I_{rb}^{k} + T_{rb}^{k} + b_{P,rb} + m_{P,rb}^{k} + n_{P,rb}^{k}\right) \\ &= \rho_{rb}^{jk} + I_{rb}^{jk} + T_{rb}^{jk} + m_{P,rb}^{jk} + n_{P,rb}^{jk} \end{aligned} \tag{3-6}$$

DD of GPS Carrier Phase measurement

$$\begin{aligned} \phi_{rb}^{jk} &= \phi_{rb}^{j} - \phi_{rb}^{k} \\ &= \rho_{rb}^{jk} - I_{rb}^{jk} + T_{rb}^{jk} + \lambda N_{rb}^{jk} + m_{\phi,rb}^{jk} + n_{\phi,rb}^{jk} \end{aligned} \tag{3-7}$$

where:

- P_{rb}^{jk} refers to the double-difference code measurement of receiver pair rb and satellite pair jk
- $\lambda\phi_{rb}^{jk}$ refers to the double-difference carrier phase measurement of receiver pair rb and satellite pair jk
- ρ_{rb}^{jk} refers to the double-difference geometry distance between the receiver pair rb and satellite pair jk
- I_{rb}^{jk}, T_{rb}^{jk} refers to the remaining double-difference ionospheric delay and tropospheric delay of receiver pair rb and satellite pair jk respectively.
- $m_{P,rb}^{jk}$, $m_{\phi,rb}^{jk}$ refer to the double-difference multipath error of the code and phase measurement respectively on the path to satellite pair jk of receiver pair rb
- N_{rb}^{jk} refers to the double-difference integer ambiguity of receiver pair rb and satellite pair jk
- $n_{P,rb}^{jk}, n_{\phi,rb}^{jk}$ refers to the noise measurement of the DD code and phase measurement of receiver pair rb respectively.

3.1.3.4. Double Difference measurements for short baselines

In the case that the distance between the reference station and the rover receiver is small (baseline <100 km), the correlation of the atmospheric errors between them is very strong so that the results after the double-difference can basically cancel them out, which means $I_{rb}^{jk} \approx 0$ and $T_{rb}^{jk} \approx 0$.

From this we can get a simplified DD code and carrier phase measurement model:

$$\begin{aligned} P_{rb}^{jk} &= \rho_{rb}^{jk} + I_{rb}^{jk} + T_{rb}^{jk} + m_{P,rb}^{jk} + \varepsilon_{P,rb}^{jk} \\ &\approx \rho_{rb}^{jk} + m_{P,rb}^{jk} + \varepsilon_{P,rb}^{jk} \end{aligned} \tag{3-8}$$

$$\begin{aligned} \phi_{rb}^{jk} &= \rho_{rb}^{jk} - I_{rb}^{jk} + T_{rb}^{jk} + \lambda N_{rb}^{jk} + m_{\phi,rb}^{jk} + \varepsilon_{\phi,rb}^{jk} \\ &\approx \rho_{rb}^{jk} + \lambda N_{rb}^{jk} + m_{\phi,rb}^{jk} + \varepsilon_{\phi,rb}^{jk} \end{aligned} \tag{3-9}$$

It can be observed that the observation model is quite simple. Only the double difference of the distances and ambiguities are present, along with a noise term comprising both the combined multipath and noise. This model will be used in the positioning algorithms proposed in Section 4.2.

3.1.4. Comparison of PPP and RTK Technologies

The different characteristic of PPP and RTK precise positioning technologies makes them suited to specific applications. Table 3-1 presents the comparison of some key parameters between PPP and RTK algorithms:

Table 3-1 Comparison of some key parameters between PPP and RTK algorithms

Performance Parameter	RTK	PPP
Accuracy	cm	cm - dm
Coverage Area	Less than 50km	Worldwide
Error removed	- Orbit error - Clock error - Bias - Ionospheric delay - Tropospheric delay	- Orbit error - Clock error - Bias
Convergence Time	Several seconds (Good GNSS visibility condition)	Up to 20 – 30 mins

The RTK system requires at least two RTK capable receivers (one base station and one or more rovers), a GNSS antenna for each receiver, and a communication link between the receivers. Also, to achieve a high level of accuracy, the base station must be very precisely set up at a known location. A PPP system has a simpler configuration: a single PPP compatible receiver, an antenna capable of receiving GNSS and L-Band frequencies, and a subscription to a corrections service provider [43].

PPP provides global coverage of moderate-accuracy positioning for an unlimited number of rovers using broadcast correction. As PPP is not reliant upon regional CORS networks, it can deliver standardized performance in all regions of the globe. This independence from local infrastructure makes it well suited to sparsely populated areas and marine applications. While the accuracy provided by PPP is significantly better than standalone GNSS, it is not comparable to the accuracies achieved using RTK. In addition, the long convergence times of PPP may act as a barrier to the technology's adoption within the mass market.

Conversely, RTK provides regional, near-instantaneous high-accuracy positioning. As one of the earliest signal augmentation technologies, RTK is well proven and has been widely adopted within many industries such as agriculture. Capable of providing cm-level accuracy, RTK delivers the highest precision solution available on the market and further developments of the RTK technology have helped to address the range limitations which hindered the original technology [41].

Another differentiator is the length of the baseline. The distance between the base station and the rover (length of the baseline) on an RTK system has a direct impact on the accuracy of the system. At short base lengths (a few kilometers), the RTK is very accurate. However, as the length of the baseline increases, the accuracy, and availability of a solution decrease. At long-baseline lengths, RTK can no

longer be used. Since PPP does not use a base station, it is not affected by the length of the baseline and can then provide full accuracy anywhere in the world.

3.2. Integer Ambiguity resolution

Resolving the unknown cycle ambiguities of the double-differenced carrier phase data to integers is the key to rapid and very precise (cm-level) GNSS positioning. The process is referred to as **integer ambiguity resolution (IAR).**

GNSS ambiguity resolution can be divided into three steps, as shown in Figure 3-7:

Figure 3-7 GNSS ambiguity resolution process

- First, the integer nature of the ambiguities is discarded, and the so-called 'float' solution is obtained by a **standard least-squares adjustment**.
- In the second step, the real-valued float solutions of the ambiguities are adjusted to take the integer constraints into account.
- Finally, the float solution of the remaining parameters (notably the position unknowns and possibly additional parameters such as atmospheric delays) are corrected by virtue of their correlation with the ambiguities.

The float solution is obtained using an Extended Kalman Filter that takes advantage of the constant value of the ambiguities (if cycle slips are avoided). Once the estimated states are obtained in the EKF measurement update, the float carrier-phase ambiguities can be resolved into integer values to improve accuracy and convergence time. The final solution is referred to as the 'fixed' solution, which can be at the mm-cm level.

Ambiguity resolution is an integer ambiguity resolution problem and standard linear estimators such as parametric least-squares cannot be used to estimate the integer ambiguities [53]. For this reason, different integer ambiguity resolution methods have been studied in the literature and classified as follows [54].

The methods based on the decision approach are the first class of techniques. They use multiple hypotheses tests that check a thousand combinations to find the most consistent one. Amongst these methods, there are the Ambiguity Function Method (AFM), the Least Squares Ambiguity Search Technique (LSAST), the Maximum A Posteriori Ambiguity Search (MAPAS) method, and the Ambiguity Resolution using Constraint Equation (ARCE).

The methods based on the estimation approach are the second class of techniques and they estimate the best integer ambiguities in two steps:

- Step 1: estimation of the float carrier phase ambiguities. This is the so-called “float solution”,
- Step 2: mapping of the float ambiguities to integer values, and validation of those integers.

These methods are called integer estimating procedures.

The most basic integer estimating procedures are integer rounding and bootstrapping [53]. In integer rounding, each real-valued ambiguity is rounded to the nearest integer. Bootstrapping is a variation of integer rounding: after one ambiguity is rounded to the nearest integer, the real-valued estimates of the remaining unrounded ambiguities are corrected according to their correlation with the first ambiguity [55].

More sophisticated integer estimating procedures such as the search method has been investigated. The integer least-squares method has been demonstrated as the optimal search method in terms of maximizing the probability of correct fix [55]. Float estimation is used to initialize a search space over the integer ambiguities. The integer least-squares method then seeks to minimize the weighted sum of squared ambiguity residuals, or the distances between the initial float and final integer ambiguity estimates [56]. It is also noted that pre-processing of the ambiguities have also been investigated with positive results in terms of reducing search spaces. The most important of these is the Least-squares AMBiguity Decorrelation Adjustment method (LAMBDA), which applies a linear transformation to the ambiguities to decorrelate them for more efficient searching [57]. Other integer estimating procedures include the Fast Ambiguity Search Filter (FASF), the Fast Ambiguity Resolution Approach (FARA), and the Direct Integer Ambiguity Search (DIAS) technique.

If the integer ambiguities estimated by one of the previous methods are correct, then the double-differenced phase measurements can directly observe the satellite-to-user ranges (and consequently the user’s position) with up to millimeter-level precision, whereas the double-differenced phase measurements estimate the position’s user with a meter-level precision if the initial float ambiguities are used [15]. However, it is noted that some estimating procedures, called float estimating procedures, only make the first estimation step, providing a good floating-point estimate of the ambiguities that enable the receiver to reach decimeter-level positioning after a few seconds [54].

The Integer Ambiguity Resolution methods utilized in this Ph.D. contribution will be further introduced in Section 4.5.

3.3. Problems Raised by Urban Environments

An urban environment is generally referred to as an area with a high density of interfering objects, such as buildings, bridges, and trees [42], [48], [58]. Signals are more prone to blockages and reflections. Consequently, severe local effects are expected such as significant multipath delays on GNSS observations, especially on Code and Doppler measurements and tracking of NLOS signals. In addition, the attenuated signals are received at a lower signal carrier to noise density ratio C/N0. Therefore, cycle slips and loss of lock for carrier phase measurements are more common.

As aforementioned, the single-frequency PPP methodology requires a longer convergence time to achieve precise ambiguity resolution compared to RTK. What is more, the management of frequent cycle slips can furthermore deteriorate the performance of PPP. That is the reason why the RTK

methodology was finally chosen in this contribution to explore the performance of GNSS navigation in urban environments.

However, the urban environment is still challenging for the RTK solution, due to frequency cycle slip that should be well detected in order to allow the float ambiguities to be estimated with sufficient accuracy to permit the integer ambiguity resolution process to succeed.

To this end, multi-constellation receivers will provide a benefit in terms of the number of available satellites, especially if some of them have a high elevation and are not affected too much by multipath and cycle slips.

3.3.1. Cycle-slip Problem in the Urban Environment

As we discussed above, in environments with strong signal attenuation or blocking, the used range measurements (pseudorange) are noisy and cannot maintain the accuracy needed for applications in modern road vehicles, such as autonomous driving. Using the carrier phases of the GNSS signal enables the reduction of this noise and allows a more precise localization result. However, due to short signal outages or strong attenuations in GNSS unfriendly environments such as urban canyons discontinuities in the phase measurements can be introduced, known as phase jumps or cycle slips, to get a better positioning result, they must be detected and corrected before using those measurements for localization.

A cycle slip is a discontinuity of the measured carrier phase resulting from a temporary loss of lock in the carrier tracking loop of a GNSS receiver, the occurrence of a cycle slip describes the fact that the value of a carrier phase ambiguity term does not hold constant between two consecutive epochs. According to [48], the 3 main causes of CS are signal obstruction, low C/N0, failure in the receiver software. A fourth cause pointed out by [59] is the receiver dynamic which may cause a phase error exceeding the PLL discrimination linear domain. Although usually relatively rare in static conditions, cycle slips occurrence can be very frequent for low-cost moving receivers. It is then very important to detect them and if it is possible to repair them in order to estimate ambiguities as constants.

When a cycle slip occurs, the corresponding ambiguity state in the KF shall be re-initialized, which will lead to the degradation of the estimated position accuracy. Preferably, the value of the CS should be estimated and added to the ambiguity state to maintain the high accuracy of fixed estimation. The aim of a Cycle Slip Detection and Repair (CS-DR) scheme is thus to detect the occurrence of CS and to enable the continuous use of constant carrier phase ambiguity when no CS is detected (either to be able to fix it or to be able to use its accurately estimated value).

The entire cycle slip processing is in theory composed of four sequential stages [60]:

(1) Cycle slip detection to check for the occurrence of cycle slips.

(2) Cycle slip determination to quantify the sizes of cycle slips.

(3) Cycle slip validation to verify the determined sizes of cycle slips.

(4) Cycle slip removal to remove the cycle slips out of the associated phase measurements.

The steps (2) – (4) are also referred to as cycle slip repair or cycle-slip correction. Figure 3-8 shows a typical CS-DR process.

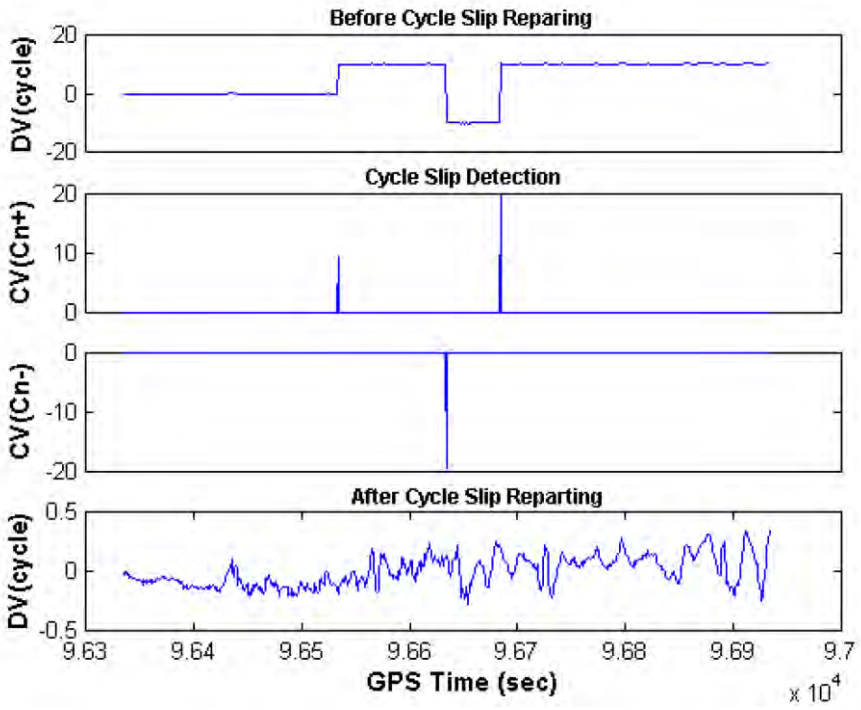

Figure 3-8 Typical Cycle Slip Detection and Repair Process [61]

Cycle slip detection and repair are crucial to maintain continuity of carrier phase observations and to benefit the precise GPS carrier phase observations for high-precision GPS positioning. There are currently many methods to detect and repair the cycle slips. However, it is still a challenging issue, in particular in the case of single-frequency measurements. The CS-DR methods utilized in this Ph.D. contribution will be further introduced in Section 4.4.

3.4. The GNSS-based Attitude Estimation Problem

Attitude determination using Global Navigation Satellite System (GNSS) signals is one of the many applications of satellite navigation. In fact, multiple GNSS antennas installed on a given platform are used to provide orientation estimates, thus adding attitude information to the standard positioning service [62].

Precise attitude estimates are obtained by exploiting the higher-ranking resolution of the carrier phase observables, which are of two orders of magnitude more accurate than pseudorange measurements. However, each carrier phase measurement is ambiguous by an unknown integer number of cycles.

Carrier phase integer ambiguity resolution is the key to high-precision GNSS positioning, navigation, and attitude determination. It is the process of resolving the unknown cycle ambiguities of the carrier phase data as integers. After resolving the ambiguity, precise baseline estimates become available, which can be used to derive the attitude of a platform equipped with multiple antennas.

The purpose of this contribution is to present, analyze and test a novel RTK performance amelioration and attitude determination method, it is thus important to review the current GNSS-based attitude estimation problem and give an overview and classification of current mathematical algorithms and techniques utilized in the process of GNSS-based attitude estimation. To do so, the first thing is to

know how to represent the attitude of one rigid body or platform. In the following sections, the most popular attitude representation methods are then first presented.

3.4.1. Attitude Representation

An attitude representation is often defined as a set of coordinates that describe the orientation of a given reference frame with respect to a second reference frame. Defining the rotational orientation of a rigid body requires a minimum of three parameters, however, many attitude representations utilize more than three parameters in defining the orientation [62].

The attitude of a rigid body belongs to the configuration space known as Special Orthogonal group $SO(3)$ and is represented in most general terms as a 3 × 3 rotation matrix. Most of the time, we use the rotation matrix $\mathcal{R}$ to represent the attitude of a rigid body in a specific frame, where $\mathcal{R}$ is an admissible orthonormal attitude matrix. In three-dimensional space, the orthonormality of R imposes six constraints, therefore only three components of $\mathcal{R}$ are independent. This implies that the matrix $\mathcal{R}$ can be described by a set of three independent parameters, which is named the minimal set.

The orthonormal matrix $\mathcal{R}$ can be parameterized in different ways, each one with its own properties and more adopted to be applied to a certain class of problems. In fact, each attitude representation has advantages and disadvantages over the others. Therefore, some representations are more suitable for certain applications than others. For instance, the Euler angles representation is more practical when describing the orbital parameters of a spacecraft in orbit, because the best representation for the modeling of free moving bodies is the roll, pitch, and yaw angles. While quaternions are the best representation choice for stable numerical algorithms and linear kinematic simulations, etc. A comprehensive overview of the various attitude representations can be found in [63] and references therein. In the following subsections, four of the most common representation methods are described.

First, the direction cosine matrix is introduced. Then, the axis/angle parametrization (also called the Euler parameters or pair of rotation), arising from the Euler Theorem of rotations, is developed [64]. Right immediately, the important redundant combinations are presented, corresponding to the unit quaternion representation (also referred to as the Euler–Rodrigues representation. Finally, the Euler angles called the roll-pitch-yaw are presented, which corresponds to the extrinsic combination x-y-z (performed on fixed frame) which has a natural physical meaning for free moving 3D rigid objects.

3.4.1.1. Direction cosine matrix

Direction cosines are cosines of angles between a vector and a base coordinate frame. A **Direction Cosine Matrix (DCM)** is a transformation matrix that transforms one coordinate reference frame to another. The DCM is one of the many ways to mathematically represent an object's orientation and utilizes nine parameters. Each of these parameters is referred to as the direction cosine values between an initial reference frame and a second reference frame [65].

The direction cosine matrix, representing the attitude of the body frame relative to the reference frame, is specified by a 3 × 3 rotation matrix $\boldsymbol{C}$, the columns of which represent unit vectors in the body axes projected along the reference axes. Here, C_b^n is the rotation matrix transforming a 3D vector r from frame $\boldsymbol{b}$ to frame $\boldsymbol{n}$.

$$C_b^n = \begin{bmatrix} c_{11} & c_{12} & c_{13} \\ c_{21} & c_{22} & c_{23} \\ c_{31} & c_{32} & c_{33} \end{bmatrix} \tag{3-10}$$

The element in the x-th row and the y-th column represents the cosine of the angle between the x-axis of the reference frame and the y-axis of the body frame.

For a vector r^i defined in frame $\boldsymbol{i}$, it can be expressed in reference frame $\boldsymbol{j}$ by pre-multiplying the vector by the direction cosine matrix C_i^j as:

$$r^j = C_i^j r^i \tag{3-11}$$

This representation fully defines the mutual orientation of the two frames, using a set of nine parameters. The advantage of DCM is that each configuration can be described without incurring any singularity or ambiguities such as double cover in attitude space in their representation as the rotation matrix is uniquely determined for a given configuration.

Although the direction cosine matrix is an important and commonly used method of representing the attitude of an object, this approach has a major drawback. The DCM uses nine parameters to describe an orientation. Since only three parameters are needed, six of the DCM values are redundant. For this reason, DCM is hardly ever used to track attitude in real-time and is mainly used to project vectors onto different reference frames.

3.4.1.2. Euler axis/angle parametrization

In mathematics, the **axis/angle representation** of a rotation parameterizes a rotation in a three-dimensional Euclidean space by two quantities: a unit vector $\boldsymbol{e}$ indicating the direction of an axis of rotation, and an angle θ describing the magnitude of the rotation about the axis. Since the unit vector has a norm constraint, three parameters are required for representation, 2 for unit vector and 1 for rotation angle [66].

$$\boldsymbol{\theta} = \theta \boldsymbol{e} \tag{3-12}$$

The axis/angle representation is equivalent to the more concise rotation vector, also known as the Euler vector. In this case, both the axis of rotation and the angle are represented by a codirectional vector with the axis of rotation whose length is the angle of rotation θ, the relation can be shown in Figure 3-9.

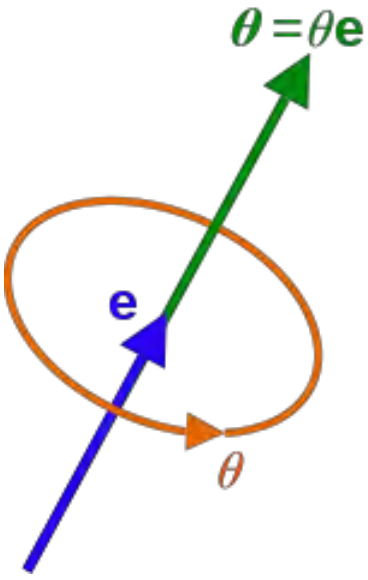

Figure 3-9 The angle θ and axis unit vector e define a rotation, concisely represented by the rotation vector θe. [66]

The representation is not unique and an additional rotation of 360° gives the same rotation matrix. However, it has many advantages too. The representation is minimal and does not require any constraints on parameters such as the unit modulus of quaternions used to represent rotations. It is easier to understand the pose (for example a twist about the y-axis) and the derivatives of rotation matrix $\mathcal{R}$ with respect to rotation angle can easily be computed.

The axis/angle representation is convenient when dealing with rigid body dynamics. It is useful to both characterize rotations, and also for converting between different representations of rigid body motion, such as homogeneous transformations and twists. However, when describing the attitude of the car, this method is too abstract and not intuitive enough.

3.4.1.3. Quaternions

Quaternions were initially defined by William Hamilton in 1843, a 19th-century Irish mathematician, to describe a Cayley-Dickson construction in four dimensions. Since then, many interpretations have appeared for different applications. The most common definition of a quaternion $\boldsymbol{q}$ is as an ordered expression of the form [67], [68]:

$$\boldsymbol{q} = w + xi + yj + zk \tag{3-13}$$

where w, x, y and z are real numbers and i, j and k are three imaginary unit numbers defined so that:

$$i^2 = j^2 = k^2 = ijk = -1 \tag{3-14}$$

A quaternion can be used as an attitude representation that uses a normalized four-dimensional vector to describe a three-dimensional orientation. This approach is based upon Euler's principal rotation. The structure of a quaternion can be used to describe a rotation with an axis/angle representation such that:

$$\boldsymbol{q} = \begin{bmatrix} q_w \\ q_x \\ q_y \\ q_z \end{bmatrix} = \begin{bmatrix} \cos\frac{\theta}{2} \\ v_x \sin\frac{\theta}{2} \\ v_y \sin\frac{\theta}{2} \\ v_z \sin\frac{\theta}{2} \end{bmatrix} = \begin{bmatrix} \cos\frac{\theta}{2} \\ \boldsymbol{v}\sin\frac{\theta}{2} \end{bmatrix} \tag{3-15}$$

where $\boldsymbol{v} = [v_x \quad v_y \quad v_z]$ is a unit vector describing the axis of rotation about which a vector rotates by an angle θ.

This is only valid if the quaternion is normalized, the normalized quaternion is then:

$$\boldsymbol{q} = \frac{1}{\sqrt{q_w^2 + q_x^2 + q_y^2 + q_z^2}} \begin{bmatrix} q_w \\ q_x \\ q_y \\ q_z \end{bmatrix} \tag{3-16}$$

Owing to parametrization by 4 variables compared to 3 in Euler angles, these do not have singularity problems. Also, any rotation sequence can be represented by a continuous quaternion trajectory and does not suffer any discontinuity like Euler angles. These are also computationally more efficient than Euler angles since the computation of sines and cosines is more expensive than the simple operator

on numbers. That is the reason why the quaternion representation is of common use in attitude estimation and control applications since it guarantees high numerical robustness.

However, this does create an over-defined attitude representation and requires the constraint that the norm of the quaternion be equal to one. Besides, they possess the ambiguity of dual covering because the quaternions $\boldsymbol{q}$ and $-\boldsymbol{q}$ represent the same quaternion. It is also easier to interpolate between rotations and to chain rigid transformations.

3.4.1.4. Euler angles

The Euler angles are three angles introduced by Leonhard Euler to describe the orientation of a rigid body with respect to a fixed coordinate system. The orientation of a rigid body with respect to a reference frame can be described by a sequence of three rotations, each about a single axis in the body frame. These three rotations are the most frequently used method for representing an object's attitude and are known as the Euler angles [62], [63], [69].

These are more intuitive and easier to interpret physically. However, they suffer from a singularity in mathematical formulations such as in Roll-Pitch-Yaw, also known as gimbal lock. At a Pitch angle of 90, it is unable to differentiate between Yaw and Roll degrees of freedom. There may also be a discontinuity when moving the angles in the parameter space, say, at $\pm\pi$. One of the Euler angles changes suddenly in response to a small change in rotation.

Even with the above shortcomings, the Euler angles are still the most widely used attitude representation method because of their minimalistic (3 parameters for 3 Degrees of Freedom) and intuitive physical representation. That is the reason why we choose this representation method to be used in this Ph.D. thesis. A detailed introduction about Euler angles is presented in the following sections.

3.4.2. Vehicle Attitude Representation and Estimation

As explained in the previous sections, there exist several ways to transform a vector's coordinates from one coordinate frame to another. Although attitude can be represented by using any three independent angular parameters such as Euler angles, quaternion with one constraint, or the direction cosine matrix with six constraints on the elements [70], [71], the most often used parameters in the navigation literature are the three Euler angles of roll, pitch, and yaw [72], which are defined in the body frame with respect to the local North (N), East (E) and Down (D) directions or the NED frame [71], [73].

3.4.2.1. Attitude Parametrization using Euler Angles

In our solution, we rely on the Euler angles rotation matrices, which rotate the vector consequently around each coordinate axes by angles that are named Euler angles. In this transformation, neither scaling nor transposition are taken into account, but only rotations are involved.

The Euler rotations are a predefined sequence of three rotations in a three-dimensional, Cartesian space. It is performed by successive application of the three rotation matrices about specific axes. The rotation matrices are defined as follows [74]:

$$R_1(\alpha) = \begin{bmatrix} 1 & 0 & 0 \\ 0 & \cos\alpha & \sin\alpha \\ 0 & -\sin\alpha & \cos\alpha \end{bmatrix} \tag{3-17}$$

$$R_2(\alpha) = \begin{bmatrix} \cos\alpha & 0 & -\sin\alpha \\ 0 & 1 & 0 \\ \sin\alpha & 0 & \cos\alpha \end{bmatrix} \tag{3-18}$$

$$R_3(\alpha) = \begin{bmatrix} \cos\alpha & \sin\alpha & 0 \\ -\sin\alpha & \cos\alpha & 0 \\ 0 & 0 & 1 \end{bmatrix} \tag{3-19}$$

where $R_j(\alpha)$ represents the rotation about the j-th axis by the angle. They are orthogonal matrices, so $R_j^{-1}(a) = R_j^{\mathrm{T}}(a) = R_j(-a)$. It is important to denote that the specific order of the rotations has to be taken into account because the rotation operations are not commutative: $R_1(\alpha)R_2(\beta) \neq R_2(\beta)R_1(\alpha)$. This property can be clarified when considering the transformation of a vector, say $\vec{x}^s$ from a certain t-frame to another s-frame:

$$\vec{x}^s = R_3(\psi)R_2(\theta)R_1(\varphi)\vec{x}^t \tag{3-20}$$

The vector $\vec{x}^t$ is first rotated around the (common) 1-axis, then rotated around the (new) 2-axis, and finally rotated around the (even newer) 3-axis. The successive rotation process is shown graphically in Figure 3-10.

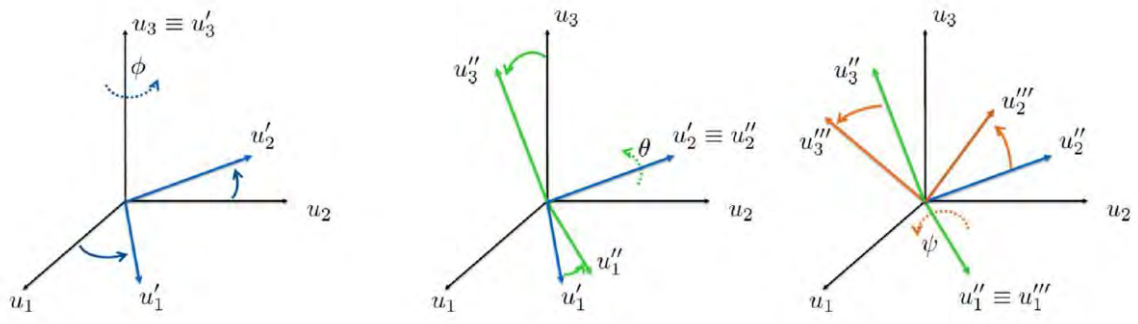

Figure 3-10 Successive rotations about θ, φ and ψ respectively [74]

3.4.2.2. Vehicle attitude presentation

Vehicles that are free to operate in three dimensions, such as aircraft and submarines, can change their attitude and rotation about the three orthogonal axes centered on the vehicle's center of gravity — the longitudinal, vertical, and horizontal axes. Motion about the longitudinal axis is termed **roll** and in aircraft determines how much the wings are banked. Motion about the perpendicular axes is called **yaw** and for aircraft, it determines which way the nose is pointed. Motion about the lateral axis is called **pitch** and it is a measure of how far an airplane's nose is tilted up or down.

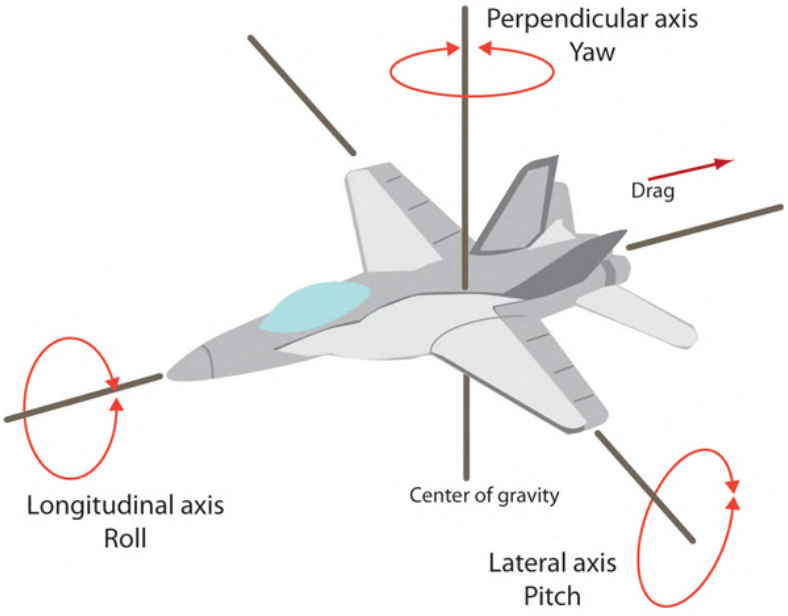

Figure 3-11 Pitch, yaw, and roll [75]

Cars also experience yaw (heading), pitch, and roll, but the amounts for the last 2 angles are relatively small and are usually the result of the suspension reacting to turns, accelerations, and road conditions.

To describe the position and attitude of the vehicle, one must define the coordinate frames in which the values are referred to.

3.4.2.2.1. The Earth-centered earth fixed coordinate frame

The Earth-centered earth fixed coordinate frame (ECEF) depicted in Figure 3-12, is where, in our model, we express the position vector of the vehicle. This frame is mostly used in GPS, because of its convenient definition. It is an orthogonal right-handed coordinate frame that has its origin fixed in the center of the ellipsoid on which the earth's surface is modeled, and it is earth-fixed: that means that it rotates with the earth itself on the same rotation axis.

It is important to note that the GNSS Control Segment generates the position and velocity of the satellites themselves in ECEF coordinates. It follows that most modern GNSS software provides also the GNSS positions in ECEF. Further, the ends of baselines determined by GNSS observation are typically given in ECEF coordinates, so that the vectors themselves become the difference between those *x*, *y*, and *z* coordinates.

3.4.2.2.2. The Navigation coordinate frame

The navigation coordinate frame, also called local navigation or local-level frame, is always centered in the point for which the navigation solution is sought for (e.g., the position of the reference station in our case). As can be seen in Figure 3-12, its orientation can be defined in several ways: If one takes the plane that is tangent to the earth's ellipsoid in the origin point, the y-axis is usually defined as the projection of the line connecting the origin with the true north pole on the just mentioned plane, whereas the x-axis is pointing, orthogonal to the y-axis, in eastern direction, being always on the tangent plane. We assume that the third axis is pointing upwards away from the ellipsoid center, orthogonal to both the x and y-axis, so as to be normal to the x-y plane. In this case, the navigation frame is called East-North-Up (ENU) frame.

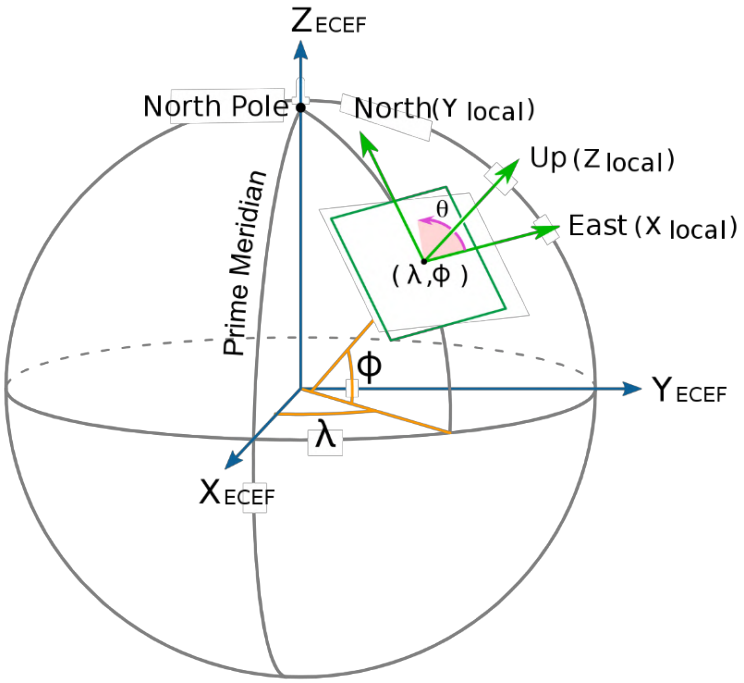

Figure 3-12 ECEF and ENU frames [Wikipedia]

The transformation from the navigation frame to the earth-centered earth-fixed frame (ECEF) is complicated by the fact that the two frames do not share the same origin. For most of the applications, however, this is not an issue as one is only interested in the relative orientation of the respective axes. The rotation matrix that describes the transformation from the navigation to the ECEF frame can be derived using Euler angles [74]. First, rotate about the East-axis (y-axis) of the North-East-Down navigation frame (NED) by the positive angle (right-hand rule) $\phi + \frac{\pi}{2}$, then rotate about the (new) Down axis (z-axis) by the negative angle $-\lambda$:

$$R_n^e = R_3(-\lambda)R_2\left(\phi + \frac{\pi}{2}\right) \tag{3-21}$$

where with (ϕ, λ) it is meant respectively the latitude and longitude in radians of the origin of the considered navigation frame w.r.t. the earth-centered earth fixed frame [76].

The rotation matrix becomes the notation R_s^t, where the subscript s is the origin coordinate frame, and the superscript t is the destination coordinate frame for the rotation. In other words, R_s^t describes the rotation from the s-frame to the t-frame. Since R_n^e is a product of orthogonal matrices and thus orthogonal itself, the inverse transform from the ECEF to the navigation frame can be performed simply as:

$$R_e^n = (R_n^e)^{-1} = R_2\left(-\phi - \frac{\pi}{2}\right)R_3(\lambda) \tag{3-22}$$

3.4.2.2.3. The body-fixed coordinate frame

The body coordinate frame as shown in Figure 3-13, simply called body frame, is usually centered in a specific point of an object for which one wants to estimate its position. Its origin is so coincident with those of the navigation frame, but its orientation remains fixed with the moving object.

Usually, the three axes are aligned so that the x-axis is oriented along the main movement direction of the vehicle, so to point in the “forward” direction, the y-axis is orthogonal to the x-axis pointing “right" and the z-axis is pointing “down", being orthogonal to both the x and the y-axis. Usually, the plane spanned by the x and y-axis is aligned so to match the horizontal section of the vehicle. These axes often take the name of roll (x-axis), pitch (y-axis), and yaw or heading axis (z-axis), and they are also the axes to which the inertial sensors are aligned to.

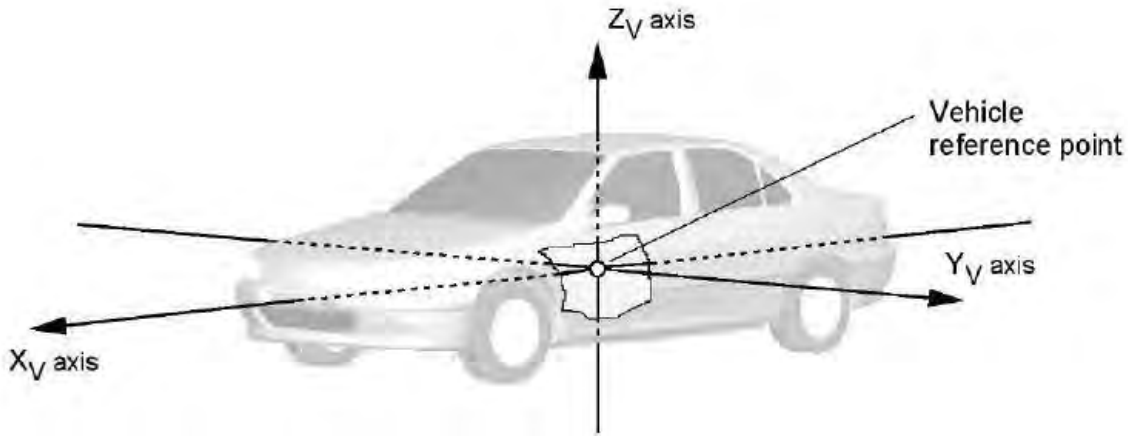

Figure 3-13 Body coordinate frame of a car [77]

The transformation from the body-fixed frame into the navigation frame can be performed as usual by using the Euler attitude angles. In this case, the angles are the bank (denoted by ‘φ’), elevation (denoted by ‘θ’), and heading (denoted by ‘ψ’) angles. In our model, the heading angle is defined as the angle between the North-axis of the NED navigation frame and the projection of the roll-axis or x-axis of the body frame into the North-East plane of the NED frame, whereas the elevation angle is defined as the angle between the roll-axis or x-axis of the body frame and its projection on the North-East plane of the NED frame [74].

By applying successive rotations and using Euler rotation matrices, to rotate from the body to the navigation frame one must first apply a rotation around the x-axis by the negative angle $-\varphi$, then apply a rotation about the new y-axis by the negative angle $-\theta$, finally apply a third rotation around the even newer z-axis by a negative angle of $-\psi$:

$$R_b^n = R_3(-\psi)R_2(-\theta)R_1(-\varphi) \tag{3-23}$$

Again, using the orthogonality property of the rotation matrix one can define the inverse rotation as:

$$R_n^b = (R_b^n)^{-1} = R_1(\varphi)R_2(\theta)R_3(\psi) \tag{3-24}$$

The latter rotation definition is represented in Figure 3-14:

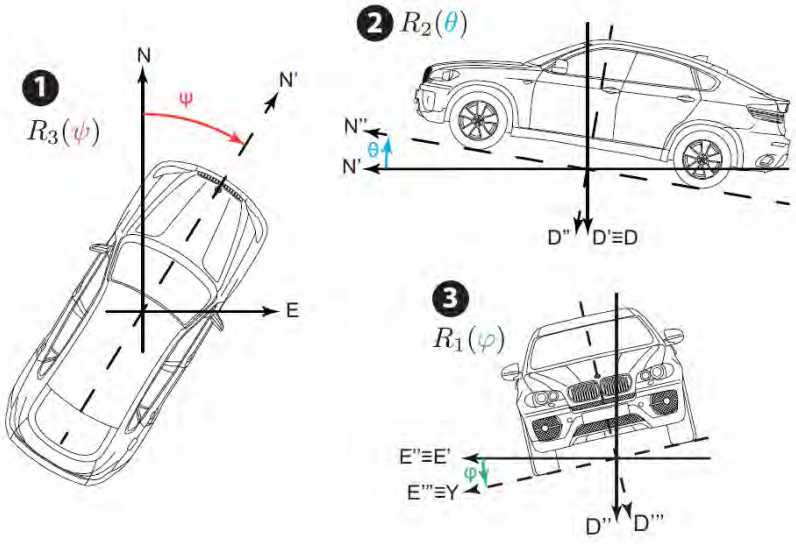

Figure 3-14 Graphical representation of the three successive rotations (attitude) of vehicle [74]

3.4.2.3. Vehicle Attitude Estimation Methods

The attitude of a platform or vehicle can be obtained by collecting direction measurements or baseline coordinates with different devices, such as gyroscopes, magnetometers, GNSS receivers, IMU, digital compasses, etc. The rotation matrix must be estimated from measured observations. However, these observations are affected by a certain amount of error most of the time, which would generally give non-orthonormal solutions. In the following, the vehicle attitude is modeled as a rotation matrix, which is the orthonormal matrix that transforms vector components from a local frame (integral with the platform whose attitude needs to be estimated) to the reference frame.

In general, the attitude estimation methods can be classified into two classes:

- The methods which extract the orthonormal matrix from a set of baseline observations
- The methods which calculate the best orthonormal approximation of an approximate attitude matrix (usually not orthonormal).

The first class of problems is described by the following minimization problem:

$$\bar{R} = \text{argmin}_{R\in\mathbb{O}^{3\times3}} \sum_{i=1}^{n} w_i \, \|b_i - Rf_i\|^2 \tag{3-25}$$

The corresponding attitude matrix is then the orthonormal matrix $\bar{R}$ that minimizes the sum of squared weighted distances between the observed baseline vectors b_i and the rotated local baseline vectors Rf_i. The solution to this problem is known as Orthogonal Procrustes Problem (OPP). In addition, as can be seen from **Equation (3-25)**, different baseline observations can be individually weighted by adding the coefficients w_i . We may be also interested in weighting the single components of each baseline observation: this gives a so-called Weighted Orthogonal Procrustes Problem (WOPP).

The second class of problems is represented by the following minimization expression:

$$\bar{R} = \text{argmin}_{R\in\mathbb{O}^{3\times3}} \|\text{vec}(\hat{R} - R)\|_Q^2 \tag{3-26}$$

Where the matrix $\hat{R}$ is a given approximate solution for which the orthonormality constraint is generally not satisfied and the Q is the weight matrix that weighs all the entries of the observed matrix $\hat{R}$. In this case, the corresponding attitude matrix is the solution $\bar{R}$ that minimizes the weighted distance between the sought orthonormal matrix with respect to a float (or non-orthonormal) solution $\hat{R}$.

This classification is purely academic: under certain circumstances, which will be stated, problems of the first class can be reduced to problems of the second class, and vice versa.

In this dissertation, the general attitude estimation problem is not the focus, so the detailed process of the introduced methods above will not be presented. One will focus on the GNSS-based attitude determination (estimation) problem, which will be introduced in the next section.

3.4.3. GNSS-based Attitude Determination

As discussed in the previous chapter, the Global Navigation Satellite Systems are a valid aid in support of aeronautic science. Thanks to the nature of GNSS that it can provide accurate, fast, and driftless positioning solutions, GNSS technology has been successfully implemented in aircraft design, so as to provide accurate position, velocity, and heading estimations. One of the main issues in airborne navigation is the determination of the aircraft's attitude, which can also be understood as the orientation of the aircraft with respect to a given reference system [78].

In addition to being used on aircraft, attitude determination systems are widely implemented in satellites, vehicles, ships, drones, and other moving objects. Many sensors and technologies are available to estimate the attitude of these objects, including Inertial measurement units (IMUs), GNSS receivers, magnetometers, digital compasses, gyroscopes, and accelerometers, etc. Recently, there is a growing interest in GNSS-based attitude determination, due to its stable operation, cost efficiency, and low power consumption [62], [78], [79]. Although the accuracy of a stand-alone GNSS attitude system may not be comparable to other modern attitude sensors, a GNSS-based system has several advantages. It is inherently drift-free, a GNSS receiver has low power consumption, requires minor maintenance, and it is not as expensive as other high-precision systems, such as laser gyroscopes [78].

GNSS-based attitude determination employs several antennas rigidly mounted on the platform, the orientation of a body with respect to a defined reference frame can be estimated by employing two or more antennas. By processing the tracked GNSS signals, precise baseline estimates can be made available. The orientation of each of the baselines formed between the antennas can then be determined by computing their relative positions, which is able to be translated directly into angular estimations of the attitude [78].

Given a matrix of baseline coordinates B and a matrix of local baseline coordinates F relative to the platform, estimating the platform attitude is found using the orthonormal rotation matrix R that transforms B into F, with $B = R * F$. This is the general formulation that applies to any attitude sensor that relies on baseline observations to derive the platform's orientation. GNSS-based attitude estimation is based on the same working principle: processing code and phase observations to yield baseline estimates, which are then used to estimate the attitude angles.

Due to the geometrical nature of the GNSS observations, the accuracy of the GNSS-based attitude determination systems depends primarily on two main factors [29], [72], [80]:

1. The quality of the GNSS observations:
   a) Noise level of carrier phases observables
   b) Residual errors of systematic types
   c) Correct ambiguity resolution for carrier phase observables
2. The geometrical size of a platform (The length of baselines between antennas on a platform)

Most of the time, we have no control over the latter, as the size and geometry of the platform limits the maximum distance that antennas can be placed. Thus, the challenge of obtaining accurate attitude estimates lies in the precision and quality of the GNSS observations. To this day, this is still an issue worthy of attention and research. Due to this, the GNSS-based attitude determination of a moving object using readings from GNSS is an active area of research. In the following sections, a literature survey of the GNSS-based attitude determination will be presented.

3.4.3.1. GNSS-based Attitude Determination Models

GNSS attitude solutions can be obtained either by using the GNSS-derived baselines or directly from raw GNSS carrier phase observables [70]–[72], [80]. These two methods are essentially equivalent after the IAR process according to the equivalence theorem of parameters in a linear or linearized (real-valued) Gauss–Markov model [81]. By casting the set of double-difference (DD) GNSS code and phase observations obtained by tracking $n+1$ satellites on a single frequency into a linear or linearized (real-valued) model [5], we have:

$$\begin{gathered} E(y) = Az + Gb; z \in \boldsymbol{Z^n}, b \in \boldsymbol{R^3} \\ D(y) = Q_{yy} \end{gathered} \tag{3-27}$$

where y is the known vector of GNSS DD code and phase observations, z and b are the unknown parameter vectors of integer ambiguities and real-valued baseline coordinates correspondingly. $E(:)$ and $D(:)$ denote the expectation and dispersion operators, and A and G are the given design matrices which bound the data vector to the unknown parameters. Matrix A, a $2n*n$ matrix includes the carrier wavelengths, and the geometry $2n*3$ matrix G includes the receiver satellite unit line-of-sight vectors. The variance matrix of y is set to the positive definite matrix Q_{yy}.

For attitude determination applications, the distance between antennas is usually limited to a few meters, and rarely exceeds tens of meters. In this case, we may disregard all the atmospheric delays, which are canceled by the differencing operations. The only real-valued unknowns are thus the baseline coordinates.

We assume a Gaussian noise distribution for the collected observables, whose dispersion D(y) is characterized by the variance-covariance (V-C) matrix Q_{yy}. The integer nature of the ambiguities is given explicitly through the notation, whereas the baseline vector belongs to the space of real vectors, $b \in \boldsymbol{R^3}$. **Equation (3-27)** can be extended for arrays of, say, m+1 antenna. So, the multi-baseline model becomes [5]:

$$\begin{gathered} E(Y) = AZ + GB; Z \in \boldsymbol{Z^{n\times m}}, B \in \boldsymbol{R^{3\times m}} \\ D(\mathrm{vec}(Y)) = Q_{YY} \end{gathered} \tag{3-28}$$

where Y is the $2n*m$ matrix whose columns are the linearized DD code and phase observations at each baseline, Z is the $n*m$ matrix whose columns are the integer-valued ambiguity vectors at each baseline, and B is the $3*m$ matrix whose columns are the real-valued baseline coordinates. The matrix Q_{yy}

describes the dispersion of the vector of observables $vec(Y)$, where vec is the operator that stacks the columns of a matrix.

To derive the attitude of the platform, we need to solve for the unknowns in **Equation (3-28)**, and then estimate the rotation matrix which transforms the baseline matrix B into the local (body frame) baseline coordinates F. This is the most classical approach used in many GNSS-based attitude algorithms available in the literature.

In principle, the integer LS method can be directly applied to **Equation (3-28)** to resolve the integer parameters Z. For the unconstrained situation, same as the case of precise positioning in Section 3.1, the LAMBDA method is the most popular algorithm to solve the GNSS integer ambiguity resolution problem [72]. The well-known method LAMBDA is first described for GNSS precise relative positioning by Teunissen in 1995 [57] and further significantly improved by Chang [82] and Xu [83]. What is more, since the multi-antenna configuration can be measured precisely a priori, several baseline-constrained ambiguity resolution methods have been developed under the framework of GNSS attitude determination [71], [84], [85], including the single baseline constrained LAMBDA method and the Multivariate Constrained LAMBDA method (MCLAMBDA).

Once the ambiguity resolution is finished, we can then continue to solely determine the attitude of the considered platform. If the baselines of a GNSS attitude system are properly estimated by using precise relative positioning RTK and/or PPP, then we can directly use them to determine the attitude of the platform [72]. Mathematically speaking, given a number of unit vectors in both the local level NED and body frames, say $(b_1, b_2, \dots, b_n)$ in the NED frame and $(f_1, f_2, \dots, f_n)$ in the body frame, one will then solve for the unknown attitude matrix by minimizing the objective function which was introduced in **Equation (3-25)**.

$$\bar{R} = \text{argmin}_{R\in\mathbb{O}^{3\times3}} \sum_{i=1}^{n} w_i \|b_i - Rf_i\|^2 \tag{3-29}$$

If the rotation matrix is first properly parameterized with, in our case, the three Euler angles, one can then deduce the three Euler angles from the solution $\bar{R}$ of the unconstrained minimization problem and the attitude of the platform is determined [72].

3.4.3.2. Literature Review of GNSS-based Attitude Determination

As introduced in [72], in general, GNSS use precise geometrical carrier phase observables between GNSS satellites, and the receivers fixed on a platform to determine the attitude of the considered platform ([70], [71], [80], [86]–[91]), though the code measurements can be very useful at the stage of integer ambiguity resolution. Thus, unlike magnetometers, accelerometers, or gyroscopes, GNSS attitude determination is usually free of drift biases.

Until now, many studies have been carried out to investigate the feasibility and performance of GNSS as an attitude sensor: e.g., [72], [80], [92]–[103]. Recently, Teunissen [85] proposed an array-aided PPP concept for simultaneous kinematic PPP positioning of an array and its attitude in 2012. The basic idea is to form a combined observational model, which consists of two sub-models: one with single difference (SD) observables of phases and codes between satellites for the array PPP and the other with double difference (DD) observables of phases and codes for the attitude determination of the array. The unknown parameters are treated separately but the correlations of the observables

between the two sub-models are fully taken into account. Henkel [104] followed the idea of Teunissen to integrate SD observables of phases between satellites and an inertial sensor for PPP and attitude determination. Since the major purpose of Henkel [104] was mainly for navigation applications, the tightly integrated system of PPP and attitude was required to be of low cost. Consequently, only two low-cost single-frequency GNSS receivers are used together with a low-cost IMU sensor to determine the attitude of the platform [72].

Attitude estimation via GNSS observations is also demonstrated to be a viable technique with a wide spectrum of challenging applications [62], ranging from terrestrial to maritime (guidance of land vehicles, precise docking of vessels, precision farming), and from air to space (landing assistance, Unmanned Aerial Vehicles, and guidance and control of space platforms). Examples of such applications can be found in [62], [79], [92], [93], [97], [101], [102], [105]–[108] etc.

Finally, a newest and comprehensive Literature Survey can be found in the work of ALMAT et al. which has been published in 2020 [109]. The article summarized some part of the findings based on the comprehensive and huge literature survey, more detailed information about the GNSS-based attitude determination techniques can be found in this article.

3.4.3.3. GNSS-based Attitude Determination Limitations

Currently, most of the GNSS-based attitude determination methods make use of baseline observations between antennas installed on the same rigid body to estimate its orientation with respect to a given frame. The attitude can be extracted after the baseline coordinates are estimated. Hence, the estimation of the baseline is treated separately from the attitude estimation problem.

This is a common approach for most attitude estimation systems, e.g., aircraft or any other system that relies on external information to compute its own attitude. For GNSS-based systems, this approach, although largely exploited, is somewhat unsatisfactory. The additional information given by the a priori knowledge of the antenna's placement should be exploited within the baseline estimation process, ultimately leading to a more accurate and reliable solution. The platform attitude should be integrally included as an additional unknown in the model used to describe the set of GNSS observations.

Therefore, in this Ph.D. contribution, we proposed a novel method that uses multiple low-cost, single-frequency receivers with known geometry to enable the vehicle attitude determination and RTK performance amelioration at the same time, the detailed information will be introduced in Chapter 4.

3.5. Chapter Summary

In this chapter, we have focused on the introduction and classification of the state of the art of GNSS-based precise positioning and attitude estimation technique, which helps us to identify the proper techniques that be used in this Ph.D. thesis.

The description of the GNSS precise positioning techniques is first provided, including the DGNSS, PPP, and RTK, the comparison between each technique is presented. The challenges of the GNSS's precise positioning in highly constrained environments are revealed. Overall, the RTK methodology has been preferred over the PPP methodology in constraint environments due to its fast convergence time, better precision, and easier integer ambiguity resolution process.

Finally, a review and classification of the existing attitude representation methods is given, followed by a literature review of current mathematical algorithms and techniques utilized in the process of GNSS-based attitude estimation. The limitations of current GNSS-based attitude determination methods are analyzed at the end.

Chapter 4. Proposed Multi-receiver Architecture for GNSS Precise Positioning and Attitude Estimation

In chapter 3, we have seen precise positioning and attitude determination techniques. As we discussed in chapter 3, precise positioning with a stand-alone GPS receiver or using differential corrections is known to be strongly degraded in an urban or sub-urban constrained environment due to frequent signal masking, strong multipath effect, frequent cycle slips on carrier phase, etc.

In order to achieve precise positioning in these GNSS signal-degraded environments, the RTK methodology has been preferred over the PPP methodology. The reason for this is that for the low-cost GNSS receivers which provide only single-frequency GNSS measurement, the lack of accurate atmosphere correction models, as well as the long PPP convergence time, restrict the application of the PPP methodology in a constrained area.

The objective of this work is to explore the possibility of achieving RTK precise positioning with a low-cost architecture using multiple installed low-cost receivers with known geometry to enable vehicle attitude determination and RTK performance amelioration. The use of multiple installed receivers' architecture is expected to improve the robustness of the RTK positioning by taking advantage of the known geometry and measurement redundancy. Also, the additional observability of attitude can be an interesting feature for some specific applications.

In this chapter, the detailed implementations of our proposed installed multi-receiver architecture for GNSS RTK precise positioning and vehicle attitude estimation adapted to the constrained environment are provided.

The structure of this chapter is as follows:

- Section 4.1 describes the standard Kalman Filter Methodology. The Kalman filter is chosen as the estimation technique in order to take into account the dynamics of the rover and to use an epoch-to-epoch geometric link for states refinement.
- Section 4.2 illustrates our proposed multi-receiver RTK precise positioning and vehicle attitude estimation algorithm. This includes our RTK measurement model, state vector as well as system configuration and geometry.
- Section 4.3 presents our observables pre-processing module. Several pre-processing procedures of the GNSS observables are proposed in response to their vulnerabilities to outliers notably in the constrained areas. For instance, the elevation mask is set to exclude the measurement outliers, an innovation test is implemented to further ensure the reliability of the GNSS navigation solution.
- Section 4.4 is dedicated to the handling of the precise carrier phase measurements. Procedures to detect and repair cycle slips are introduced.

- Section 4.5 provides the elaborations of the integer ambiguity resolution theory. This includes the well-known LAMBDA method and its updated version MLAMBDA method.
- Section 4.6 finally explains the expected benefits of the proposed installed multi-receiver architecture and summary this chapter.

4.1. Overview of the Kalman Filter

The Kalman filter (KF) and its extended versions have great importance in the global navigation satellite system (GNSS) applications [110]. Most GNSS receivers compute their positions using Kalman filtering (more common) or least-squares (less common) estimation algorithms. Applications of the KF can also be found in a wide variety of integrated navigation systems (e.g., GNSS integrated with IMU) as well as precise positioning techniques like RTK.

The KF is a recursive algorithm that allows the optimal parametric estimation of a Gaussian state vector characterizing a time-varying (i.e., dynamic) system [111] with gaussian observation errors. Unlike the Least-Squares algorithm which provides an estimate based only on measurements of the current epoch, the Kalman filter combines the observation from the current epoch with the state prediction obtained from previous epochs to update the state variables, as well as the associated error covariance.

The KF comprises basically two alternating steps: the state prediction step and the state update step. In the first step, the system model is applied to predict the behavior of the system at the next epoch using a-priori information such as information coming from the movement model. In the second step, the update step, the predicted measurement is compared to the actual measurements, and a trade-off between the two estimates is chosen as optimal.

This estimation is provided thanks to the knowledge of a **measurement model** and a **state transition model**. At each epoch, the algorithm uses the state estimation obtained from the previous iteration and propagated through the state transition model, and the latest measurement vector, to provide the best estimation. This optimum is computed from the stochastic properties of the state transition and measurement models following an MMSE (minimum mean square error) Bayesian approach.

4.1.1. Measurement Model and State transition Model

The Kalman Filter provides an estimate of a time-varying system state at every epoch. The index n is used to define the epoch. Consider a linear stochastic model where the state is a continuous process observed at discrete epochs, the process can be modeled thanks to the state transition equation:

$$\mathbf{x}_n = \boldsymbol{\phi}_n \mathbf{x}_{n-1} + \boldsymbol{G}_n \boldsymbol{u}_n + \mathbf{w}_n \tag{4-1}$$

and the measurement equation:

$$\mathbf{z}_n = \mathbf{H}_n \mathbf{x}_n + \mathbf{v}_n \tag{4-2}$$

Where:

- $\mathbf{x}_n$ is the state vector
- $\mathbf{z}_n$ is the measurement vector (known)
- $\boldsymbol{\phi}_n$ is the state transition matrix from epoch $n-1$ to epoch n (known)
- $\boldsymbol{u}_n$ is the command vector (known)
- $\boldsymbol{G}_n$ is the command matrix (known)
- $\mathbf{H}_n$ is the observation matrix (known)

- $\mathbf{w}_n$ is the state noise vector
- $\mathbf{v}_n$ is the measurement noise vector

The state noise vector represents the liberty of the system evolution regarding the linear evolution model proposed by the state transition matrix, which can also be viewed as the modeling error of the linear state transition model.

To establish the Kalman Filter equations, the following hypotheses are needed:

- The measurement noise $\mathbf{v}_n$ and state noise $\mathbf{w}_n$ are white Gaussian centered noise, and they are independent of each other.
- Their covariance matrixes are supposed to be known: $\mathbf{R}_n = Cov(\mathbf{v}_n)$ and $\boldsymbol{Q_n} = Cov(\mathbf{w}_n)$.
- The initial state $\mathbf{x}_0$ is a random Gaussian vector that is independent of $\mathbf{v}_n$ and $\mathbf{w}_n$.

One can notice that, due to the recursive equation, the system state at any instant $\mathbf{x}_n$ is random and Gaussian. Therefore, it can be described by just two parameters: the mean value of $\hat{\mathbf{x}}_n = E(\mathbf{x}_n)$ and its covariance matrix $\mathbf{P_n} = Cov(\mathbf{x}_n)$. The Kalman filter provides at each instant the MMSE estimator, which minimizes the Bayesian mean square error.

In the standard KF case, all the models are supposed linear, which is usually not the case. The extension of the Kalman filter will be further introduced in Section 4.1.4 to consider non-linear models, both for state transition and measurement models.

At each epoch k, the KF proceeds in 2 steps:

1. A **state prediction** (or propagation)
2. Then a **measurement update**.

At epoch $n-1$, there is, therefore, an intermediate state estimate just after the prediction step, named *a priori state prediction*, which will be indexed by $n \mid n-1$. After the measurement update, the new estimate is called *a posteriori state* estimate and will be indexed by $n \mid n$. These steps are summarized in Figure 4-1:

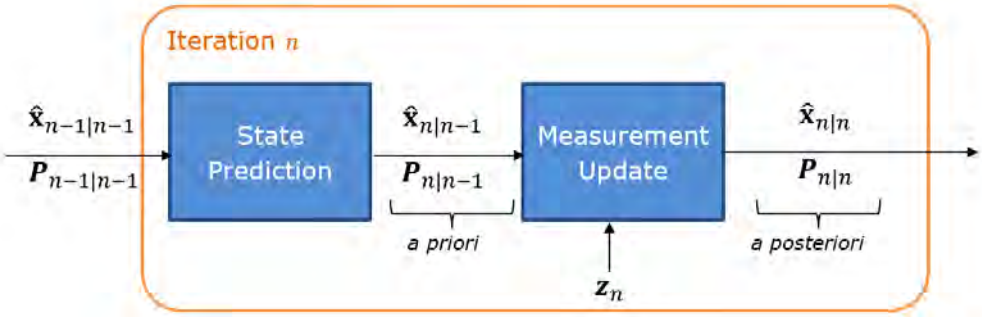

Figure 4-1 Kalman Filter steps

Being an MMSE estimator, the Kalman filter output is:

$$\hat{\boldsymbol{x}}_{n|n-1} = E[\boldsymbol{x}_n|\boldsymbol{z}_0, \dots, \boldsymbol{z}_{n-1}] = E[\boldsymbol{x}_n|\boldsymbol{z}_0^{n-1}] \tag{4-3}$$

Let us define the a priori state covariance matrix as follows:

$$\boldsymbol{P}_{n|n-1} = Cov[\boldsymbol{x}_n|\boldsymbol{z}_0^{n-1}] \tag{4-4}$$

$$\boldsymbol{P}_{n|n-1} = E[(\boldsymbol{x}_n - E[\boldsymbol{x}_n])(\boldsymbol{x}_n - E[\boldsymbol{x}_n])^T|\boldsymbol{z}_0^{n-1}] \tag{4-5}$$

$$\boldsymbol{P}_{n|n-1} = E[(\boldsymbol{x}_n - E[\boldsymbol{x}_n|\boldsymbol{z}_0^{n-1}])(\boldsymbol{x}_n - E[\boldsymbol{x}_n|\boldsymbol{z}_0^{n-1}])^T|\boldsymbol{z}_0^{n-1}] \tag{4-6}$$

Since $\mathrm{E}[\boldsymbol{x}_n|\boldsymbol{z}_0^{n-1}] = \hat{\boldsymbol{x}}_{n|n-1}$, we can write:

$$\boldsymbol{P}_{n|n-1} = E\left[\left(\boldsymbol{x}_n - \hat{\boldsymbol{x}}_{n|n-1}\right)\left(\boldsymbol{x}_n - \hat{\boldsymbol{x}}_{n|n-1}\right)^T|\, \boldsymbol{z}_0^{n-1}\right] \tag{4-7}$$

This a priori state covariance matrix is also the a priori estimation error covariance matrix. The same goes for the a posteriori state covariance matrix $\boldsymbol{P}_{n|n} = Cov(\boldsymbol{x}_n|\boldsymbol{z}_0^n)$. These matrices are used to have an indicator of the estimator's quality.

4.1.2. Kalman Filter Equations

The KF can be synthetized as a five-equation operating process. In this section, the general Kalman filter equations, as well as their corresponding derivation process, are presented.

The first step of the KF is to develop the properties of the predicted states. As introduced in Section 4.1.1, the state transition equation can be modeled as:

$$\mathbf{x}_n = \boldsymbol{\phi}_n\mathbf{x}_{n-1} + \boldsymbol{G}_n\boldsymbol{u}_n + \mathbf{w}_n \tag{4-8}$$

It follows that:

$$\hat{\boldsymbol{x}}_{n|n-1} = E[\boldsymbol{x}_n|\boldsymbol{z}_0^{n-1}] = E[\boldsymbol{\phi}_n\mathbf{x}_{n-1} + \boldsymbol{G}_n\boldsymbol{u}_n + \mathbf{w}_n|\boldsymbol{z}_0^{n-1}] \tag{4-9}$$

$$\hat{\boldsymbol{x}}_{n|n-1} = \boldsymbol{\phi}_n E[\mathbf{x}_{n-1}|\boldsymbol{z}_0^{n-1}] + \boldsymbol{G}_n E[\boldsymbol{u}_n|\boldsymbol{z}_0^{n-1}] + E[\mathbf{w}_n|\boldsymbol{z}_0^{n-1}] \tag{4-10}$$

Since $E[\boldsymbol{u}_n|\boldsymbol{z}_0^{n-1}] = \boldsymbol{u}_n$ and $E[\mathbf{w}_n|\boldsymbol{z}_0^{n-1}] = E[\mathbf{w}_n] = 0$, we can have:

$$\boxed{\hat{\boldsymbol{x}}_{n|n-1} = \boldsymbol{\phi}_n\hat{\boldsymbol{x}}_{n-1|n-1} + \boldsymbol{G}_n\boldsymbol{u}_n} \quad \textbf{(Equation 1: state prediction)} \tag{4-11}$$

The a priori covariance matrix can then be written:

$$\boldsymbol{P}_{n|n-1} = E\left[\left(\boldsymbol{x}_n - \hat{\boldsymbol{x}}_{n|n-1}\right)\left(\boldsymbol{x}_n - \hat{\boldsymbol{x}}_{n|n-1}\right)^T|\, \boldsymbol{z}_0^{n-1}\right] \tag{4-12}$$

$$\boldsymbol{P}_{n|n-1} = E\left[\left(\boldsymbol{\phi}_n\left(\boldsymbol{x}_{n-1} - \hat{\boldsymbol{x}}_{n-1|n-1}\right) + \mathbf{w}_n\right)\left(\boldsymbol{\phi}_n\left(X_k - \hat{X}_{k|k}\right) + \mathbf{w}_n\right)^T|\boldsymbol{z}_0^{n-1}\right] \tag{4-13}$$

$$\boldsymbol{P}_{n|n-1} = \boldsymbol{\phi}_n E\left[\left(\boldsymbol{x}_{n-1} - \hat{\boldsymbol{x}}_{n-1|n-1}\right)\left(\boldsymbol{x}_{n-1} - \hat{\boldsymbol{x}}_{n-1|n-1}\right)^T|\boldsymbol{z}_0^{n-1}\right]\boldsymbol{\phi}_n^T + E[\mathbf{w}_n\mathbf{w}_n^T|\boldsymbol{z}_0^{n-1}] \tag{4-14}$$

Noting $\boldsymbol{Q_n} = Cov(\mathbf{w}_n)$., we can deduce the second Kalman filter equation:

$$\boxed{\boldsymbol{P}_{n|n-1} = \boldsymbol{\phi}_n\boldsymbol{P}_{n-1|n-1}\boldsymbol{\phi}_n^T + \boldsymbol{Q_n}} \quad \textbf{(Equation 2: a priori covariance)} \tag{4-15}$$

Generally, this results in a larger uncertainty of the predicted states, compared to the last state estimation ("$\boldsymbol{P}_{n|n-1} > \boldsymbol{P}_{n-1|n-1}$"). This is due to the introduction of the state transition uncertainty modeled by $\boldsymbol{Q_n}$.

To determine $\hat{\boldsymbol{x}}_{n|n}$, the following relation on conditional probabilities is used:

$$P\underbrace{[\mathbf{x}_n|\boldsymbol{z}_0^n]}_{posterior} = P\left[\underbrace{(\mathbf{x}_n|\boldsymbol{z}_0^{n-1})}_{prior} \mid \underbrace{\boldsymbol{z}_n}_{new\ meas}\right] \tag{4-16}$$

Using this relationship,

$$\begin{aligned} P[\mathbf{x}_n|\boldsymbol{z}_0^n] &= P[(\mathbf{x}_n|\boldsymbol{z}_0^{n-1})|\boldsymbol{z}_n] \\ \Rightarrow \hat{\boldsymbol{x}}_{n|n} &= E[\mathbf{x}_n|\boldsymbol{z}_0^n] = E[(\mathbf{x}_n|\boldsymbol{z}_0^{n-1})|\boldsymbol{z}_n] \end{aligned} \tag{4-17}$$

We can then apply the result for MMSE in the case of a Gaussian linear measurement model (result from [112]) :

$$\hat{\theta} = E[\theta|y] = \mu_\theta + \Sigma_\theta H^T[H\Sigma_\theta H^T + R]^{-1}(\mathrm{y} - H\mu_\theta) \tag{4-18}$$

By considering:

- $\theta = \mathbf{x}_n|\boldsymbol{z}_0^{n-1}$, so
  - $\mu_\theta = E[\mathbf{x}_n|\boldsymbol{z}_0^{n-1}] = \hat{\boldsymbol{x}}_{n|n-1}$,
  - $\Sigma_\theta = Cov(\mathbf{x}_n|\boldsymbol{z}_0^{n-1}) = \boldsymbol{P}_{n|n-1}$
- $y = \boldsymbol{z}_n$
  - $R = Cov[\boldsymbol{z}_n] = \mathbf{R}_n$

Therefore, we have

$$\hat{\boldsymbol{x}}_{n|n} = \hat{\boldsymbol{x}}_{n|n-1} + \boldsymbol{P}_{n|n-1}\mathbf{H}_n^T\left(\mathbf{H}_n\boldsymbol{P}_{n|n-1}\mathbf{H}_n^T + \mathbf{R}_n\right)^{-1}\left(\boldsymbol{z}_n - \mathbf{H}_n\hat{\boldsymbol{x}}_{n|n-1}\right) \tag{4-19}$$

From this equation, we can define the third Kalman filter equation: Kalman Gain.

$$\boxed{\boldsymbol{K}_n = \boldsymbol{P}_{n|n-1}\mathbf{H}_n^T\left(\mathbf{H}_n\boldsymbol{P}_{n|n-1}\mathbf{H}_n^T + \mathbf{R}_n\right)^{-1}} \quad (\textbf{Equation 3: Kalman Gain}) \tag{4-20}$$

This gain permits to balance the information coming from the state prediction and the observations. If the state prediction is deemed good, then $\boldsymbol{K}_n$ will be small. On the contrary, if the state prediction is deemed bad compared to the observations, then $\boldsymbol{K}_n$ will be large which means that more trust will be put into the observations.

The fourth Kalman filter equation is the state update equation:

$$\boxed{\hat{\boldsymbol{x}}_{n|n} = \hat{\boldsymbol{x}}_{n|n-1} + \boldsymbol{K}_n\left(\boldsymbol{z}_n - \mathbf{H}_n\hat{\boldsymbol{x}}_{n|n-1}\right)} \quad (\textbf{Equation 4: state update}) \tag{4-21}$$

For the a posteriori state covariance matrix $\boldsymbol{P}_{n|n}$, we do similar reasoning.

From the Bayes theorem, we find the relationship:

$$\begin{aligned} P[\mathbf{x}_n|\boldsymbol{z}_0^n] &= P[(\mathbf{x}_n|\boldsymbol{z}_0^{n-1})|\boldsymbol{z}_n] \\ \Rightarrow \boldsymbol{P}_{n|n} &= Cov(\mathbf{x}_n|\boldsymbol{z}_0^n) = Cov[(\mathbf{x}_n|\boldsymbol{z}_0^{n-1})|\boldsymbol{z}_n] \end{aligned} \tag{4-22}$$

Similarly, by considering the θ and y in the same way as in (**4-19**), one can apply the results for MMSE in the case of a Gaussian linear measurement model:

$$Cov(\theta|y) = \Sigma_\theta - \Sigma_\theta H^T [H\Sigma_\theta H^T + R]^{-1} H\Sigma_\theta \quad (4\text{-}23)$$

Therefore, we have

$$\boldsymbol{P}_{n|n} = \boldsymbol{P}_{n|n-1} - \underbrace{\boldsymbol{P}_{n|n-1}\mathbf{H}_n^T\left(\mathbf{H}_n\boldsymbol{P}_{n|n-1}\mathbf{H}_n^T + \mathbf{R}_n\right)^{-1}}_{\boldsymbol{K}_n}\mathbf{H}_n\boldsymbol{P}_{n|n-1} \quad (4\text{-}24)$$

The a posteriori variance is, therefore:

$$\boldsymbol{P}_{n|n} = \boldsymbol{P}_{n|n-1} - \boldsymbol{K}_n\mathbf{H}_n\boldsymbol{P}_{n|n-1} \quad (4\text{-}25)$$

This can be written as:

$$\boxed{\boldsymbol{P}_{n|n} = (\boldsymbol{I} - \boldsymbol{K}_n\mathbf{H}_n)\boldsymbol{P}_{n|n-1}} \quad \textbf{(Equation 5: a posteriori variance)} \quad (4\text{-}26)$$

Which is the fifth Kalman filter equation. This equation shows a decrease of the a posteriori uncertainty, compared to the a priori uncertainty ("$\boldsymbol{P}_{n|n} < \boldsymbol{P}_{n|n-1}$").

4.1.3. Innovation

The difference between the actual observation $\boldsymbol{z}_n$ and the observation prediction $\hat{\boldsymbol{z}}_{n|n-1}$ is generally defined as '**Innovation**':

$$\boldsymbol{I}_n = \boldsymbol{z}_n - \hat{\boldsymbol{z}}_{n|n-1} = \boldsymbol{z}_n - \mathbf{H}_n\hat{\boldsymbol{x}}_{n|n-1} \quad (4\text{-}27)$$

One can notice that $\boldsymbol{I}_n$ is an error vector that appears in the correction term of the "state update" KF equation:

$$\hat{\boldsymbol{x}}_{n|n} = \hat{\boldsymbol{x}}_{n|n-1} + \boldsymbol{K}_n\underbrace{\left(\boldsymbol{z}_n - \mathbf{H}_n\hat{\boldsymbol{x}}_{n|n-1}\right)}_{\boldsymbol{I}_n} \quad (4\text{-}28)$$

The innovation is a vector containing the new information that is brought by measurement $\boldsymbol{z}_n$, compared to the measurement prediction $\hat{\boldsymbol{z}}_{n|n-1}$, hence the name "innovation". The mean and covariance matrix of the innovation vector are:

- Mean:

$$E[\boldsymbol{I}_n] = E[\boldsymbol{z}_n] - E\left[\hat{\boldsymbol{z}}_{n|n-1}\right] = E[\boldsymbol{z}_n] - E\left[E[\boldsymbol{z}_n|\boldsymbol{z}_0^{n-1}]\right] = E[\boldsymbol{z}_n] - E[\boldsymbol{z}_n] = \mathbf{0} \quad (4\text{-}29)$$

- Covariance Matrix:

$$Cov(\boldsymbol{I}_n) = \mathbf{H}_n\boldsymbol{P}_{n|n-1}\mathbf{H}_n^T + \mathbf{R}_n \quad (4\text{-}30)$$

We can see that the innovation is a vector of centered random variables, whose covariance can be computed. It can be used to verify the convergence of the Kalman filter in the measurement domain, rather than in the state domain.

Another usage of the innovation is for outlier detection, to detect a measurement that has an unexpected behavior with regards to its prediction. Once detected, this abnormal measurement can be either weighted down or excluded from the measurement update. This technique is also conducted in this Ph.D. to remove the measurement outliers, further information will be introduced in Section 4.3.3.

4.1.4. Extended Kalman Filter

As we mentioned in the previous section, in the standard KF case, all the models are supposed linear, However, it is usually not the case in the real situation. The Extended Kalman filter came into being.

The Extended Kalman filter (EKF) [113], [114] is the generalized version of the Kalman filter when the state transition function and/or the observation function are **non-linear**. By assuming that the command vector is null, the system can be modeled by the following non-linear equations:

$$\begin{cases} \mathbf{x}_n = \boldsymbol{f}(\mathbf{x}_{n-1}) + \mathbf{w}_n \\ \mathbf{z}_n = \boldsymbol{h}(\mathbf{x}_n) + \mathbf{v}_n \end{cases} \tag{4-31}$$

We consider $\widehat{\boldsymbol{x}}_{n|n}$ and $\widehat{\boldsymbol{x}}_{n|n-1}$ as recent and reasonably accurate approximations of $\mathbf{x}_n$. Then, it is possible to develop the functions f and h in the Taylor series in the neighborhood of $\widehat{\boldsymbol{x}}_{n|n}$ and $\widehat{\boldsymbol{x}}_{n|n-1}$. We can obtain (only consider the first order in the thesis):

$$\begin{cases} \boldsymbol{f}(\mathbf{x}_n) = \boldsymbol{f}\left(\widehat{\boldsymbol{x}}_{n|n}\right) + \left.\dfrac{\partial \boldsymbol{f}}{\partial \mathbf{x}_n}\right|_{\mathbf{x}_n=\widehat{\boldsymbol{x}}_{n|n}} .\left(\mathbf{x}_n - \widehat{\boldsymbol{x}}_{n|n}\right) \\ \boldsymbol{h}(X_k) = \boldsymbol{h}\left(\widehat{\boldsymbol{x}}_{n|n-1}\right) + \left.\dfrac{\partial \boldsymbol{h}}{\partial \mathbf{x}_n}\right|_{\mathbf{x}_n=\widehat{\boldsymbol{x}}_{n|n-1}} .\left(\mathbf{x}_n - \widehat{\boldsymbol{x}}_{n|n-1}\right) \end{cases} \tag{4-32}$$

To simplify the notation, we note $\boldsymbol{\phi}_n = \left.\frac{\partial \boldsymbol{f}}{\partial \mathbf{x}_n}\right|_{\mathbf{x}_n=\widehat{\boldsymbol{x}}_{n|n}}$ and $\boldsymbol{H}_n = \left.\frac{\partial \boldsymbol{h}}{\partial \mathbf{x}_n}\right|_{\mathbf{x}_n=\widehat{\boldsymbol{x}}_{n|n-1}}$, which are the Jacobian matrices of f and h. By definition, let a vector function of a vector variable: $f: X = \begin{bmatrix} x_1 \\ \vdots \\ x_m \end{bmatrix} \rightarrow \begin{bmatrix} z_1 \\ \vdots \\ z_p \end{bmatrix}$, the corresponding Jacobian matrix $(p \times m)$ of f is computed with the partial derivatives at a particular point of the starting space:

$$\frac{\partial \boldsymbol{f}}{\partial X} = \begin{bmatrix} \dfrac{\partial z_1}{\partial x_1} & \cdots & \dfrac{\partial z_1}{\partial x_m} \\ \vdots & \ddots & \vdots \\ \dfrac{\partial z_p}{\partial x_1} & \cdots & \dfrac{\partial z}{\partial x_m} \end{bmatrix} \tag{4-33}$$

Adopting this notation, we can write the system's equations as follows:

$$\begin{cases} \mathbf{x}_n = \boldsymbol{f}\left(\widehat{\boldsymbol{x}}_{n-1|n-1}\right) + \boldsymbol{\phi}_{n-1}\mathbf{x}_{n-1} - \boldsymbol{\phi}_{n-1}\widehat{\boldsymbol{x}}_{n-1|n-1} + \mathbf{w}_n \\ \mathbf{z}_n = h\left(\widehat{\boldsymbol{x}}_{n|n-1}\right) + \boldsymbol{H}_n\mathbf{x}_n - \boldsymbol{H}_n\widehat{\boldsymbol{x}}_{n|n-1} + \mathbf{v}_n \end{cases} \tag{4-34}$$

Let us define $\widetilde{\boldsymbol{U}}_{\boldsymbol{n}} = \boldsymbol{f}\left(\widehat{\boldsymbol{x}}_{n-1|n-1}\right) - \boldsymbol{\phi}_{n-1}\widehat{\boldsymbol{x}}_{n-1|n-1}$ and $\tilde{\boldsymbol{z}}_n = h\left(\widehat{\boldsymbol{x}}_{n|n-1}\right) - \boldsymbol{H}_n\widehat{\boldsymbol{x}}_{n|n-1}$. The system can be rewritten as:

$$\begin{cases} \mathbf{x}_n = \boldsymbol{F}_{n-1}\mathbf{x}_{n-1} + \widetilde{\boldsymbol{U}}_{\boldsymbol{n}} + \mathbf{w}_n \\ \mathbf{z}_n - \tilde{\boldsymbol{z}}_n = \boldsymbol{H}_n\mathbf{x}_n + \mathbf{v}_n \end{cases} \tag{4-35}$$

The system is now linear, and the terms $\widetilde{\boldsymbol{U}}_{\boldsymbol{n}}$ and $\tilde{\boldsymbol{z}}_n$ are known and can be computed at each iteration. After the linearization process, it is now possible to apply the standard KF equations to solve this system. In this case, $\widetilde{\boldsymbol{U}}_{\boldsymbol{n}}$ would contribute to the system command and the term $\mathbf{z}_n - \tilde{\boldsymbol{z}}_n$ would be the observation vector of the system.

So, to conclude, similarly to the Kalman filter, the Extended Kalman filter is composed of 5 equations which are iterated, these equations of the EKF can be resumed as follows:

State prediction	$\hat{\boldsymbol{x}}_{n\|n-1} = \boldsymbol{f}\left(\hat{\boldsymbol{x}}_{n-1\|n-1}\right)$	(4-36)
A priori covariance	$\boldsymbol{P}_{n\|n-1} = \boldsymbol{\Phi}_n \boldsymbol{P}_{n-1\|n-1} \boldsymbol{\Phi}_n^T + \boldsymbol{Q_n}$	(4-37)
Kalman Gain	$\boldsymbol{K}_n = \boldsymbol{P}_{n\|n-1} \mathbf{H}_n^T \left(\mathbf{H}_n \boldsymbol{P}_{n\|n-1} \mathbf{H}_n^T + \mathbf{R}_n\right)^{-1}$	(4-38)
State update	$\hat{\boldsymbol{x}}_{n\|n} = \hat{\boldsymbol{x}}_{n\|n-1} + \boldsymbol{K}_n \left(\boldsymbol{z}_n - \boldsymbol{h}\left(\hat{\boldsymbol{x}}_{n\|n-1}\right)\right)$	(4-39)
A posteriori covariance	$\boldsymbol{P}_{n\|n} = (\boldsymbol{I} - \boldsymbol{K}_n \mathbf{H}_n) \boldsymbol{P}_{n\|n-1}$	(4-40)

What needs to be emphasized is, for the assumptions of the EKF to be valid and avoid divergence of results, several conditions need to be noted:

- Concerning the linearization of the state transition and measurement models, the estimated states should be close to the true states ($\hat{\boldsymbol{x}}_{n|n}$ and $\hat{\boldsymbol{x}}_{n|n-1}$ close to $\mathbf{x}_n$).
- The initial state must be chosen carefully.
- The filter must remain in a "convergence state" so that the linearization error remains low.

4.1.5. Reasons to Choose EKF as the Navigation Solution

The integration of the data commonly uses filters [115]. At the moment, the most widely used filter is the Extended Kalman Filter detailed in the previous section. However other filters, such as the Unscented Kalman Filter (UKF) [116], [117], and the Particle Filter (PF) [118], are also used very frequently.

The Unscented Kalman Filter is a nonlinear adaptation of the KF not requiring the linearization process by Jacobian computation like in EKF. Instead, the UKF approximates the distribution of states by capturing its mean and covariance using a minimal set of carefully chosen sample points called sigma points. The filter propagates each point through the non-linear process and measurement models, then computes the weighted averages of the transformed points to determine the state covariance and the posterior state mean. Despite its capacity to provide good results [117], the UKF is slightly more computationally expensive than the EKF due to the necessity to compute sigma points.

The Particle Filter is a type of sequential Monte Carlo estimation algorithm. The state estimates are represented as a set of discrete state vectors, called particles, which are distributed in their joint probability distribution [36]. The main advantage of the Particle Filter compared to the KF is the possibility to overcome the Gaussian distribution constraint typically required for KFs to provide an optimal estimate. Moreover, the PF is robust to non-linearities. However, this filter has the drawback of the high computational cost resulting from the high number of particles required to achieve good precision.

Overall, the most widely used filter in the literature is still the EKF. The linearization process for the non-linear systems can degrade the performance of the filter process in high dynamics situations. Nevertheless, in constrained environments such as urban environments, the vehicle dynamics are in general low, and the hazardous effect of the linearization process is negligible. Besides, the EKF is very efficient in terms of computational cost, especially for applications where there are a great number of

states and observations compared to the other filters [119]. That is the reason why we decided to utilize the EKF rather than the other filter to be our navigation and vehicle attitude estimation solution. In the following sections, our proposed multi-receiver RTK EKF architecture will be presented.

4.2. Description of the proposed multi-receiver RTK EKF

As we discussed in the previous chapter, the precision performance of a receiver implementing stand-alone GNSS positioning is far from being satisfactory for certain applications in a constrained environment, in particular when a low-cost receiver is envisaged. The high noise level, the lack of multi-frequency measurement, the low-quality receiver oscillator, and the shortage of embedded robust processing techniques can all prevent low-cost receivers from providing reliable and stable positioning performance.

In order to overcome and improve the above problems as much as possible, 5 main axes are looked at in this thesis to improve the low-cost GNSS receiver RTK performance:

- Differential measurements should be used, to take advantage of the temporal and spatial correlation characteristics of most measurements' errors.
- The high-accuracy carrier phase measurements must be utilized, to profit from its much better precision compared to the code measurement.
- Multi-constellation GNSS systems should be considered (in our case GPS, Galileo) to improve the DOP (Dilution Of Precision) and therefore improve the positioning performance.
- Multi-receiver architecture is developed, aiming at providing measurement redundancy, which may be helpful to weaken the multipath effect and improve the EKF performance.
- The multi-receiver architecture enables the estimation of the attitude of the vehicle, thus providing additional information beyond the positioning.

Based on these ideas, in this work, an Extended Kalman Filter-based RTK positioning including attitude determination is developed. The navigation and attitude estimation solutions envisioned in this thesis are presented in the following sections.

4.2.1. System Configuration and Geometry

With the intention of performing precise positioning and attitude estimation, a dual antenna set-up has been considered, where two GNSS antennas each connected to a low-cost receiver are mounted on the vehicle's rooftop (along the longitudinal axis of the vehicle) to get heading and pitch estimation and the baseline length between them is known.

Furthermore, the absolute position accuracy is augmented using the RTK approach, in which the vehicle is positioned relative to a third receiver as the virtual reference station (VRS), whose position is assumed static and known. By knowing the absolute position of the VRS, the vehicle can be positioned absolutely, too. In the positioning algorithm, we strongly rely on carrier phase positioning which, thanks to its low noise characteristics, may enable centimeter-level positioning. Figure 4-2 shows the typical geometry of our measurement set-up and Figure 4-3 gives the definition of the considered attitude model (heading, pitch angles) of the vehicle.

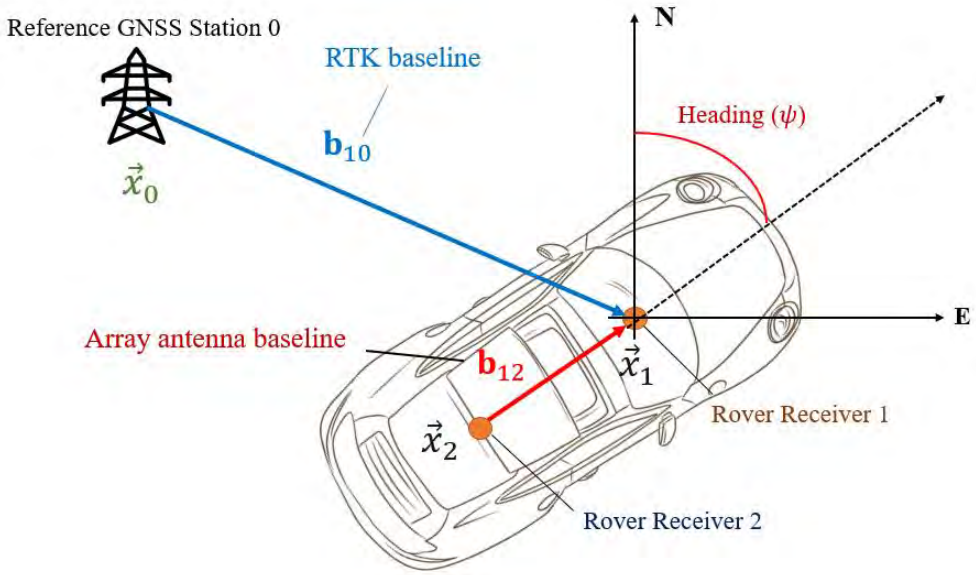

Figure 4-2 Geometry of the Model

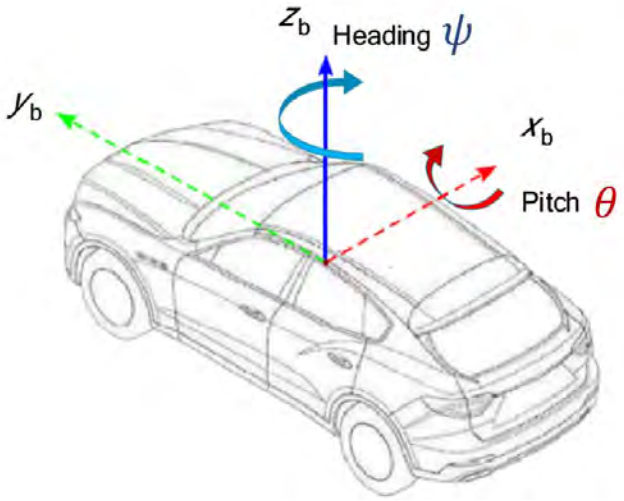

Figure 4-3 Definition of the attitude of the vehicle

According to Figure 4-2, the two GNSS antennas on the car's rooftop span the array antenna baseline named $\mathbf{b}_{12}$, which one can resolve for the Euler attitude angles to get the vehicle's orientation (heading ψ and pitch θ). The array antenna baseline vector $\mathbf{b}_{12}$ has the following coordinates in the local navigation (East, North, Up) ENU frame:

$$\mathbf{b}_{12}(\psi,\theta) = \|\mathbf{b}_{12}\|.\begin{bmatrix}\cos(\theta)\sin(\psi)\\ \cos(\theta)\cos(\psi)\\ \sin(\theta)\end{bmatrix} \tag{4-41}$$

Solving this equation for the attitude angles heading ψ and the pitch θ yields:

$$\psi(t_i) = \operatorname{atan}\left(\frac{(\mathbf{b}_{12})_e(t_i)}{(\mathbf{b}_{12})_n(t_i)}\right) \tag{4-42}$$

$$\theta(t_i) = \operatorname{atan}\left(\frac{(\mathbf{b}_{12})_u(t_i)}{\sqrt{(\mathbf{b}_{12})_e^2(t_i) + (\mathbf{b}_{12})_n^2(t_i)}}\right) \tag{4-43}$$

For every time epoch, we estimate both the RTK position and receiver array attitude. The $\mathbf{b}_{10}$, baseline spanned between one vehicle antenna and the antenna of the VRS (noted by index '0'), instead, enables locate the position of the car relative to the VRS antenna.

$$\mathbf{b}_{10} = \vec{x}_1 - \vec{x}_0 \tag{4-44}$$

As pointed out in 4.1.5, the realization of GNSS-PVT navigation is mainly based on a Kalman Filter which is the most popular choice for its optimality and simplicity to be implemented. In this study, an Extended Kalman Filter based position and attitude determination algorithm is proposed. In the following, the state and the measurement vectors are described along with the state-transition and measurement models.

4.2.2. State Transition Model

The state transition or state-space model describes how the states or parameters of the system vary over time based on a specific linear model.

In our EKF modeling, the state parameter transition between subsequent epochs is given by:

$$\mathbf{x}_n = \boldsymbol{\phi}_n \mathbf{x}_{n-1} + \mathbf{w}_n \tag{4-45}$$

Where:

- $\mathbf{x}_n$ refers to the state vector at epoch n
- $\boldsymbol{\phi}_n$ refers to the transition matrix of $\mathbf{x}_{n-1}$ from epoch $n-1$ to epoch n
- $\mathbf{w}_n$ refers to the so-called system noise vector at epoch n

Together with the process noise vector, one can define the process noise covariance matrix as:

$$\mathbf{Q}_n = E[\mathbf{w}_n \mathbf{w}_n^{\mathrm{T}}] \tag{4-46}$$

This matrix has then the variances of the state parameter's estimates based on the system model.

4.2.2.1. Description of the State Vector

The estimated parameters are collected inside the state vector. In view of our targeted application, the position and the attitude (heading and pitch angles) of the rover are the parameters that need to be estimated. The simplified state vector is then given by:

$$\mathbf{x} = [\mathbf{b}_{10}^T \quad \theta \quad \psi \quad \mathbf{N}_{10}^T \quad \mathbf{N}_{20}^T]^T \tag{4-47}$$

Here, the state vector collects 5 vehicle state parameters and 2*(N_{sat} – 1) satellite state parameters which are:

- The 3D position of GNSS receiver 1 relative to GNSS reference station 0 - $(\mathbf{b}_{10}^T)$
- The pitch angle of the vehicle - (θ)
- The heading angle of the vehicle - (ψ)
- The double-difference integer ambiguities of the visible satellites seen by GNSS receiver pair 1-0 - $(\mathbf{N}_{10}^T)$

- The double-difference integer ambiguities of the visible satellites seen by GNSS receiver pair 2-0 - $(\mathbf{N}_{20}^{T})$

Note that in this section, to simplify the notations of the models, at a given epoch, we consider only the satellites which are mutually visible by the 3 receivers. In our implementation, a different set of satellites can be visible for receivers 1 and 2, and the estimated ambiguities are the single-difference integer ambiguities of GPS and Galileo constellations, respectively.

4.2.2.2. Transition model for position and attitude-related state parameters

In our EKF modeling, for the position and attitude-related state parameters, we suppose that they follow a random walk model, meaning that the speed and the angular rate are a zero-mean Gaussian process.

$$\begin{aligned} \mathbf{b}_{10,n} &= \mathbf{b}_{10,n-1} + \mathbf{w}_{10,n} \\ \theta_n &= \theta_{n-1} + w_{\theta,n} \\ \psi_n &= \psi_{n-1} + w_{\psi,n} \end{aligned} \tag{4-48}$$

Where:

- $\mathbf{w}_{10}$ is a centered Gaussian vector with a covariance matrix $\mathbf{Q}_{10}$
- w_θ is a centered Gaussian variable with a standard deviation σ_θ
- w_ψ is a centered Gaussian variable with a standard deviation σ_ψ

4.2.2.3. Transition model for satellite-related state parameters

In the case of the satellite-related parameters, they are all assumed as constant over subsequent epochs with a very small noise compared to the position and attitude-related state parameters. These assumptions require that an efficient cycle slip detection process is implemented in order to validate the constant nature of the ambiguities. This process is described in Section 4.4.

$$\begin{aligned} \mathbf{N}_{10,n} &= \mathbf{N}_{10,n-1} + \mathbf{w}_{amb,n} \\ \mathbf{N}_{20,n} &= \mathbf{N}_{20,n-1} + \mathbf{w}_{amb,n} \end{aligned} \tag{4-49}$$

Where:

- $\mathbf{w}_{amb,n}$ is a centered Gaussian vector with a covariance matrix $\mathbf{Q}_{amb} = \sigma_{amb}^2 * \mathbf{I}_{N_{sat}-1}$
- $\mathbf{I}_N$ is the identity matrix of size N

The resulting state transition matrix $\boldsymbol{\phi}_n$ is then given by an identity matrix and different values of process noise variance are added to complete the model.

$$\boldsymbol{\phi}_n = \begin{bmatrix} 1 & \cdots & 0 \\ \vdots & \ddots & \vdots \\ 0 & \cdots & 1 \end{bmatrix} \tag{4-50}$$

And the corresponding process noise matrix $\mathbf{Q}$ is given as follows:

$$\mathbf{Q}_n = \begin{bmatrix} \mathbf{Q}_{10} & \mathbf{0}_{3\times1} & \mathbf{0}_{3\times1} & \mathbf{0}_{3\times(N_{sat}-1)} & \mathbf{0}_{3\times(N_{sat}-1)} \\ \mathbf{0}_{1\times3} & \sigma_\theta^2 & 0 & \mathbf{0}_{1\times(N_{sat}-1)} & \mathbf{0}_{1\times(N_{sat}-1)} \\ \mathbf{0}_{1\times3} & 0 & \sigma_\psi^2 & \mathbf{0}_{1\times(N_{sat}-1)} & \mathbf{0}_{1\times(N_{sat}-1)} \\ \mathbf{0}_{(N_{sat}-1)\times3} & \mathbf{0}_{(N_{sat}-1)\times1} & \mathbf{0}_{(N_{sat}-1)\times1} & \mathbf{Q}_{amb} & \mathbf{0}_{N_{sat}-1} \\ \mathbf{0}_{(N_{sat}-1)\times3} & \mathbf{0}_{(N_{sat}-1)\times1} & \mathbf{0}_{(N_{sat}-1)\times1} & \mathbf{0}_{N_{sat}-1} & \mathbf{Q}_{amb} \end{bmatrix} \quad (4\text{-}51)$$

4.2.3. Measurement Model

The measurement model describes how the individual sensor measurements are related to system states. In general, for every epoch n, the measurement vector $\mathbf{z_n}$, which contains all measured values, can be described as a function of the state vector $\mathbf{x_n}$ as:

$$\mathbf{z_n} = \mathbf{h}_n(\mathbf{x_n}) + \mathbf{v}_n \quad (4\text{-}52)$$

with $\mathbf{h}_n$ the function that relates one or more states with each measured value and $\mathbf{v}_n$ the measurement noise vector, which describes the centered Gaussian noise of every measured value. As for the process noise covariance matrix, the definition of the measurement noise covariance matrix follows as:

$$\mathbf{R}_n = E[\mathbf{v}_n\mathbf{v}_n^{\mathrm{T}}] \quad (4\text{-}53)$$

The centered assumption of the noise is not straightly valid for GNSS measurements in GNSS challenged environments like the urban environment, due to multipath or undetected cycle slips. However, it is common to use this assumption by inflating the noise covariance matrix in order to consider those errors.

4.2.3.1. Description of the Measurement Vector

In our model, the measurement vector $\mathbf{z}_n$ comprises the following measured values:

- Double-difference (DD) code phase measurement vector of receiver 1 $-$ $(\mathbf{P}_{10})$
- DD code phase measurement vector of receiver 2 $-$ $(\mathbf{P}_{20})$
- DD carrier phase measurement vector of receiver 1 $-$ $(\lambda\boldsymbol{\phi}_{10})$
- DD carrier phase measurement vector of receiver 2 $-$ $(\lambda\boldsymbol{\phi}_{20})$

$$\mathbf{z}_n = [(\mathbf{P}_{10})^T \quad (\mathbf{P}_{20})^T \quad \lambda(\boldsymbol{\phi}_{10})^T \quad \lambda(\boldsymbol{\phi}_{20})^T]^T \quad (4\text{-}54)$$

In this measurement model, the position of receiver 2 is expressed in terms of the position of receiver 1 and the baseline vector between the 2 receivers of the array ($\mathbf{b}_{20} = \mathbf{b}_{10} - \mathbf{b}_{12}$), such that it contains the known array baseline length information and the attitude information that we want to estimate. The individual double-differenced corrected pseudorange and phase GPS and Galileo measurement for our short baseline case (less than 3 km) can be modeled as:

$$P_{10}^{kl} = \left(\mathbf{e}^{kl}\right)^T \mathbf{b}_{10} + n_{P,10}^{kl} \quad (4\text{-}55)$$

$$P_{20}^{kl} = \left(\mathbf{e}^{kl}\right)^T \left(\mathbf{b}_{10} - |\mathbf{b}_{12}| \begin{bmatrix} \cos\theta \sin\psi \\ \cos\theta \cos\psi \\ \sin\theta \end{bmatrix}\right) + n_{P,20}^{kl} \quad (4\text{-}56)$$

$$\lambda\phi_{10}^{kl} = \left(\mathbf{e}^{kl}\right)^T \mathbf{b}_{10} + \lambda N_{10}^{kl} + n_{\phi,10}^{kl} \tag{4-57}$$

$$\lambda\phi_{20}^{kl} = \left(\mathbf{e}^{kl}\right)^T \left(\mathbf{b}_{10} - |\mathbf{b}_{12}| \begin{bmatrix} \cos\theta \sin\psi \\ \cos\theta \cos\psi \\ \sin\theta \end{bmatrix}\right) + \lambda N_{20}^{kl} + n_{\phi,20}^{kl} \tag{4-58}$$

Where:

- P_{np}^{kl} refers to the double-differenced code phase measurement vector of receiver pair np and satellite pair kl
- $\lambda\phi_{np}^{kl}$ refers to the double-differenced carrier phase measurement vector of receiver pair np and satellite pair kl
- $\mathbf{e}^{kl}$ is the difference between the Line-of-Sight vector of satellite k and l towards the receiver
- N_{np}^{kl} refers to the double-differenced integer ambiguity of receiver pair np and satellite pair kl
- $n_{P,np}^{kl}, n_{\phi,np}^{kl}$ refers to the noise measurement of the double-differenced code and phase measurement, respectively.

Additionally, the LOS vectors are modeled by using the azimuth $\varphi_{k,r}$ and elevation $\theta_{k,r}$ of the satellites with respect to the corresponding receiver, thanks to the following formula that defines the LOS (Line Of Sight) vector between satellite *k* and receiver *r* in the ENU frame:

$$\mathbf{e}_r^k = \begin{bmatrix} \cos\theta_{k,r}\cos\varphi_{k,r} \\ \cos\theta_{k,r}\sin\varphi_{k,r} \\ \sin\theta_{k,r} \end{bmatrix} \tag{4-59}$$

To reflect the difference in accuracy between the code measurement and the carrier phase measurement, a fixed scale factor is applied:

$$\sigma_{phase} = a * \sigma_{code} \tag{4-60}$$

Where:s

- σ_{code} refers to the standard deviation of code measurement error at the zenith
- σ_{phase} refers to the standard deviation of carrier phase measurement error at the zenith
- a refers to the ratio between σ_{code} and $\sigma_{carrier}$ to account for the much better accuracy of carrier phase measurements.

In our model, a pre-defined critical value $\boldsymbol{a = 1/100}$ is chosen by referring to [120].

4.2.3.2. Measurement Covariance Matrix

An elevation-dependent measurement noise variance between all satellites is defined to complete the measurement model, defining the measurement covariance matrix $\mathbf{R}$. Firstly, the measurement covariance matrix $\mathbf{R}_{\text{SD}}$ for the single difference code measurements will have the following shape:

$$\mathbf{R}_{\text{code,SD}} = 2 * \sigma_{code}^2 \begin{bmatrix} diag\left(\dfrac{1}{\sin^2(\mathbf{el})}\right) & \mathbf{0}_{N_{sat}} \\ \mathbf{0}_{N_{sat}} & diag\left(\dfrac{1}{\sin^2(\mathbf{el})}\right) \end{bmatrix} \tag{4-61}$$

Similarly, for the carrier phase measurements, we have:

$$\mathbf{R}_{\text{carrier,SD}} = 2 * a^2 * \sigma_{code}^2 \begin{bmatrix} diag\left(\frac{1}{\sin^2(\mathbf{el})}\right) & \mathbf{0}_{N_{sat}} \\ \mathbf{0}_{N_{sat}} & diag\left(\frac{1}{\sin^2(\mathbf{el})}\right) \end{bmatrix} \quad (4\text{-}62)$$

Where:

- $diag\left(\frac{1}{\sin^2(\mathbf{el})}\right)$ is a diagonal matrix with the terms $1/\sin(el^k)$ on its diagonal
- el^k is the elevation of satellite k in radians

The measurement covariance matrix $\mathbf{R}$ for the double-difference measurements can then be deduced using the following formula:

$$\mathbf{R} = \mathbf{D} \begin{bmatrix} \mathbf{R}_{\text{code,SD}} & \mathbf{0}_{2*N_{sat}} \\ \mathbf{0}_{2*N_{sat}} & \mathbf{R}_{\text{carrier,SD}} \end{bmatrix} \mathbf{D}^{\boldsymbol{T}} \quad (4\text{-}63)$$

Where:

$$\boldsymbol{D} = \begin{bmatrix} -1 & 0 & \cdots & 0 & 1 \\ 0 & -1 & \ddots & \vdots & 1 \\ \vdots & \ddots & \ddots & 0 & \vdots \\ 0 & \cdots & 0 & -1 & 1 \end{bmatrix} \quad (4\text{-}64)$$

is the single-differencing matrix used for computing the double difference. The location of the column full of 1's correspond to the reference satellite for this particular epoch.

Two alternating steps which are the state prediction step and the state update step are then conducted to complete the proposed EKF algorithm.

4.2.4. The State Prediction Step

As mentioned in Section 4.1.1, in the state prediction step, the system model is used to estimate the state variable's value for the subsequent epoch. In this phase, a prediction on the state parameter's values on the subsequent epoch is done only by assuming a linear model, such as a movement model. The equation that describes this prediction uses the section state transition model excluding the state noise component.

$$\hat{\boldsymbol{x}}_{n|n-1} = \boldsymbol{\phi}_n \hat{\boldsymbol{x}}_{n-1|n-1} \quad (4\text{-}65)$$

Where:

- $\hat{\boldsymbol{x}}_{n-1|n-1}$ is the estimate of the state vector coming from the last update phase epoch $n-1$
- $\hat{\boldsymbol{x}}_{n|n-1}$ is the estimate of the predicted state vector for the current epoch n

Together with the state vector, there is also another quantity that should be updated: namely the state covariance matrix, which is defined as the expected value of the state vector residuals, which in turn are defined as the difference or error between the real and estimated state vector:

$$\mathbf{P} = E[(\mathbf{x} - \hat{\mathbf{x}})(\mathbf{x} - \hat{\mathbf{x}})^{\mathrm{T}}] \quad (4\text{-}66)$$

where $\mathbf{x}$ is the true and $\hat{\mathbf{x}}$ is the estimated state vector. This matrix could be related either to the prediction or update step, in which case the matrix is called a-priori or a-posteriori state covariance matrix.

In the prediction step, the a-priori state covariance matrix $\boldsymbol{P}_{n|n-1}$ is updated as:

$$\boldsymbol{P}_{n|n-1} = \boldsymbol{\Phi}_n \boldsymbol{P}_{n-1|n-1} \boldsymbol{\Phi}_n^T + \boldsymbol{Q_n} \tag{4-67}$$

where $\boldsymbol{P}_{n-1|n-1}$ represents the a-posteriori state covariance matrix of the previous state update step.

4.2.5. The State Update Step

In the state update step, the measured values are taken into account and "fed back" to the system. The relationship between the state and measurement vector has been mentioned in the Measurement model section:

$$\mathbf{z}_n = \mathbf{h}_n(\mathbf{x}_n) + \mathbf{v}_n \tag{4-68}$$

The relationship between the state vector and the measurement vector (function $\mathbf{h}_n(\mathbf{x_n})$) is obviously not linear thus we need to conduct a linearization process, in order to linearize this non-linear measurement function and obtain the measurement matrix H (Jacobian matrix of $\mathbf{h}_n(\mathbf{x_n})$) to apply an Extended Kalman Filter.

4.2.5.1. Linearization Process

Applying the derivative formula, the non-linear measurement function $\mathbf{h}_n(\mathbf{x}_n)$ can be linearized to the measurement matrix $\mathbf{H}_n$ as:

$$\mathbf{h}_n(\mathbf{x}_n) \approx \mathbf{H}_n \mathbf{x}_n = \mathbf{h}_n\left(\widehat{\boldsymbol{x}}_{n|n-1}\right) + \mathbf{H}_n\left(\mathbf{x}_n - \widehat{\boldsymbol{x}}_{n|n-1}\right) \tag{4-69}$$

which is then used to calculate the Kalman gain matrix $\mathbf{K}_n$ and the a-posteriori covariance matrix $\mathbf{P}_n^+$, as will be seen later in this section. The measurement matrix is computed around the predicted position $\hat{\mathbf{x}}_n^-$ as:

$$\mathbf{H}_n|_{\mathbf{x}_n=\hat{\mathbf{x}}_{n|n-1}} = \frac{\partial}{\partial \mathbf{x}_n} \mathbf{h}_n(\mathbf{x}_n)\Big|_{\mathbf{x}_n=\widehat{\boldsymbol{x}}_{n|n-1}} \tag{4-70}$$

In our case,

$$\frac{\partial P_{10}^{kl}}{\partial \mathbf{x}} = \left[\left(\mathbf{e}^{kl}\right)^T, 0, 0, \mathbf{0}_{1\times N_{sat}-1}, \mathbf{0}_{1\times N_{sat}-1}\right] \tag{4-71}$$

$$\frac{\partial P_{20}^{kl}}{\partial \mathbf{x}} = \left[\left(\mathbf{e}^{kl}\right)^T, h_\theta, h_\psi, \mathbf{0}_{1\times N_{sat}-1}, \mathbf{0}_{1\times N_{sat}-1}\right] \tag{4-72}$$

$$\frac{\partial \phi_{10}^{kl}}{\partial \mathbf{x}} = \left[\left(\mathbf{e}^{kl}\right)^T, 0, 0, \boldsymbol{\lambda_k}, \mathbf{0}_{1\times N_{sat}-1}\right] \tag{4-73}$$

$$\frac{\partial \phi_{20}^{kl}}{\partial \mathbf{x}} = \left[\left(\mathbf{e}^{kl}\right)^T, h_\theta, h_\psi, \mathbf{0}_{1\times N_{sat}-1}, \boldsymbol{\lambda_k}\right] \tag{4-74}$$

where $\boldsymbol{\lambda_k}$ is a vector of $N_{sat} - 1$ zero, except for one value which is equal to λ_{GPS} in the k-th position.

with $h_\theta = \left(\mathbf{e}^{kl}\right)^T * (-l) * \begin{bmatrix} -\sin\theta\sin\varphi \\ -\sin\theta\cos\varphi \\ \cos\theta \end{bmatrix}$ and $h_\psi = \left(\mathbf{e}^{kl}\right)^T * (-l) * \begin{bmatrix} cos\theta\cos\varphi \\ -cos\theta\sin\varphi \\ 0 \end{bmatrix}$ respectively.

Therefore, the corresponding Matrix $\mathbf{H}$ can be defined as follows:

$$\mathbf{H} = \begin{bmatrix} e_e^1 & e_n^1 & e_u^1 & 0 & 0 & 0 & \dots & 0 & 0 & \dots & 0 \\ \vdots & \vdots & \vdots & \vdots & \vdots & \vdots & \ddots & \vdots & \vdots & \ddots & \vdots \\ e_e^{Nsat-1} & e_n^{Nsat-1} & e_u^{Nsat-1} & 0 & 0 & 0 & \dots & 0 & 0 & \dots & 0 \\ e_e^1 & e_n^1 & e_u^1 & h_\theta & h_\psi & 0 & \dots & 0 & 0 & \dots & 0 \\ \vdots & \vdots & \vdots & \vdots & \vdots & \vdots & \ddots & \vdots & \vdots & \ddots & \vdots \\ e_e^{Nsat-1} & e_n^{Nsat-1} & e_u^{Nsat-1} & h_\theta & h_\psi & 0 & \dots & 0 & 0 & \dots & 0 \\ e_e^1 & e_n^1 & e_u^1 & 0 & 0 & \lambda^{GPS} & \dots & 0 & 0 & \dots & 0 \\ \vdots & \vdots & \vdots & \vdots & \vdots & 0 & \ddots & 0 & 0 & \ddots & 0 \\ e_e^{Nsat-1} & e_n^{Nsat-1} & e_u^{Nsat-1} & 0 & 0 & 0 & \dots & \lambda^{GPS} & 0 & \dots & 0 \\ e_e^1 & e_n^1 & e_u^1 & h_\theta & h_\psi & 0 & \dots & 0 & \lambda^{GPS} & 0 & 0 \\ \vdots & \vdots & \vdots & \vdots & \vdots & 0 & \ddots & 0 & \vdots & \ddots & \vdots \\ e_e^{Nsat-1} & e_n^{Nsat-1} & e_u^{Nsat-1} & h_\theta & h_\psi & 0 & \dots & 0 & 0 & 0 & \lambda^{GPS} \end{bmatrix} \quad (4\text{-}75)$$

Note that the values of $\mathbf{H}$ are computed around the predicted position $\hat{\boldsymbol{x}}_{n|n-1}$

4.2.5.2. State Vector and Covariance Matrix Update

The update of the state vector is performed as:

$$\hat{\boldsymbol{x}}_{n|n} = \hat{\boldsymbol{x}}_{n|n-1} + \boldsymbol{K}_n\left(\boldsymbol{z}_n - \mathbf{H}_n\hat{\boldsymbol{x}}_{n|n-1}\right) \quad (4\text{-}76)$$

As introduced before, $\mathbf{K}_n$ stands for the Kalman gain matrix and the term $\boldsymbol{z}_n - \mathbf{H}_n\hat{\boldsymbol{x}}_{n|n-1}$ is defined as measurement innovation. This discrepancy between what the sensors are telling and what the linear model is pointing out is weighted by the Kalman gain matrix $\mathbf{K}_n$ and then finally added to the just calculated predicted state vector $\hat{\boldsymbol{x}}_{n|n-1}$ coming from the last prediction phase.

The a-posteriori state covariance matrix is updated as follows:

$$\boldsymbol{P}_{n|n} = (\boldsymbol{I} - \boldsymbol{K}_n\mathbf{H}_n)\boldsymbol{P}_{n|n-1} \quad (4\text{-}77)$$

with $\mathbf{I}$ being the identity matrix, and $\mathbf{K}_n$ the Kalman gain matrix, which is defined as:

$$\boldsymbol{K}_n = \boldsymbol{P}_{n|n-1}\mathbf{H}_n^T\left(\mathbf{H}_n\boldsymbol{P}_{n|n-1}\mathbf{H}_n^T + \mathbf{R}_n\right)^{-1} \quad (4\text{-}78)$$

The updated state vector $\hat{\boldsymbol{x}}_{n|n}$ contains now optimal state estimates, by taking advantage of both the new information provided by the measurements and the prediction of the linear model. This procedure then is iterated in every epoch that new measurement data is available, to converge to optimal estimation of the state vector in every epoch.

4.3. Pre-Processing of Observations

As mentioned previously, the positioning performance of a GNSS system is highly dependent on the User Equivalent Range Error (UERE) and the Dilution of Precision (DOP). The vulnerability of the signal processing of the GNSS receiver with respect to several sources of perturbations, in particular in constrained environments like the urban environment, makes the preprocessing of the measurements necessary.

The impact of an outlier in the estimation filter invalidates the assumption that the measurements are unbiased and can lead to huge inaccuracy in the solution. In other words, an undetected fault has a negative impact on accuracy. In the case of GNSS navigation, the GNSS measurements outliers should be eliminated through preprocessing steps to get a better PVT solution.

In this section, three schemes conducted in this thesis for restricting or eliminating measurement outliers are presented.

4.3.1. Elevation Mask

In the first place, it is essential and significant to maintain sufficient GNSS measurement quality. In the literature, it is widely accepted that the higher the satellite elevation and C/N0, the less noisy the GNSS measurements are if the antenna is pointing to the zenith. An a-priori elevation mask can be applied for all GNSS measurements to remove the measurements that are most likely severely degraded by multipath or NLOS effects. This step is necessary because the models for the corresponding measurements might be quite erroneous and might lead to extremely inaccurate assessment of the position quality or large estimation errors.

However, the choice of an a-priori mask value is a very difficult task because the final quality of the position depends both on the geometry of the satellite and on the precision of the measurements. To further explain, the masking of low elevation satellites could indeed improve the expected measurement accuracy, however, it also degrades the geometry of the satellites. The higher the elevation mask value, the lower the quality of the satellite geometry and the availability, thus leading to an increase of the DOP. Therefore, the optimal elevation mask value is in fact a compromise between the strength of the geometry and high-quality measurements [48].

Eventually, as the optimal elevation mask value is very difficult to determine a-priori, it will be determined a-posteriori in the following chapters for the different data collections and scenarios, by taking a compromise value depending on the environmental conditions.

4.3.2. Proposed Measurement Weighting Scheme

According to [48], [121], it is generally not optimal to weigh all GNSS measurements with the same weight in the positioning filter. Reasonably, various weighting schemes can be found in the literature. For example, [122] used the mapping function existing between the noise variance and the C/N0 value. However, it is not very practical because the internal receiver parameters required are usually not available to the user [123]. Besides, as the noise error can be significantly lower than the multipath error, the formula may be overly optimistic when dealing with a highly multipath-contaminated environment.

In this thesis, for sake of simplicity, the following measurement weighting schemes are conducted to quantify the accuracy of the measurements in different situations.

1. To reflect the differences in measurements accuracy in different environments, the predefined value of the σ_{code}^2 which is the variance of the GNSS code measurement, is set to different practical values under different environmental conditions. The values selected in this thesis will be described in detail in the next chapter.
2. To reflect the differences in accuracy between different tracked satellites, an elevation-based weighting algorithm is conducted. For instance, for the code measurement of the k-th satellite, its variance σ_k^2 is defined as:

$$\sigma_k^2 = \sigma_{code}^2 * \frac{1}{\sin^2(el^k)} \tag{4-79}$$

3. In addition, to consider the differences in accuracy between code measurements and the carrier phase measurements at the zenith, a fixed scale factor $\boldsymbol{a = 1/100}$ is applied by referring to [120] as presented in (**4-60**)

4.3.3. Implementation of the Innovation Test

According to [42], [124], in the constrained environment, GNSS measurements are more severely degraded by non-Gaussian error sources like the multipath and NLOS signals. The detection of outliers is thus particularly necessary to ensure a robust PVT solution. That is why in our algorithm, in addition to the two a-priori GNSS measurement selection steps presented in previous sections, another fault detection and exclusion scheme is applied based on the KF innovations to handle more potential outliers, called the **Innovation Test**.

This detection scheme takes advantage of the system consistency and redundancy considering a-priori knowledge of the statistical distribution that the KF innovations in the fault-free case should follow [42], [125]. The two essential implementation steps of the innovation test are **Detection** and **Outlier Exclusion**.

As we mentioned in Section 4.1.3, the Innovation is defined as the difference between the actual observation $\boldsymbol{z}_n$ and the observation prediction $\hat{\boldsymbol{z}}_{n|n-1}$:

$$\boldsymbol{I}_n = \boldsymbol{z}_n - \hat{\boldsymbol{z}}_{n|n-1} = \boldsymbol{z}_n - \mathbf{H}_n \hat{\boldsymbol{x}}_{n|n-1} \tag{4-80}$$

The mean and covariance matrix of the innovation vector are:

- Mean:

$$E[\boldsymbol{I}_n] = \mathbf{0} \tag{4-81}$$

- Covariance Matrix:

$$Cov(\boldsymbol{I}_n) = \mathbf{H}_n \boldsymbol{P}_{n|n-1} \mathbf{H}_n^T + \mathbf{R}_n \tag{4-82}$$

Here the $\mathbf{R}_n$ can be considered as the measurement variance matrix and $\mathbf{H}_n \boldsymbol{P}_{n|n-1} \mathbf{H}_n^T$ is the predicted variance of the parameters mapped into the observation domain.

A measurement innovation is then considered bias-free by the null hypothesis H_0:

$$\boldsymbol{I}_n|_{H_0} \sim N\big(0, Cov(\boldsymbol{I}_n)\big) \tag{4-83}$$

Contrarily, the alternative hypothesis H_a states that a bias, represented by the outlier indicator δ_I, is present.

$$\boldsymbol{I}_n|_{H_a} \sim N\big(\delta_I, Cov(\boldsymbol{I}_n)\big) \tag{4-84}$$

Generally, it is more convenient to apply a test to a normalized test statistic [126]. For the n-th epoch, considering the innovation term $I_{n,i}$, with $i \in [1,2,\dots,p]$, where p is the length of the innovation term vector $\boldsymbol{I}_n$.

$$t_i|_{H_0} \sim N(0,1) \tag{4-85}$$

$$t_i|_{H_a} \sim N(\delta_0, 1) \tag{4-86}$$

Where t_i is given by:

$$t_i = \frac{I_{n,i}}{\sqrt{Cov(I_{n,i})}} \tag{4-87}$$

and δ_0 is:

$$\delta_0 = \frac{\delta_I}{\sqrt{Cov(I_{n,i})}} \tag{4-88}$$

After the normalization, If the ith measurement is not an outlier, t_i is supposed to follow a standard normal distribution [127], which is the local null hypothesis H_0. The null hypothesis is then approved when an innovation is normally distributed with zero mean and variance of 1.

Otherwise, if t_i follows a biased normal distribution with a bias denoted δ_0, this situation corresponds to the local alternative hypothesis H_a. The H_0 is then rejected if $t_i < n_{\alpha/2}$ or $t_i > n_{1-\alpha/2}$, where α is the significance level of the test and $n_{\alpha/2}$ and $n_{1-\alpha/2}$ are points (**Threshold values**) such that $P(n_{\alpha/2} < t_i < n_{1-\alpha/2}) = 1 - \alpha$. Figure 4-4 gives an illustration of the detection process.

As an example, the three-sigma test, $P(-3\sigma < t_i < 3\sigma) = 99.74\%$, considers an α value of 0.26%, which means that our acceptable probability of false alarm is 0.26%.

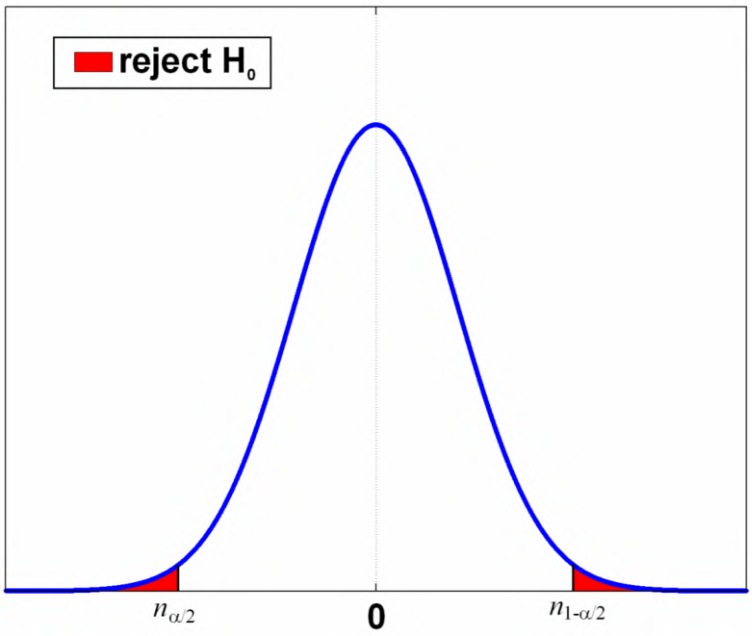

Figure 4-4 The null hypothesis is that the standardized innovation is normally distributed [126]

Note that the innovation test is conducted before the states update process in the EKF. If the null hypothesis is rejected, the measurement is simply not used to update the filter. Thus, it is not necessary to recompute the solution or correct the outliers. In addition, as the innovations are tested by sequence, at each epoch, no assumption about the number of outliers needs to be defined.

4.4. Cycle Slip Detection and Repair

As we mentioned in Section 3.3.1. Cycle slip detection and repair are crucial to maintain continuity of carrier phase observations and to benefit the precise GPS carrier phase observations for high-precision

GPS positioning. There are currently many methods to detect and repair the cycle slips. However, it is still a challenging issue, in particular in the case of the **single-frequency** measurements [125].

In this contribution, two types of cycle slip detection processes are studied, namely the Standard Phase–Code Comparison method, and the Differential Phases of Time Cycle Slip Resolution Method.

4.4.1. The Standard Phase–Code Comparison method

The Standard Phase–Code Comparison method is based on the observation of code-minus-carrier (CMC) combinations, The cycle slips of the phase observable can be detected by using the following formula according to [128]:

$$\Delta_t P = \lambda \Delta_t \Phi - \lambda \Delta_t N + \varepsilon \tag{4-89}$$

Where:

- Δ_t is the time difference operator, used to differentiate the observation equations between two adjacent epochs
- P refers to the code range measurement
- Φ refers to the carrier phase measurement
- N refers to the ambiguity
- λ refers to the wavelength
- ε refers to residual

From (**4-89**), we can deduce that:

$$\Delta_t N = \frac{\lambda \Delta_t \Phi - \Delta_t P}{\lambda} + \varepsilon \tag{4-90}$$

This operation removes the geometry term and the other frequency-independent (or non-dispersive) terms, but it will enlarge the ionospheric error and introduce large thermal noise and potential multipath error from code data. The remaining errors are summarized by the term ε.

In the case of no cycle slips, the time difference of the ambiguity is zero, i.e., $\Delta_t N = 0$. In the case of a cycle slip, $\Delta_t N \neq 0$ and we can have the following formula:

$$\left| \frac{\lambda \Delta_t \Phi - \Delta_t P}{\lambda} \right| > \varepsilon \quad if\ \Delta_t N \neq 0 \tag{4-91}$$

The residual between the prediction and the observation can then be used as a detector metric, to be compared to a predefined detection threshold ε_T. The a priori value of ε_T is determined according to the quality of code data and the potential multipath error and the desired false alarm probability. A larger value will lower the sensitivity, whereas tuning it down to a small number might cause false detection. This approach facilitates only a rough detection of cycle slips. It is not suitable for small cycle slips due to large measurement noise and multipath in code pseudorange. The minimal detectable size of the cycle slip (in cycle) can be estimated by rounding ε_T / λ.

4.4.2. The Differential Phases of Time Cycle Slip Resolution Method

The second cycle slip detection process [19] is based on the observation of the differential phases between two adjacent epochs, which should exhibit the actual ambiguity, plus some clock errors and remaining noise term as shown in the following equation:

$$\lambda \Delta_t \Phi = \Delta_t \rho - \Delta_t (\delta t_r - \delta t_k) c + \lambda \Delta_t N + \varepsilon_p \tag{4-92}$$

Where:

- ρ refers to the geometric distance between the satellite and the receiver antennas.
- δt_r , δt_k refer to the clock errors of the receiver and satellite, respectively.
- c is the speed of light.
- ε_p refers to remaining errors of the phase measurement.

For moderate dynamics, except for the ambiguity term, all other terms on the right side are of low variation. Any cycle slip will lead to a sudden jump in the time difference of the phases. Based on the past observation of differential phases measurement, a prediction of the current differenced data can be obtained by polynomial extrapolation or interpolation [128]. For moderate dynamics, the residual between the prediction and the observation can then be used as a detector metric, to be compared to the detection threshold to decide if there is any cycle slip. Note that this detector works independently for each phase measurement.

4.4.3. Cycle slip Validation, Size Determination, and Repair

The last process of cycle slip detection is to set a proper threshold for the detection value. The detection threshold is the magnitude of the detection metric that must be exceeded in order to consider the occurrence of a cycle slip. An optimal threshold should always be sensitive to small cycle slips. In our model, the threshold is determined by the metric noise and the significance level:

$$Threshold = \sqrt{2} * \alpha * \sigma_m \tag{4-93}$$

Where:

- α refers to the significance level related coefficient. ($e.g.$: $\alpha = 2$, significance level is 0.05)
- σ_m refers to the standard deviation of the considered metric, which corresponds to σ_{code} for the Standard Phase–Code Comparison method and σ_{phase} for the Differential Phases of Time Cycle Slip Resolution Method

After the cycle slips detection process, cycle slip validation and size determination processes are needed to verify the determined sizes of cycle slip. Cycle slips can be repaired using integer vector estimation similarly to ambiguity resolution in the position domain.

After detecting all the possible cycle slips at a given epoch, one may obtain the estimates of the float value cycle slips x_j (j ranges from 1 to number of detected cycle slips) together with their covariance matrix. Then, an integer estimation technique is employed to determine the integer cycle slip vector from the float cycle slips x_j and their covariance matrix. In our case, this is achieved by means of the least-squares ambiguity decorrelation adjustment (LAMBDA) method [57], [130]. An advantage of the LAMBDA method is that it comprises both an estimation step to determine the integer value of the cycle slips, and a validation step, to determine if the confidence level associated with the estimate is sufficient for the user. If LAMBDA gives an integer cycle slip value equal to 0 at one specific epoch, it means that the cycle slip has not taken place at that epoch which means we have a false detection. Another case is that if the cycle slip is detected by the metric, but that LAMBDA does not provide an integer solution with enough confidence, we re-initialize the state associated with the ambiguity of the satellite in the state vector to ensure a better RTK performance.

Once the sizes of cycle slips are determined, we conduct the cycle-slip removal (repair) step to remove the cycle slips out of the associated phase measurements.

4.5. Integer Ambiguity Resolution

In the previous process of our proposed EKF, we obtained a float estimation of the double-difference integer ambiguity. The accuracy of the position state estimate is further improved by fixing the DD ambiguities to integer numbers by using the well-known LAMBDA [57] [130] algorithm.

As we can notice, resolving the unknown cycle ambiguities of the double-differenced carrier phase data to integers is the key to rapid and very precise (cm-level) GNSS positioning. The process is referred to as **Integer Ambiguity Resolution (IAR).**

Once the IAR process is declared successful, a new position is computed using the DD carrier phase measurements corrected by the validated DD integer ambiguities. This final position is the fixed solution.

The details of this process conducted in this thesis are introduced in the following sections.

4.5.1. Integer Ambiguity Resolution Process

Let us consider the GNSS mixed integer linear model [131], [132]:

$$\boldsymbol{y} = \mathbf{A}\mathbf{a} + \mathbf{B}\mathbf{b} + \boldsymbol{e} \tag{4-94}$$

Where:

- $a \in \mathbb{Z}^n$ and $b \in \mathbb{R}^p$ are the integer and real parameter vectors, respectively.
- $A \in \mathbb{R}^{m\times n}$ and $B \in \mathbb{R}^{m\times p}$ are the design matrices of a and b with $[\mathrm{A\ B}]$ full column rank.
- $y \in \mathbb{R}^m$ refers to the observation vector contaminated by the normally distributed random noise $\boldsymbol{e}$ with zero means and covariance matrix $\boldsymbol{Q_{yy}}$.

As we discussed in Section 3.2, the general GNSS ambiguity resolution can be divided into three steps.

1) **Float Solution**
2) **Integer Ambiguity Solution Validation**
3) **Fixed solution**

The GNSS mixed integer model can then be solved in these 3 steps.

4.5.1.1. Float Solution

First, the integer nature of the ambiguities is discarded, and the so-called 'float' solution is obtained by a **Standard Least-Square's adjustment**, together with its covariance matrix:

$$\begin{bmatrix}\hat{\boldsymbol{a}}\\ \hat{\boldsymbol{b}}\end{bmatrix} \sim N\left(\begin{bmatrix}\boldsymbol{a}\\ \boldsymbol{b}\end{bmatrix}, \begin{bmatrix}\boldsymbol{Q}_{\hat{a}\hat{a}} & \boldsymbol{Q}_{\hat{a}\hat{b}}\\ \boldsymbol{Q}_{\hat{b}\hat{a}} & \boldsymbol{Q}_{\hat{b}\hat{b}}\end{bmatrix}\right) \tag{4-95}$$

4.5.1.2. Integer Ambiguity Solution and Validation

In the second step, the real-valued float solution of the ambiguities is adjusted to take the integer constraints $a \in \mathbb{Z}^n$ into account. Therefore, a mapping function $I: \mathbb{R}^n \mapsto \mathbb{Z}^n$ is introduced that maps the float ambiguities to corresponding integer values:

$$\breve{\boldsymbol{a}} = I(\hat{\boldsymbol{a}}) \tag{4-96}$$

According to the literature [133], [134], there exists many integer mappings AR Strategies "$I(\cdot)$":

- Simple Integer rounding (IR), integer bootstrapping (IB), Integer Least-Squares (ILS)

- Multi-frequency wide-lane and narrow-lane generation
- Search in coordinate domain
- Search in ambiguity domain
- AFM, FARA, LSAST, **LAMBDA**, ARCE, HB-L
- Modified Cholesky Decomposition, Null Space, FAST, OMEGA

Among all the methods, the ILS is optimal, because it can be shown to have the largest success rate of all integer estimators. To solve the ILS problem in the process of finding the integer Ambiguity Resolution, the two most well-known efficient search strategies are **LAMBDA** and its extension **MLAMBDA**. These algorithms have shown their superiority in terms of both performance and processing time when compared to other algorithms in [135].

LAMBDA and MLAMBDA offer the combination of a linear transformation to shrink the integer vector search space and a skillful tree-search procedure in the transformed space, that is the reason why we choose LAMBDA to be our IAR method in this dissertation. The detailed process of LAMBDA and MLAMBDA will be further introduced in Sections 4.5.2 and 4.5.3, respectively.

Once the integer estimates of the ambiguities have been calculated, another step consists of deciding whether to accept the integer solution should be conducted. Examples include the ratio-test, the difference-test, and the projection-test in the framework of integer aperture estimation.

In our EKF algorithm, the ratio-test is utilized to decide whether we accept or reject the integer estimates from the IAR. One selects the integer candidates based on the sum of squared errors to get a fixed solution. The candidate with the lowest error norm is chosen once the ratio of the Maximum A-Posteriori error norm between the second-best candidate and the best candidate is bigger than a threshold. It is a pre-defined threshold or the critical value that the squared norm of ambiguity residuals of the best and second-best candidates should overpass to validate the integer estimation. In this thesis, an empirical fixed value of **3** is taken as in [136].

Additionally, to evaluate the expected quality of the mapping function I, another definition named **Ambiguity Success Rate**, defined as the integral of the probability density function (PDF) of the float solution over the pull-in region can be analyzed.

4.5.1.3. Fixed solution

Finally, the float solution of the remaining parameters (notably the position unknowns and possibly additional parameters such as atmospheric delays) are corrected by virtue of their correlation with the ambiguities. Once $\breve{\boldsymbol{a}}$ is accepted, the float estimator $\hat{\boldsymbol{b}}$ is re-adjusted to obtain the so-called fixed solution:

$$\breve{\boldsymbol{b}} = \hat{\boldsymbol{b}} - \boldsymbol{Q}_{\hat{b}\hat{a}}\boldsymbol{Q}_{\hat{a}\hat{a}}^{-1}(\hat{\boldsymbol{a}} - \breve{\boldsymbol{a}}) \tag{4-97}$$

In our EKF, once the estimated states are obtained in the EKF measurement update process, the float carrier-phase ambiguities will be tried to be resolved into integer values to **improve accuracy and convergence time.** If the IAR process is declared successful, a new position is computed using the DD carrier phase measurements corrected by the validated DD integer ambiguities using (**4-97**). This final position is a fixed solution, which can be at the mm-cm level in the ideal situation. If the IAR process is not declared successful, the final position is kept as the float solution.

4.5.2. LAMBDA Method

The acronym LAMBDA denotes the Least-squares AMBiguity Decorrelation Adjustment method. It has been theoretically proven to be the most optimal integer ambiguity determination technique [135]. It was developed by Teunissen since 1993, [57], [137], [138].

Within the LAMBDA method, the (Integer Least Square) ILS method is implemented, and the search of AR is executed by enumerating all integer candidates inside the search ellipsoid with a fixed ellipsoid size. Its two main features are:

- ***Sequential conditional least squares estimation***
- ***Preceded by a decorrelation float ambiguity solution instead of the original one***

Taking advantage of the full information of $\boldsymbol{Q}_{\hat{a}\hat{a}}$, the ILS AR is defined as

$$\breve{\boldsymbol{a}} = \text{argmin}(\boldsymbol{z} - \hat{\boldsymbol{a}})^T \boldsymbol{Q}_{\hat{a}\hat{a}}^{-1}(\boldsymbol{z} - \hat{\boldsymbol{a}}), \forall \boldsymbol{z} \in \mathbb{Z}^m \tag{4-98}$$

The optimal solution of **Equation (4-98)** is obtained through a search over the integer grid points of an n-dimensional hyper-ellipsoid defined by:

$$F(\boldsymbol{z}) = (\boldsymbol{z} - \hat{\boldsymbol{a}})^T \boldsymbol{Q}_{\hat{a}\hat{a}}^{-1}(\boldsymbol{z} - \hat{\boldsymbol{a}}) \leq \chi^2 \tag{4-99}$$

The integer grid point $\boldsymbol{z}$ inside the hyper-ellipsoid that gives the minimum value of function $F(\boldsymbol{z})$ is then the optimal ILS solution $\breve{\boldsymbol{a}}$.

Here, the search efficiency is governed by the size χ^2 and the shape of the ellipsoid. The constant χ^2 can be predetermined using different strategies and can also be narrowed down during the search [82], [132], [139]. The shape and orientation of the ellipsoid are defined by the covariance matrix $\boldsymbol{Q}_{\hat{a}\hat{a}}$, while highly correlated covariance matrices usually cause research to be stopped.

To improve the efficiency of the searching process, instead of using directly the $\hat{\boldsymbol{a}}$ and $\boldsymbol{Q}_{\hat{a}\hat{a}}$, LAMBDA employed the following decorrelated, but still an integer, variables by using the Z transformation:

$$\hat{\boldsymbol{z}} = \boldsymbol{Z}^T \hat{\boldsymbol{a}}, \quad \boldsymbol{Q}_{\hat{z}\hat{z}} = \boldsymbol{Z}^T \boldsymbol{Q}_{\hat{a}\hat{a}} \boldsymbol{Z} \tag{4-100}$$

After the decorrelation of the float ambiguities, we still need to estimate the integer ambiguities. The search can be carried out efficiently by using the sequential conditional adjustment. This adjustment determines the ambiguities step by step in a sequential manner.

In this case, the minimizer problem **Equation (4-98)** becomes:

$$\breve{\boldsymbol{z}} = \underset{\boldsymbol{z} \in \boldsymbol{Z}^n}{argmin}\ (\hat{\boldsymbol{z}} - \boldsymbol{z})^T \boldsymbol{Q}_{\hat{z}\hat{z}}^{-1}(\hat{\boldsymbol{z}} - \boldsymbol{z}) \tag{4-101}$$

Once the integer minimizer $\breve{\boldsymbol{z}}$ is found, the ILS AR $\breve{\boldsymbol{a}}$ can be deduced by:

$$\breve{\boldsymbol{a}} = \boldsymbol{Z}^{-T} \breve{\boldsymbol{z}} \tag{4-102}$$

By doing the decorrelating reparameterization of the float ambiguities, the integer least-squares estimates can be computed faster, the efficiency of the integer search is significantly improved.

4.5.3. MLAMBDA Method

For RTK GNSS applications where a large number of satellites are being tracked, the ambiguity search space becomes high-dimensional. In such cases, the computational speed becomes crucial. The modified LAMBDA method (MLAMBDA) [82] reduced the computational complexity of the LAMBDA method including both the reduction stage and the search stage while maintaining the quality of the solution.

The key of the MLAMBDA is the improvement of the decorrelation stage, it is referred to as a reduction process involving three strategies [82]:

- **Symmetric Pivoting**: This step handles the $\boldsymbol{L^T DL}$ factorization (of the variance-covariance matrix $\boldsymbol{Q_{\hat{a}\hat{a}}}$). The algorithm computes a permutation $\boldsymbol{P}$, a lower unit triangular matrix $\boldsymbol{L}$ and a diagonal $\boldsymbol{D}$ such that: $\boldsymbol{P^T Q_{\hat{a}\hat{a}} P = L^T DL}$. The lower triangular part of $\boldsymbol{Q_{\hat{a}\hat{a}}}$ is overwritten by that of $\boldsymbol{L}$ and the diagonal part of $\boldsymbol{Q_{\hat{a}\hat{a}}}$ is overwritten by that of $\boldsymbol{D}$.
- **Greedy Selection**: To make the reduction process more efficient, the number of permutations is reduced by scrapping the sequential order in the LAMBDA method. Differently, the MLAMBDA algorithm chooses the order adaptively.
- **Lazy Transformation**: MLAMBDA applies the integer Gauss transformations only to some of the sub diagonal elements initially and then performs the permutations to avoid possible multiple calculations situations when using LAMBDA.

As for the search process, the **ellipsoidal region** is also **shrunk** to save computational time. As we mentioned, In LAMBDA, the valueχ^2 plays an important role in controlling the volume of the search region during the search process.

For finding the optimal integer estimate, Teunissen [138] proposed a shrinking strategy in order to reduce the search region in an iterative manner. Once a candidate integer vector $\boldsymbol{z}$ in the ellipsoidal region is found, the corresponding $F(\boldsymbol{z})$ is taken as a new value for the value χ^2, thereby shrinking the ellipsoid region. This shrinking strategy can greatly benefit the search process by making it more efficient, however it was not implemented in the original LAMBDA algorithm. MLAMBDA algorithm takes this into account and further improves the computation efficiency of the search process in [57].

Since the core algorithms of the two methods are the same, LAMBDA and MLAMBDA gave **the same computed solution for the same ILS problem**. Therefore, there is no difference between the two algorithms in terms of accuracy. However, as for the calculation time, MLAMBDA is faster than LAMBDA for almost all cases. Usually, the time difference between the two algorithms becomes bigger and bigger as the dimension increases.

In this thesis, both the LAMBDA and MLAMBDA are utilized. Considering that they give the same IAR result, in the following sections, we will not deliberately distinguish between these two methods.

4.6. Chapter Summary

In this chapter, the main modules of the proposed multi-receiver architecture for GNSS RTK precise positioning and attitude estimation have all been presented and detailed, our EFK estimates the rover 3D position as well as the attitude (heading and pitch angles) of the vehicle.

After the selection of GNSS measurements by basic C/N0 and elevation masks, several measurement weighting schemes are conducted to quantify the accuracy of the measurements in different situations.

Then, a further check on the code and carrier phase measurements based on an Innovation test is conducted. Considering the importance of ambiguity states, any potential state change, i.e., Cycle slips, should be noticed and properly handled.

Therefore, the single-frequency CS-DR process followed. In the end, to further improve the accuracy of the state estimates, the attempts to fix the float ambiguities as integers are conducted by using the well-known LAMBDA method. When they succeed, the fixed PVA solution after the LAMBDA adjustment will be used in the next positioning epoch if the IAR process is declared successful, a new position is computed using the DD carrier phase measurements corrected by the validated DD integer ambiguities. This final position is a fixed solution. If the IAR process is not declared successful, the final position is kept as the float solution.

4.6.1. Scheme of Our Implemented GNSS Positioning Extended Kalman Filter

Figure 4-5 gives a detailed scheme of the implemented GNSS RTK positioning EKF.

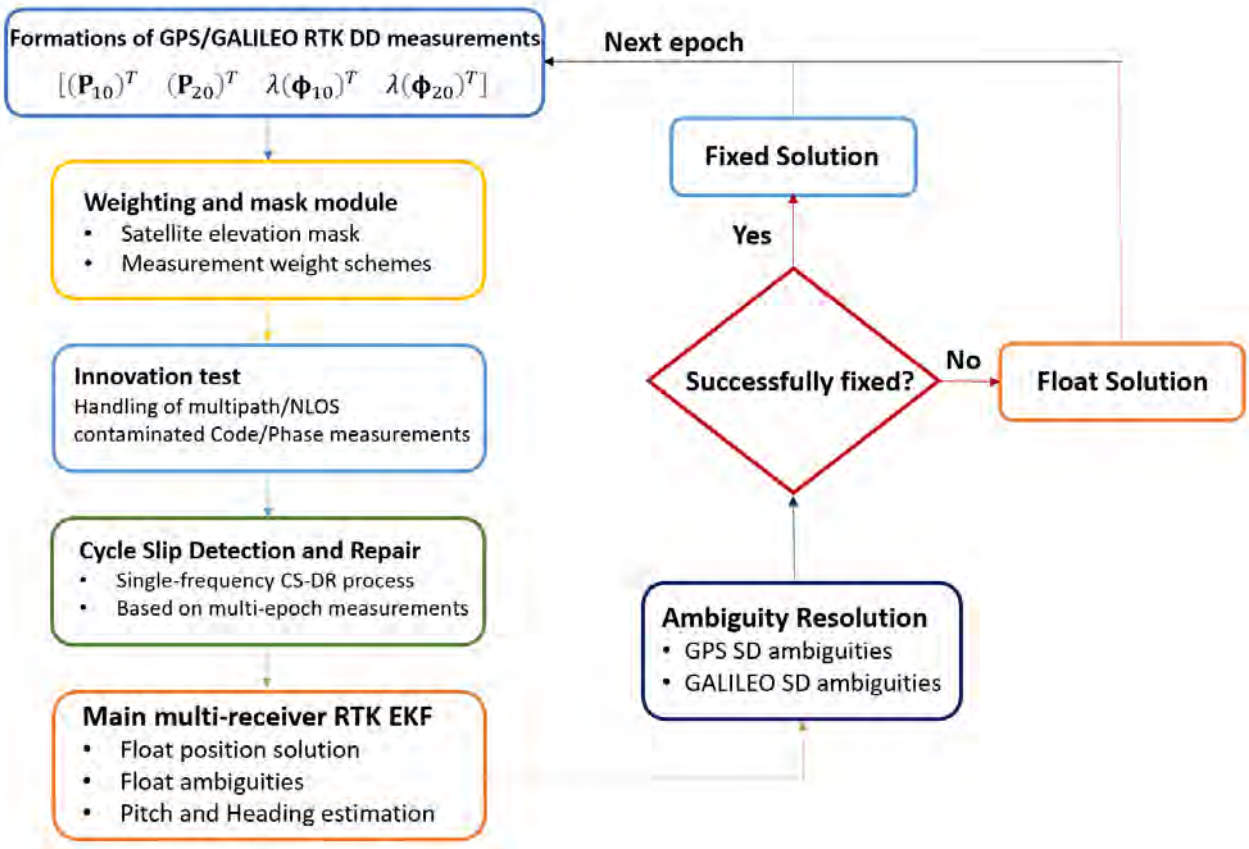

Figure 4-5 Scheme of the implemented GNSS Multi-receiver RTK positioning EKF

4.6.2. Expected Benefits of the Proposed Multi-receiver Architecture

In this thesis, we proposed a multi-receiver RTK precise positioning algorithm, which combines multi-constellation (GPS+Galileo) GNSS measurements of both antennas by making use of the previously known geometric constraint between them. This method allows more information involved and aims to improve RTK positioning performance in constrained areas.

In the case envisaged, by doing so, the reception diversity between two antennas can be harnessed to improve the availability and geometric distribution (i.e., DOP) of GNSS satellites, and the redundant measurements from a second antenna are expected to be able to help to weaken the multipath effect on the first antenna, thus, it is fair to expect the improvement of the RTK performance. Additionally, taking advantage of the attitude information and the known geometry of the array of receivers, the improvement of some internal steps of RTK precise positioning may be realized.

To summarize, the expected benefits of the proposed multi-receiver architecture can be listed as follows:

1) **Make the estimation of attitude possible:**

   This method also gives the estimation of the attitude of the vehicle which provides additional information beyond the positioning.

2) **Improvement of the Positioning accuracy:**

   a. Improved fixed success rate and accuracy of RTK in constrained environments are expected, even if neither of the two single-antenna receivers can successfully solve the AR problem.

   b. Improved the CS-DR process by considering a centralized cycle slips detection method shared between the two receivers.

3) **Positioning result availability increase:**

   In some extremely harsh situations (GNSS denied environments), the number of satellites is not sufficient to enable a PVT solution. The multi-receiver system algorithm is expected to perform better than the traditional single receiver system thanks to the doubled observations redundancy.

The improvement seems to be certain and clear. However, there is another question that we need to think about: although new information is introduced to the single-receiver model from known geometry and redundant GNSS measurements of the auxiliary rover, the number of states to be estimated increases too (attitude-related states), making it harder to precisely resolve the float ambiguities and converge the Kalman filter. Then, is there really any benefit from the dual-receiver architecture?

To find the answer to the question and evaluate the performance gain of our proposed method with respect to the single-receiver condition, all the points and expectations raised above will be verified and tested by the experimental results obtained through simulation and real data processing in Chapter 5 and Chapter 6. The robustness and precision of the proposed algorithm in GNSS-challenged environments will also be investigated.

Chapter 5. Simulation Results and Performance Analysis

In chapter 4, the proposed algorithm for RTK precise positioning and attitude determination in a constrained environment with the multiple installed low-cost single-frequency GNSS receivers has been introduced and presented.

To validate this concept and give a reference to our multi-receiver system's performance, the proposed algorithm is first tested using a simulator, by using the simulated code pseudo-range measurements and carrier phase measurements derived from realistic mathematical models.

In the current chapter, we focus then on the experimental validation of the proposed multi-receiver method based on the simulated data. The tests carried out are described, as well as the details about the experimental procedures of the proposed algorithm using simulated GNSS measurements. Different scenarios are conducted to analyze the benefits of the proposed architecture in various environmental situations. The performance of the developed RTK navigation solutions (position and attitude determination) is assessed based on these tests. Performance indicators such as fix success rate, position estimation accuracy, and attitude estimation accuracy are analyzed.

The structure of this chapter is as follows:

- Section 5.1 presents the configuration of the multi-receiver simulator, including the GNSS data generation process and the movement configuration of the simulated vehicle dynamic system.
- Section 5.2 describes all the simulation scenarios conducted in this thesis and their corresponding performance when compared to the traditional single receiver system. Different scenarios are conducted including varying the distance between the 2 antennas of the receiver array, the satellite geometry condition, the amplitude of the noise measurement, and the correlation level between the measurement of rover receivers to verify the impact and potential benefits of the use of an array of installed receivers.
- Section 5.3 focuses on showing the improvements and advantages of our proposed multi-receiver RTK algorithm observed in the cycle slip detection and repair process compared to the single receiver system.
- Section 5.4 is dedicated to presenting the results of a specific case of study, where we try to improve the reliability and efficiency of RTK ambiguity resolution using multiple installed rover receivers connected to the same antenna. This can be considered as the extreme case of our proposed method, where the distance between the two rover receivers is zero.
- Section 5.5 finally concludes this chapter.

5.1. Simulator configuration

To assess the proposed method's performance in a perfectly controlled environment with only a limited number of error sources, simulations were performed. In our simulator, a series of simulated data were generated with a priori noise levels, a different number of observations (satellite geometries), and various baseline relative lengths. This enabled precise test control in order to assess the proposed multi-receiver architecture's performance in terms of success fixing rate, position, and attitude estimation accuracy. In addition, all conditions being equal, a comparison between different simulated scenarios can be conducted.

In this section, the configuration and data generation steps of our simulator are firstly introduced in detail. The movement model of the simulated vehicle dynamic system is also presented.

5.1.1. Data Generation

To simulate the RTK positioning process for both the proposed multi-receiver system and the single receiver system, the first thing we need to do is to generate the GNSS code and carrier phase measurements for all the rover receivers as well as the virtual reference station.

5.1.1.1. Code and carrier phase measurement

To simplify the data generation process, rather than generating the raw GNSS measurement then calculate the DD measurements for RTK processing, we directly generate the double-difference (DD) code and carrier phase measurements between the rover receivers (noted by subscripts 1 and 2) and the reference station (noted by subscript 0) by utilizing the following formulas (**4-55,56,57,58**) mentioned in chapter 4:

$$P_{10}^{kl} = \left(\mathbf{e}^{kl}\right)^T \mathbf{b}_{10} + n_{P,10}^{kl} \tag{5-1}$$

$$P_{20}^{kl} = \left(\mathbf{e}^{kl}\right)^T \left(\mathbf{b}_{10} - |\mathbf{b}_{12}| \begin{bmatrix} \cos\theta \sin\psi \\ \cos\theta \cos\psi \\ \sin\theta \end{bmatrix}\right) + n_{P,20}^{kl} \tag{5-2}$$

$$\lambda\phi_{10}^{kl} = \left(\mathbf{e}^{kl}\right)^T \mathbf{b}_{10} + \lambda N_{10}^{kl} + n_{\phi,10}^{kl} \tag{5-3}$$

$$\lambda\phi_{20}^{kl} = \left(\mathbf{e}^{kl}\right)^T \left(\mathbf{b}_{10} - |\mathbf{b}_{12}| \begin{bmatrix} \cos\theta \sin\psi \\ \cos\theta \cos\psi \\ \sin\theta \end{bmatrix}\right) + \lambda N_{20}^{kl} + n_{\phi,20}^{kl} \tag{5-4}$$

Where:

- P_{np}^{kl} refers to the double-difference code phase measurement vector of receiver pair np and satellite pair kl
- $\lambda\phi_{np}^{kl}$ refers to the double-difference carrier phase measurement vector of receiver pair np and satellite pair kl
- $\mathbf{e}^{kl}$ is the difference between the Line-of-Sight vector of satellite k and l towards the receiver
- N_{np}^{kl} refers to the double-difference integer ambiguity of receiver pair np and satellite pair kl
- $n_{P,np}^{kl}, n_{\phi,np}^{kl}$ refers to the noise measurement of the double-difference code and phase measurement, respectively.

It should be emphasized that this individual double-difference corrected code and carrier phase GPS/Galileo measurement model is only valid for the short baseline case (normally less than 3 km). To complete the data generation process, every parameter in the DD equations should be defined, in the following sections, the methods to simulate these parameters are described.

5.1.1.2. Carrier Phase Integer Ambiguities

First, the carrier phase integer ambiguities are defined. Normally, in a short period of time, if there is no cycle slip, the ambiguities do not change. The ambiguities corresponding to the satellites are then set as a constant.

In our simulator, the DD carrier ambiguities are arbitrarily taken as fixed values separated by 10 cycles for each DD carrier measurements. For example, if we consider 7 visible satellites, the 6 DD carrier measurements will have constant ambiguities from 10 to 60 cycles.

5.1.1.3. Added Noise Measurements

The level of the noise measurement has a crucial influence on the position estimation as well as the cycle slip detection process, thus it is a significant parameter that needs to be analyzed.

The measurement noise is considered additive white Gaussian noise and is uncorrelated between the different satellites and between code and phase measurements.

For the added noise measurement of the DD code and phase measurement in the data generation model, its standard deviation is considered as a predefined fixed parameter for different environmental situations, and its value changes depending on the current considered environment.

The additive noise standard deviation for the carrier phase is assumed to be equal to the standard deviation for the code measurements divided by 100.

Later, there will be a section to analyze the impact of its value on the RTK positioning result for each system (Multiple receiver and Single receiver), and the robustness of each system under a certain level of noise will also be discussed.

5.1.2. System Configuration and Trajectory

5.1.2.1. Trajectory

To get enough change of the attitude of the vehicle during the simulation so as to observe the algorithm performance for different heading and pitches, the vehicle is assumed to make a uniform circular motion around the fixed reference receiver 0 with a constant radius (R = 100 m) in all the scenarios. The speed of the vehicle is 10 m/s, the duration of the simulated trajectory is 1000 s, and the sampling rate is defined as 1 Hz.

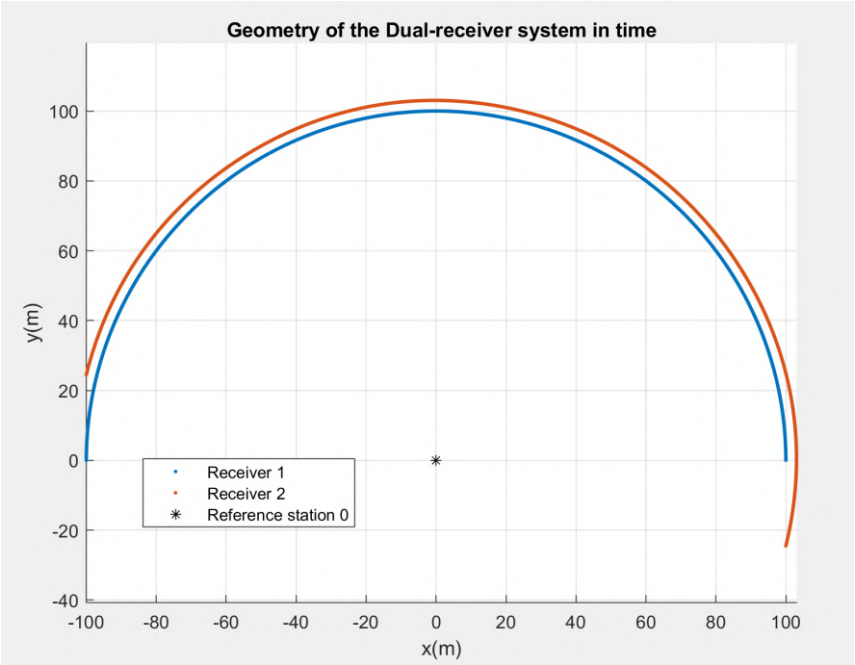

Figure 5-1 Illustration of the simulated geometry of the dual-receiver system in time for a 20 m array baseline

The relative horizontal positions of the dual-receiver system and the single receiver system in time are shown in Figure 5-1 and Figure 5-2, respectively.

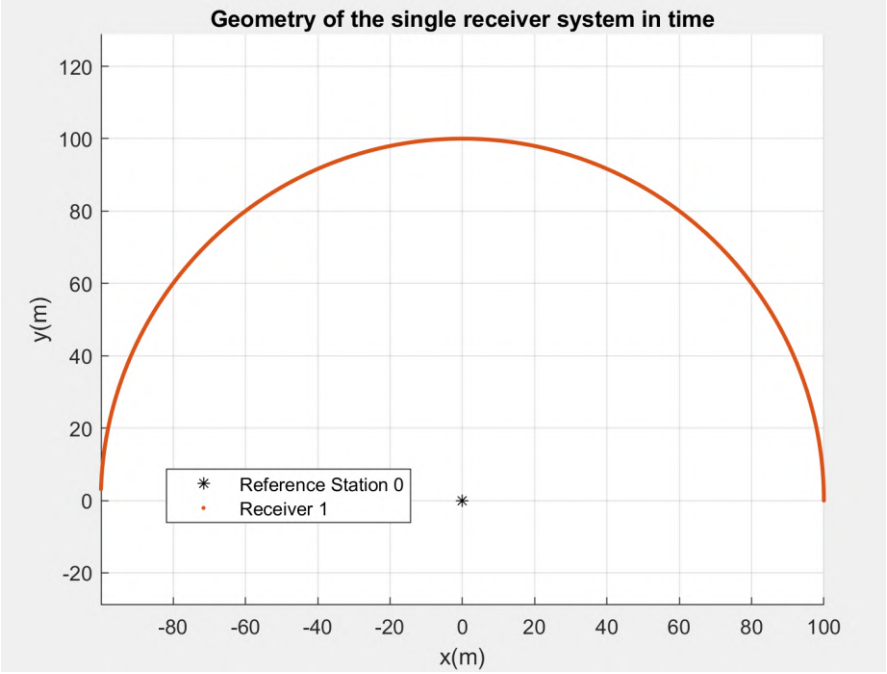

Figure 5-2 The geometry of the single receiver system in time

5.1.2.2. Altitude and pitch variations

In 5.1.2.1, we have modeled the 2D horizontal position coordinates of the vehicle and its heading over time, we still need to define the pitch and altitude parameters to complete our data generation model.

In order to make the pitch angle and the relative altitude between receiver 1 and 2 observable, the ground is considered to be undulated thus we also add a small altitude and pitch variation as shown in Figure 5-3.

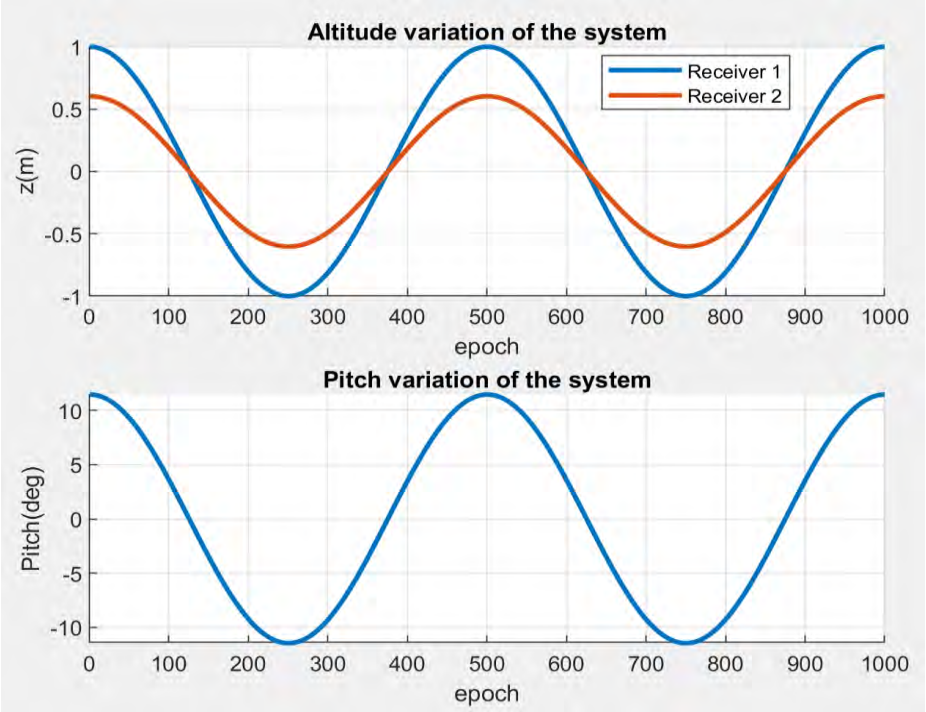

Figure 5-3 Altitude and Pitch angle variation of the Dual-Receiver system

5.1.3. GNSS and Satellite-related Parameters

The remaining unknown parameters in the DD measurements model are the GNSS and satellite-related parameters.

5.1.3.1. DD Line-Of-Sight Vector

First of all, the DD Line-Of-Sight (LOS) vector $\mathbf{e}^{kl}$ should be defined. In the general GNSS applications, to get the LOS vector, we need first to calculate the considered satellite's 3D position from the GNSS navigation message, then deduce the corresponding LOS vector by considering an approximate position of the GNSS receiver.

Here in our simulator, the LOS vectors are modeled by using the azimuth φ_r^k and elevation θ_r^k of the satellites with respect to the corresponding receiver, thanks to the following formula that defines the LOS vector between satellite *k* and receiver *r* in the ENU frame:

$$\mathbf{e}_r^k = \begin{bmatrix} \cos\theta_r^k \cos\varphi_r^k \\ \cos\theta_r^k \sin\varphi_r^k \\ \sin\theta_r^k \end{bmatrix} \tag{5-5}$$

And its geometric relationship can be shown in Figure 5-4:

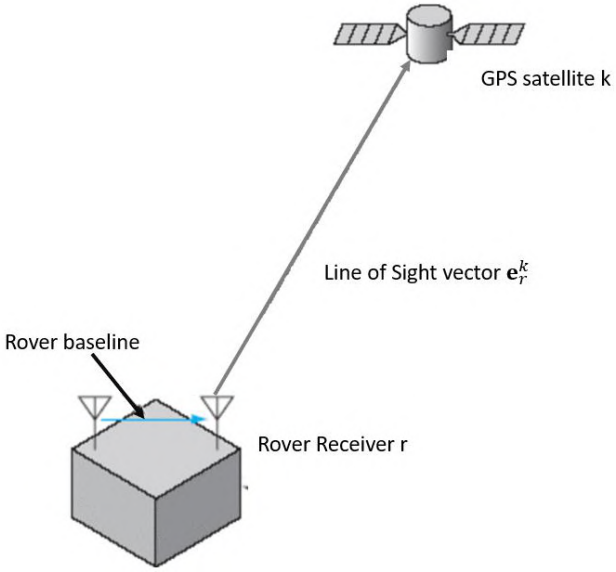

Figure 5-4 LOS vector between satellite k and receiver r

Again, to simplify the data generation process, we directly generate the azimuth and elevation angles of each tracked satellite with respect to the considered receiver from a randomly selected real Almanac. Besides, since we consider a short baseline measurement model, the rover receivers are considered to share the same LOS vector with the reference station when tracking the same satellite. In this case $\mathbf{e}_1^k = \mathbf{e}_0^k = \mathbf{e}^k$, and the SD LOS vector is then also $\mathbf{e}^k$ because the SD measurements are obtained by differentiating the raw measurements made by the rover and the base station on the same satellite.

Once we have all the SD LOS vector $\mathbf{e}^k$ for all the tracked satellites, the DD LOS vector $\mathbf{e}^{kl}$ can be calculated by using the following simple formula:

$$\mathbf{e}^{kl} = \mathbf{e}^k - \mathbf{e}^l \tag{5-6}$$

5.1.3.2. Satellite Geometry

Regarding the considered GNSS satellite geometry, we used the same randomly selected Almanac in Section 5.1.3.1 to give the sky plot for satellite locations in different environments. In our simulator, the satellites are simulated with a fixed position.

As an example, In the open sky environment, for each considered GNSS constellation, we consider 6 satellites with fairly good geometry, i.e., well-spaced in azimuth and elevation. This would correspond to a typical case of a single constellation in an open sky environment. The corresponding sky plot in this situation is shown in Figure 5-5.

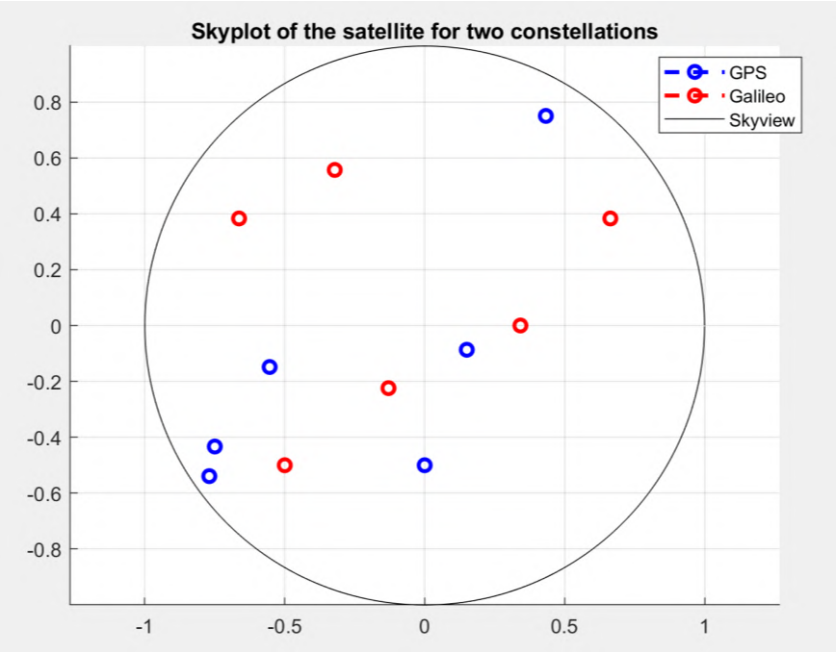

Figure 5-5 Typical sky plot for an open sky environment for 2 constellations

5.1.3.3. Signal Wavelength

Finally, to reflect the representative situation of the current single-frequency low-cost GNSS receiver, the GNSS signal is considered to be transmitted at the GPS L1 frequency (1575.42 MHz), which corresponds to a wavelength λ of 0.1905 meters.

5.2. Simulation scenarios and results

In this section, we present results obtained by applying the novel installed multi-receiver method to simulated data sets. All simulation scenarios conducted and their corresponding results, when compared to the traditional single receiver system, are described. In fact, by utilizing the simulated data, one main benefit is that the environmental situation can be perfectly controlled, thus some key parameters that have a great influence on the positioning accuracy, normally fixed in real data, can be changed in the simulator to explore different scenarios.

Taking advantage of this feature, a variety of studies are conducted to test the RTK performance by using an array of receivers with known geometry. The variation parameters included here are:

1. The length of the rover baseline l between the 2 installed receivers,
2. The amplitude of the measurement noise σ_{code} and $\sigma_{carrier}$,
3. The satellite geometry condition (mainly the number of visible satellites),
4. The correlation level between the measurement errors of rover receivers

In all the scenarios, we conduct the analysis by comparing the results obtained by the single receiver RTK algorithm and the multi-receiver RTK algorithm. To assess the improvement brought by the proposed algorithm, two performance metrics are defined to give quantitative values comparison between approaches under the same conditions:

a) **3D positioning error statistics:** its mean value, standard deviation, and 95th percentiles over the total number of epochs. The 3D positioning error is the distance between the true and estimated location in all 3 orientations. As the proposed algorithm typically targets road users,

positioning accuracy is the most important parameter to be considered in land vehicle applications.

b) **Fix success rate:** The fix success rate is defined as the number of epochs during which ambiguities are successfully fixed as integers over the total number of epochs.

In addition, the other two performance metrics are defined to evaluate the precision of the attitude estimation of the multi-receiver approach in different scenarios:

c) **Absolute heading error statistics:** mean value, standard deviation, and 95th percentiles over the total number of epochs.

d) **Absolute pitch error statistics:** mean value, standard deviation, and 95th percentiles over the total number of epochs.

Finally, in order to make the results more in line with the actual situation, the values of the performance metrics shown in the presented tables later are based on the average running result of **100 Monte-Carlo simulations**, where the noise and initial states (3D position coordinates, heading, pitch and ambiguities) are drawn randomly.

5.2.1. Typical Results of the Proposed Multi-receiver Method

Before the comparison between approaches, in this section, the representative results of the proposed multi-receiver system are first presented using the most common parameter values. Typical results of the Kalman filter states estimations are then given in the following subsections. The configuration of the parameters used in this section are:

- The number of satellites $N_{sat} = 7$
- The predefined noise value $\sigma_{code} = 1\ m$
- The rover baseline length $\mathrm{l} = 2\ m$ between the two installed receivers

5.2.1.1. Position-related states estimation

Figure 5-6 depicts the estimated baseline vector between receiver 1 and the reference station 0 in the ENU coordinate for one Monte-Carlo simulation.

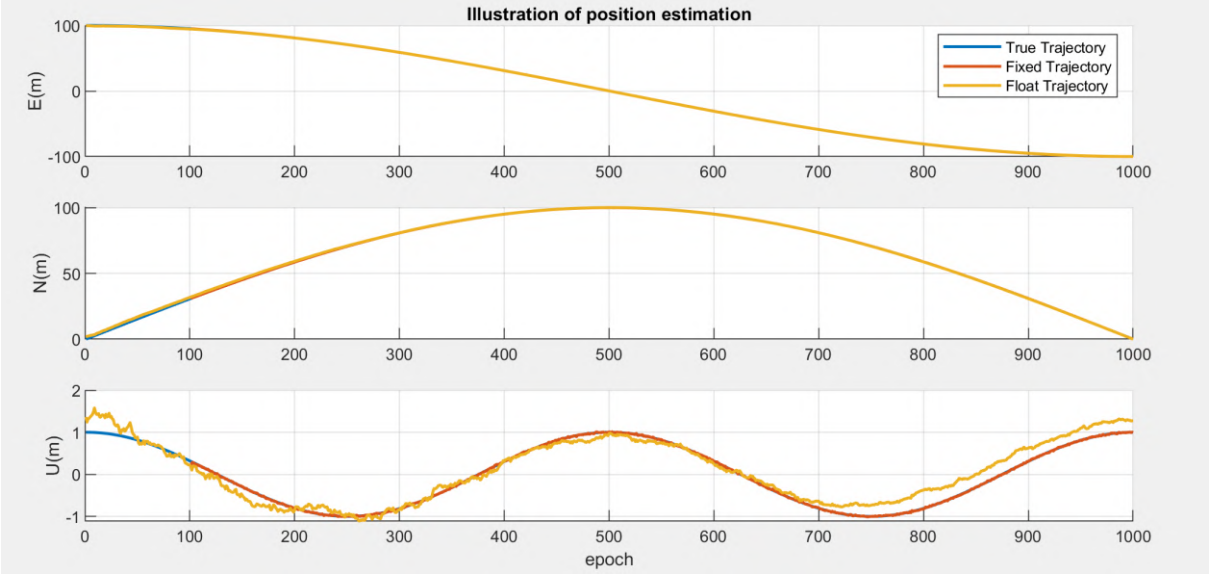

Figure 5-6 Illustration of the position estimation

The three curves in the figure correspond to the true trajectory, float solution trajectory, and the fixed solution trajectory, respectively. Comparisons with the traditional single receiver system will be presented in the next sections.

In order to show the difference between the results of the two solutions more clearly, Figure 5-7 illustrates the positioning error comparison between the float and the fixed solution. One can see from the figure that the fixed solution is not available until the 102nd epoch.

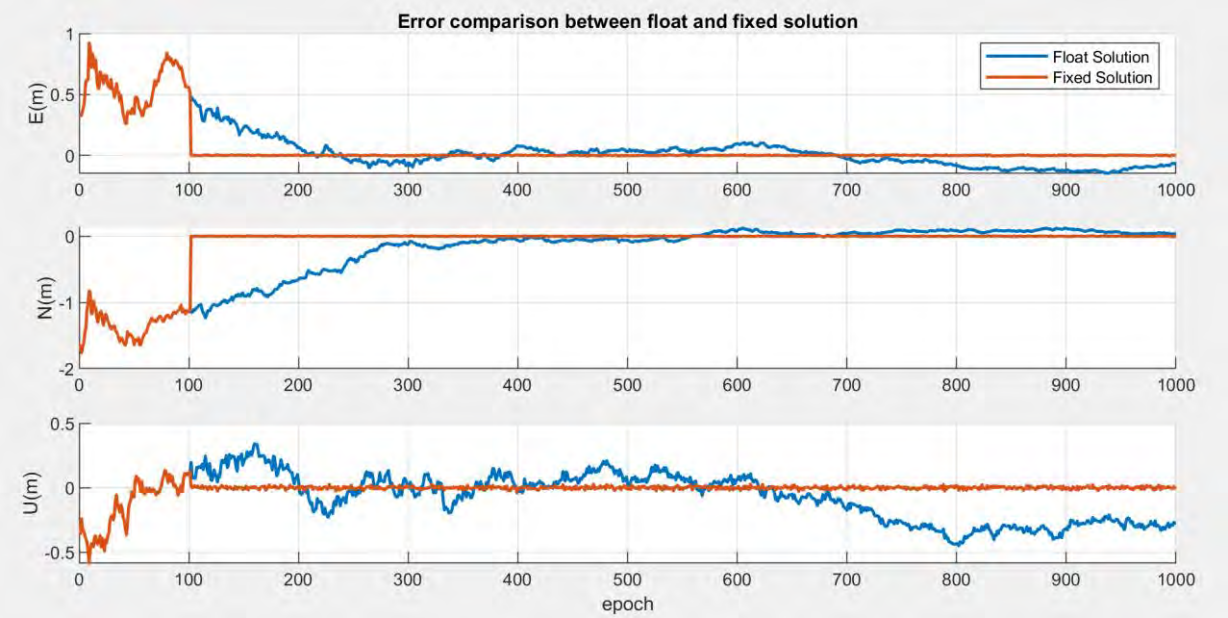

Figure 5-7 Illustration of float vs fixed solution

In Figure 5-7, the fixed solution is defined depending on the IAR validation process. For every epoch, if the IAR process is declared successful, a new position is computed using the DD carrier phase measurements corrected by the validated DD integer ambiguities. This position then is used to update the fixed solution. If the IAR process is not declared successful, we keep the float solution. This combined 'fixed solution' is considered to be the result of our proposed muti-receiver method.

From Figure 5-7, one can notice that some convergence period is present on the position states for both the float and fixed solutions. However, once they successfully converge, the error between the estimated result and the true value is extremely small.

In addition, we can see that the system fixes the ambiguities from the 102nd epoch and once the IAR is declared successful, the positioning results of the fixed solution become much more accurate compared to the float solution. A centimeter-level accuracy could be obtained when the ambiguities are successfully fixed.

5.2.1.2. Ambiguities estimation

The DD ambiguities are included in the state vector of the proposed EKF architecture and are estimated during the EKF process. Figure 5-8 shows the estimation results of the DD carrier phase measurements integer ambiguities of rover receivers 1 and 2. At each epoch, the float integer ambiguities are attempted to be fixed to integers by using the LAMBDA method. Comparisons with the traditional single receiver system will be presented in the next sections.

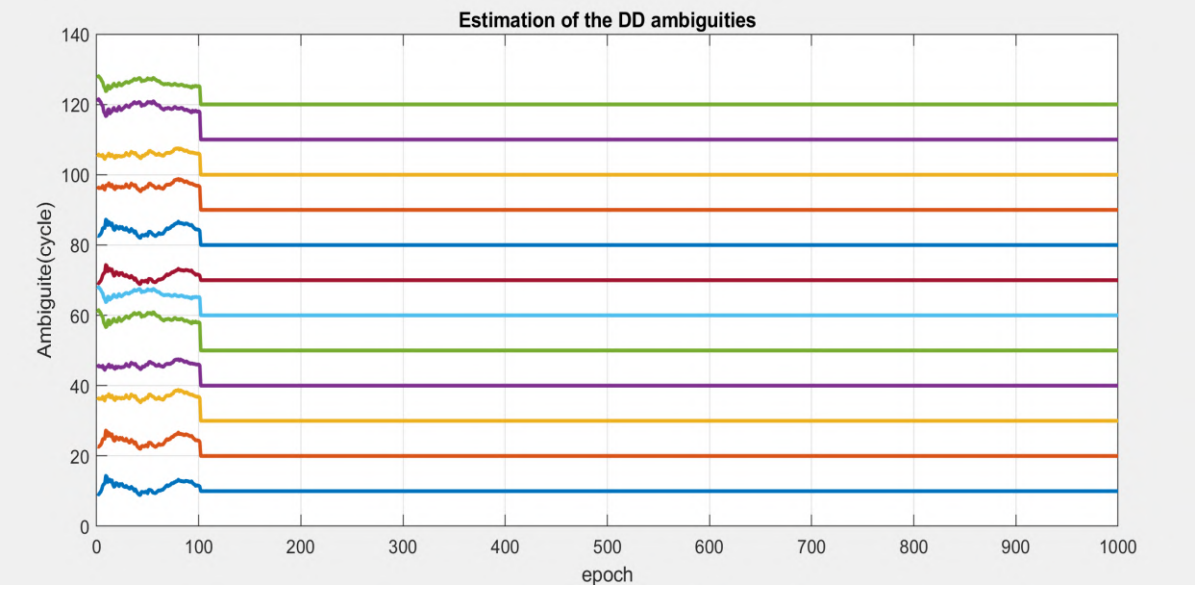

Figure 5-8 Estimation of the DD ambiguities of 2 rover receivers

Figure 5-9 shows the error of the estimation of the DD fixed ambiguities. As can be seen from Figure 5-9, the DD ambiguities are successfully fixed to integer numbers from the 102nd epoch. Combined with the results in Figure 5-7, we can infer that it is the successful fixing of the DD ambiguities that drives the great improvement of the positioning accuracy, which confirms the importance of finding the correct integer ambiguity resolution in RTK precise positioning. The IAR is indeed the key to obtaining a fast and centimeter-level navigation solution by benefiting the integer nature of the ambiguities.

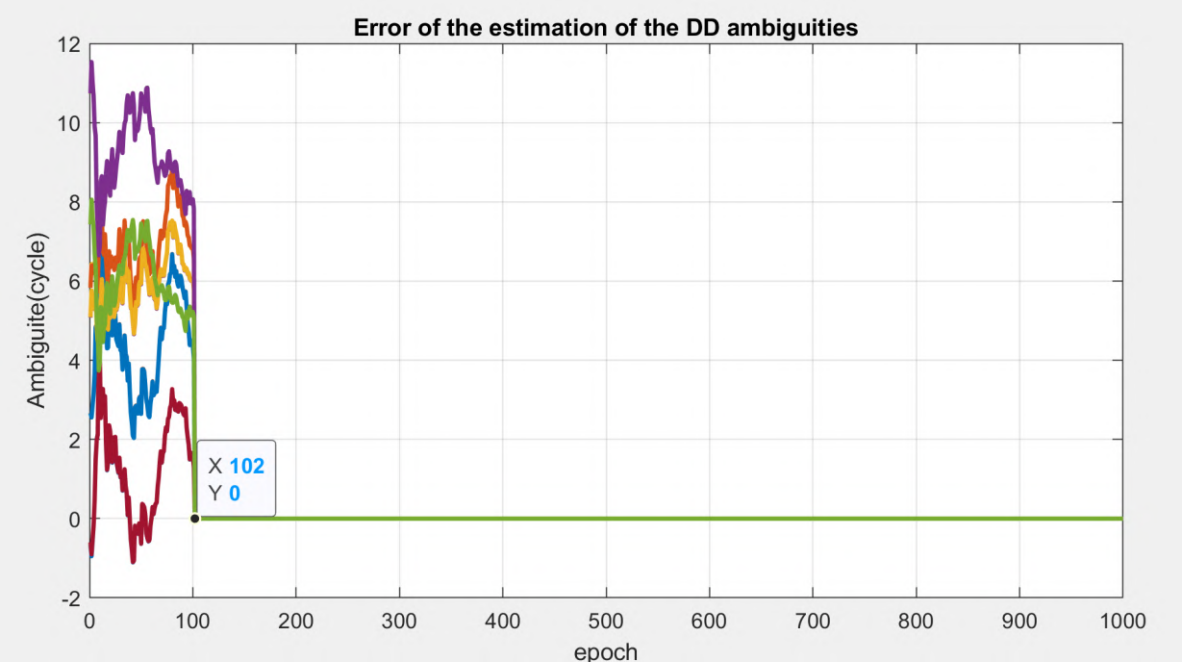

Figure 5-9 Errors of the estimation of the DD fixed ambiguities

5.2.1.3. Attitude-related states estimation

For the proposed multi-receiver architecture, the last two terms to be estimated in the EKF state vector are the vehicle attitude-related parameters: heading and pitch angles of the considered vehicle's

platform. Figure 5-10 shows an illustration of the estimation of the attitude-related states comparing to the true values. Comparisons with the traditional single receiver system will be presented in next sections.

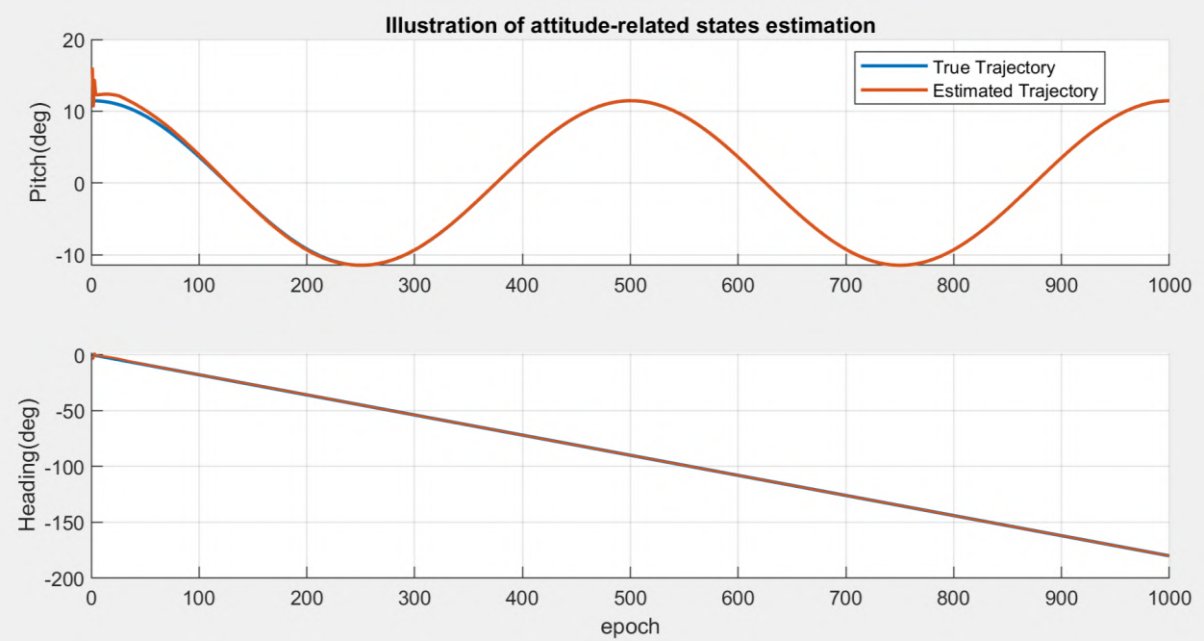

Figure 5-10 Illustration of attitude-related states estimation

As can be seen from the result, the time it takes to converge to the reference value is basically the same as the estimation of the position-related states. Similarly, once the ambiguities are fixed and they successfully converge, a sufficiently accurate attitude estimate can be obtained. In order to show the accuracy of the estimated value more clearly, Figure 5-11 compares the attitude estimates error of the fixed solution with the float solution.

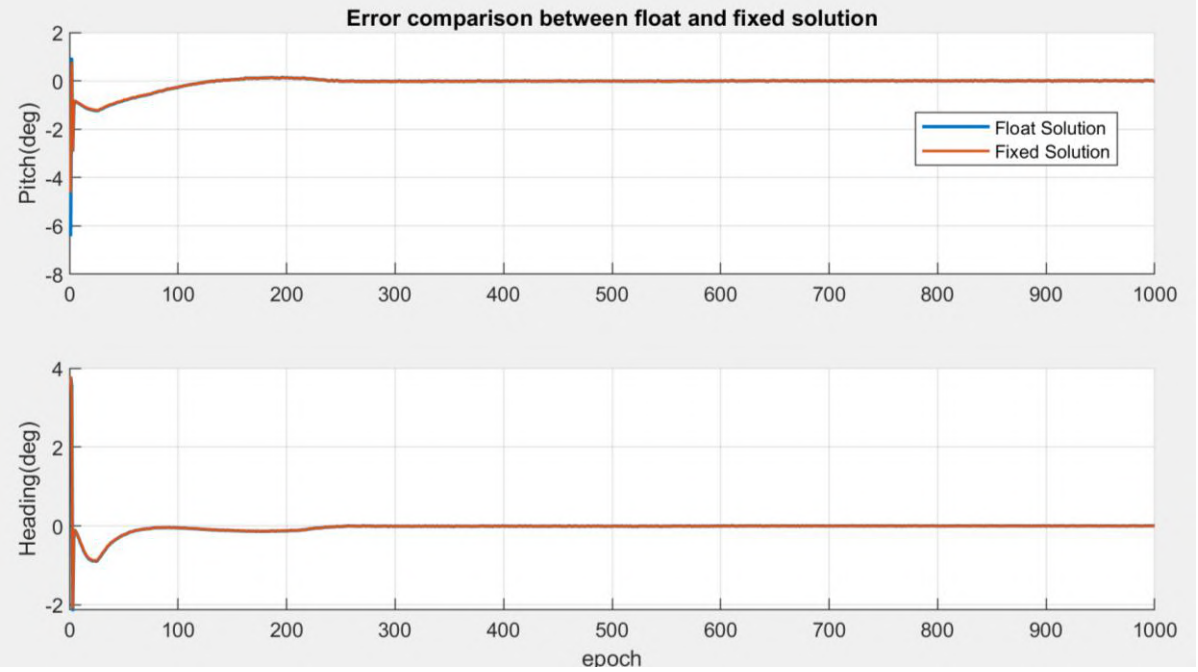

Figure 5-11 Error comparison between float and fixed solution for attitude estimation

From the result presented in Figure 5-11, we can see that a 0.1 degree-level accuracy of the attitude estimates is obtained when the EKF converges. Additionally, it is observed that, unlike the position-related state's estimates, the precision is not much improved in the fixed solution. We speculate that it is because the attitude precision is already good enough (under degree-level) in the float solution.

In the following sections, all the simulation scenarios conducted in this thesis and their corresponding statistical results are presented.

5.2.2. Rover Baseline length Effect Analyses

Precise attitude information is essential for autonomous driving of any vehicle. By using an array of receivers, we can additionally get the attitude information of the vehicle. Nevertheless, this attitude information is calculated based on the known geometry of the multi-receiver system in which the length of the baseline between the two receivers of the array plays an important role.

That is why in the first scenario, we want to analyze the influence of the system when the length of the baseline changes. The geometry of the array of receivers is then not fixed in this situation, by varying the receiver baseline while keeping the same noise measurement ($\sigma_{code} = 1$ m, which is the value that best fits the actual environment) and a favorable single constellation satellite geometry (all 7 satellites in Figure 5-5), we intended to confirm the effect of the length of the array baseline on the performance of the RTK and attitude determination.

Table 5-1 Performance comparison for different array baseline, σ_code=1 m, N_sat=7

Variation	Performance indicator	Unit	Mean	Standard deviation	95% bound
Single receiver	3D position error	m	0.1725	0.2591	0.3723
	Fix success rate	%	89.35	16.08	51.13
Dual receiver $l = 1$ m	3D position error	m	0.1410	0.2089	0.2258
	Absolute heading error	deg	3.9229	4.9453	5.1283
	Absolute pitch error	deg	0.9250	1.8582	2.0495
	Fix success rate	%	94.69	N/A	N/A
Dual receiver $l = 2$ m	3D position error	m	0.1185	0.1940	0.2142
	Absolute heading error	deg	1.8666	2.8054	3.1071
	Absolute pitch error	deg	0.7824	1.2755	1.4552
	Fix success rate	%	94.69	N/A	N/A
Dual receiver $l = 10$ m	3D position error	m	0.0723	0.1546	0.1968
	Absolute heading error	deg	1.5194	2.3028	2.7344
	Absolute pitch error	deg	0.4820	1.1681	0.9283
	Fix success rate	%	94.69	N/A	N/A

The analysis given in Table 5-1 shows that the dual receiver array system always provides better performance than the single receiver RTK solution, in terms of the fix success rate and also the positioning result. What can be also noticed is, the success fix rate reaches a threshold value of 94.69% for every multi-receiver solution, which should correspond to the maximum fixed rate after the brief convergence period.

In addition, as expected, the accuracy of the attitude estimates greatly improves as the array baseline increases, which also led to the improvement of the positioning results. However, taking into account the actual situation, where the vehicle has size limitations, a baseline of 2m is acceptable and would be practical to be installed on a real vehicle given the favorable assumptions.

To be more straightforward, the comparisons of several key parameters between the dual receiver array system and the single receiver system includes the 3D position error, the fix success rate, the heading error, and the pitch error are shown in Figure 5-12 and Figure 5-13.

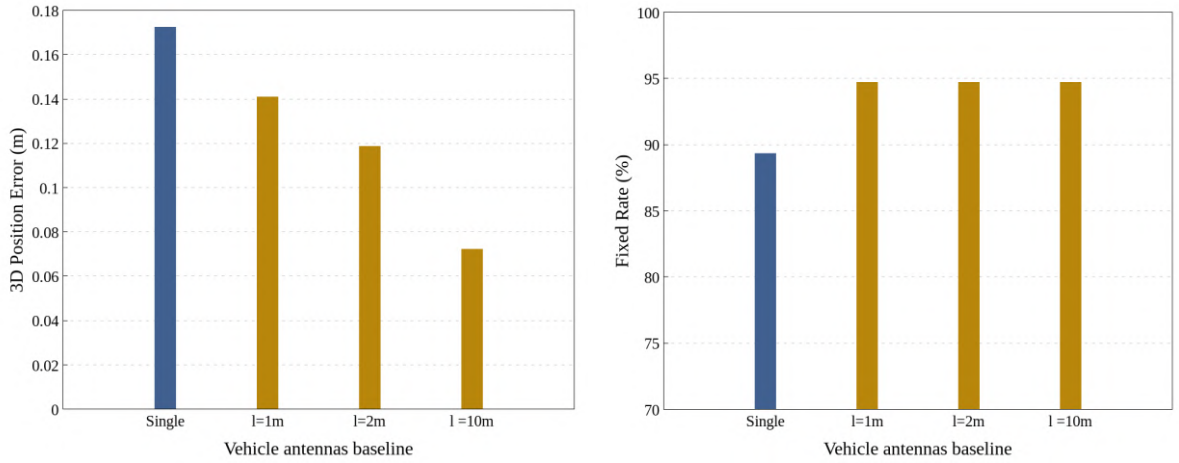

Figure 5-12 The comparisons of position accuracy and fix success rate under different lengths of array baseline

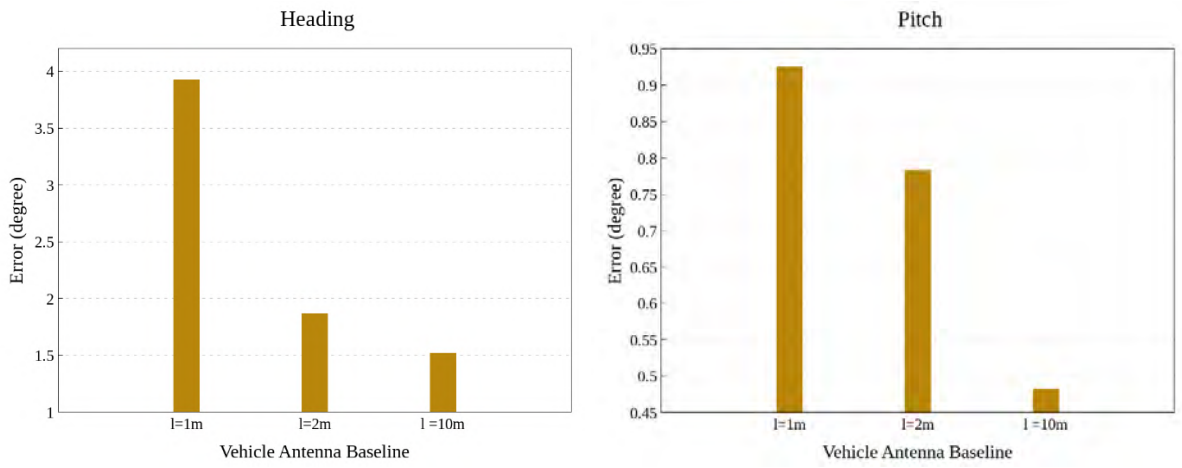

Figure 5-13 The comparison of attitude estimates precision under different lengths of array baseline

5.2.3. Satellite Geometry Effect Analyses

As aforementioned, the positioning performance of a satellite system highly depends on the DOP. A favorable satellite geometry is essential to get an accurate positioning result. That is why in this section, we want to analyze the influence of the system when the geometry of the satellite changes. In addition, in our proposed method, a GPS/Galileo dual-constellation GNSS system is considered to improve the

DOP, and therefore ameliorate the RTK performance, it is thus interesting to simulate this situation and further verify its impact.

Consequently, to consider different environmental situations and analyze the benefits brought by the multi-constellation GNSS systems configuration, 3 different GNSS situations are considered:

- Only GPS in GNSS-denied environment – less than 5 satellites most of the time.
- Only GPS in GNSS-favorable environment – 6 to 8 satellites most of the time.
- GPS/Galileo in GNSS-favorable environment – more than 10 satellites most of the time.

In all the scenarios, the geometry of the array ($l = 2$ m) and the noise measurement ($\sigma_{code} = 1$ m) are fixed and by degrading the geometry of the satellite (by removing one satellite at a time), we observe the robustness against degraded satellite geometry of proposed multiple rover receivers RTK systems. The results of each scenario are presented as follows.

5.2.3.1. Only GPS in GNSS-denied Environment

In the first case, the most difficult case is considered, where the vehicle is in a GNSS-denied environment (e.g., urban environment with lots of buildings, under the bridge, light indoor, etc.) and can only track no more than 5 satellites most of the time.

To this end, two simulated scenarios are conducted as shown in Figure 5-14. In the first situation, we assume that only 4 satellites can be tracked during the data collection while 5 satellites can be tracked in the second situation.

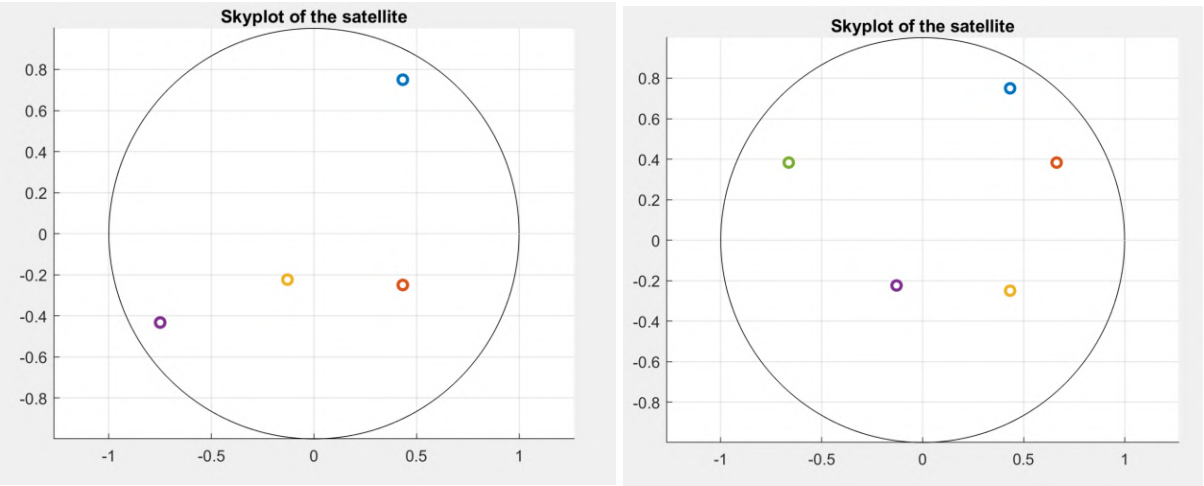

Figure 5-14 Considered satellite geometry with N_sat=4 (left) and N_sat=5 (right)

From Table 5-2, one can notice that when there are only 4 available satellites, it is extremely difficult to fix the ambiguity for both systems. However, the analysis of Table 5-2 shows that the use of the receiver array improves the fix success rate for all considered satellites geometries. Besides, the dual receiver array provides always better performance than the single receiver RTK solution under the same satellites geometry situation which confirms the interest of our approach.

Table 5-2 Performance comparison for different satellite geometry in GNSS-denied environment, l=2 m, σ_code=1 m

Variation	Performance indicator	Unit	Mean	Standard deviation	95% bound
Single receiver $N_{sat} = 5$	3D position error	m	0.5111	0.4649	0.6116
	Fix success rate	%	41.92	N/A	N/A
Dual receiver $N_{sat} = 5$	3D position error	m	0.4194	0.2276	0.4322
	Absolute heading error	deg	2.1331	3.8637	4.5871
	Absolute pitch error	deg	2.3642	2.4387	3.0455
	Fix success rate	%	84.40	N/A	N/A
Single receiver $N_{sat} = 4$	3D position error	m	0.6264	0.2324	0.8812
	Fix success rate	%	0.82	N/A	N/A
Dual receiver $N_{sat} = 4$	3D position error	m	0.5432	0.3618	0.6758
	Absolute heading error	deg	3.0569	3.3308	4.7031
	Absolute pitch error	deg	3.7220	3.0152	3.8678
	Fix success rate	%	1.86	N/A	N/A

5.2.3.2. *Only GPS in GNSS-favorable Environment*

In the second case, the GNSS friendly environment (ex. Suburban environment, open sky, etc.) is considered, which means that the receiver has great visibility of the satellites. However, the receiver is assumed to process only the GPS signal. Under these circumstances, more than 6 satellites but less than 8 satellites should be able to be tracked by the receiver most of the time. Figure 5-15 illustrates the two situations studied in this section, with 7 and 8 tracked satellites during the data collection, respectively.

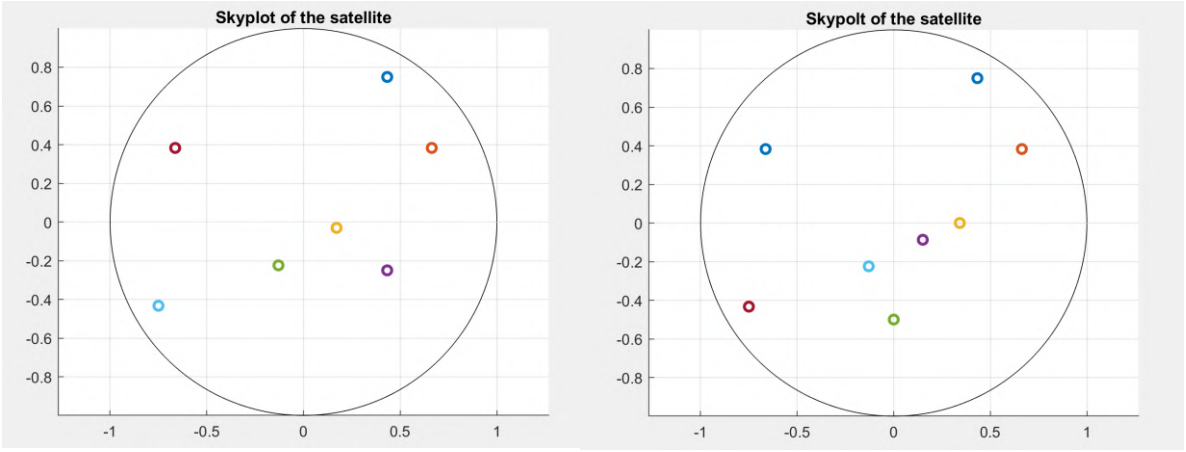

Figure 5-15 Considered satellite geometry with N_sat=7 (left) and N_sat=8 (right)

Table 5-3 reports the performance comparison between the single receiver system and the proposed multi-receiver system, for different satellite geometries in GNSS-favorable environments. As we can see, with the increase in the number of satellites, the positioning accuracy and fix success rate of both systems have all been greatly improved. Still, the dual-receiver system can always give a better solution compared to a single receiver system.

Table 5-3 Performance comparison for different satellite geometry in GNSS-favorable environment, l=2 m, σ_code=1 m

Variation	Performance indicator	Unit	Mean	Standard deviation	95% bound
Single receiver $N_{sat} = 7$	3D position error	m	0.1725	0.2591	0.3272
	Fix success rate	%	89.35	N/A	N/A
Dual receiver $N_{sat} = 7$	3D position error	m	0.1185	0.1940	0.2142
	Absolute heading error	deg	1.8666	2.8054	3.1071
	Absolute pitch error	deg	0.7824	1.2755	1.4552
	Fix success rate	%	94.69	N/A	N/A
Single receiver $N_{sat} = 8$	3D position error	m	0.1437	0.2318	0.2787
	Fix success rate	%	91.45	N/A	N/A
Dual receiver $N_{sat} = 8$	3D position error	m	0.1054	0.1724	0.1818
	Absolute heading error	deg	1.6298	2.4054	2.8073
	Absolute pitch error	deg	0.7315	1.1825	1.3485
	Fix success rate	%	95.36	N/A	N/A

In order to make an intuitive comparison, to reflect the huge impact of the number of satellites on positioning accuracy, the comparison of the results of the GNSS-denied and GNSS-favorable environments are visualized in Figure 5-16.

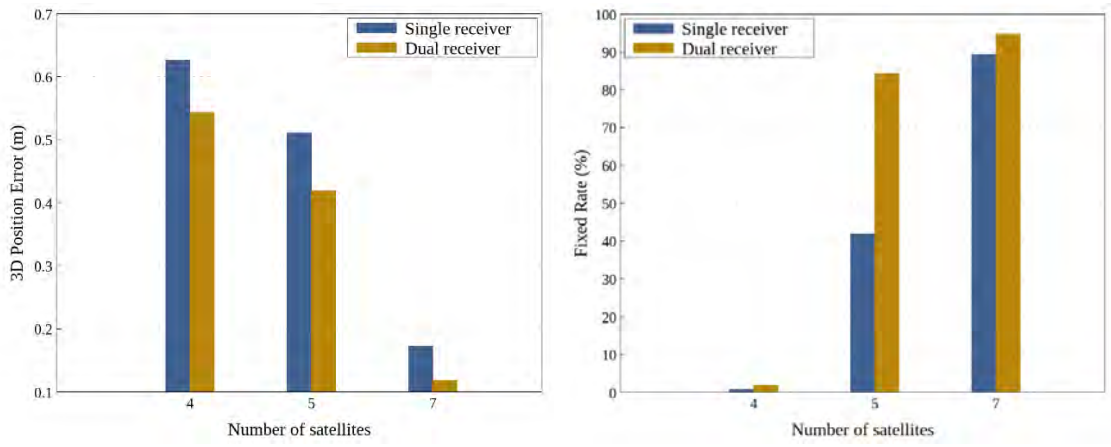

Figure 5-16 The comparisons of Position accuracy and fix success rate under different satellite geometries

Equally important, for the attitude estimates of the dual-receiver system, as shown in Figure 5-17, the accuracy of the attitude estimation has also been greatly improved in the case of the increased satellite visibility.

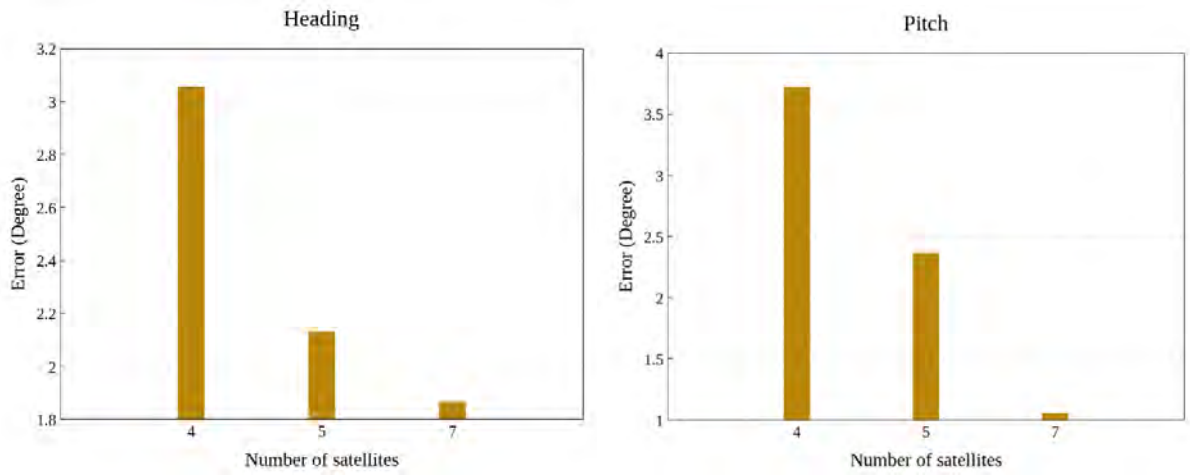

Figure 5-17 The comparisons of Heading and pitch estimates under different satellite geometries

5.2.3.3. GPS/Galileo in GNSS-favorable environment

For the last scenario in this section, we intend to study the advantages of using a multi-constellation GNSS system configuration in positioning results.

By considering a GPS/Galileo dual-constellation GNSS system in a GNSS-favorable environment, more than 10 satellites should be tracked most of the time. As shown in Figure 5-18, two simulated scenarios with 10 and 12 tracked satellites are then conducted and the performance comparison for these scenarios is reported in Table 5-4.

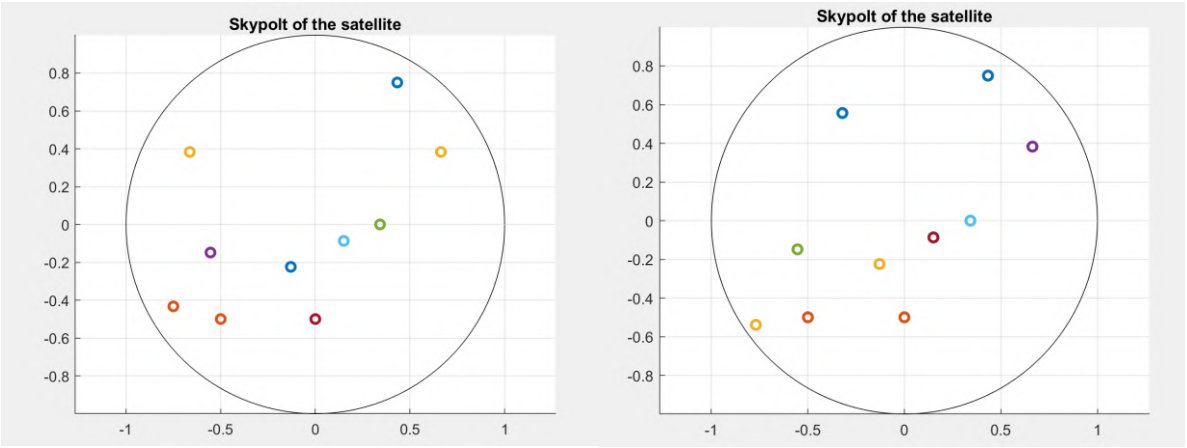

Figure 5-18 Considered GPS/Galileo satellite geometry with N_sat=10 (left) and N_sat=12 (right)

From Table 5-4, the improvement on the positioning results is evident and demonstrates that a good GNSS satellite geometry situation and a multi-constellation configuration are crucial in the precise positioning applications. In particular, the convergence period is reduced. Besides, the improvement brought by the proposed multi-receiver system is also further confirmed.

Table 5-4 Performance comparison for different satellite geometry for GPS/Galileo dual-constellation, l=2 m, σ_code=1 m

Variation	Performance indicator	Unit	Mean	Standard deviation	95% bound
Single receiver $N_{sat} = 10$	3D position error	m	0.1125	0.2238	0.2327
	Fix success rate	%	92.35	N/A	N/A
Dual receiver $N_{sat} = 10$	3D position error	m	0.0985	0.1438	0.1557
	Absolute heading error	deg	1.5534	2.6138	2.9714
	Absolute pitch error	deg	0.6524	1.1342	1.2835
	Fix success rate	%	96.65	N/A	N/A
Single receiver $N_{sat} = 12$	3D position error	m	0.1085	0.2118	0.2187
	Fix success rate	%	93.45	N/A	N/A
Dual receiver $N_{sat} = 12$	3D position error	m	0.0954	0.1325	0.1318
	Absolute heading error	deg	1.4238	1.9845	2.2138
	Absolute pitch error	deg	0.5138	0.9825	1.1845
	Fix success rate	%	98.48	N/A	N/A

5.2.4. Noise Level Effect Analyses

As discussed before, in GNSS precise positioning, the PVT quality depends mainly on

- On the satellite geometry (DOP), which has been studied in Section 5.2.3
- On the code and phase pseudorange quality (UERE)

UERE denotes the User Equivalent Ranging Error, it is the sum of all equivalent residual errors affecting the corrected pseudorange measurements used by the PVT algorithm. In our proposed architecture of this thesis, the measurement model consists of the DD code and carrier phase measurements from receivers, even though a large part of correlated errors is removed by differentiating, there is still a certain level of noise errors remaining. The level of the remaining noise has then a great influence on UERE and eventually the positioning accuracy. Therefore, it is a parameter worthy of detailed analysis of its impact. The results when varying the level of the noise in the simulator are presented in this section.

In this scenario, the geometry of the array of receivers ($l = 2$ m) and the satellite geometry ($N_{sat} = 7$) are fixed, while varying noise measurement σ_{code}, we observe the robustness against the noise of the multi-receiver RTK system. We recall that the phase measurement noise standard deviation is scaled by a factor of 1/100, to account for the difference in accuracy between the code measurement and the carrier phase measurement.

The analysis of Table 5-5 shows that as the level of noise amplitude increases, the positioning accuracy and attitude estimation precision have been greatly degraded. What is more important, the use of the receiver array improves the success fix rate for all considered σ_{code} values, and shows its robustness against high-level noise, thus demonstrating the interest of such an approach.

Table 5-5 Performance comparison for different measurement noise, l=2 m, N_sat=7

Variation	Performance indicator	Unit	Mean	Standard deviation	95% bound
Single receiver $\sigma_{code} = 1$ m	3D position error	m	0.1725	0.2591	0.3272
	Fix success rate	%	89.35	N/A	N/A
Dual receiver $\sigma_{code} = 1$ m	3D position error	m	0.1185	0.1940	0.2142
	Absolute heading error	deg	1.8666	2.8054	3.1071
	Absolute pitch error	deg	0.7824	1.2755	1.4552
	Fix success rate	%	94.69	N/A	N/A
Single receiver $\sigma_{code} = 2$ m	3D position error	m	0.1815	0.2672	0.2976
	Fix success rate	%	66.25	N/A	N/A
Dual receiver $\sigma_{code} = 2$ m	3D position error	m	0.1338	0.2095	0.2219
	Absolute heading error	deg	2.2210	3.2912	3.8163
	Absolute pitch error	deg	1.1442	1.9707	2.1213
	Fix success rate	%	79.66	N/A	N/A
Single receiver $\sigma_{code} = 10$ m	3D position error	m	0.3456	0.2886	0.5597
	Fix success rate	%	19.44	N/A	N/A
Dual receiver $\sigma_{code} = 10$ m	3D position error	m	0.1768	0.2584	0.4346
	Absolute heading error	deg	3.6595	4.7813	5.2577
	Absolute pitch error	deg	3.8268	6.3318	8.2472
	Fix success rate	%	24.98	N/A	N/A

Same as in the previous scenarios, Figure 5-19 and Figure 5-20 give the comparisons of several key parameters between the dual receiver array system and the single receiver system includes the 3D position error, the fix success rate, the absolute heading error, and the absolute pitch error.

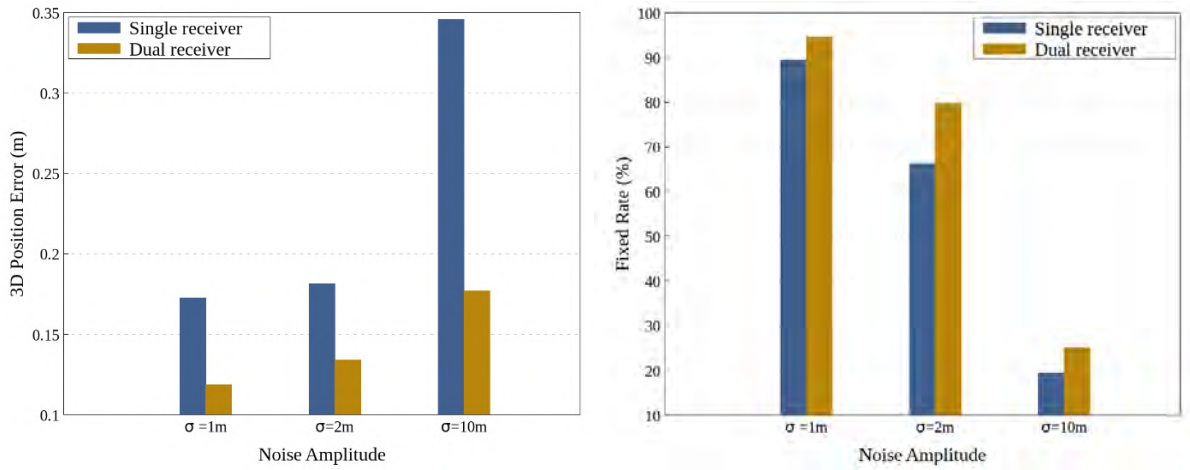

Figure 5-19 The comparisons of Position accuracy and fix success rate under different measurement noise

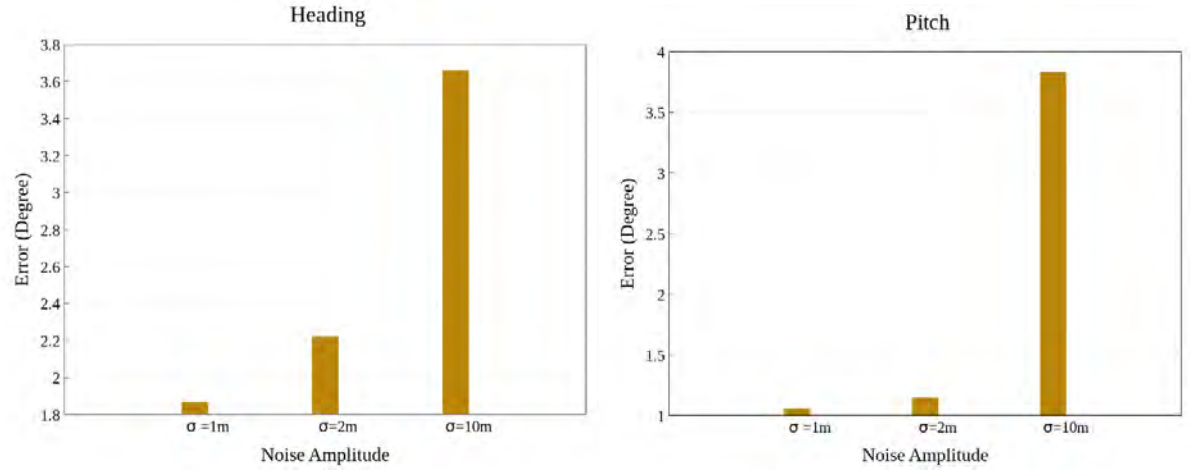

Figure 5-20 The comparisons of Heading and pitch estimates under different measurement noise

5.2.5. Correlation between Measurement Effect Analyses

In this thesis, we studied a multi-receiver RTK system. As the measurements are coming from signals received by the closely placed antennas from the array rover receivers, it is safe to consider a certain level of correlation between these noise measurements. For example, the multipath error may be similar in the measurements performed by the 2 closely mounted receivers from the same satellite. It is then interesting to conduct an analysis to study the effect of the correlation level between measurement from the rover receivers.

Therefore, in this section, the effect brought by this correlation parameter between measurements from the array pair receivers is presented. To do so, we need first define the correlation coefficient and then redefine the noise and related variance matrix model in the EFK to take the level of this correlation parameter into account in the state estimations.

5.2.5.1. Definition of the Correlation Coefficient in the Simulator and Modified EKF

Firstly, the covariance coefficient between the 2 receivers is given by

$$cov_{12}^{k} = \rho_{12}\sigma_1^k\sigma_2^k \tag{5-7}$$

Where:

- cov_{12}^{k} is the covariance of the noise affecting the measurement performed by receivers 1 and 2 on satellite k
- ρ_{12} is the correlation coefficient of the noise affecting the measurement performed by receivers 1 and 2, which is considered when generating the code and phase measurement
- σ_n^k is the standard deviation of the noise affecting the measurement performed by receiver n on satellite k

Similar to chapter 4, we consider a simplifying assumption that the noise standard deviation does not depend on the satellite or the receiver ($\sigma_n^k = \sigma$), and that the code measurement noise standard deviation and the phase measurement one are related by a simple factor $\sigma_{carrier} = k * \sigma_{code}$, with a value *k* equals 1/100 to account for the much better accuracy of carrier phase measurements. Taking into account the correlation between the measurements, the measurement covariance matrix $\mathbf{R}_{\mathrm{SD}}$ for the single difference measurements is no longer a diagonal matrix as shown in equations **(4-61,62)**, and will now have the following shape:

$$\mathbf{R}_{\mathrm{code,SD}} = 2 * \sigma_{code}^2 \begin{bmatrix} \mathbf{I}_{N_{sat}} & \rho_{12}\mathbf{I}_{N_{sat}} \\ \rho_{12}\mathbf{I}_{N_{sat}} & \mathbf{I}_{N_{sat}} \end{bmatrix} \tag{5-8}$$

$$\mathbf{R}_{\mathrm{carrier,SD}} = 2 * k^2 * \sigma_{code}^2 \begin{bmatrix} \mathbf{I}_{N_{sat}} & \rho_{12}\mathbf{I}_{N_{sat}} \\ \rho_{12}\mathbf{I}_{N_{sat}} & \mathbf{I}_{N_{sat}} \end{bmatrix} \tag{5-9}$$

The measurement covariance matrix $\mathbf{R}$ for the double-difference measurements can then be deduced using the following formula as described in chapter 4:

$$\mathbf{R} = \mathbf{D} \begin{bmatrix} \mathbf{R}_{\mathrm{code,SD}} & \mathbf{0}_{N_{sat}} \\ \mathbf{0}_{N_{sat}} & \mathbf{R}_{\mathrm{carrier,SD}} \end{bmatrix} \mathbf{D}^{\boldsymbol{T}} \tag{5-10}$$

Where $\mathbf{D}$ is the single-differencing matrix used for computing the double-difference.

5.2.5.2. Correlation Coefficient Impact Analysis

In probability theory and statistics, correlation (or correlation coefficient) is used as a measure of the linear correlation between two variables X and Y. The most widely used is the Pearson product-moment correlation coefficient (PPMCC). It is defined as the covariance of two variables divided by the standard deviation of the two variables as shown in (**5-11**):

$$\rho_{X,Y} = \frac{\mathrm{cov}(X,Y)}{\sigma_X \sigma_Y} = \frac{E[(X-\mu_X)(Y-\mu_Y)]}{\sigma_X \sigma_Y} \tag{5-11}$$

The significance of the magnitude of the correlation coefficient is currently inconsistent in the statistical world, but it is usually considered as follows:

Table 5-6 Significance of the magnitude of the correlation coefficient

0.00- ± 0.30 slightly correlated	± 0.30- ± 0.50 medium correlation
± 0.50- ± 0.80 significantly correlated	± 0.80- ± 1.00 highly correlated

As we discussed in the previous section, in our model, the measurements are coming from signals received by the closely placed GNSS receivers antennas, thus it is paramount to consider a certain level of correlation of these noise measurements to make it closer to the real situation.

Consequently, in this scenario, we want to verify what level of correlation is acceptable to keep an improvement compared to a single receiver RTK system. In this case, the correlation level of the noise measurement ρ_{12} is not fixed, several representative values in each interval in Table 5-6 are chosen to conduct the experiments while keeping the same noise measurement amplitude ($\sigma_{code} = 1$ m), the same geometry of the array of receivers ($l = 2$ m) and a favorable satellite geometry ($N_{sat} = 7$).

The different scenarios of the magnitude of the correlation coefficient are shown in Figure 5-21.

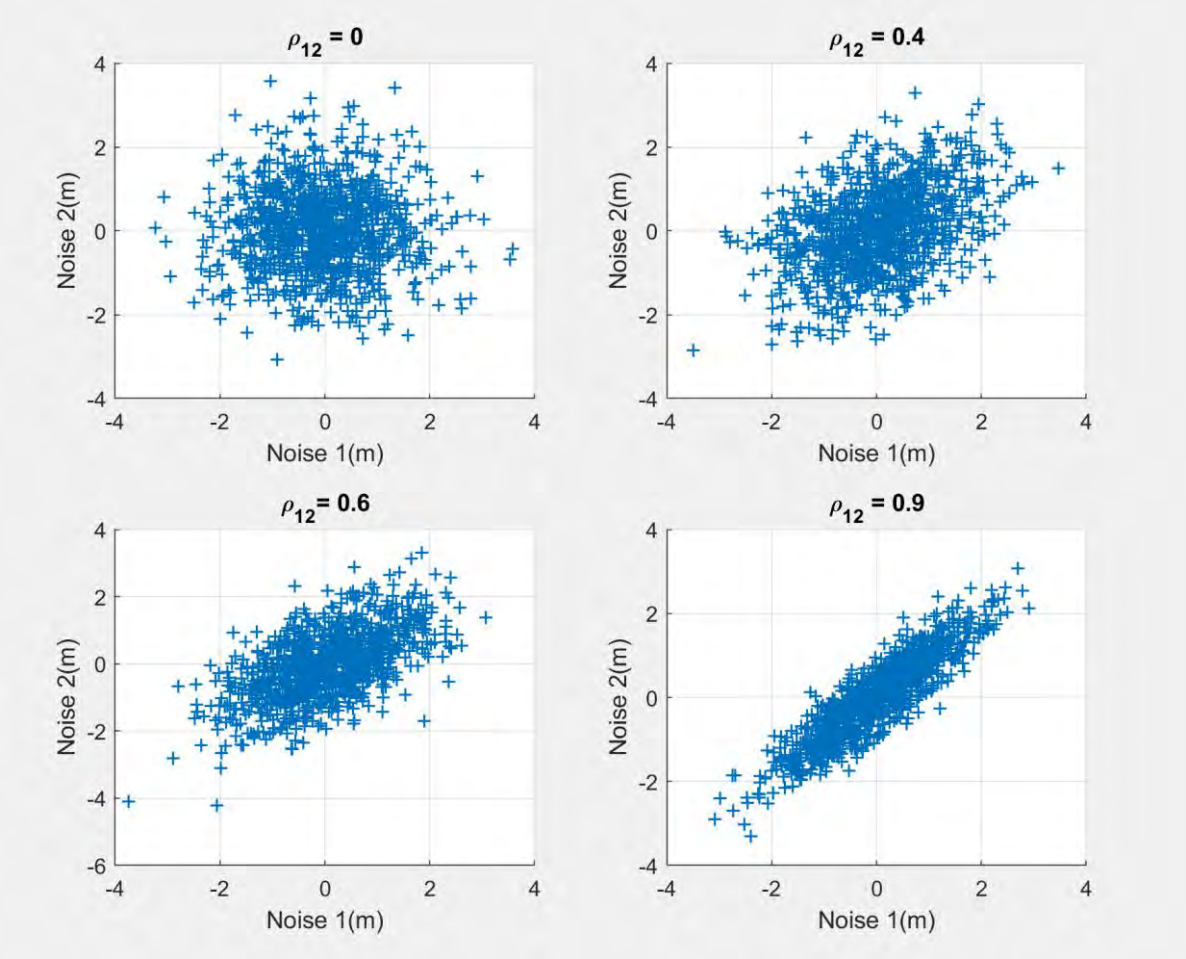

Figure 5-21 Considered Noise Correlation Distribution

The statistical results of each considered scenario are presented in Table 5-7, from the result one can conclude that the dual receiver RTK system provides always better performance than the single receiver RTK solution, even when dealing with highly correlated noise between the rover receivers.

Table 5-7 Performance comparison for different measurement noise correlation coefficient, σ_code=1 m, N_sat=7, l=2 m

Variation	Performance indicator	Unit	Mean	Standard deviation	95% bound
Single receiver	3D position error	m	0.1725	0.2591	0.3272
	Fix success rate	%	89.35	N/A	N/A
Dual receiver $\rho_{12} = 0$	3D position error	m	0.1185	0.1940	0.2142
	Absolute heading error	deg	1.8666	2.8054	3.1071
	Absolute pitch error	deg	0.7824	1.2755	1.4552
	Fix success rate	%	94.69	N/A	N/A
Dual receiver $\rho_{12} = 0.4$	3D position error	m	0.1198	0.1995	0.2185
	Absolute heading error	deg	1.9138	2.9238	3.1977
	Absolute pitch error	deg	0.7981	1.3255	1.4845
	Fix success rate	%	94.28	N/A	N/A
Dual receiver $\rho_{12} = 0.6$	3D position error	m	0.1213	0.2058	0.2284
	Absolute heading error	deg	1.9656	2.9879	3.2518
	Absolute pitch error	deg	0.8124	1.3855	1.5352
	Fix success rate	%	94.15	N/A	N/A
Dual receiver $\rho_{12} = 0.9$	3D position error	m	0.1252	0.2145	0.2325
	Absolute heading error	deg	2.0284	3.0854	3.3412
	Absolute pitch error	deg	0.8244	1.4754	1.6524
	Fix success rate	%	94.06	N/A	N/A

Furthermore, as we can notice from Figure 5-22, the positioning accuracy, as well as the heading and pitch estimation precision are slightly improved as the magnitude of the correlation coefficient decreases. In addition, one noticed that the fix success rate and positioning accuracy are not significantly reduced even under highly correlated noise situations, which proves that our system is exceedingly robust and stable when handling high correlation noise situations.

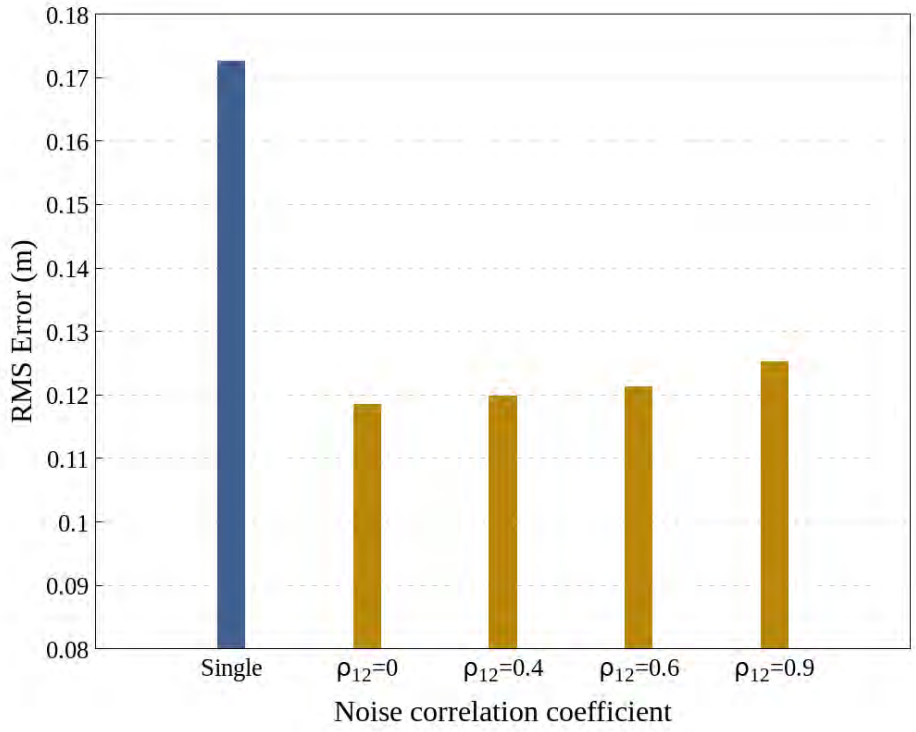

Figure 5-22 Performance comparison for different pre-defined correlation coefficient value

5.2.6. Conclusions

In this section, the proposed multi-receiver method is tested using the simulation data. All the simulation scenarios conducted in this thesis and their corresponding performance when compared to the traditional single receiver system are presented. Different scenarios are conducted including varying the distance between the 2 antennas of the receiver array, the satellite geometry condition, the amplitude of the noise measurement, and the correlation level between the measurement of rover receivers to verify the impact and potential benefits of the use of an array of receivers.

The simulations results show that our multi-receiver RTK system is more robust to noise and degraded satellite geometry, in terms of ambiguity fixing rate, and gets a better position accuracy under the same conditions when compared with the single receiver system. In addition, satisfactory vehicle attitude estimation accuracy can be obtained by using the proposed method. The result is quite favorable and demonstrates the interest of such an approach, the findings from this section have yielded one publication in [140].

5.3. Case study: Cycle Slip Detection Amelioration

As previously mentioned in Section 4.5, cycle slip (CS) detection and repair processes are necessary to maintain the continuity of carrier phase observations and to benefit from the precise GPS carrier phase observations for high-precision GPS positioning. This is especially true in urban areas, which complicates the process to resolve the carrier phase ambiguities.

The proposed multi-receiver EKF scheme assumes that the carrier phase measurements have a constant carrier phase ambiguity. However, it is well known that this does not necessarily hold for very long especially in an urban environment where frequent CSs occur. But assuming that a CS occurs at each epoch is detrimental to the PVT algorithm accuracy performance since it implies a constant re-estimation of the float ambiguity states without benefiting from their potential continuity. It is, however, the least risky. Consequently, it might be important to closely monitor the occurrence of CS continuously to follow the continuous-phase ambiguity model with confidence.

In this case study, we focus on the improvement of cycle slip detection and repair for RTK processing by using an array of two receivers with known geometry. Two types of single-frequency cycle slip detection processes are studied. The Standard Phase–Code Comparison method and the Differential Phases of Time Cycle Slip Resolution Method, which have been introduced in Section 4.4.

To take full advantage of the multi-receiver configuration, several assumptions need to be made in the simulator, a centralized Cycle Slip Detection method is utilized as introduced in Section 5.3.1.

5.3.1. Centralized Cycle Slips Detection Using an Array of Receiver

In our model, the cycle slips are simulated as correlated in both the receivers, with a correlation of 100% for the occurrence of simultaneous cycle slips on the same satellite. The reason that we chose this assumption is that here we consider that the cycle slip is due to an event external to the receiver, which is mostly the case in reality, such as an obstruction or severe multipath environment. In this case, there could be a strong correlation between the occurrence of cycle slips in the 2 receivers who are very close to each other. This means that if the cycle slip occurs on one receiver, then there is a great chance (100% in the simulated scenario) that it occurs for the other receiver, even though the amplitudes of the simultaneous cycle slips are not necessarily correlated.

So, in this section, a centralized cycle slips detection methodology is used. This means that there are 3 different possible situations:

- The algorithm detects that there is a cycle slip in both the receivers at a specific epoch: cycle slip validation and determination process are needed for both the receivers in this epoch.
- The algorithm detects that there is a cycle slip in one receiver at a specific epoch, while no cycle slips in another receiver: we consider there is also a cycle slip occurring in the other receiver at the same epoch. We then conduct the cycle slip validation, size determination process for both the receivers separately to validate and repair their own cycle slip.
- The algorithm detects no cycle slip in both the receivers at a specific epoch: no cycle slip validation process is needed.

In this situation, the use of observations from the two receivers of the array will double the chance to detect the possible small cycle slips, which can increase the probability of successful detection, so it is expected that an array of receivers can improve the performance of the cycle slip detector. However, there should also be an increase in the false alarm rate. This section aims at studying the benefits of such a centralized CS detection process.

5.3.2. Simulated Cycle Slips Configurations

During the observation period, m simulated cycle slips were manually added to the simulated data to test the cycle slip detection and repair process. For each satellite, the m cycle slips were consecutively added to its carrier phase measurements from their random given start epoch. The sizes of the cycle slips are predefined fixed values that depend on the ongoing scene.

Figure 5-23 gives an example of the distribution of the simulated cycle slip for each satellite during the simulation. The added cycle slips are depicted in the red cross as shown in the figure.

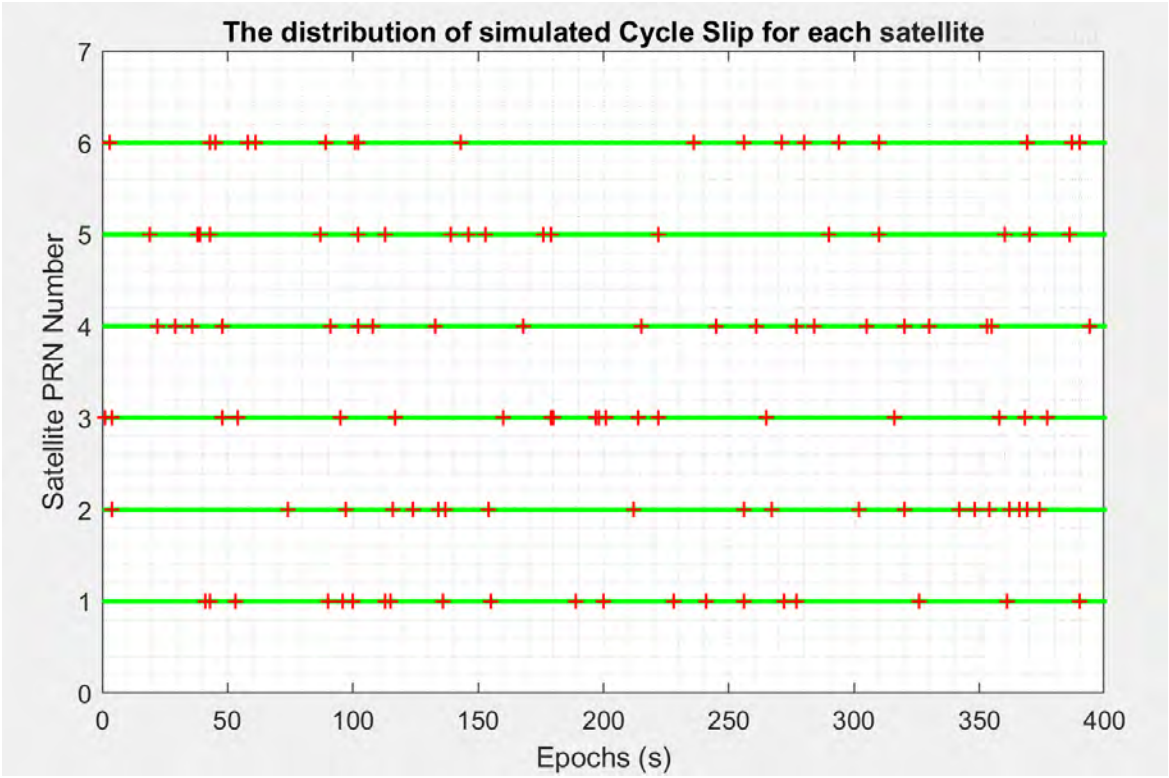

Figure 5-23 The distribution of simulated Cycle Slip for each satellite

5.3.3. Typical Results of the Cycle-Slips Detection Using Array Receiver System

To conduct the CS detection, both methods proposed in Section 4.5 need the raw GNSS measurement. Figure 5-24 shows our simulated code and carrier phase measurements on the L1 frequency with noise $\sigma_{phase} = 10\ mm$, $\sigma_{code} = 1\ m$ and a sampling interval of 1 s for PRN 03 based on a real almanac on February 04, 2020. Both carrier phase and pseudorange measurements are plotted versus time. The Carrier phase is multiplied by its wavelength to be presented in units of meters.

Ten cycle slips with the size of 1, 2, or 4 cycles have been added to the original L1 carrier phase observation of Figure 5-24 at the epoch instant of 100, 120, …, 280, respectively, as shown in Figure 5-25.

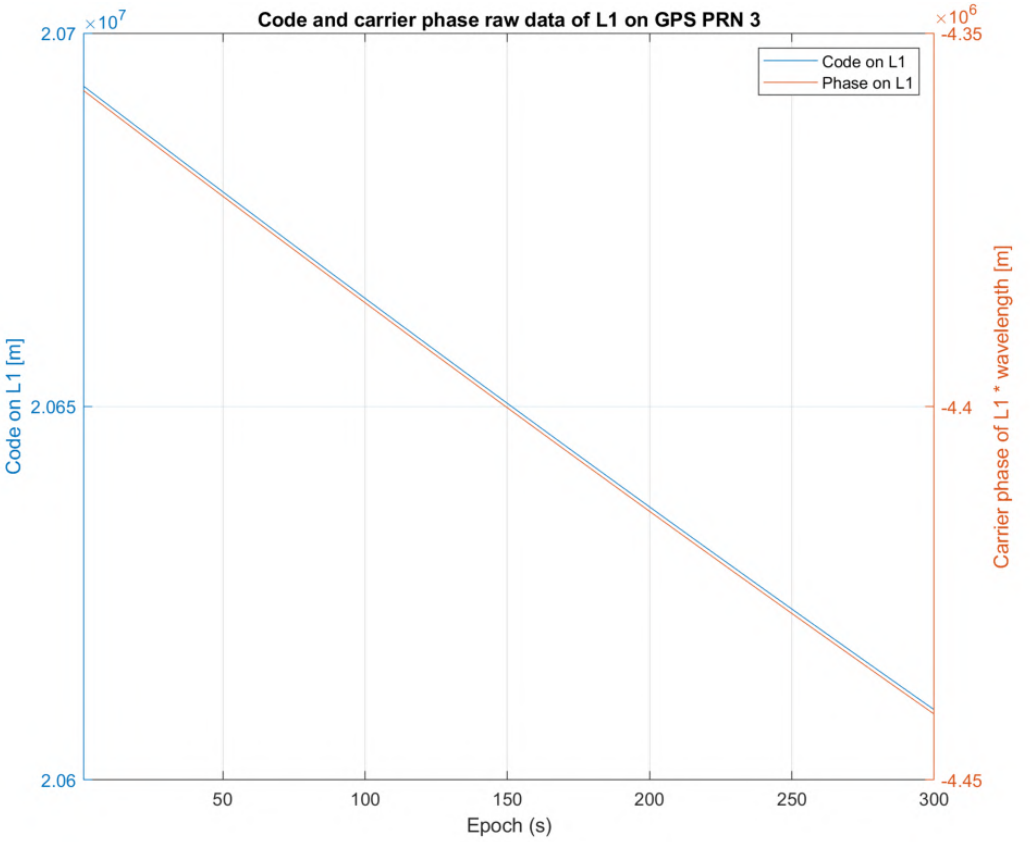

Figure 5-24 Simulated L1 code and carrier phase data

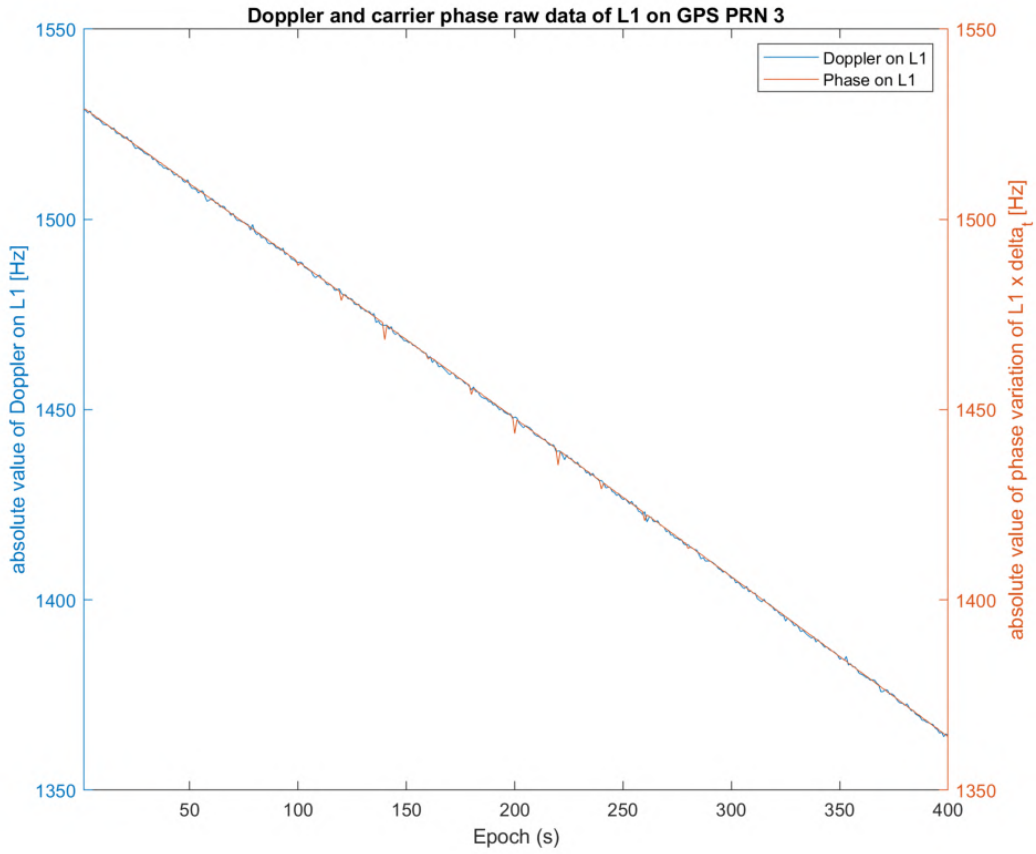

Figure 5-25 Simulated L1 carrier phase and doppler data with added cycle slips

The two proposed methods (Standard Phase–Code Comparison method and Differential Phases of Time Cycle Slip Resolution Method) are now applied to this data set.

5.3.3.1. Result of The Standard Phase–Code Comparison method

Figure 5-26 depicts the result of the Standard Phase–Code Comparison method, in the figure, the black point stands for the difference between the between-epoch phase variation and code variation, the green line is the threshold which is dependent on the code quality identified by the predefined σ_{phase} and σ_{code}, with significance level related coefficient $\alpha = 2$ to make the significance level equal to 0.05. Cycle slips that are successfully detected are marked with red stars, and cycle slips that are not successfully detected are marked with blue stars.

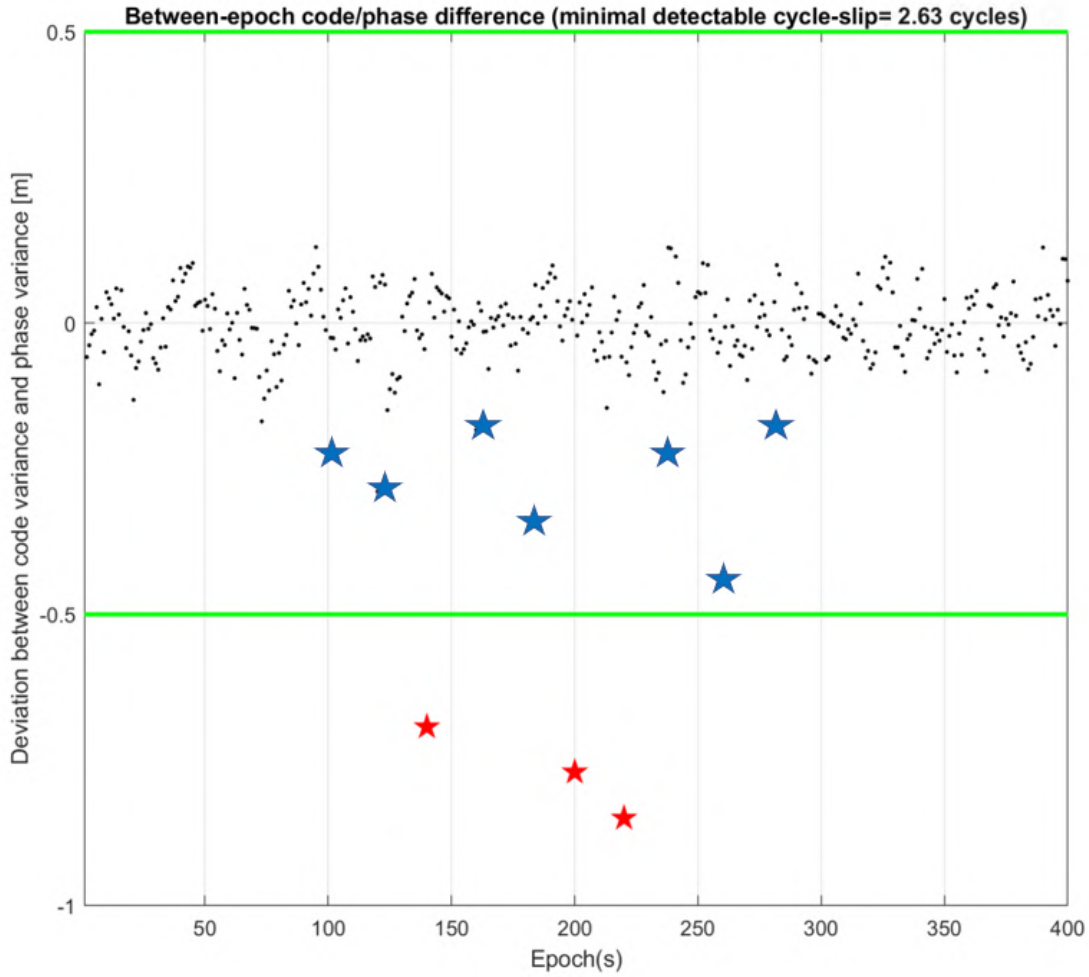

Figure 5-26 The result of the Standard Phase–Code Comparison method

Considering Figure 5-26, one can see that there are several outlier points (blue stars) that correspond to the added cycle slips. However, the difference is not big enough to pass the threshold thus these cycle slips are not detected successfully. Only the big cycle slips whose size is 4 are detected. In our case with the predefined standard deviation value of the phase and code noise, the minimal detectable cycle slip is 2.86 cycles which are too large to enable the detection of the small cycle slips.

5.3.3.2. Result of The Differential Phases of Time Cycle Slip Resolution Method

Unlike the first method, the Differential Phases of Time Cycle Slip Resolution Method shows its superiority in detecting the small cycle slips.

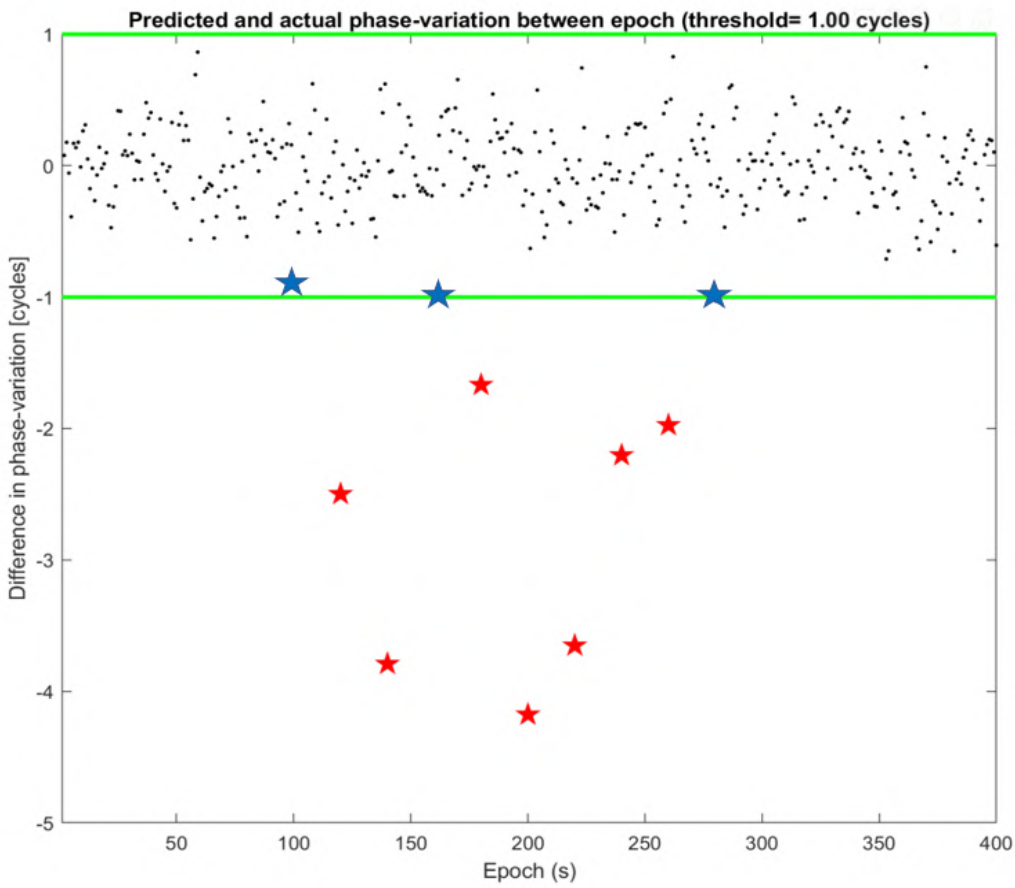

Figure 5-27 The result of the Differential Phases of Time Cycle Slip Detection Method

As can be seen in Figure 5-27, a large jump indicates a cycle slip, as shown by the red star. More added cycle slips are detected timely and accurately compared to the first method. Even though there are still some of the smaller cycle slips (size=1) are not detected, this method is much better than the first method. Due to the fact that the noise level of the code measurements is much higher than that of the phase, the Standard Phase–Code Comparison method can be used only for the detection of large cycle slips.

Thus, in the following part of this article, we will only present the CS detection result by using the Differential Phases of Time Cycle Slip Resolution Method.

5.3.4. Cycle Slip Detection and Related RTK Performance Using Array Receiver System

In our simulator, after detecting the occurrence of cycle slips, we applied the LAMBDA method to determine the integer cycle slip vector from the suspected cycle slips epochs then conduct the cycle-slip repair step to remove the cycle slips out of the associated phase measurements. In the case where LAMBDA does not provide a validated CS size, we keep the ambiguity without CS corrections.

In our RTK simulator, if the cycle slips are not correctly detected, a certain level of deviation with respect to CS-DR result for each satellite will be added in the corresponding DD carrier phase measurements to reflect this situation (because we directly use the DD measurements in the simulator), which will ultimately decrease the RTK positioning accuracy. It is thus interesting to know how the system performs under different cycle slips situations and the robustness of the proposed multi-receiver RTK system. The performance to detect the cycle slips by using the single frequency CS-DR method can be also assessed.

In the following sections, one will then analyze the CS-DR performance and the related RTK result of the dual receiver system and the single receiver system by conducting 3 different scenarios:

1) The noise measurement effect Analyses
2) Impact of the sizes of the added Cycle slips
3) Impact of the occurrence rate of the added Cycle slips

Same as before, the performance criteria shown in the presented tables are obtained by computing the mean, standard deviation, and 95% bound of indicators, based on the running of 100 Monte-Carlo simulations, where the noise and initial states are drawn randomly to remove the contingency of a single experiment. In addition, two specific metrics are defined to evaluate the performance of the cycle slip detection process:

a) **Mean number of correctly detected and repaired cycle slips:** After adding the same number of cycle slips to all considered satellites, this metric is defined as the average number of cycle slips that are successfully detected.

b) **Mean Corrected Rate:** It is defined as the average proportion of correct cycle slip alarms to the total number of added cycle slips for all the simulated satellites.

5.3.4.1. The noise measurement effect

The level of the noise measurement has a crucial influence on the estimation of the cycle slip detection metric which will decide whether there is a cycle slip or not, huge noise levels can mask the cycle slips and make the CS detector have a wrong judgment, thus it is a significant parameter that needs to be analyzed.

In the first scenario, the size and the occurrence rate of the added cycle slip are fixed, while varying the level of the noise measurement σ_{phase} (σ_{code} changes also by a ratio of 100), we observed the robustness against the noise of our proposed multi-receivers RTK system.

The analysis of Table 5-8 shows that the use of the receiver array improves the correctly CS-DR rate for all the bad noise level situations, thus demonstrating the advantage of such an approach in detecting the cycle slip.

Table 5-8 CS-DR Comparison with cycle slip (Size = 2), Mean NO.CS =20

System configuration	*No. of simulated CS*	*Mean No. of correctly detected and repaired cycle slips*	*Mean Corrected Rate*
Single receiver $\sigma_{phase} = 5$ mm	**20**	**20**	**100%**
Dual receiver $\sigma_{phase} = 5$ mm	**20**	**20**	**100%**
Single receiver $\sigma_{phase} = 20$ mm	**20**	**17.8**	**89%**
Dual receiver $\sigma_{phase} = 20$ mm	**20**	**18.5**	**92.5%**
Single receiver $\sigma_{phase} = 50$ mm	**20**	**9.5**	**42.5%**
Dual receiver $\sigma_{phase} = 50$ mm	**20**	**11.8**	**55.4%**

In terms of the RTK related parameters, an intuitive display of the results and is shown in Figure 5-28 and the detailed statistical result is presented in Table 5-9.

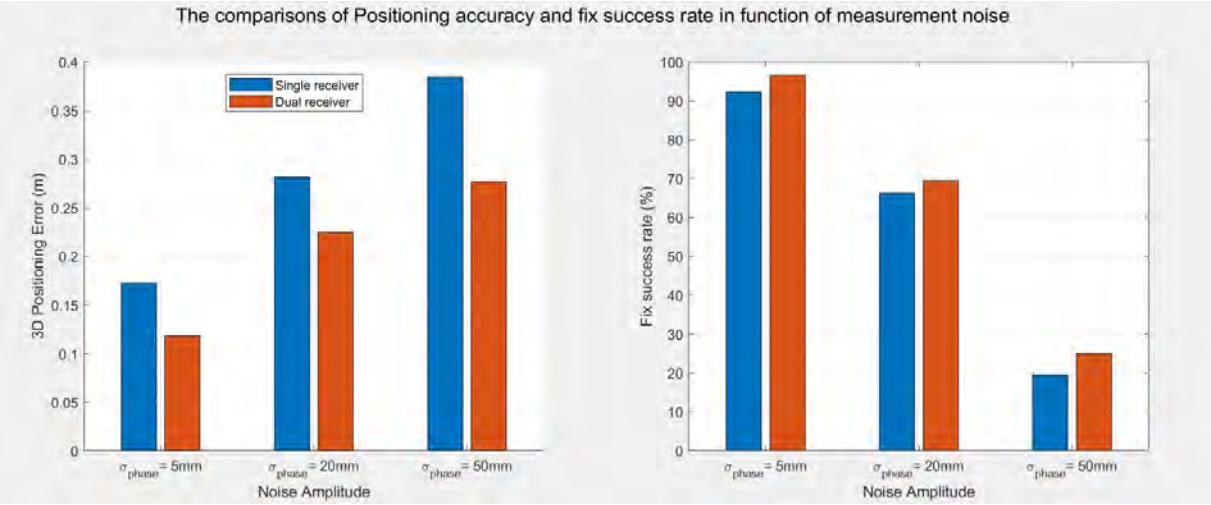

Figure 5-28 The comparisons of Position accuracy and fix success rate under different measurement noise (CS case study)

one can see from Table 5-9 that the undetected cycle slips deteriorate greatly the RTK positioning performances and the fix success rate has been reduced from 96.69% to 24.98% when the $\sigma_{phase} = 50$ mm. Still, one can find that the dual receiver array system provides better performance than the single receiver RTK solution in all situations, due to its measurement redundancy and also better CS-DR performance at this time, which is consistent with the previous results presented in Section 5.2.

Table 5-9 RTK Performance comparison for the different systems with cycle slip (Size = 2), Mean NO.CS =20

System	Terms	Unit	Mean	Std	95% bound
Single receiver $\sigma_{phase} = 5$ mm	3D error	m	0.1725	0.2591	0.2872
	Fix success rate	%	92.35	N/A	N/A
Dual receiver $\sigma_{phase} = 5$ mm	3D error	m	0.1185	0.1940	0.2318
	Fix success rate	%	96.69	N/A	N/A
Single receiver $\sigma_{phase} = 20$ mm	3D error	m	0.2815	0.4649	0.5716
	Fix success rate	%	66.25	N/A	N/A
Dual receiver $\sigma_{phase} = 20$ mm	3D error	m	0.2247	0.2876	0.3322
	Fix success rate	%	69.40	N/A	N/A
Single receiver $\sigma_{phase} = 50$ mm	3D error	m	0.3846	0.4824	0.8512
	Fix success rate	%	19.44	N/A	N/A
Dual receiver $\sigma_{phase} = 50$ mm	3D error	m	0.2768	0.3584	0.5577
	Fix success rate	%	24.98	N/A	N/A

5.3.4.2. *Impact of the size of the added Cycle slips*

Obviously, the smaller the size of the cycle slip, the more difficult it is to detect and repair it. In this second scenario, we analyze the impact of the size of the added cycle slips on the single receiver system and our proposed multi-receivers RTK system.

The result in Table 5-10 indicates that when the size of the cycle-slip is big enough, both the systems can perfectly detect and repair the cycle slips. While the multi-receiver system shows its advantage when dealing with the small-size cycle slip situation by using the proposed centralized cycle slip detection method.

Table 5-10 CS-DR Comparison with σ_{phase}=10 mm, Mean No.CS =20

System configuration	*No. of simulated CS*	*Mean No. of correctly detected and repaired cycle slips*	*Mean Corrected Rate*
Single receiver (CS Size = 1)	**20**	**13.5**	**67.5%**
Dual receiver (CS Size = 1)	**20**	**13.8**	**69%**
Single receiver (CS Size = 2)	**20**	**18.16**	**90.8%**
Dual receiver (CS Size = 2)	**20**	**18.83**	**94.1%**
Single receiver (CS Size = 4)	**20**	**20**	**100%**
Dual receiver (CS Size = 4)	**20**	**20**	**100%**

Figure 5-29 plots the performance comparisons between the single receiver system and dual receiver system after the conduction of corresponding CS detection algorithms, in terms of the positioning accuracy and fix success rate, for different added CS sizes.

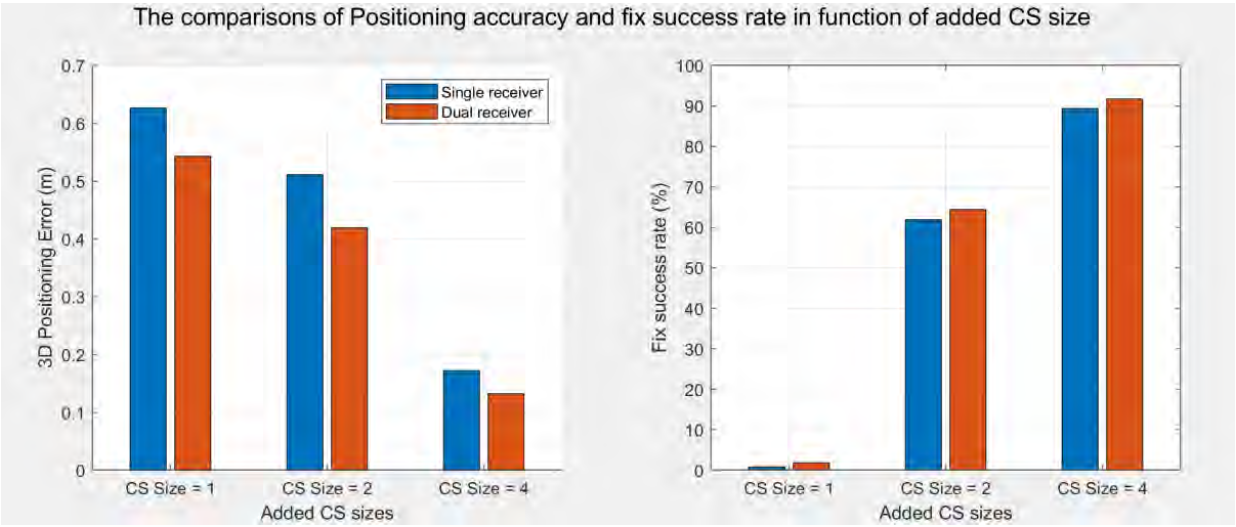

Figure 5-29 The comparisons of Positioning accuracy and fix success rate under different added CS size

One can see from the detailed result in Table 5-11 that, when the size of the added cycle slip is too small, our CS-DR cannot successfully remove all the cycle slips, thus the fixing rate of our RTK system drops sharply which has led to greatly increased inaccuracy in positioning as illustrated in Figure 5-29.

It should be pointed out that the accuracy and fix success rate difference between the two systems are not large, however, the dual receiver array always improves slightly the fixing rate which confirms the interest of our approach.

Table 5-11 RTK Performance comparison for the different systems with σ_{phase}=10 mm, Mean No.CS =20

System	Terms	Unit	Mean	Std	95% bound
Single receiver (CS Size = 1)	3D error	m	0.6264	0.5324	0.8812
	Fix success rate	%	0.82	N/A	N/A
Dual receiver (CS Size = 1)	3D error	m	0.5432	0.3618	0.6758
	Fix success rate	%	1.86	N/A	N/A
Single receiver (CS Size = 2)	3D error	m	0.5111	0.4649	0.6116
	Fix success rate	%	61.92	N/A	N/A
Dual receiver (CS Size = 2)	3D error	m	0.4194	0.2276	0.3322
	Fix success rate	%	64.40	N/A	N/A
Single receiver (CS Size = 4)	3D error	m	0.1725	0.2591	0.2872
	Fix success rate	%	89.35	N/A	N/A
Dual receiver (CS Size = 4)	3D error	m	0.1323	0.1546	0.1619
	Fix success rate	%	91.69	N/A	N/A

5.3.4.3. Impact of the occurrence rate of the added Cycle slips

The method that we utilize to detect the cycle slips is based on the previous observation of the raw measurement, a frequent appearance of cycle slips may make the detection process becomes more difficult.

So, in the third scenario, we wanted to see the performance when the two systems deal with the diverse occurrence rates of the added cycle slip, this is realized by adding the different numbers of the cycle slip during the same 400 s observation period.

Table 5-12 CS-DR Comparison with σ_{phase}=10 mm, Cycle slip (Size = 2)

System configuration	*No. of simulated CS*	*Mean No. of correctly detected and repaired cycle slips*	*Mean Corrected Rate*
Single receiver	**20**	**18.16**	**90.8%**
Dual receiver	**20**	**18.83**	**94.1%**
Single receiver	**40**	**36.72**	**91.8%**
Dual receiver	**40**	**37.56**	**93.9%**
Single receiver	**80**	**73.12**	**91.4%**
Dual receiver	**80**	**75.44**	**94.3%**

As follows from Table 5-12 shown above, the occurrence rate of the added cycle slips does not have much influence on the CS-DR success rate. The main reason is due to our detector works independently for each phase measurement, so it is reasonable to have such a result.

5.3.5. Conclusions

In this case study, we present a centralized cycle slip detection method that includes an array of receivers with known geometry to enhance the performance of the CS-DR process for RTK positioning in different environments.

From the simulations that have been carried out, it is possible to conclude that our multi-receiver centralized cycle slip detection method is more robust to cycle slips with lower amplitude or a higher level of the noise measurement in the data, in terms of percentage of epochs with integer cycle slip correctly detected and repaired. In fact, by taking advantage of the diverse data observations from an array of receivers with known geometry, the prediction accuracy of the differential phase in time is ameliorated, thus the occurrence of CS can be detected more accurately and timely.

Besides, consistent with the results in Section 5.2 for the RTK positioning, we always get a better positioning accuracy under the same conditions when compared with the single receiver system. Experimental tests confirm the gain obtained by employing the proposed approach for cycle slip detection and RTK robustness amelioration and the result obtained has been published in [141].

Based on this proof-of-concept, several future works for this case study are possible. Other types of CS-DR techniques could be tested, notably, those who would benefit from the improved accuracy of the receiver array solution, a more evident improvement can be expected by taking full advantage of the known geometry of the array receivers.

5.4. Case study: Multiple Receivers Connected to Same Antenna

The proposed multi-receiver architecture uses 2 GNSS receivers, but in fact, arrays with more than 2 receivers could also be assessed, as well as the consideration of several receivers connected to the same antenna (zero vehicle antenna baseline configuration).

In this case section, we will focus on one specific scenario which is the improvement of RTK processing by using an array of two single-frequency receivers with zero baseline constraint which can be realized by connecting the receivers to the same antenna. This can be considered as the extreme case of our proposed method, where the distance between the two rover receivers is zero (**zero baseline**).

The approach presented here aims at developing a method that takes full advantage of the measurement redundancy and diversity, along with the geometric constraints, between two closely placed rover receivers that share the same antenna to improve the accuracy of the float ambiguity estimation and, consequently, the AR success rate.

A similar analysis as in Section 5.2.5 is also conducted here. By varying the correlation coefficient of the noise between the measurements to the same satellite performed by the different receivers, we can verify the advantage of this zero-baseline multi-receiver system when dealing with highly correlated noise between multiple rover receivers.

In the following sections, the changes that brought the new zero-baseline multi-receiver algorithm compared to the normal architecture are firstly presented, including the modified EKF measurement model and modified states vector.

5.4.1. Modified Measurement Model

In this new zero-baseline multi-receiver system, the measurement vector comprises the same measured values as the normal proposed multi-receiver system: Double-difference (DD) code phase

measurement vector of receiver 1, DD code phase measurement vector of receiver 2, DD carrier phase measurement vector of receiver 1, and DD carrier phase measurement vector of receiver 2.

$$\mathbf{z}_n = [(\mathbf{P}_{10})^T \quad (\mathbf{P}_{20})^T \quad \lambda(\boldsymbol{\phi}_{10})^T \quad \lambda(\boldsymbol{\phi}_{20})^T]^T \tag{5-12}$$

However, in this measurement model, the position of receiver 2 is assumed to share the same position as receiver 1, as they are assumed to receiver the GNSS signal from the same antenna. The individual double-difference corrected pseudo-range and phase GPS measurement can then be modeled as:

$$P_{10}^{kl} = \left(\mathbf{e}^{kl}\right)^T \mathbf{b}_{10} + n_{P,10}^{kl} \tag{5-13}$$

$$P_{20}^{kl} = \left(\mathbf{e}^{kl}\right)^T \mathbf{b}_{10} + n_{P,20}^{kl} \tag{5-14}$$

$$\lambda\phi_{10}^{kl} = \left(\mathbf{e}^{kl}\right)^T \mathbf{b}_{10} + \lambda N_{10}^{kl} + n_{\phi,10}^{kl} \tag{5-15}$$

$$\lambda\phi_{20}^{kl} = \left(\mathbf{e}^{kl}\right)^T \mathbf{b}_{10} + \lambda N_{20}^{kl} + n_{\phi,20}^{kl} \tag{5-16}$$

5.4.2. Modified States Vector

The estimated parameters are collected inside the state vector. Considering the zero-baseline situation, the estimation of the attitude of the vehicle is no longer possible. In this case, the state vector collects 3 vehicle state parameters and 2*(N_{sat}− 1) satellite state parameters which are: the 3D position of GNSS receiver 1 relative to GNSS reference station 0, double-difference phase ambiguity of the GNSS receiver pair 1-0, and the double-difference phase ambiguity of the receiver pair 2-0. which is given by:

$$\mathbf{x} = [\mathbf{b}_{10}^T \quad \mathbf{N}_{10}^T \quad \mathbf{N}_{20}^T]^T \tag{5-17}$$

where:

$\mathbf{N}_{np}$ refers to the vector of the double-difference GPS integer ambiguity between receiver n and p

$\mathbf{b}_{10}^T$ refers to the relative position vector between reference station0 and rover receiver 1

And the corresponding process noise matrix $\mathbf{Q}$ is given as follows:

$$\mathbf{Q} = \begin{bmatrix} \mathbf{Q}_{10} & \mathbf{0}_{3\times(N_{sat}-1)} & \mathbf{0}_{3\times(N_{sat}-1)} \\ \mathbf{0}_{(N_{sat}-1)\times 3} & \mathbf{Q}_{amb} & \mathbf{0}_{N_{sat}-1} \\ \mathbf{0}_{(N_{sat}-1)\times 3} & \mathbf{0}_{N_{sat}-1} & \mathbf{Q}_{amb} \end{bmatrix} \tag{5-18}$$

where:

$\mathbf{Q}_{10}$ is the covariance matrix of the transition model for position-related state parameters

$\mathbf{Q}_{amb}$ is the covariance matrix of the transition model for satellite-related state parameters

5.4.3. Simulation Result of RTK Performances Using Multiple Rover Receivers Connected to the Same Antenna

Same as the previous sections, we keep the similar dynamic situation of the vehicle as described in Section 5.2. The vehicle is assumed to make a uniform circular motion around the fixed reference receiver 3 with a constant radius (R = 100 m) in all the scenarios. The speed of the vehicle is 10 m/s, the duration of the simulated trajectory is 1000s and the sampling rate is 1 Hz.

In our simulator, the satellites are simulated with a fixed position. We consider 7 satellites with a good geometric condition, i.e., well-spaced in azimuth and elevation. This would correspond to a typical case of a single constellation in an open sky environment. Finally, the DD carrier ambiguities are taken as fixed values separated by 10 cycles. This means that the DD ambiguities go from 10 to 120.

Typical results of the state estimations including the estimation of the integer ambiguity by using LAMBDA are given in Figure 5-30.

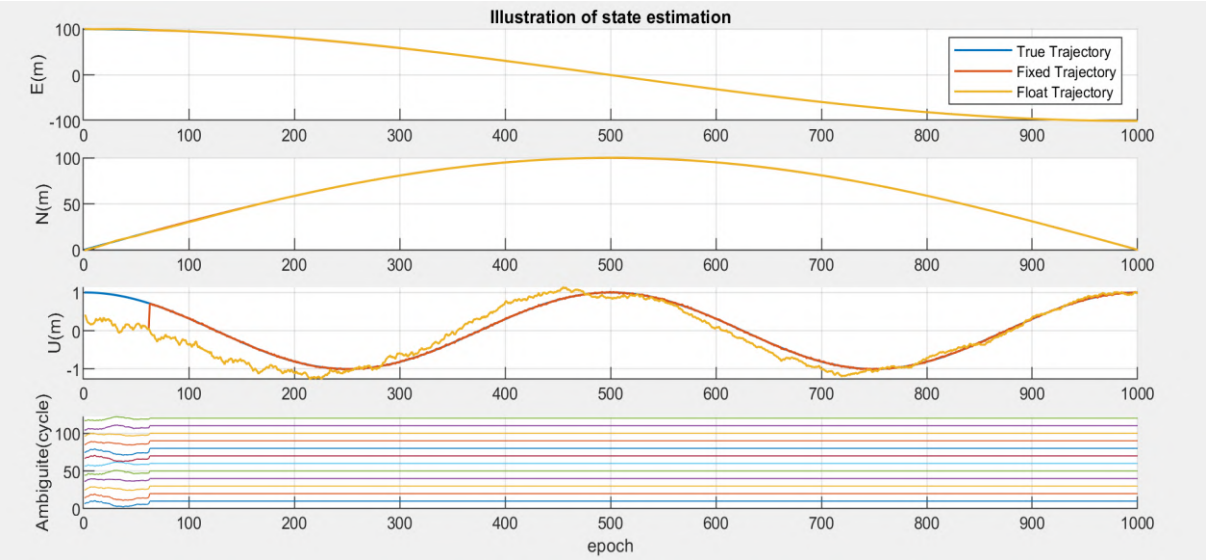

Figure 5-30 Illustration of state estimation including IAR (0 baseline)

Figure 5-31 gives the error comparison between the float and fixed solution.

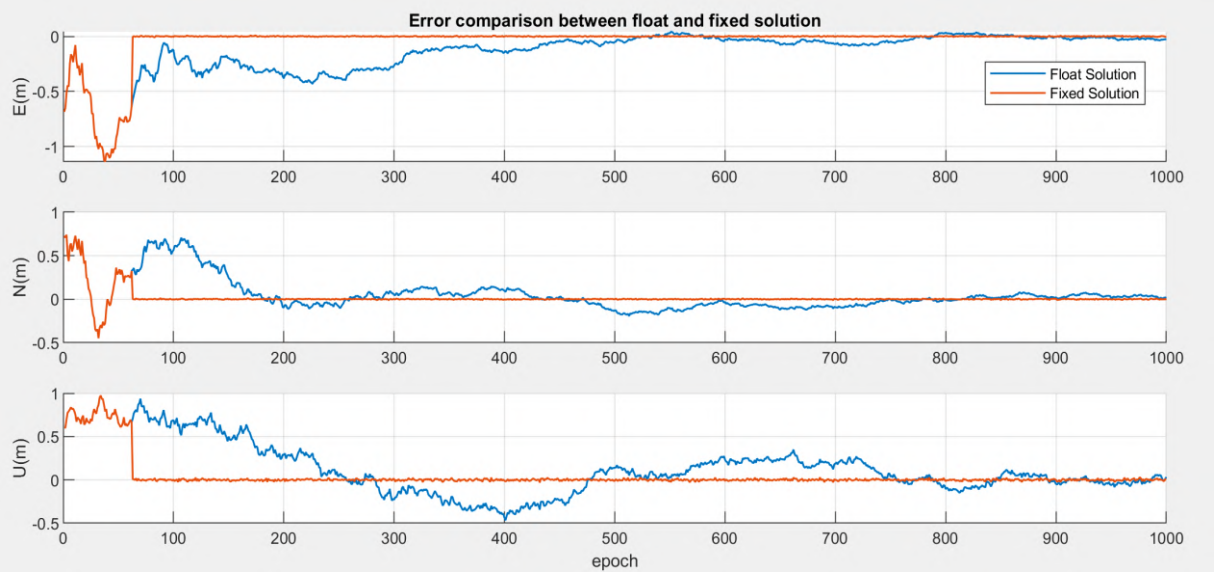

Figure 5-31 Illustration of float vs fixed solution (0 baseline)

We can see from Figure 5-31 that the same convergence period is present in all states for the fixed solution. In the case of the float solution, the East, North orientations converge rapidly to the true value, however, due to the observability issue, the altitude takes more time to converge. In addition, once they converge, the error between the estimated result and the true value is extremely small especially in the case of the fixed solution. From the figure, one can also notice that the system fixes

the IAR in the 64th epoch and once the IAR is fixed, the positioning results become much more accurate compared to the float solution.

Moreover, compared to the normal multi-receiver system, we found that the zero-baseline system converges more rapidly to the true value and the time to fix (TTF) of the integer ambiguities are much shorter. This result is not surprising, because the using of a zero-baseline configuration is an ideal situation. Compared with the previous model, we simply doubled the number of observations, and there are no new attitude-related states to be estimated, the number of states decreased compared to the normal multi-receiver model, making it easier to precisely resolve the float ambiguities and converge the Kalman filter.

To validate the influence of the using of an array of receivers with zero-baseline configuration, several scenarios which are similar to the Section 5.2 are conducted.

5.4.3.1. Geometry of satellite effect analyses

In the first scenario, we want to analyze the influence of the system when the geometry of the satellite changes. In this scenario, both the correlation level ($\rho_{12} = 0$) and the amplitude of the noise measurement ($\sigma_{code} = 1$ m) are fixed and by degrading the geometry of the satellite, we observe the robustness against degraded satellite geometry of multiple rover receivers RTK systems.

The results are shown in Table 5-13 and Figure 5-32 illustrates the comparison of the positioning accuracy and fix success rate under different satellite geometries.

Table 5-13 Performance comparison for different satellite geometry, ρ_12=0, σ_code=1 m

Variation of scenario 1	Performance indicator	Unit	Mean	Standard deviation	95% bound
Single receiver $N_{sat} = 7$	3D position error	m	0.1436	0.1975	0.2126
	Fix success rate	%	89.35	N/A	N/A
Dual receiver $N_{sat} = 7$	3D position error	m	0.0323	0.1634	0.1814
	Fix success rate	%	98.59	N/A	N/A
Single receiver $N_{sat} = 5$	3D position error	m	0.1839	0.2848	0.3148
	Fix success rate	%	72.43	N/A	N/A
Dual receiver $N_{sat} = 5$	3D position error	m	0.1431	0.2228	0.2526
	Fix success rate	%	85.21	N/A	N/A
Single receiver $N_{sat} = 4$	3D position error	m	0.6264	0.3324	0.4812
	Fix success rate	%	0.82	N/A	N/A
Dual receiver $N_{sat} = 4$	3D position error	m	0.3298	0.2881	0.3736
	Fix success rate	%	34.71	N/A	N/A

As we can notice from the result, under the same satellite geometry situation, the zero-baseline dual receiver model provides always better performance than the single receiver, for both the fix success rate and the RTK positioning accuracy, which confirms the advantage of this approach.

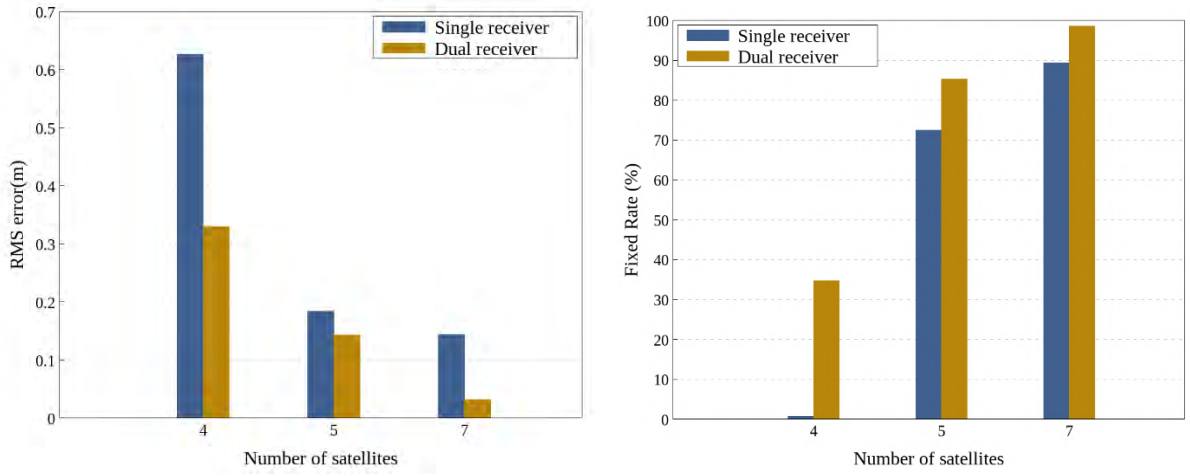

Figure 5-32 The comparisons of Position accuracy and fix success rate under different satellite geometries (0 baseline)

5.4.3.2. Noise measurement effect analyses

In the second scenario, the correlation level of the noise measurement ($\rho_{12} = 0$) and the satellite geometry ($N_{sat} = 7$) are fixed, by varying the amplitude of the noise measurement, we expected to be able to observe the robustness against the noise of the multi-receiver RTK system, and the results are shown in Table 5-14.

Table 5-14 Performance comparison for different measurement noise, ρ_12=0, N_sat=7

Variation of scenario 2	Performance indicator	Unit	Mean	Standard deviation	95% bound
Single receiver $\sigma_{code} = 1$ m	3D position error	m	0.1436	0.1975	0.2126
	Fix success rate	%	89.35	N/A	N/A
Dual receiver $\sigma_{code} = 1$ m	3D position error	m	0.0323	0.1634	0.1814
	Fix success rate	%	98.59	N/A	N/A
Single receiver $\sigma_{code} = 2$ m	3D position error	m	0.1815	0.2672	0.3176
	Fix success rate	%	66.25	N/A	N/A
Dual receiver $\sigma_{code} = 2$ m	3D position error	m	0.0678	0.1561	0.2145
	Fix success rate	%	83.61	N/A	N/A
Single receiver $\sigma_{code} = 10$ m	3D position error	m	0.4355	0.3584	0.8710
	Fix success rate	%	15.03	N/A	N/A
Dual receiver $\sigma_{code} = 10$ m	3D position error	m	0.2162	0.2287	0.4808
	Fix success rate	%	49.08	N/A	N/A

An intuitive results display of some important parameters includes the 3D position error and the fix success rate is shown in Figure 5-33. The analysis of the results shows that the use of the receiver array improves the success fix rate for all considered σ_{code} values, thus demonstrating the interest of such an approach for GNSS RTK positioning.

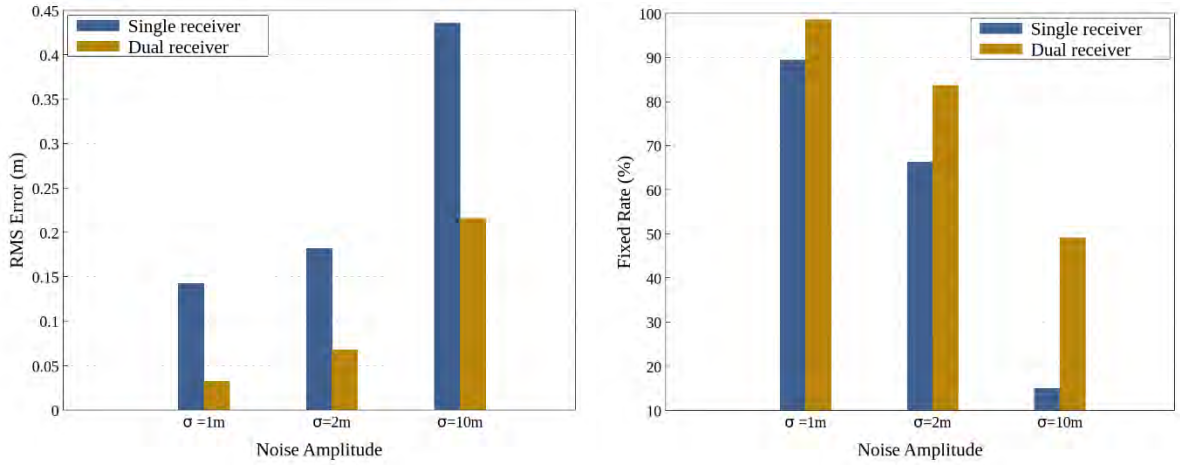

Figure 5-33 The comparisons of Position accuracy and fix success rate under different measurement noise (0 baseline)

5.4.3.3. Noise measurement correlation level effect analyses

As we introduced at the beginning of this section, in our zero-baseline model, the measurements are coming from signals received by the same antenna, thus it is paramount to consider a certain level of correlation of these noise measurements (e.g., multipath error) to make it closer to the real situation.

Consequently, in this scenario, we intended to verify what level of correlation is acceptable to keep an improvement compared to a single receiver RTK system. The correlation level of the noise measurement is not fixed, by varying the noise correlation coefficient while keeping the same noise measurement amplitude ($\sigma_{code} = 1$ m) and a favorable satellite geometry ($N_{sat} = 7$), the effect of the noise correlation level could be analyzed.

Figure 5-34 gives the illustration of the 3D position error and the success fixing rate results for the different pre-defined correlation coefficient values. The detailed statistical results are shown in Table 5-15.

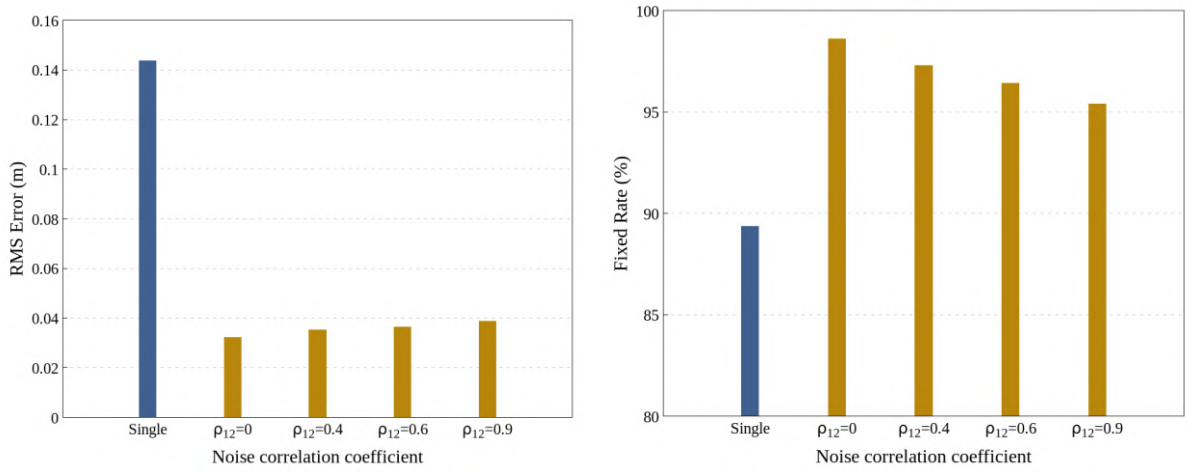

Figure 5-34 Performance comparison for different pre-defined correlation coefficient value (0 baseline)

Table 5-15 Performance comparison for different noise correlation level, σ_code=1 m, N_sat=7

Variation of scenario 3	Performance indicator	Unit	Mean	Standard deviation	95% bound
Single receiver	3D position error	m	0.1436	0.1975	0.2126
	Fix success rate	%	89.35	N/A	N/A
Dual receiver $\rho_{12} = 0$	3D position error	m	0.0323	0.1634	0.1814
	Fix success rate	%	98.59	N/A	N/A
Dual receiver $\rho_{12} = 0.4$	3D position error	m	0.0353	0.1822	0.1914
	Fix success rate	%	97.30	N/A	N/A
Dual receiver $\rho_{12} = 0.6$	3D position error	m	0.0365	0.1862	0.1925
	Fix success rate	%	96.40	N/A	N/A
Dual receiver $\rho_{12} = 0.9$	3D position error	m	0.0388	0.1930	0.1942
	Fix success rate	%	95.40	N/A	N/A
$\hat{\rho}_{12} = 0.4$ $\rho_{12} = 0.9$	3D position error	m	0.0392	0.1948	0.1945
	Fix success rate	%	95.30	N/A	N/A

From the detailed result shown in Table 5-15, one can conclude that the dual receiver RTK system provides always better performance than the single receiver RTK solution and the position accuracy sightly improves as the magnitude of the correlation coefficient decreases.

In addition, the fixing rate and positioning accuracy are not significantly reduced even when dealing with highly correlated noise, which proves that our system is exceedingly robust and stable when handling high correlation noise situations. The reason for this probably is that the LAMBDA algorithm takes into account the correlation of the measurements in the IAR process, which is assumed perfectly known in our EKF simulation.

For verifying the sensitivity of the LAMBDA algorithm to a correct correlation coefficient, a last set of simulations has been conducted, where the correlation coefficient considered in the algorithm is different from the one used to generate the measurement ($\hat{\rho}_{12} = 0.4$ for all the simulations), a similar result is obtained as shown in the last line of Table 5-15.

5.4.4. Conclusions

In this case study, the method using multiple receivers connected to the same antenna (zero-baseline configuration) for the RTK positioning in different environments is studied. Taking advantage of the doubled quantity of the observations while keeping the same number of estimated states, we are able to improve some internal steps of precise position computation.

We demonstrate through simulation results that our multi-receiver zero-baseline RTK system is more robust to noise and degraded satellite geometry and gets a better fix success rate as well as positioning accuracy under the same conditions when compared with the single receiver system. Furthermore, the mitigation of highly correlated noise between receivers is permitted by using our system.

An article [142] was published thanks to the obtained results of this case study.

5.5. Chapter Summary

To conclude, in this chapter, the proposed precise position and attitude determination algorithm has been tested and quantified through the experimental data set, to enable the conduction of several specific comparison scenarios between our multi-receiver system and the traditional single receiver system, and the results obtained have been presented.

Different scenarios are conducted including varying the distance between the 2 antennas of the receiver array, the satellite geometry, the amplitude, and the correlation level of the noise measurement to validate the influence of the using of an array of receivers.

The simulation results show that our multi-receiver RTK system is more robust to noise and degraded satellite geometry, in terms of ambiguity fix success rate, and gets a better position accuracy under the same conditions when compared with the single receiver system. Additionally, our method achieves a relatively accurate estimation of the attitude of the vehicle which provides additional information beyond the positioning.

Two specific cases study are also presented,

- Cycle Slip Detection and Repair Using an Array of Receivers with Known Geometry for RTK Positioning
- Improving reliability and efficiency of RTK ambiguity resolution using multiple rover receivers connected to the same antenna

Both studies result in interesting findings and have further strengthened our confidence in using the multi-receiver architecture for RTK positioning and attitude determination. Three publications [140]–[142] are yielded thanks to the interesting findings presented in this chapter. The positive results obtained from the simulation make us eager to use real data collections to verify and improve our multi-receiver model. In the next chapter, the concept will be tested against real conditions by setting up an experiment on a test vehicle.

Chapter 6. Real Data Tests and Results

In our preliminary experiments conducted in chapter 5, the proposed multi-receiver RTK precise positioning and attitude determination system has been tested on a simulator, by using the simulated DD code and carrier phase measurements derived from realistic mathematical models. The simulation results demonstrated that our multi-installed receiver RTK system is more robust to noise and degraded satellite geometry, in terms of ambiguity fix success rate, and gets a better position accuracy under the same conditions when compared with the single receiver RTK system. In addition, our method achieves a relatively accurate estimation of the attitude of the vehicle which provides additional information beyond the positioning. All the results obtained offered compelling evidence for the utility of the proposed multi-installed receiver system and encouraged us to use actual data to verify and further improve our proposed model.

In the current chapter, the algorithm will then be tested using real data. To reflect different environmental situations, 3 different GNSS raw observation data collections campaigns under various satellite visibility conditions are conducted in Toulouse, France. The environmental conditions of these 3 data collection scenarios are first reviewed, as well as the details about the data collection set-ups. The availability statistics of the GNSS measurements in different scenarios are also presented. In addition, it needs to be emphasized that all the data is collected by low-cost GNSS receivers

Finally, the performance of our proposed multi-installed receiver RTK navigation solution (position estimation and attitude determination accuracy) is then assessed based on the test results using the collected real GNSS data in all the considered environmental conditions. The impact of the distance between the 2 antennas of the installed receiver array and the advantage brought by the GPS/Galileo dual constellation are also analyzed and presented.

The structure of this chapter is as follows:

- Section 6.1 presents the hardware setup and the environmental conditions of the three data collections campaigns, as well as the measurements availability statistics of the reference equipment and rover receiver.
- Section 6.2 describes the investigation plan of this chapter and shows the measurements pre-processing results, including the implementation of the elevation mask, the innovation test, and the cycle-slip detection process. The correlation of the measurement errors affecting observations taken by the array receivers has also been investigated to tune the Kalman filter.
- Section 6.3 illustrates the experimental results using the real data. The results are compared between the single receiver RTK system and our proposed multi-installed receiver system, in terms of the fix success rate, horizontal positioning (east and north directions) error statistics (mean, standard deviation, and 50%, 95% bound), and array attitude error statistics for all 3 data collections.
- Section 6.4 finally summarizes the results obtained and further concludes this chapter.

6.1. Data Collection Presentation

Aiming at evaluating the performance of the proposed multi-installed receiver RTK positioning and attitude determination algorithm, three data campaigns have been collected. In this section, the equipment and the hardware set-up embedded in the test vehicle will be first presented, followed by descriptions of the three data collections scenarios.

6.1.1. Equipment Description

6.1.1.1. Data Collection Set-up Description

To investigate the feasibility of our proposed precise positioning and attitude determination algorithm, we set up a measurement campaign using 4 low-cost U-blox multi-band GNSS patch antennas, where each antenna is connected to a low-cost U-blox F9P GNSS receiver and are all mounted on the rooftop of the car. Measurements have been taken by recording the GPS/Galileo pseudo-range and carrier phase measurements simultaneously. Figure 6-1 presents the four U-blox GNSS receivers inside the equipped Citroën Jumpy car.

Figure 6-1 Illustration of the four U-blox GNSS receivers inside the vehicle

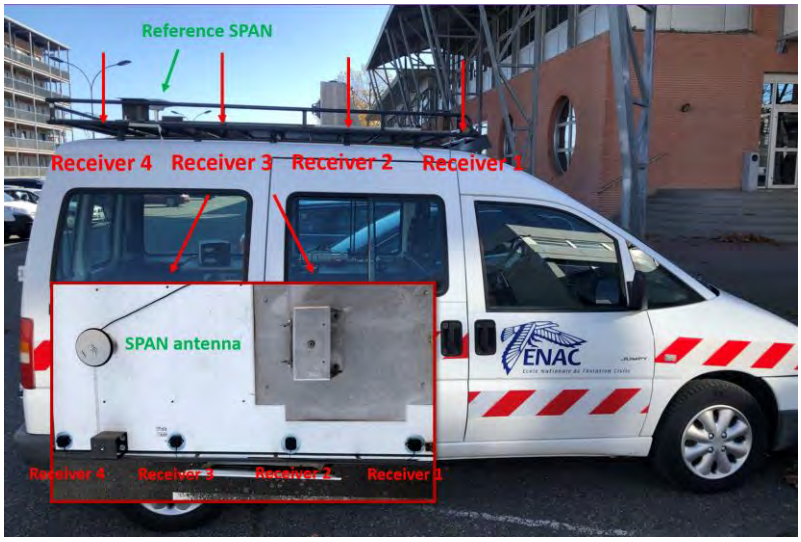

Figure 6-2: Real data collection set-up: 4 GNSS u-blox antennas and one Novatel SPAN Receiver on the car rooftop

To verify the impact of the rover baseline length on the estimation accuracy, we took measurements by putting the 4 patch antennas at various distances between each other, from 60 cm up to about 2.0 meters. Figure 6-2 shows a typical set-up of the GNSS antennas for one of the measurement sessions.

As we presented in chapter 4, according to Figure 4-2, any two GNSS antennas on the vehicle's rooftop define a $\mathbf{b}_{12}$ vehicle antenna baseline, which one can resolve for the pitch and heading attitude angles to get the vehicle's orientation. The $\mathbf{b}_{10}$ baseline spanned between one vehicle antenna and the VRS antenna, instead, is able to position the car relative to the VRS antenna. If the VRS antenna location is known, the absolute position of the car can be determined. In our case, one Septentrio AsteRx-U receiver 0 is mounted on the roof of a building as the reference station for RTK processing, whose position is static and known.

Finally, to provide the reference trajectories, the Novatel SPAN equipment is used, which is composed of a Hexagon|NovAtel ProPak6 multi-band GNSS receiver, a Novatel GPS-702-GG antenna, and an integrated tactical-grade IMU. A Northrop-Grumman inertial module with fiber optical gyroscope is also placed inside the vehicle. A multi-baseline post-processing RTK mode is used to calculate the reference trajectory. A picture of the vehicle roof where the SPAN antenna is placed can be viewed in Figure 6-2 and Figure 6-3 illustrates the SPAN receivers that are utilized during the data collection.

Figure 6-3 Illustration of the SPAN receiver used

In the next section, the detailed parameter information of all the hardware used for our data collection campaigns is summarized.

6.1.1.2. Mounted Hardware Parameters Description

To summarize, the measurement test was performed with a vehicle on which the following hardware was mounted:

- 4 U-blox (*www.ublox.com*) C099-F9P GNSS Receivers with 1 Hz data rate connected to its magnetic ANN-MB series multi-band patch antennas, as shown in the picture below. The 4 patch antennas are L1/L2 antennas, however, in our study, only the L1 band is utilized. They are mounted on the roof of a vehicle along its longitudinal axis as shown in Figure 6-2.

Figure 6-4 U-blox F9P GNSS Receivers (Left) and its magnetic ANN-MB series multi-band patch antenna (Right)

- 1 Septentrio (*www.septentrio.com*) AsteRx-U GNSS receiver with a Hexagon|Leica (*leica-geosystems.com*) AR20 choke ring antenna on the roof of a building as the base station for RTK processing.

Figure 6-5 Septentrio AsteRx-U GNSS receiver (Left) and the connected Hexagon|Leica AR20 choke ring antenna(Right)

- 1 Hexagon|NovAtel (*www.novatel.com*) ProPak6 SPAN GNSS receiver with tightly-coupled integrated tactical-grade IMU from Northrop-Grumman Litef Gmbh (UIMU-LCI). and a NovAtel Pinwheel GPS-702-GG dual-Frequency GPS+GLONASS Pinwheel Antenna, on multi-baseline post-processing RTK to give the reference position and attitude solution of the vehicle for error analysis.

Figure 6-6 NovAtel ProPak6 SPAN GNSS receiver the connected a NovAtel GPS-702-GG Pinwheel Antenna

6.1.1.3. Data collection scenarios

To test the performance of the proposed methodology under different environmental conditions and further verify its robustness in a highly constrained environment, we performed the data recordings in several different environments. As shown in Table 6-1, three data collections are processed in this study to consider all typical GNSS applications environments. This includes an urban environment, a suburban environment, and an open sky environment. The details of each data collection scenario are introduced in the following sections.

Table 6-1 Summary of data collects scenarios

Data ID	Description	Duration	Comment
1	A fixed point in the open sky	20 min	Mainly used for validation of the algorithm implementation. Only 2 receivers separated by 2 m
2	Car driving in a light urban environment	1 hour	4 receivers separated by [0.6, 1.3, 2.0] m
3	Car driving in a constrained urban environment	3 hours	4 receivers separated by [0.6, 1.3, 2.0] m

6.1.2. Presentation of the First Data Collection (Open-sky environment)

The first data collection campaign aims at providing the raw GNSS observations in an ideal GNSS-favorable environment (open sky environment) in a static case. This scenario is mainly used to validate the implementation of the proposed algorithm using real measurements and to give a reference of the performance of our multi-receiver system.

6.1.2.1. Rover Trajectory Description

To get an open-sky and stable environment, the first measurement session took place at the ENAC's (École Nationale de l'Aviation Civile) football field on October 20th, 2020, in Toulouse. As shown in Figure 6-7, the two receivers are static, and their positions are fixed on the football field with favorable satellite visibility. The rover baseline length between these two receivers is 2 m.

Figure 6-7 Receiver fixed position for dataset 1 (Google Map)

6.1.2.2. Reference Position Generation

For the first dataset, since it is in the open-sky environment and the receivers are on static mode, the RTKLIB [120], [143] program package, which has great performance in good signal condition, will be used in this dataset to provide reference positioning results. RTKLIB is an open-source software for standard and precise GNSS positioning (RTK and PPP) developed by Akio Yasuda and Tomoji Takasu in 2006 and constant refinements have been added since then. Thanks to the continuous update, it has become the most widely used tool to provide GNSS signal statistics or positioning results in the GNSS community. The version used in this study is the latest version 2.4.3 b34 that is released in 12/2020.

To get a relatively precise positioning result, the RTKPOST module with Kinematic model is utilized. In addition, the GPS/Galileo/GLONASS constellations are considered to have better satellite visibility. Considering the open sky dataset 1, more than 20 satellites can be guaranteed to be tracked at each epoch. The corresponding skyplot is shown in Figure 6-8:

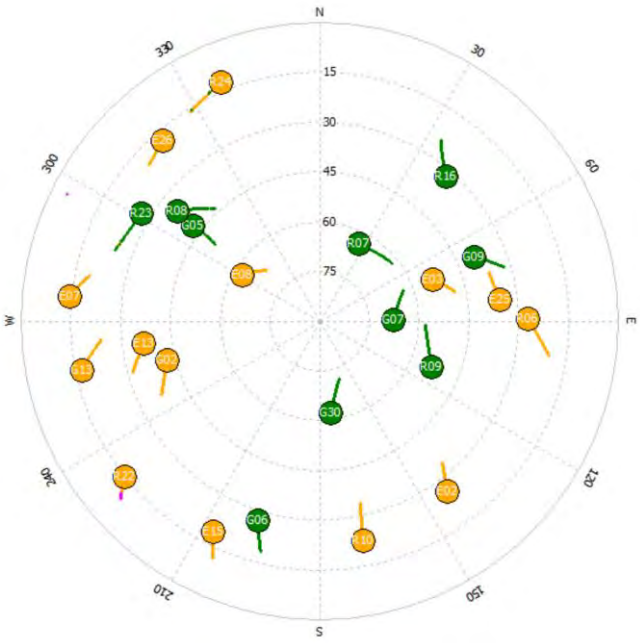

Figure 6-8 Skyplot in RTKLIB to calculate the reference position for Dataset 1

As for integer ambiguities resolution, a continuous ambiguity resolution mode is chosen so that ambiguities are considered constant when no cycle slip is detected. It matches the common knowledge on ambiguities. The embedded default algorithm for the IAR is the LAMBDA method and the validation test algorithm is the classic FT-RT (Fixed Threshold Ratio Test) with a default ratio threshold of 3. The default RTKLIB measurements weighting scheme stays unmodified. Figure 6-9 shows the estimation result of RTKLIB for dataset 1. With an almost 100% fix success rate, the result is reliable to be considered as the reference solution.

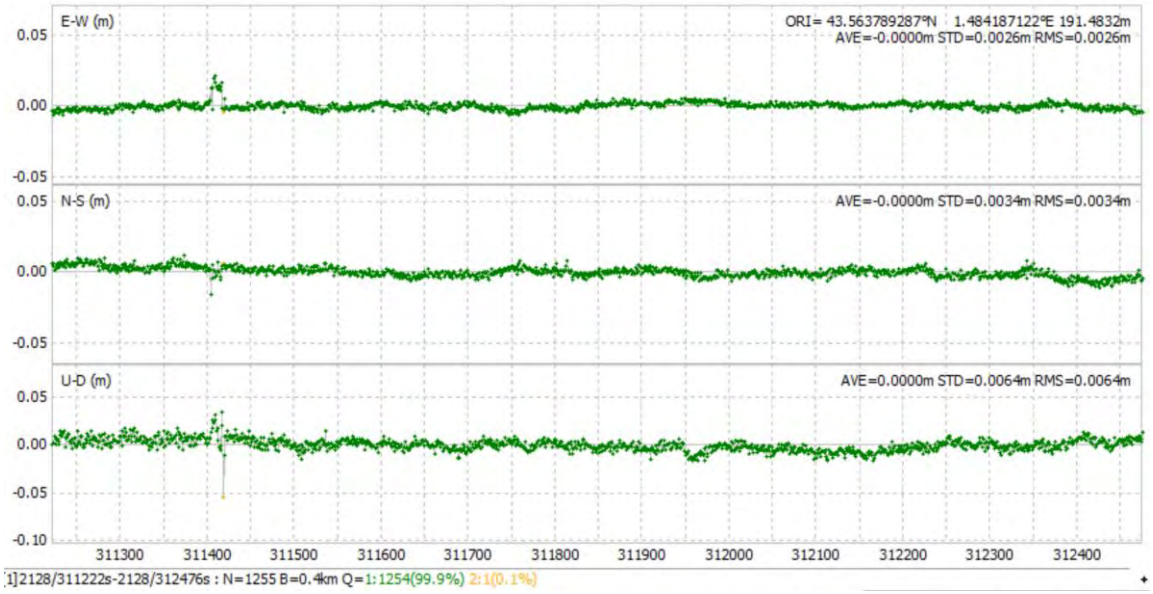

Figure 6-9 Estimation result of RTKLIB for dataset 1

6.1.2.3. GNSS Measurement Availability Statistics on Rover Side

In this part, the availability of the tracked GNSS L1/E1 measurements tracked by the low-cost rover receivers is also presented. The number of tracked GPS/Galileo satellites for the open-sky environment (dataset 1) is plotted in Figure 6-10. It should be noted that neither an elevation mask nor the innovation test is applied yet to filter the data. Unquestionably, some measurements should be disregarded or excluded for their low quality during the EKF process.

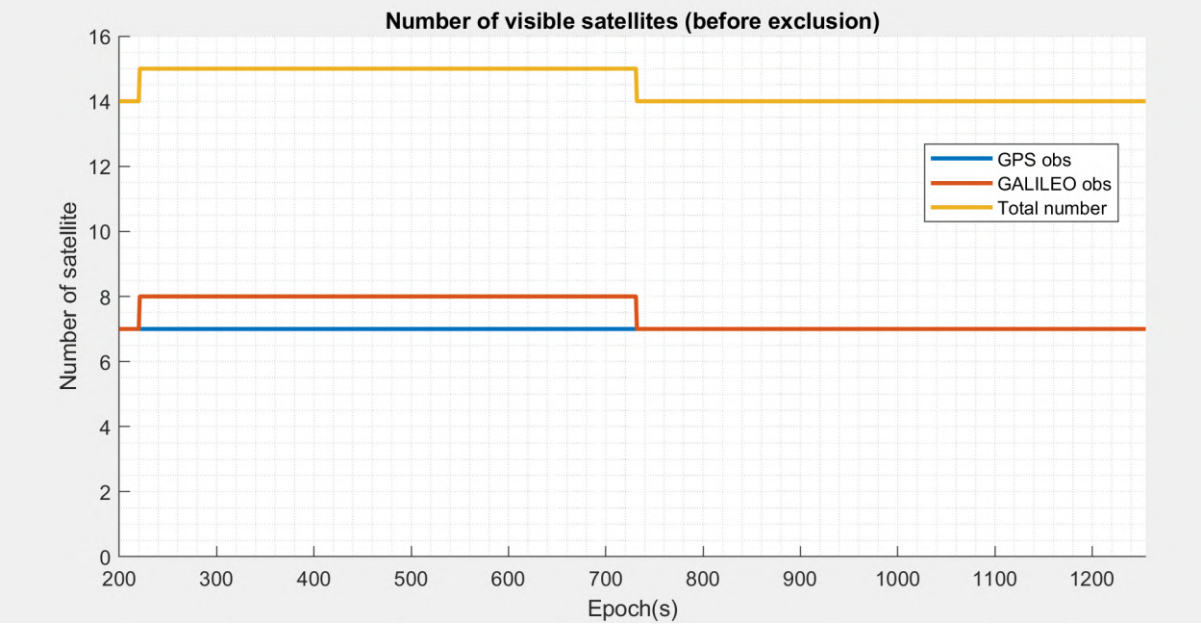

Figure 6-10 The number of visible (tracked) GPS/GALILEO satellites for the open-sky environment (dataset 1)

As we can see from the figure, in such an open-sky environment, even when only GPS is considered, at least 7 observables are available all along with the data collection. Additionally, when a dual constellation GPS/Galileo is considered, the minimum number of observations has increased to 14, which improves greatly the DOP of the satellites.

6.1.3. Presentation of the Second Data Collection (Suburban environment)

The second dataset is considered to assess the proposed method's performance for low-dynamic applications. Slowly moving vehicle navigating in a suburban environment with a few buildings is used to test the method in low-dynamic environments.

6.1.3.1. Rover Trajectory Description

To achieve the data collection in such a suburban environment, the second data campaign session took place at the ENAC premises, on November 18th, 2020, in Toulouse, France. The environmental condition in the campus is that there are lots of low-to-high buildings (between 1 and 5 stories) and trees, but with relatively good satellite visibility compared to the dense urban environment because the buildings are quite spaced and distant from the traveled road.

The vehicle moved at a relatively low speed from 0 to 20 km/h. The whole trajectory of dataset 2 is depicted in Figure 6-11, and Figure 6-12 shows the corresponding satellite visibility during this data collection.

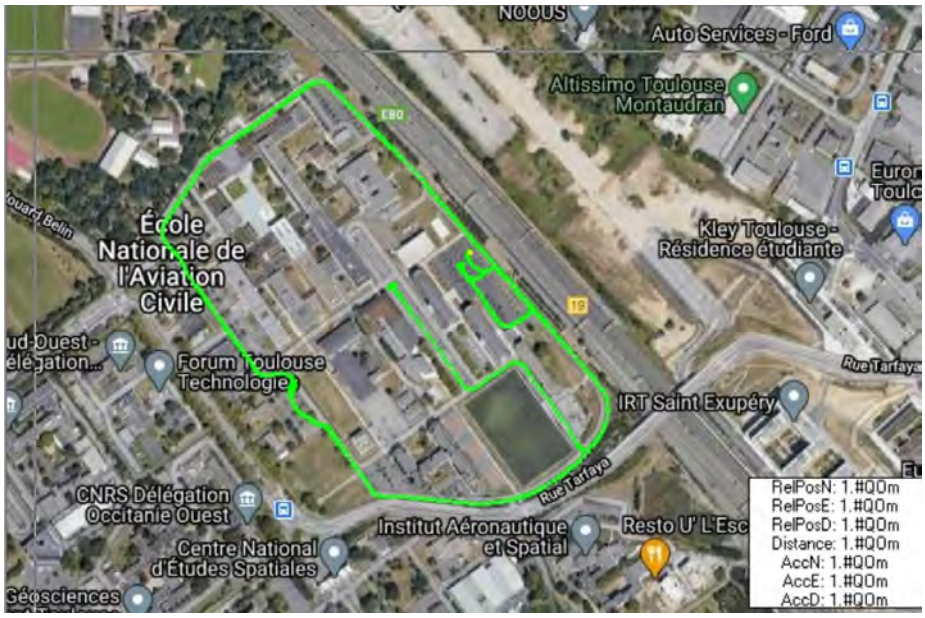

Figure 6-11 The whole trajectory (in green) of dataset 2 (Google Map)

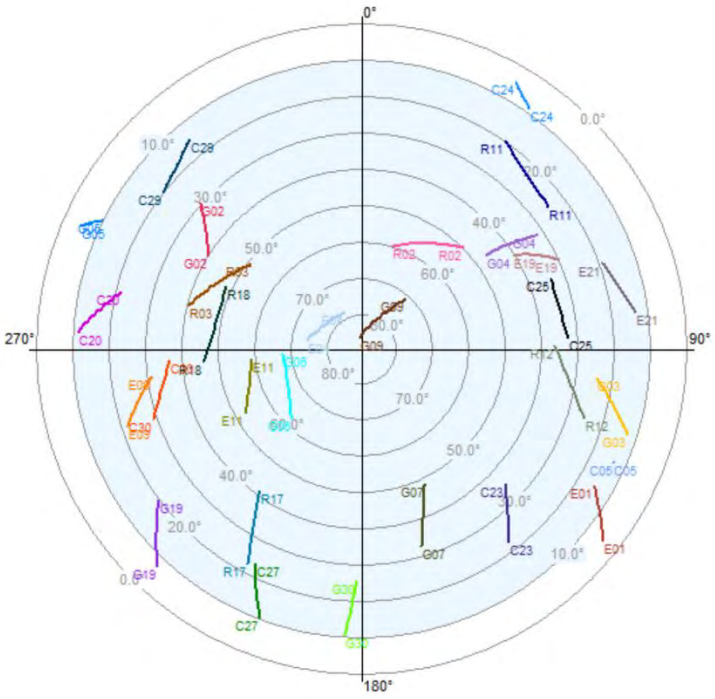

Figure 6-12 Corresponding satellite visibility during the data collection of dataset 2

6.1.3.2. *Reference Trajectory Generation*

As mentioned before, for error analysis, the reference position and vehicle attitude (heading and pitch angles) results are generated by the NovAtel SPAN system. This device consists of a ProPak6 receiver processing multi-frequency multi-constellation GNSS signals and a tactical grade IMU. The reference solution is computed in post-processing with the NovAtel Inertial Explorer 8.70 software.

The tightly coupled strategy is applied to combine multi-frequency GPS/GLONASS/Galileo and IMU data in forward and backward smoothed RTK mode with multi-station configuration. The base reference stations used are TLSE, TLIA, TLSG, and TLMF from the Reseau GNSS Permanent (RGP) network around Toulouse, whose locations are not far away from the studied trajectory.

The accuracy (estimated standard deviations) of the reference solution in the local ENU frame estimated by the NovAtel software is plotted in Figure 6-13:

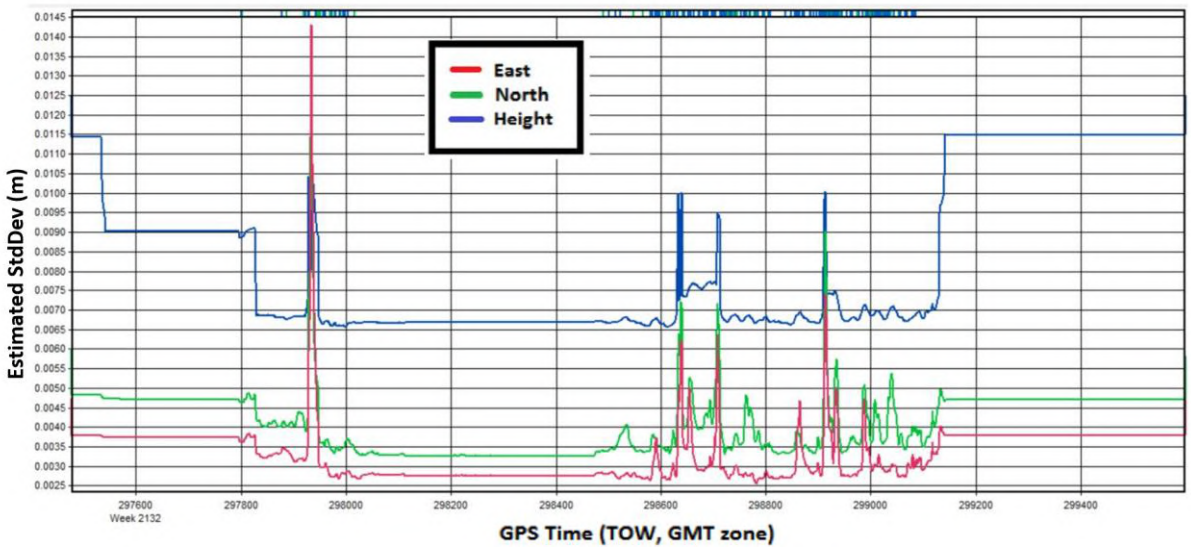

Figure 6-13 Estimated position standard deviation in ENU frame of the reference solution for dataset 2

It can be noticed that a centimeter-level accuracy can be globally guaranteed for all the 3 directions, which means that the integer ambiguities are successfully fixed. However, a few increases of the standard deviation exist which indicate the occasional signal blockages or a loss of tracking due to the buildings or trees. The number of tracked GPS/GLONASS/Galileo satellites seen by the SPAN system during the data collection is illustrated in Figure 6-14.

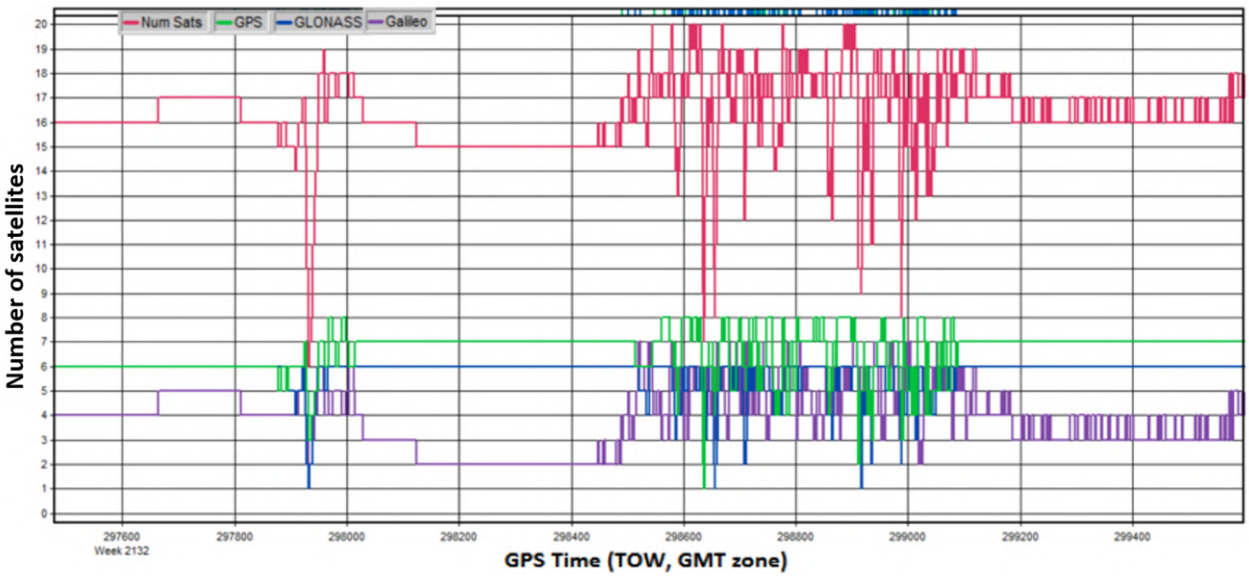

Figure 6-14 Number of tracked GPS/GLONASS/GALILEO satellites seen by the SPAN system for dataset 2

The reference attitude-related parameters (heading and pitch estimation) are also obtained, they are used in the attitude determination performance assessment of the proposed multi-receiver algorithm. The heading angle has a 0.1-degree level of accuracy while the pitch angle accuracy is in the order of 0.01-degree.

6.1.3.3. GNSS Measurement Availability Statistics on Rover Side

In this section, the availability of the tracked GNSS measurements viewed by the rover receiver is analyzed. The number of tracked GPS/Galileo satellites is plotted in Figure 6-15.

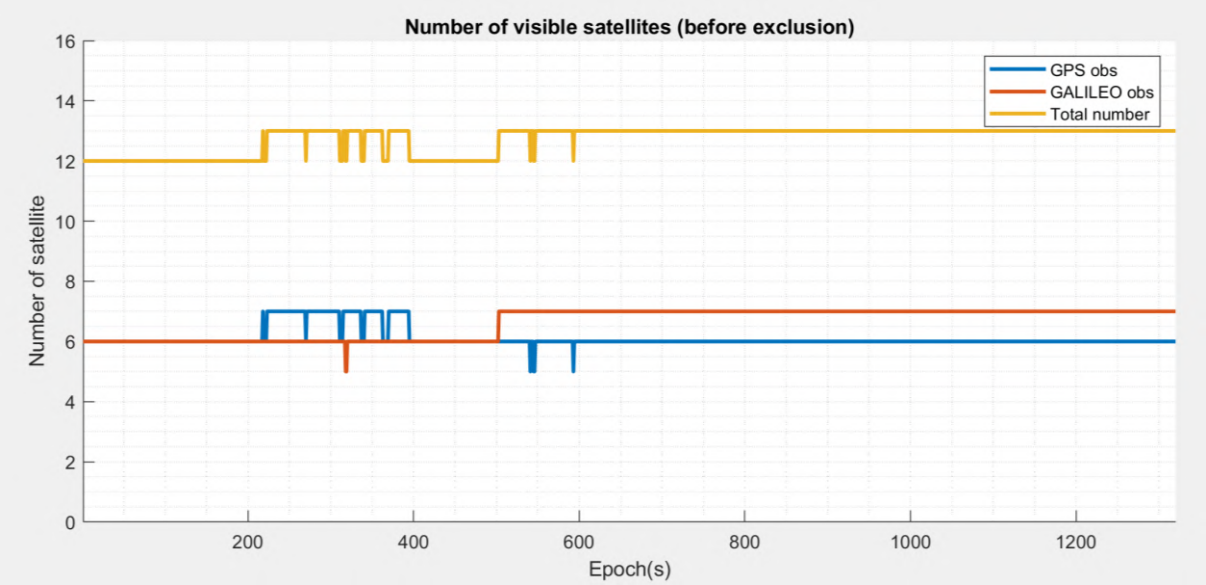

Figure 6-15 The number of visible (tracked) GPS/GALILEO satellites for the Suburban environment (dataset 2)

Here, similarly to dataset 1, neither an elevation mask nor the innovation test is applied yet to filter the data. Compared to the number of tracked satellites in the Novatel receiver's view, the high sensitivity of the u-blox rover receiver provides a higher number of available satellite measurements, especially for the Galileo constellation. However, part of the measurements should be excluded due to their low quality before conducting the EKF process.

Considering the number of observables, in such a suburban environment, more than 6 GPS satellites can be tracked most of the time, only on a few occasions the number of GPS satellites is less than 5. In addition, when the Galileo system is also considered, the total minimum number of observations has doubled to 12, which improves greatly the DOP of the system.

6.1.4. Presentation of the Third Data Collection (Urban environment)

The third data collection campaign is conducted aims at testing the performance and robustness of the proposed methodology when dealing with the most GNSS-challenging environment and high dynamic applications.

6.1.4.1. Rover Trajectory Description

To conduct the data collection in such an urban environment, the third measurement session was performed when the vehicle was driven from ENAC to the city center, on November 26th, 2020, in Toulouse, France. The speed of the vehicle varies from 0 to 50 km/h with frequent stops due to the traffic. Half part of the trajectory is when the vehicle was driven in the city center, and the vehicle is either along narrow roads with important buildings on both sides or on streets covered by trees.

In such a dense urban environment with frequent urban canyons and important building mask angles, the probability that the rover receiver measurements are affected by a very multipath and NLOS occurrence is extremely high. Figure 6-16 depicts two typical street-view pictures in the city center.

Figure 6-16 Example of the Urban environment during the collection of dataset 3. (Google Map)

The full trajectory in the Google Map of dataset 3 is illustrated in Figure 6-17, and Figure 6-18 shows the corresponding satellite visibility during this data collection.

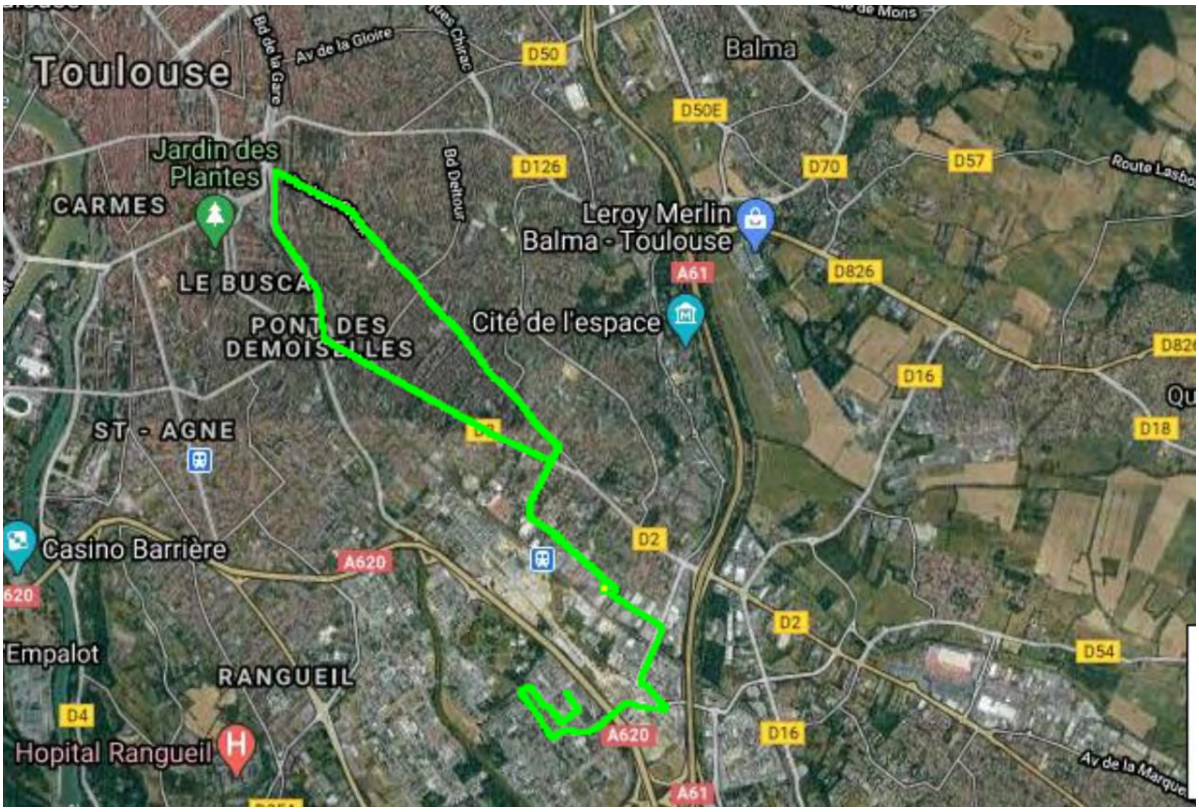

Figure 6-17 The whole trajectory (in green) of dataset 3 (Google Map)

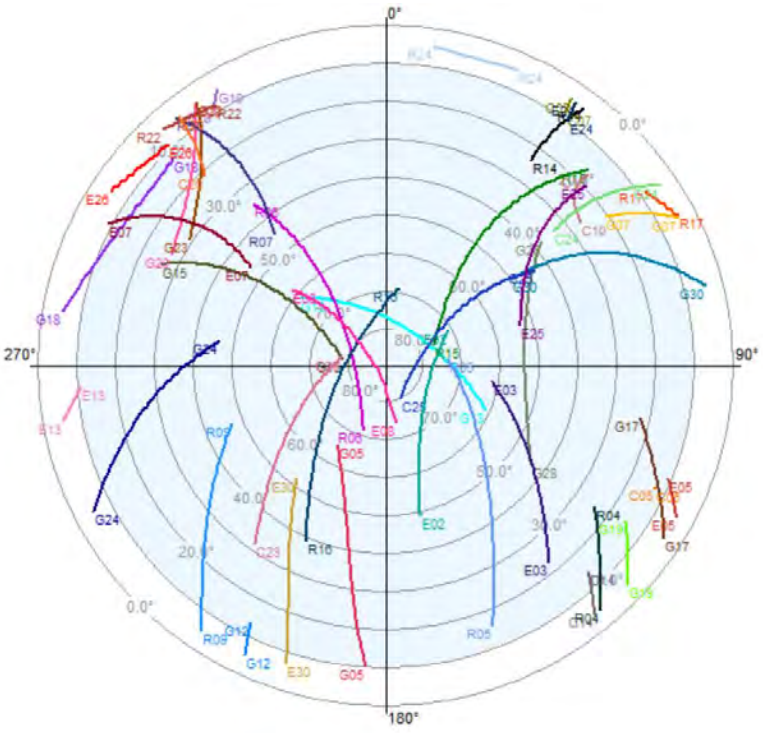

Figure 6-18 Corresponding satellite visibility during the data collection of dataset 3

6.1.4.2. Reference Trajectory Generation

Same as the previous dataset, the reference position, and vehicle attitude (heading and pitch angles) results are generated by the NovAtel SPAN system, and the reference solution is computed in post-processing in forward and backward smoothed RTK mode with the NovAtel Inertial Explorer 8.70 software. The tightly coupled strategy is implemented to combine the multi-frequency GPS/GLONASS/Galileo/BeiDou and IMU data in the RTK with a multi-station configuration. The base reference stations used are the same as the dataset 2.

The accuracy (estimated standard deviations) of the reference solution for dataset 3 in the local ENU frame estimated by the NovAtel software is plotted in Figure 6-19:

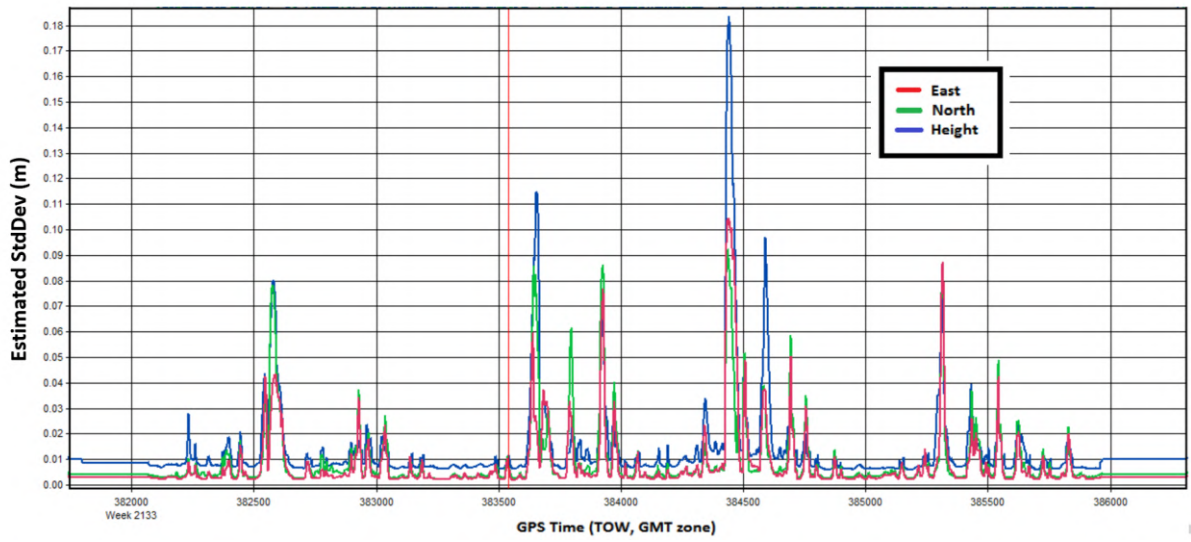

Figure 6-19 Estimated position standard deviation in ENU frame of the reference solution for dataset 3

From the illustration above we can notice that, due to severe signal blockages experienced during the third measurement campaign in the city center, the reference trajectory cannot be expected to be always at centimeter-level, even in post-processing mode. The reference position has decimeter level uncertainty, up to 0.2 m in the worst case, as computed by the NovAtel SPAN equipment. Deduced from Figure 6-19, ambiguities are even rarely fixed with the dual-frequency Novatel Span module in a post-processing mode when the vehicle is in the city center.

Indeed, compared to dataset 2, a much denser urban environment was experienced during dataset 3, and severer signal masking was expected. The bad GNSS condition is also reflected in the number of available satellites tracked by the Novatel set, referring to Figure 5-10. Even four GNSS constellations are considered, the total number of satellites can be less than 5 in some epochs.

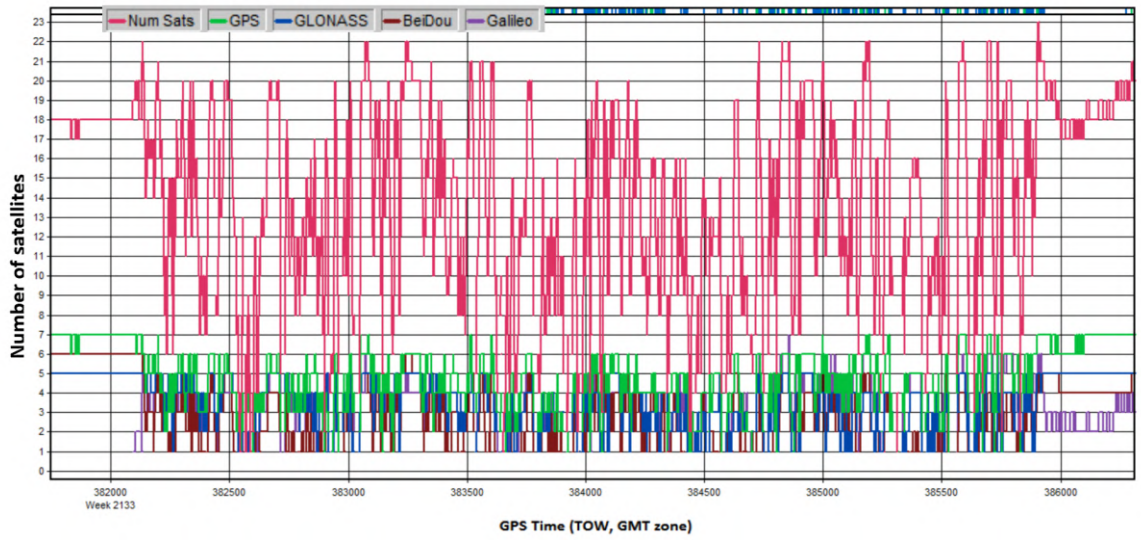

Figure 6-20 Number of tracked GPS/GLONASS/GALILEO/BEIDOU satellites seen by the SPAN system for dataset 3

Furthermore, the reference attitude-related parameters (heading and pitch estimation) are also obtained, they are used to assess the performance of the attitude determination of the proposed multi-receiver algorithm. For dataset 3, The accuracy of attitude-related estimators is also reduced due to the bad signal quality. The heading angle has a 1-degree level of accuracy while the pitch angle accuracy is in the order of 0.2-degree as shown in Figure 6-21:

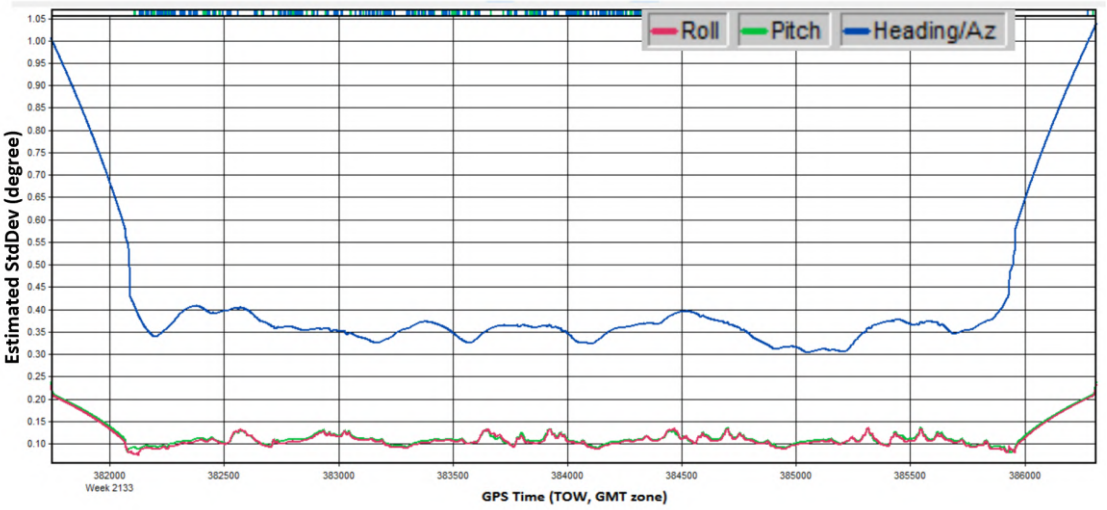

Figure 6-21 Estimated attitude-related estimators' standard deviation of the reference solution for dataset 3

6.1.4.3. GNSS Measurement Availability Statistics

As for the availability of the tracked GNSS measurements viewed by the rover receiver, the number of tracked GPS/GALILEO satellites is illustrated in Figure 6-22:

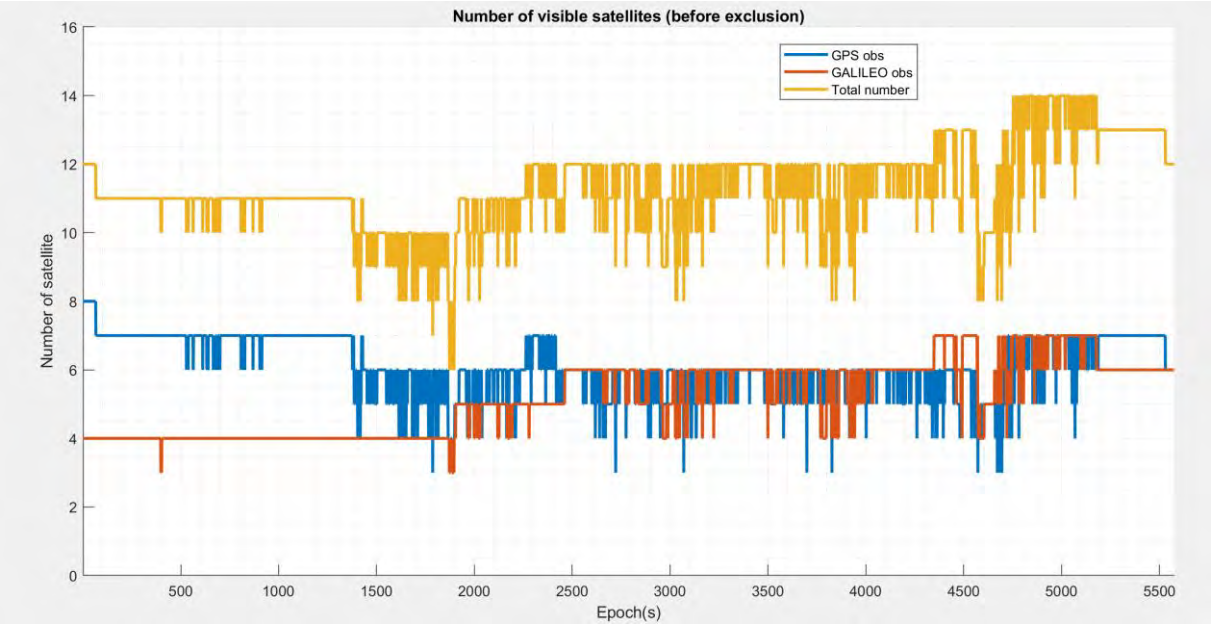

Figure 6-22 The number of visible (tracked) GPS/GALILEO satellites for the Urban environment (dataset 3)

As we can notice, when only GPS is considered, in dataset 3 which is a more challenging environment for the GNSS, the percentage of having at least 5, or 6 tracked satellites is on a severe decrease compared to the previous datasets. Especially in a more complex environment like the city center, the number of satellites will be less than 3 during some epochs. It should also be noted that if we remove low-quality signals tracked from low-elevation satellites, this number will still decrease, it can thus frequently drop to very low values due to frequent bridges or buildings in the city center.

To improve the GNSS measurement availability especially in the city center, the Galileo constellation is considered. The advantage of considering the Galileo constellation is very clear as shown in Figure 6-22. It almost doubles the total number of available satellites at each epoch and therefore can significantly improve the measurements availability statistics in all the considered environments.

6.2. Investigation Plan and Signal Pre-processing Results

To evaluate the advantage brought by the proposed novel methodology, an investigation and analysis plan should be defined. Therefore, in this section, the investigation plan to analyze the performance of the proposed multi-receiver RTK algorithm using real data is first introduced.

In addition, to tune and ameliorate the performance of the EKF, before the state estimation step in the EKF, some signal pre-processing steps are conducted either to improve the signal quality by detecting and eliminating measurement outliers (Elevation mask, Innovation test, Cycle-slip detection and repair, etc.) or to get some specific EKF tuning parameters (The analyze of the correlation of measurement error in the measurements collected by the array receivers). The results of these steps are then also presented in this section.

6.2.1. Investigation Plan

Thanks to the diversity of the data collection, the datasets we collected as presented in Section 6.1 allow us to investigate a certain number of results that were obtained through simulations in Chapter 5 and previous papers [140]–[142], and some more. Our data collection set-up allows to vary the distance between the 2 rover antennas, named array baseline length in the rest of the thesis, as well as the type of environment. In the following sections, the impact of these 2 parameters (array baseline and type of environment) will be addressed for the following 3 points:

- Correlation of measurement error in the measurements collected by an array of receivers
- Improvement of cycle-slip detection and repair
- Improvement of positioning and attitude accuracy and ambiguity-fixed solution availability

Point 1 can provide us some information about the possibility of changing the SD observation covariance matrix, by replacing the diagonal matrix (with only variances) with one including non-diagonal terms (covariances). By having measurements taken from close antennas, it is assumed that some of the measurement errors are correlated, notably the multipath. The degree of correlation will depend on the array baseline length. Considering the correlation between different measurements will improve the tuning of the EKF and, hopefully, the estimation performance.

Point 2 investigates the detection of cycle slips. To have a reference for the true occurrence of cycle slips in our datasets, a post-processing method using dual-frequency measurements is used. Depending on the observed performance of the cycle-slip detection algorithm, the process noise of the ambiguity evolution model, involved in the definition of $\mathbf{Q}_{amb}$ can be optimized.

Finally, using optimal tuning with regard to points 1 and 2, point 3 is addressed so as to determine the optimal positioning and attitude estimation performance of the proposed algorithm using real data. To summarize, our investigation plan provides some EKF tuning parameters and also an indication of which array baseline length provides the best positioning performances in all the environment types tested.

The detailed results of point 3 will be further presented in Section 6.3, and before we present the result of point 1 and point 2, some typical results of the signal pre-processing process include the applied elevation mask and the implementation of the Innovation test are illustrated in Section 6.2.2 and 6.2.3, respectively.

6.2.2. Elevation Mask Implementation Results

As aforementioned in Section 4.3.1, an a-priori elevation mask is applied in our algorithm for all tracked GNSS measurements to remove the measurements that are most likely severely degraded by multipath or NLOS effects. This step is essential and important because the corresponding measurements might be quite erroneous and might lead to extremely inaccurate assessment of the position quality or large estimation errors due to the unremoved outliers.

In order to have as many satellites as possible to perform Kalman filter calculations while ensuring signal quality, different elevation mask values are chosen for different datasets.

6.2.2.1. The open-sky environment (dataset 1)

For the first dataset which is in a relatively good environmental condition, the number of satellites received by the receiver is usually sufficient and fully guaranteed. In this case, a bigger value of the

elevation mask (**20 degrees**) is set to ensure the quality of the observations as much as possible. Figure 6-23 depicts the number of tracked GPS/Galileo satellites for the open-sky environment after the exclusion by applying the elevation mask.

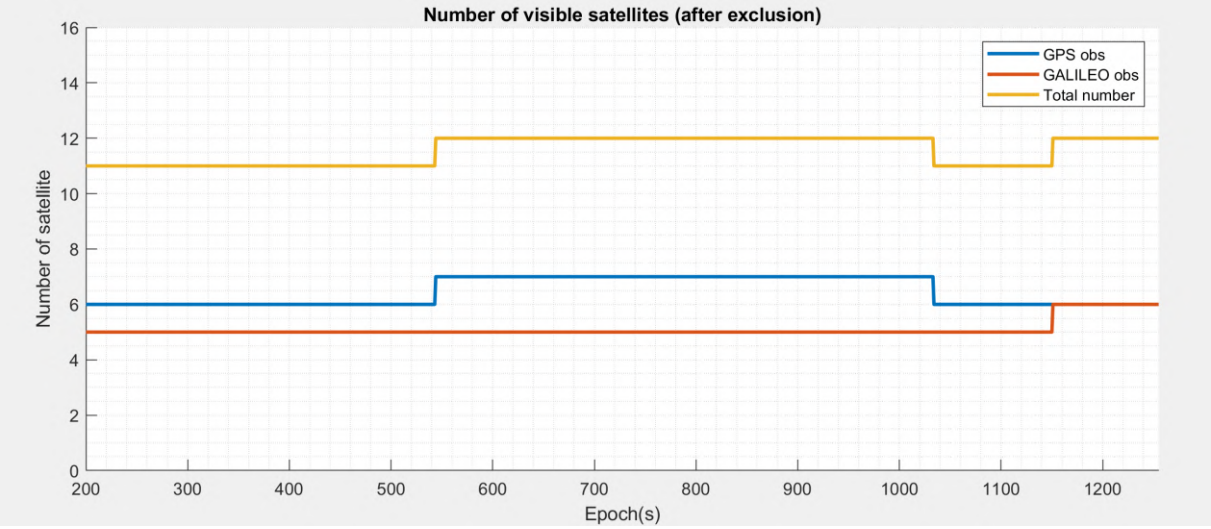

Figure 6-23 The number of tracked GPS/GALILEO satellites for the open-sky environment after exclusion (dataset 1)

It can be seen that the number of satellites has been clearly reduced compared to Figure 6-10, but the total number is still favorable.

6.2.2.2. The Suburban environment (dataset 2)

As for the second dataset, an elevation mask of **15 degrees** is chosen which is a compromise value to maintain a relatively good geometry of the satellite while maintaining a satisfactory precision of the measurements. The number of tracked GPS/Galileo satellites for the Suburban environment after the exclusion by applying the elevation mask is shown in Figure 6-24:

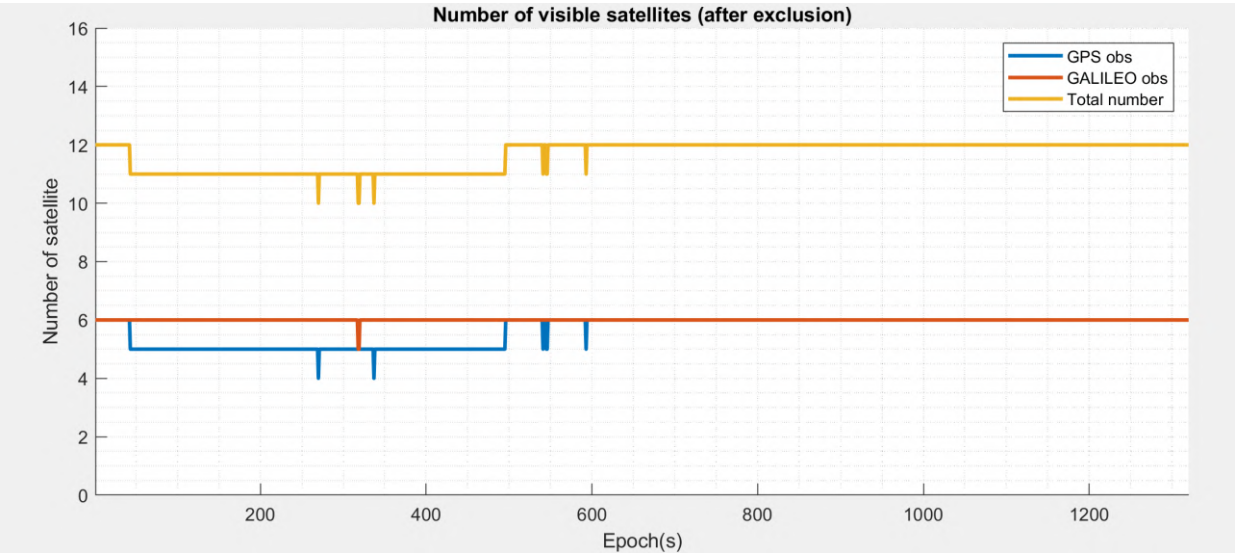

Figure 6-24 The number of tracked GPS/GALILEO satellites for the Suburban environment after exclusion (dataset 2)

Similar to the first case, the number of satellites has been reduced by a certain amount for both the GPS and Galileo constellation.

6.2.2.3. The Urban environment (dataset 3)

Considering the relatively poor satellite visibility condition compared to the other datasets, an elevation mask of **10 degrees** is applied to ensure that a sufficient number of satellites can be maintained throughout the entire time period. Figure 6-25 Illustrates the number of tracked GPS/Galileo satellites for the Urban environment after the exclusion by applying the elevation mask.

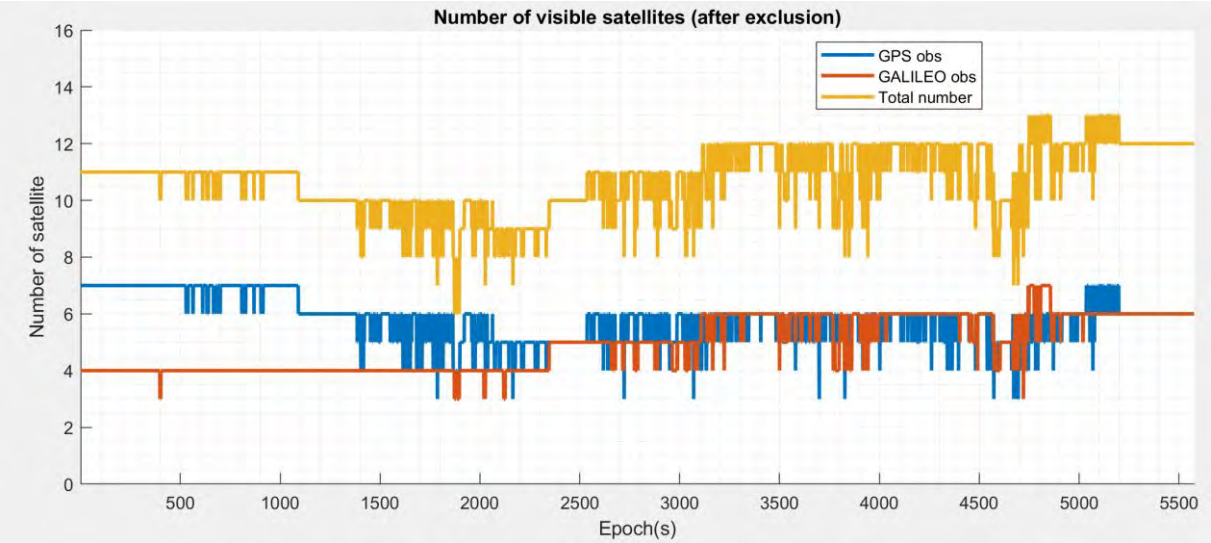

Figure 6-25 The number of tracked GPS/GALILEO satellites for the Urban environment after exclusion (dataset 3)

6.2.3. Measurement Weighting Scheme Values

As aforementioned in Section 4.3.2, a measurement weighting scheme is conducted in this thesis to quantify the accuracy of the measurements in different situations. To reflect the differences in measurements accuracy in different environments, the predefined value of the σ_{code} which is the standard deviation of the GNSS code observation at the zenith, is set to different practical values under different environmental conditions [144]. The values selected in this thesis are described in Table 6-2. Note that, same values are utilized for the GPS and Galileo systems.

Table 6-2 Threshold Value and the Corresponding Detected and Excluded Blunders Proportion

Data Scenario	Dataset 1 -Open Sky	Dataset 2 -Suburban	Dataset 3 -Urban
σ_{code}	$1m$	$2m$	$3m$

To consider the differences in accuracy between code measurements and the carrier phase measurements, a fixed scale factor $\boldsymbol{a = 1/100}$ is applied to obtain the std of the GNSS carrier phase observation σ_{phase}, by referring to [120] as presented in (**4-60**).

An elevation-based weighting algorithm is finally conducted in the EKF to consider the differences in accuracy between different tracked satellites.

6.2.4. Experimental Results of the Innovation test

As we introduced in Section 4.3.3, the detection and exclusion of the deteriorated observables are crucial for an accurate solution. In addition to the GNSS measurement selection steps based on the elevation mask and the weighting scheme, another fault detection and exclusion scheme is applied based on the KF innovations to handle more potential outliers in our proposed algorithm, called the Innovation Test.

In our case, the threshold to decide whether an observable is an outlier is based on the covariance value from the previous epoch and a predefined constant number γ:

$$\text{Threshold } (n_{1-\alpha/2}) = \gamma * \sqrt{Cov(I_{n,i})} = \gamma * \sigma \quad (6\text{-}1)$$

As we introduced in Section 4.3.3, $\gamma = 3$ corresponds to the three-sigma test: $P(-3\sigma < t_i < 3\sigma) = 99.74\%$, which means that our acceptable probability of false alarm α is 0.26%.

The measurement with the local test statistic t_i that exceeds the local threshold will be excluded. This procedure can be repeated several times in a loop until no outlier exists in the current measurement set. By doing so, most abnormal measurements can be removed thus a better estimation accuracy can be expected. To clearly illustrate the huge difference when conducting the Innovation test in different environments, the innovations of the code pseudorange measurement and carrier phase measurement are shown in Figure 6-26 and Figure 6-27, respectively.

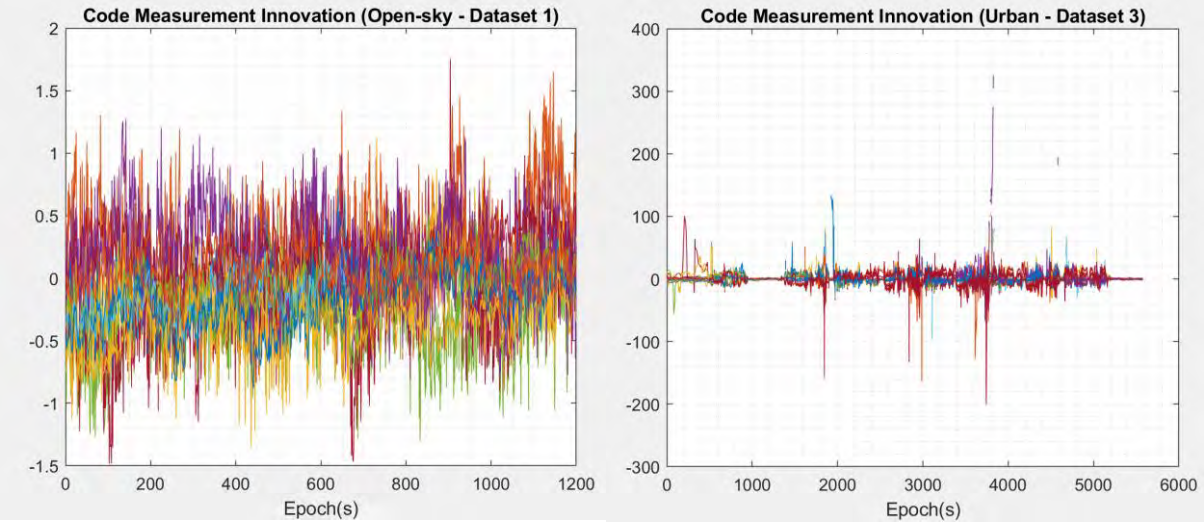

Figure 6-26 Code Measurement Innovation in meters (Left: Open-sky, Right: Urban)

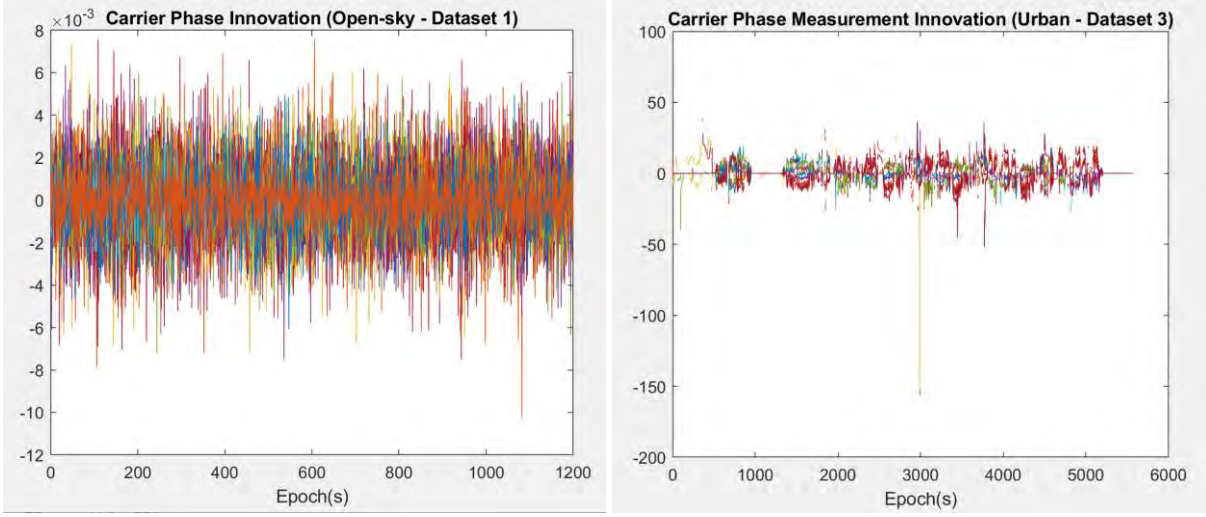

Figure 6-27 Carrier Phase Measurement Innovation in meters (Left: Open-sky, Right: Urban)

As we can notice from the figures, a clear uncertainty and a great number of outliers can be observed for both the code and carrier phase measurement in dataset 3. Especially when compared to the first

dataset, the magnitude of outliers is a hundred times worse. The significance to perform such an innovation test to remove the outliers and improve the tracked signal quality before the PVT process is self-evident, in particular for the data collected in the high-constrained environment.

To optimize the performance of the proposed algorithm under different environmental conditions, different threshold values have been tested. Due to the limited satellite visibility condition, a bigger value (3σ) is chosen for dataset 3 to keep more available GNSS observables. Table 6-3 shows the chosen threshold value and the corresponding proportion of detected (and excluded) blunders over the entire data length for different datasets.

Table 6-3 Threshold Value and the Corresponding Detected and Excluded Blunders Proportion

Data Scenario	Dataset 1- **Open Sky**	Dataset 2 - **Suburban**	Dataset 3 - **Urban**
Innovation Test Threshold (α)	2σ ($\alpha = 0.45\%$)	2σ ($\alpha = 0.45\%$)	3σ ($\alpha = 0.26\%$)
Detected and Excluded Outliers	0.1%	2.5%	11.8%

As one can notice from Table 6-3, compared to the other two datasets, even though the threshold is bigger, a much greater proportion of outliers is still detected for dataset 3. These outliers are the erroneous GNSS measurements, if not detected then excluded, will significantly deteriorate the positioning results, that's why the innovation test is must be carried out.

6.2.5. Experimental Results on the Correlation of Measurement Errors

In Section 5.2.5, the effect brought by the correlation parameter between measurements from the array pair receivers has been analyzed using simulated data. In this section, we present the experimental results on the correlation of measurement errors using real data.

In fact, since the measurements are coming from signals received by the closely placed antennas, it is safe to consider a certain level of correlation between these noise measurements. For example, the multipath error from the same satellite may be similar in the measurements recorded by the receivers connected to the two closely-mounted antennas.

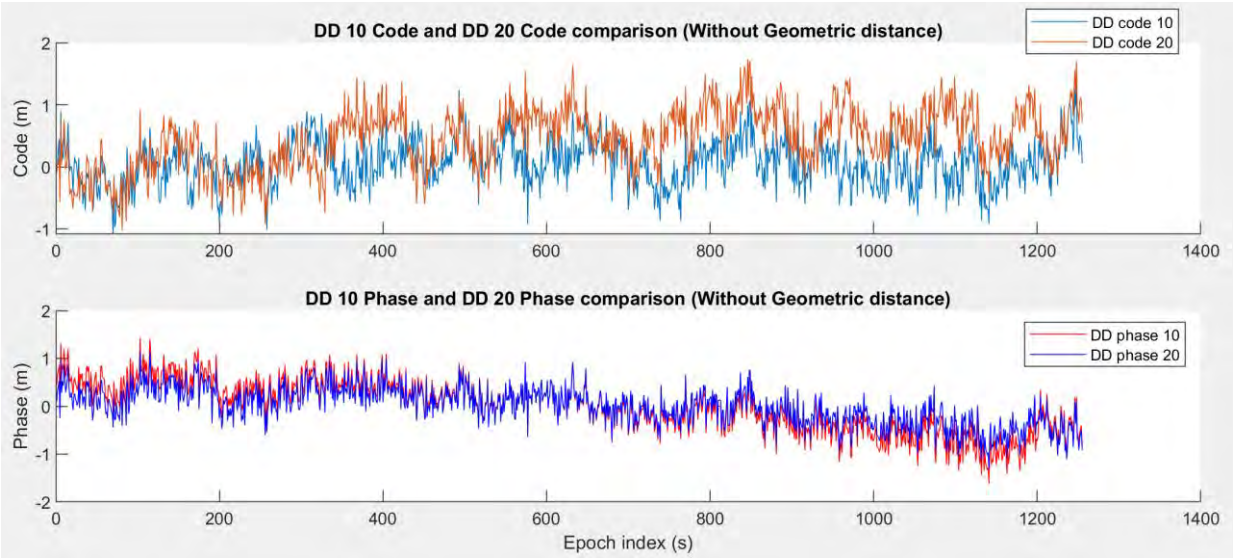

Figure 6-28 Comparison of the code and phase measurement errors for one pair of satellites

By removing the corresponding geometric distance term from the DD code pseudorange and carrier phase observations, the correlation coefficient for the DD code and carrier phase observations measured by the different antennas on the same satellite pair can be computed. Figure 6-28 illustrates an example of the comparison of the measurement errors for one pair of satellites of dataset 1.

Table 6-4 reports the result of the correlation coefficient determination of the DD pseudorange and DD carrier-phase measurement errors for different array baseline lengths and various environments (during a static period for datasets 2 and 3).

Table 6-4 Correlation coefficient of the code and phase measurement error

Array baseline length	Dataset 1- **Open Sky**		Dataset 2 - **Suburban**		Dataset 3 - **Urban**	
	Code	Phase	Code	Phase	Code	Phase
0.6 m	N/A	N/A	0.538	0.999	0.475	0.999
1.3 m	N/A	N/A	0.499	0.997	0.392	0.998
2.0 m	0.545	0.963	0.486	0.996	0.359	0.997

The numbers presented here are the average values of the correlation coefficient of all the common satellites tracked by both rover receivers. As an example, the calculation result of the correlation coefficient of the DD code and carrier phase measurement of dataset 1 is shown in Figure 6-29.

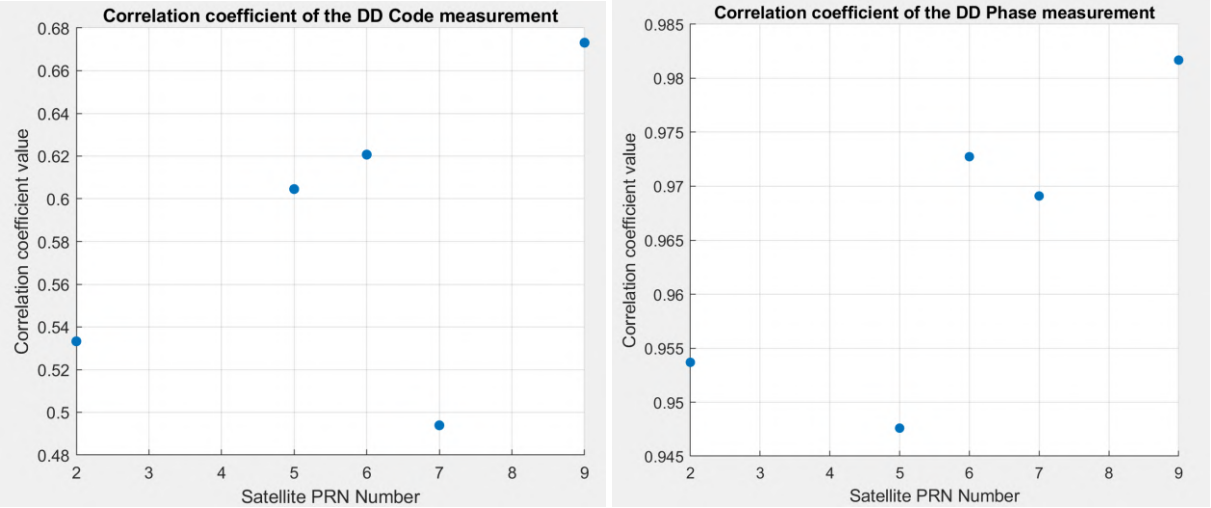

Figure 6-29 Result of the correlation coefficient of the DD code (Left) and carrier phase (Right) measurement of Dataset 1

Notice from Table 6-4 that the DD carrier phase measurement errors are very correlated for all the considered datasets, and there is also a medium degree of correlation between the pseudorange measurement. We speculate that this might be due to the characteristic of the GNSS double-difference measurement, and the much better precision property of the carrier phase measurement compared to the code measurement.

It is important to highlight the fact that there are several common contributing terms in the DD observations of the two closely-placed rover receiver antennas, including the information via the reference station and the reference satellite, especially for the carrier-phase measurements. The terms that are not correlated are quite small when compared to the common terms, which can explain the high correlation between the noise measurement of receivers 1 and 2 observed in Table 6-4. Another

finding is that one can observe a “rule” depending on the baseline length: the shorter the distance, the more significant the correlation.

To make our model closer to the real situation and thereby improve the EKF performance, we could update the observation covariance matrix in the EKF model by replacing the diagonal matrix with one including non-diagonal terms based on the correlation coefficient values in Table 6-4. Obviously, thus these non-diagonal terms take different values to reflect the difference in correlation when corresponding to the code or carrier-phase observables.

However, according to the experimental results, this correlation coefficient does not have much impact on the accuracy of the results, so this parameter is not considered in the results shown later, but it is worth further research and analysis of this parameter in future work. As an example, the correlation coefficient between the SD measurements rather than the DD measurement from the array pair receivers can be analyzed.

6.2.6. Experimental Results on the Cycle Slip Detection Performance

The cycle slip is mainly due to an event external to the receiver, such as an obstruction or severe multipath environment. In this case, there could be a strong correlation between the occurrence of cycle slips in the 2 receivers who are very close to each other. This assumption has been analyzed in in Chapter 5 using the simulation data as a special case study. At this point, we are interested in verifying if the occurrence of CS is simultaneous on all rover receivers using real GNSS observables.

We firstly run a dual-frequency algorithm [145] to obtain true cycle slips. Then compare the number of correct/incorrect CS detection/repair for all single receivers. Figure 6-30 shows a typical result of the CS detection of the tracked GPS satellites for one dataset by using these two methods.

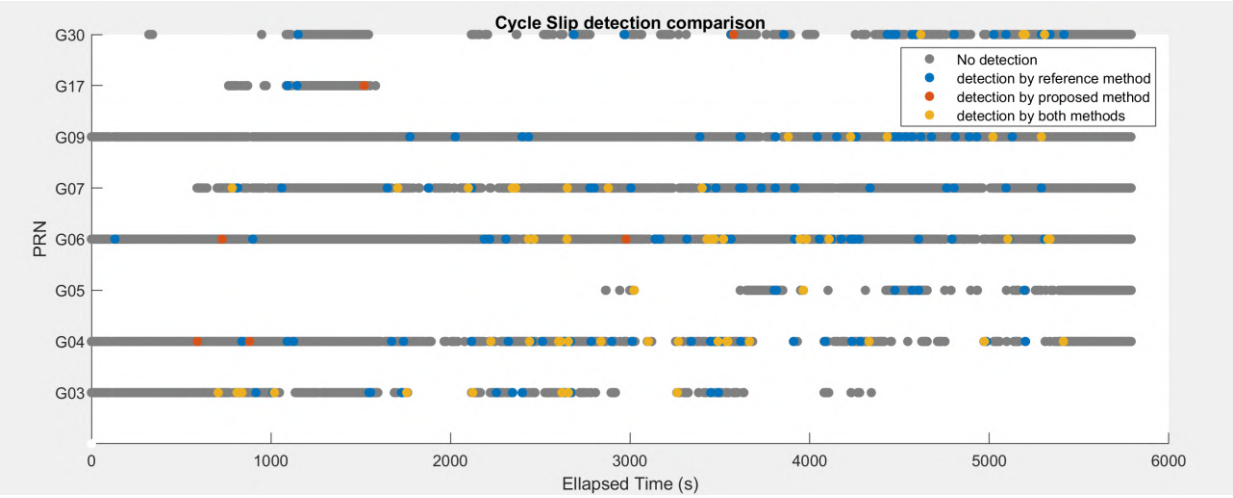

Figure 6-30 CS detection for one dataset by using dual-frequency and proposed single frequency methods

Table 6-5 summarizes the performance of the cycle-slip detection process. The detection rate here describes the ratio of the number of cycle-slips successfully detected to the total number, while the correct detection rate represents the proportion of correct cycle-slip alarms yielded by that method.

From the result one can conclude that our proposed single frequency method still has many limitations, only part of the cycle slip can be detected, but the correct correction rate is quite favorable. We also notice that the occurrence of several severe CSs is simultaneous on all receivers by both methods,

which appear consistent with our previous model thus confirms the hypothesis that we anticipated in chapter 5.

Table 6-5 Cycle Slip Detection Performances

	Dataset 1- **Open Sky**		Dataset 2 - **Suburban**		Dataset 3 - **Urban**	
	Detection Rate	Correct Detection Rate	Detection Rate	Correct Detection Rate	Detection Rate	Correct Detection Rate
Reference algorithm	1	1	1	1	1	1
Receiver 1	0.38	0.84	0.36	0.86	0.31	0.86
Receiver 2	0.39	0.89	0.38	0.85	0.26	0.85
Receiver 3	0.36	0.83	0.27	0.84	0.28	0.84
Receiver 4	0.37	0.86	0.32	0.79	0.29	0.75

Due to the imperfect detection of the cycle slip, a bigger value $\boldsymbol{\sigma_{amb} = 0.1}$ was chosen to account for possible undetected cycle slips for dataset 3. Slight improvement in positioning results is achieved when comparing with a smaller value $\boldsymbol{\sigma_{amb} = 0.01}$.

In the case of dataset 1 and dataset 2, the appearance of the cycle slips is not frequent, $\boldsymbol{\sigma_{amb} = 0.01}$ is chosen to ensure a better estimation of the integer ambiguities and thus improve the possibility to successfully fix the ambiguities to integers.

6.3. Experimental Results using Multiple receivers and Discussion

In this section, the proposed multi-receiver RTK positioning and attitude determination algorithm will be tested using the 3 different datasets presented in Section 6.1. The experimental results and the performance (in terms of the precision and availability of the estimated parameters) of the proposed EKF for different array baseline lengths and various data collections are discussed. The advantage brought by the GPS/Galileo dual-constellation configuration will also be analyzed. In each case, a comparison has been conducted between the proposed multi-receiver system and the traditional single receiver architecture.

To give quantitative values comparison between approaches under the same conditions, the performance of each scenario will be analyzed based on the evaluation of the following performance metrics.

a) **Horizontal positioning error statistics:** its mean value, standard deviation, 50th and 95th percentiles over the total number of epochs. As the proposed algorithm mainly targets land vehicle applications where the vertical component is usually of lower importance, only the horizontal positioning error is considered. It is defined as the distance between the true and estimated location in only the horizontal orientations (North, East):

$$\varepsilon_{\text{hor}} = \sqrt{\varepsilon_N^2 + \varepsilon_E^2} \tag{6-2}$$

Where:

- ε_{hor} is the horizontal position error
- ε_N and ε_E are the errors in the North and East direction in the ENU frame

b) **Fix success rate:** The fix success rate is defined as the number of epochs during which ambiguities are successfully fixed as integers over the total number of epochs.

c) **Solution Availability:** In GNSS-favorable environments, there will always be a PVT solution in each epoch. However, in some extremely harsh situation where the number of the satellite is not always enough to enable a PNT solution, the solution availability should be considered as a complementary metric to evaluate the performance of a positioning algorithm. Availability is officially defined by ICAO as the percentage of time that the services of the system are usable by the navigator, which is an indication of the ability of the system to provide reliable information within the specified coverage area [146]. In this thesis, the solution availability is defined as the number of epochs during which positions are successfully calculated and provided over the total number of epochs.

Additionally, like Chapter Chapter 5, the other two performance metrics are also defined to evaluate the precision of the attitude estimation of the multi-receiver approach in different scenarios:

d) **Absolute heading error statistics:** mean value, standard deviation, 50th and 95th percentiles over the total number of epochs.

e) **Absolute pitch error statistics:** mean value, standard deviation, 50th and 95th percentiles over the total number of epochs.

In the following sections, the performance of the proposed algorithm in different GNSS signal environments will be evaluated based on the metrics mentioned above.

6.3.1. Open-sky environment

Firstly, the experimental result of the positioning and attitude determination performance using multi-receiver architecture in an open-sky environment (Dataset 1) is illustrated, as aforementioned, this scenario is mainly used to validate the implementation of the proposed algorithm and give a reference demonstration of the performance of our multi-receiver system.

6.3.1.1. Typical States Estimation Results

Figure 6-31 shows the positioning error comparison between the float solution and the fixed solution in the ENU coordinate of the proposed multi-receiver algorithm (GPS only).

Here, the float solution indicates that the integer ambiguities are kept 'float' while the fixed solution is defined by two parts: for every estimation epoch, if the IAR process is declared successful, a new position is computed using the DD carrier-phase measurements corrected by the validated DD integer ambiguities. This position then is used to update the fixed solution. If the IAR process is not declared successful, the float solution is kept. This combined 'fixed solution' is considered to be the result of our proposed muti-receiver method.

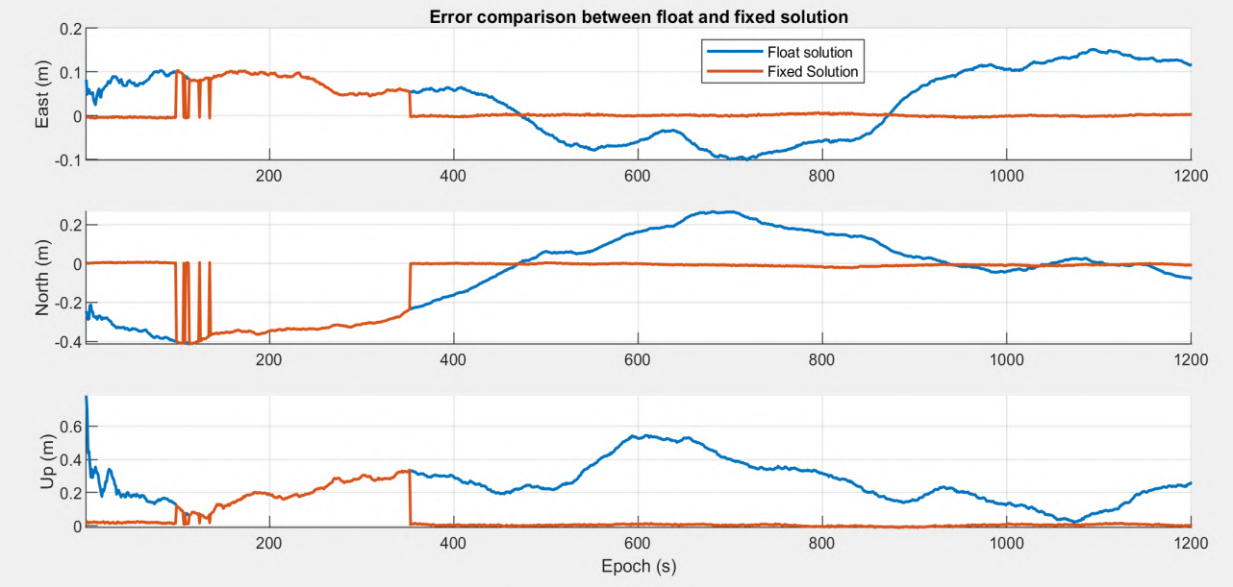

Figure 6-31 Error comparison between float and fixed solution (Dataset 1)

It can be seen from Figure 6-31 that the algorithm succeeded in outputting the right positioning result, with an accuracy of about 0.3 m for all three directions for the float solution. As for the fixed solution, once the IAR is declared successful, the positioning results of the fixed solution become much more accurate compared to the float solution. A millimeter-level accuracy could be obtained when the ambiguities are successfully fixed.

To get the precise statistics of the horizontal positioning error, different analysis has been conducted. Figure 6-32 gives an illustration of the Horizontal positioning statistics calculation and Figure 6-33 shows the corresponding cumulative density function of the horizontal error.

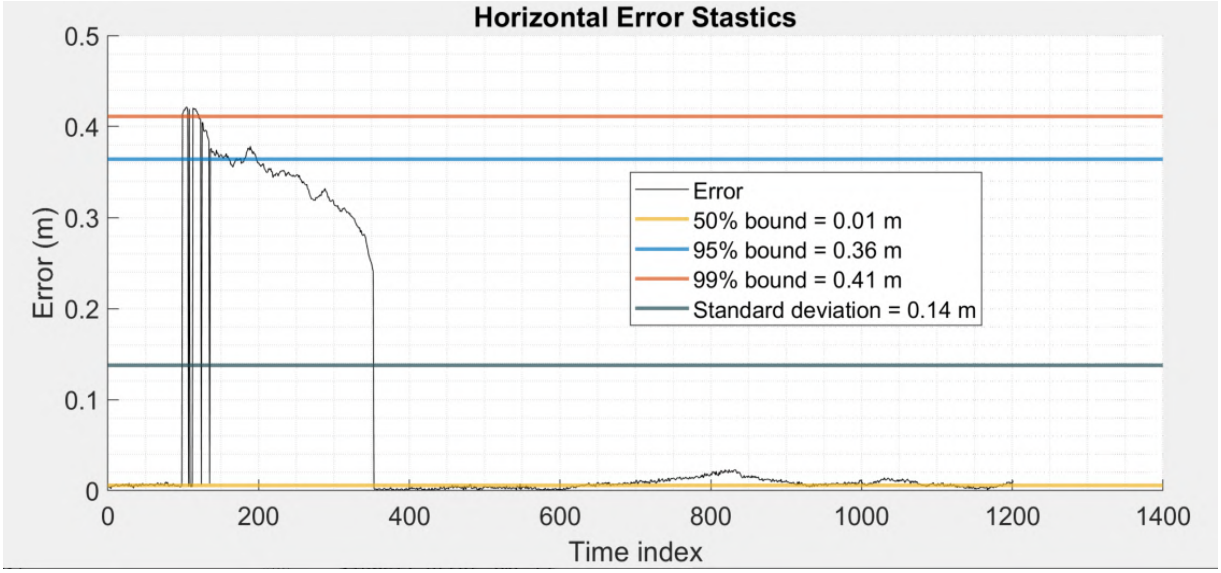

Figure 6-32 Illustration of Horizontal Positioning Error Statistics Calculation (Dataset 1)

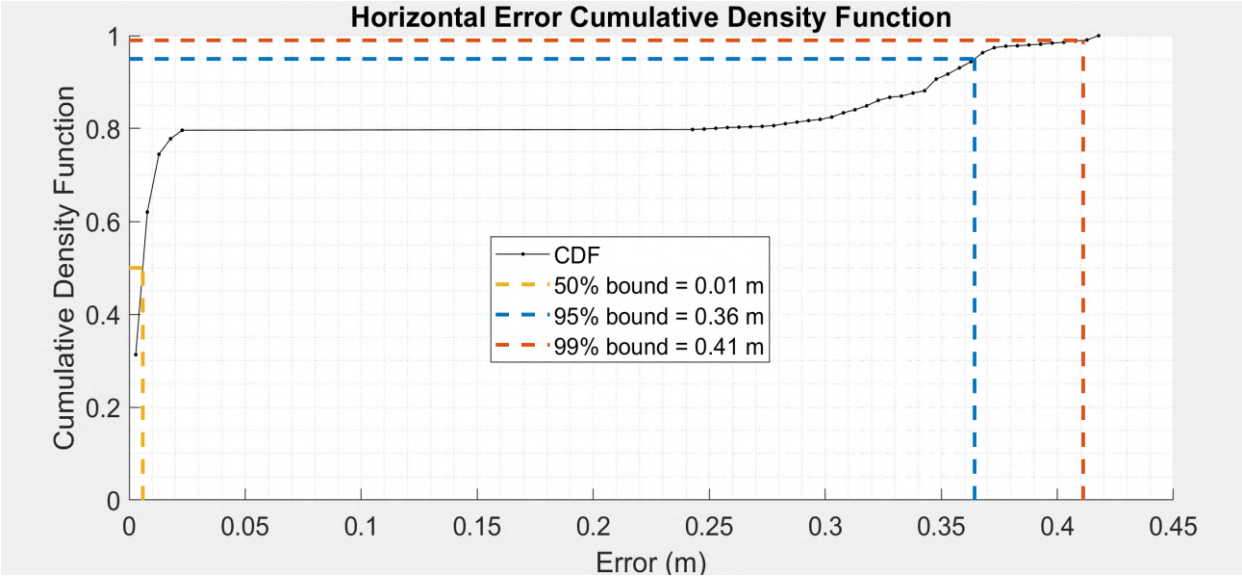

Figure 6-33 Corresponding Cumulative Density Function of the Horizontal Error (Dataset 1)

As for the estimation of the attitude-related states, Figure 6-34 plots the estimation of the pitch and heading angles of the vehicle for dataset 1, and the estimation errors are depicted in Figure 6-35.

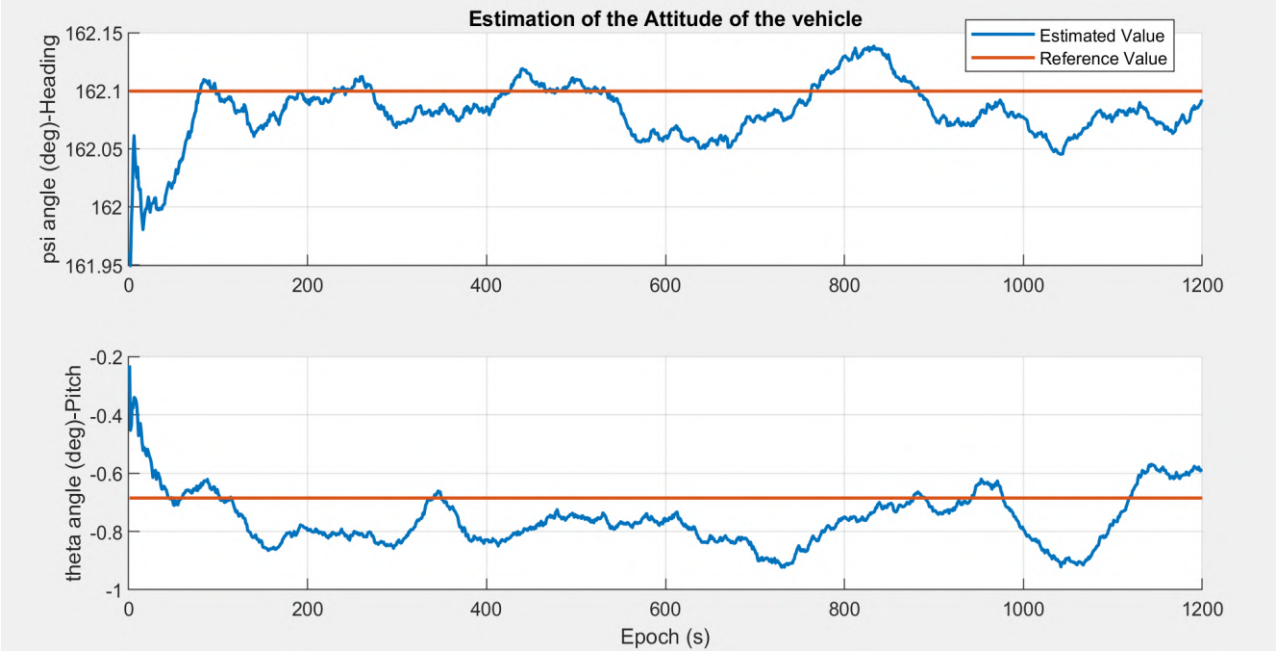

Figure 6-34 Illustration of vehicle attitude estimation (Dataset 1)

One can see from Figure 6-35 that the error between the estimated result and the true value is extremely small (less than 0.1 deg for heading and 0.3 deg for pitch most of the time), which can provide the user with a relatively accurate vehicle posture by using our proposed method.

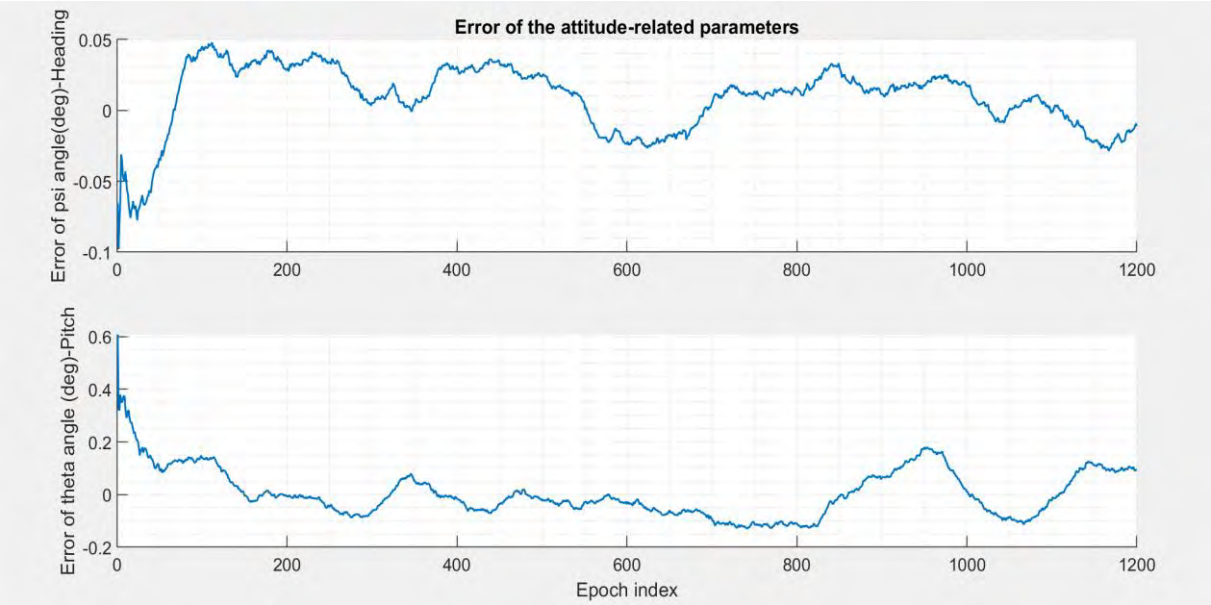

Figure 6-35 Error of the attitude-related parameters (Dataset 1)

In the following sections, the experimental performance comparison results of the single and multi-receiver system for dataset 1 will be presented, the benefits that a second constellation such as Galileo can bring are also depicted.

6.3.1.2. Performance Comparison between Single and Multi-receiver system - GPS only

In this scenario, only the GPS is taken into account. A first set of the RTK performance results for the open-sky data collect 1 is reported in Table 6-6:

Table 6-6 Performance comparison for data collection 1 -Open Sky, GPS only

Variation	Performance indicator	Unit	Mean	Standard deviation	50% bound	95% bound
Single receiver	Horizontal positioning error	m	0.098	0.185	0.014	0.465
	Success fixed rate	%	69.35	N/A	N/A	N/A
Dual receiver $l = 2$ m	Horizontal positioning error	m	0.076	0.140	0.010	0.361
	Absolute heading error	deg	0.057	0.057	0.027	0.097
	Absolute pitch error	deg	0.211	0.054	0.038	0.282
	Success fixed rate	%	84.69	N/A	N/A	N/A

As we can see from the table above, the dual receiver array system provides better performance than the single receiver RTK solution. With relatively good satellite visibility for dataset 1, even though the single receiver system can already achieve a relatively favorable fix success rate, the proposed multi-receiver system can still improve the fix success rate moderately and improve the precision of the positioning result, thus demonstrating the interest of such an approach.

6.3.1.3. Performance Comparison between Single and Multi-receiver system– GPS/GALILEO

In this scenario, the GPS/Galileo dual constellation configuration is applied in our algorithm. As we can see from the result in Table 6-7, when the Galileo system is also considered, a clear improvement of the accuracy can be found for both the single receiver and multi-receiver systems.

Table 6-7 Performance comparison for data collection 1 -Open Sky, GPS/GALILEO

Variation of scenario 1	Performance indicator	Unit	Mean	Standard deviation	50% bound	95% bound
Single receiver	Horizontal positioning error	m	0.068	0.113	0.010	0.265
	Fix success rate	%	82.58	N/A	N/A	N/A
Dual receiver $l = 2$ m	Horizontal positioning error	m	0.045	0.098	0.006	0.161
	Absolute heading error	deg	0.046	0.048	0.025	0.088
	Absolute pitch error	deg	0.181	0.049	0.035	0.195
	Fix success rate	%	94.95	N/A	N/A	N/A

In fact, when a dual constellation GPS/Galileo is considered, the minimum number of GNSS observations has augmented from 6 to 14 in such an open-sky environment, which improves greatly the DOP of the satellites, and the benefit is reflected in the final positioning accuracy.

6.3.2. Suburban environment

The results from the analysis of the datasets from the suburban and urban test drives gave us some useful information on the robustness of the multi-receiver RTK system in harsh environments. In this section, the result using the suburban data is first introduced.

As previously mentioned, the suburban data was collected when the vehicle was driven on the ENAC campus. The reference trajectory was provided with centimeter-level accuracy. The maximum standard deviation values, up to 10 centimeters, occur at around the 400-epoch mark, which corresponds to the zone having a minimum number of visible satellites. Generally, however, the environment is quite favorable with at least eight satellites in view for most of the time.

In addition, as the antenna of the SPAN system is not placed in the same place as the rover receiver antennas, to get a reference trajectory, the lever-arms between the 4 rover receiver antennas and the SPAN antenna are measured as shown in Figure 6-36:

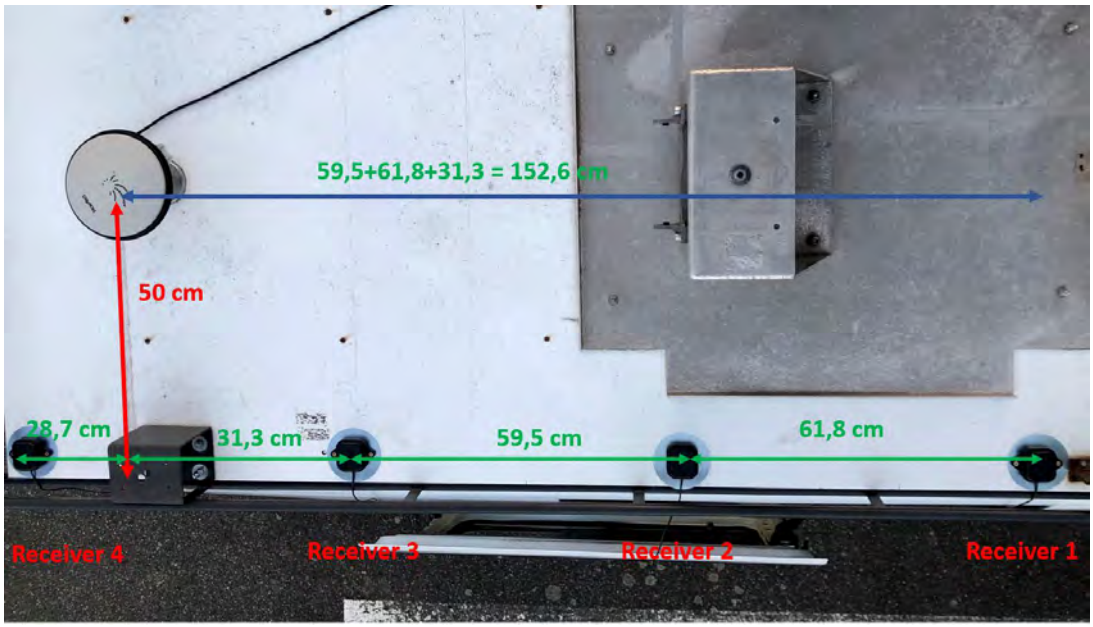

Figure 6-36 Geometric distance between the reference antenna and rover antennas

The reference solution can then be corrected by adding the projected geometric difference from the body-fixed coordinate frame of the car to the ENU frame using the attitude information provided by the integrated IMU. Although the lever-arms between the SPAN antenna and the rover antennas were measured carefully, due to the potential orientation error and the lever-arm distance, errors of a few centimeters can be expected on the reference trajectory even when the ambiguities are fixed.

6.3.2.1. Typical States Estimation Results

Typical results of the state estimations (position and attitude of the vehicle) for the second data collection are given in the following figures.

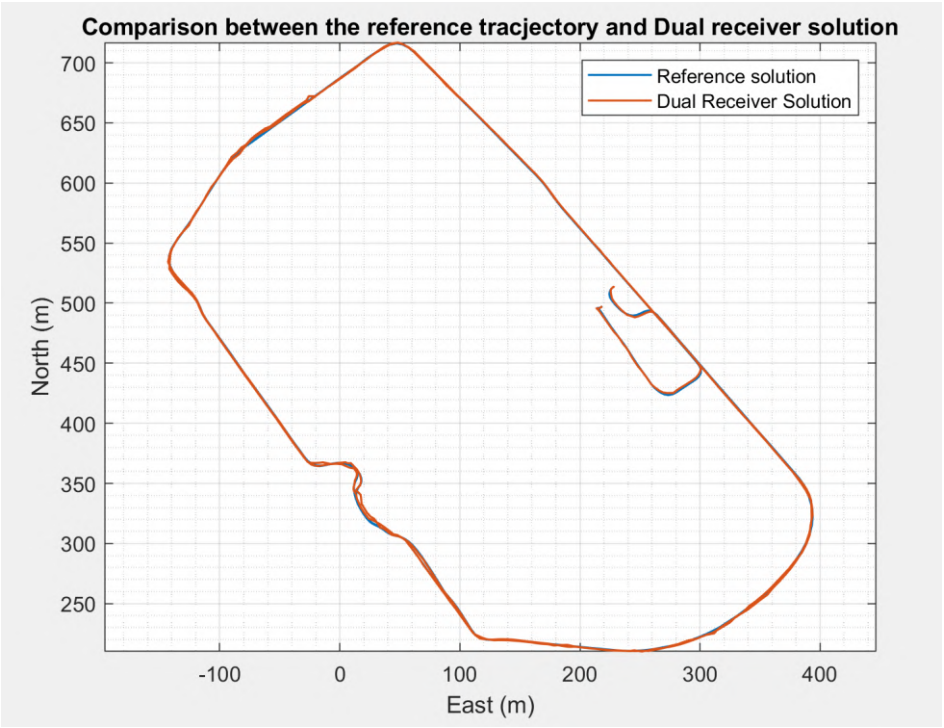

Figure 6-37 Comparison between the Reference Trajectory and the Dual-receiver Solution (Dataset 2)

Figure 6-37 plots the comparison between the reference trajectory and the dual-receiver solution, it can be seen that the results obtained by the proposed algorithm are very coincident with the reference value.

To illustrate the error more clearly, in Figure 6-38, the two panels show the estimation error of the horizontal (east and north) position coordinates respectively with respect to the true position of the receiver. The solution of the single receiver system and the dual-receiver system are both plotted. As one can notice, both the algorithms succeeded in outputting the right positioning result, with an average accuracy of about 0.5 m for all three directions, which is acceptable for a harsh environment. In addition, when the ambiguities are successfully fixed, centimeter-level accuracy can be guaranteed.

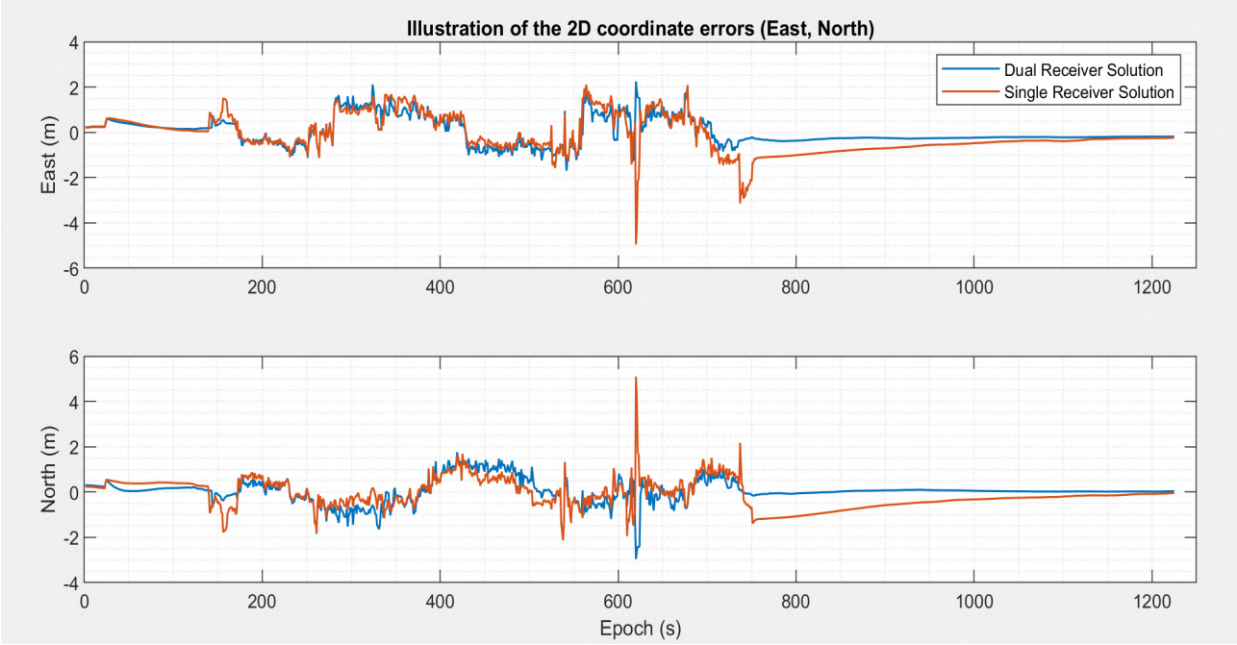

Figure 6-38 Comparison of the 2D coordinate error: Single receivers vs Dual-receiver (Dataset 2)

Overall, the superiority of the dual-receiver solution is obvious, a better positioning precision can always be obtained using the proposed multi-receiver method. In addition, it is evident from the figure that a few outliers in the positioning results appear with incorrect integer ambiguities due to the limited number of visible satellites or bad signal quality for both the algorithms.

Like dataset 1, precise statistics of the horizontal positioning error has been obtained by conducting different analysis. Figure 6-39 gives an illustration of the Horizontal positioning statistics calculation process using the proposed multi-receiver methodology and Figure 6-40 depicts the corresponding cumulative density function of the horizontal error.

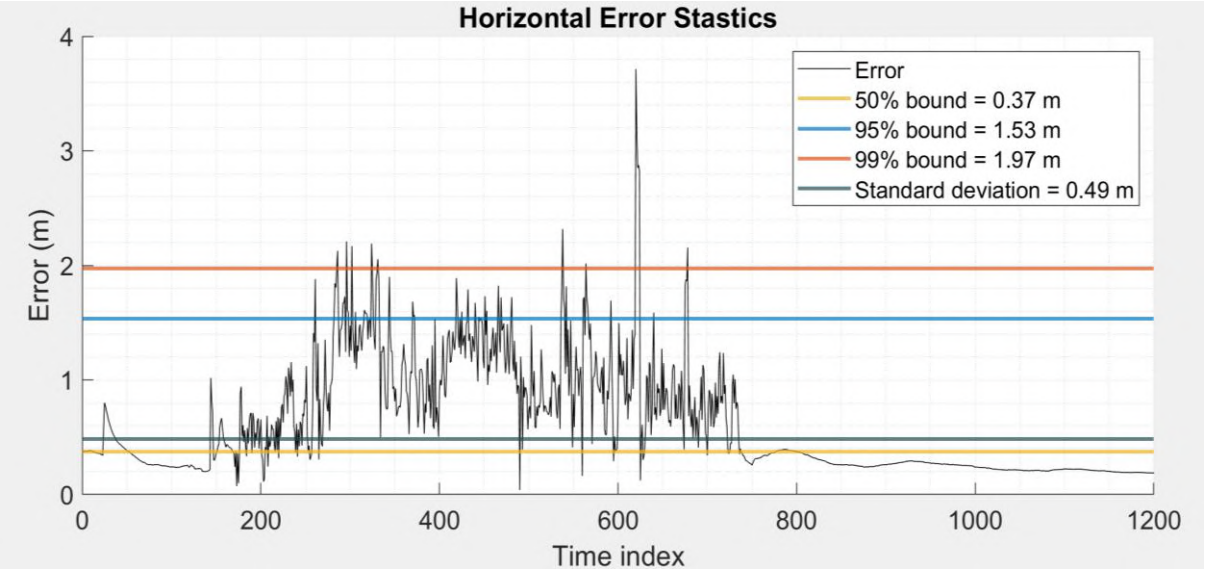

Figure 6-39 Illustration of Horizontal Positioning Error Statistics Calculation (Dataset 2)

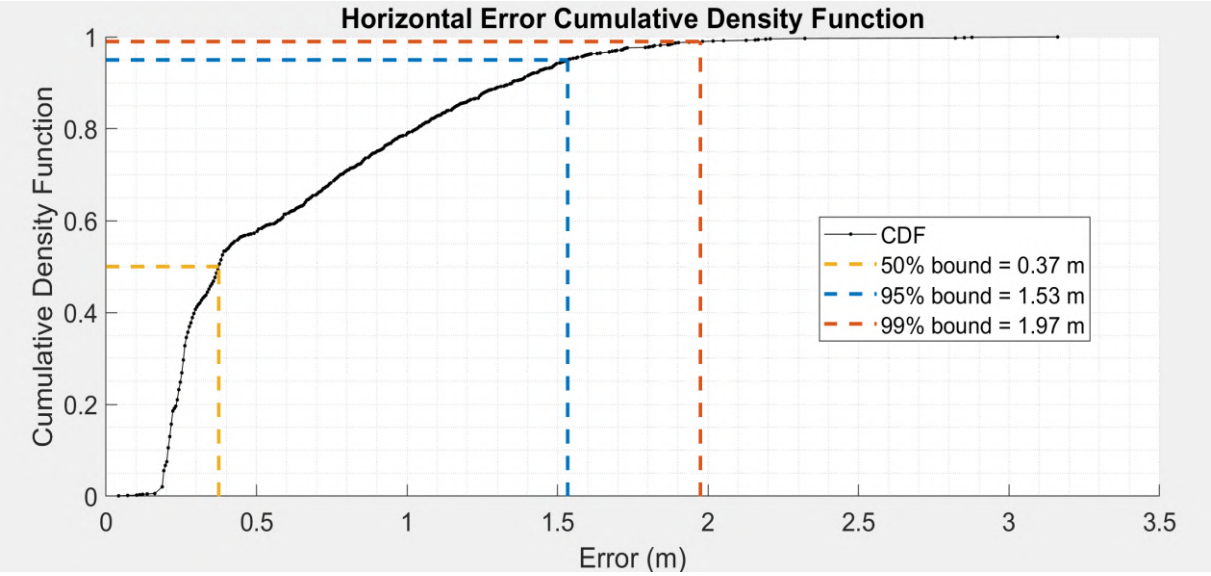

Figure 6-40 Corresponding Cumulative Density Function of the Horizontal Error (Dataset 2)

As for the estimation of the attitude-related states, Figure 6-41 plots the estimation of the pitch and heading angles of the vehicle for dataset 2. Unlike the situation where the vehicle attitude is accurately estimated in the first dataset, in the second dataset, the vehicle is moving fast with great movement dynamics. Some huge errors may appear when the car is turning especially for the heading estimation. Nevertheless, when the car is moving forward smoothly, a relatively accurate estimation of car attitude can be obtained, which can still provide the user with an appropriate reference result of the vehicle's posture by using our proposed method.

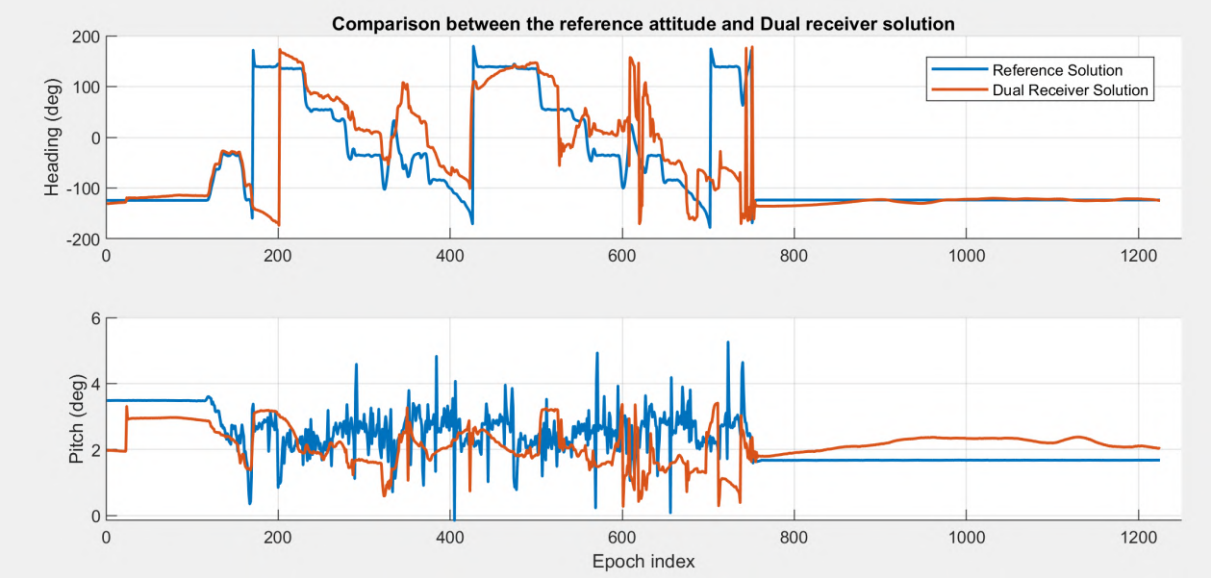

Figure 6-41 Illustration of vehicle attitude estimation (Dataset 2)

In the following sections, the detailed performance comparison results of the single and multi-receiver system in the suburban environment will be presented, as well as the benefits that a second constellation such as Galileo can bring.

6.3.2.2. Performance Comparison between Single and Multi-receiver system - GPS only

In this first scenario, only the GPS constellation is considered. Figure 6-42 plots the performance comparison between our dual-receiver system and the single-receiver system in the suburban environment and for different array baseline lengths and Table 6-8 gives the corresponding detailed statistical result.

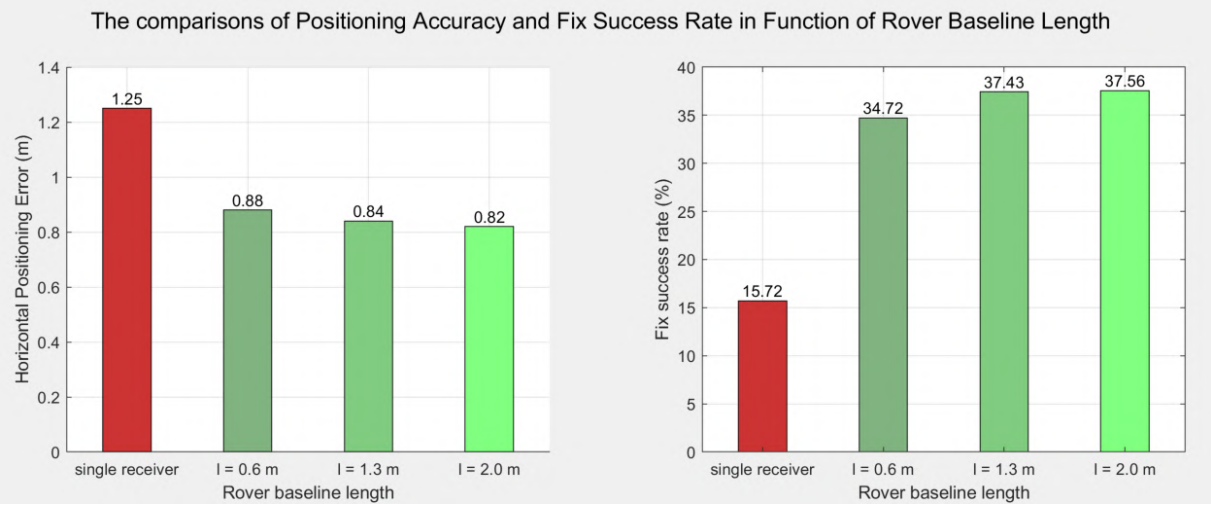

Figure 6-42 Comparisons of Positioning Accuracy and Fix Success Rate w.r.t Rover Baseline Length (Dataset2 - GPS only)

Due to the degradation of signal quality, compared with the results of the first data set, the accuracy of each parameter has been reduced to a certain extent for both methodologies (from centimeter-level accuracy to decimeter-level accuracy), but a better accuracy result is still obtained in the dual-receiver situation. Moreover, there is no huge difference in the accuracy of the positioning results between the different dual-receiver variations. However, as expected, the attitude accuracy does improve slightly as the array baseline length increases as shown in Figure 6-43.

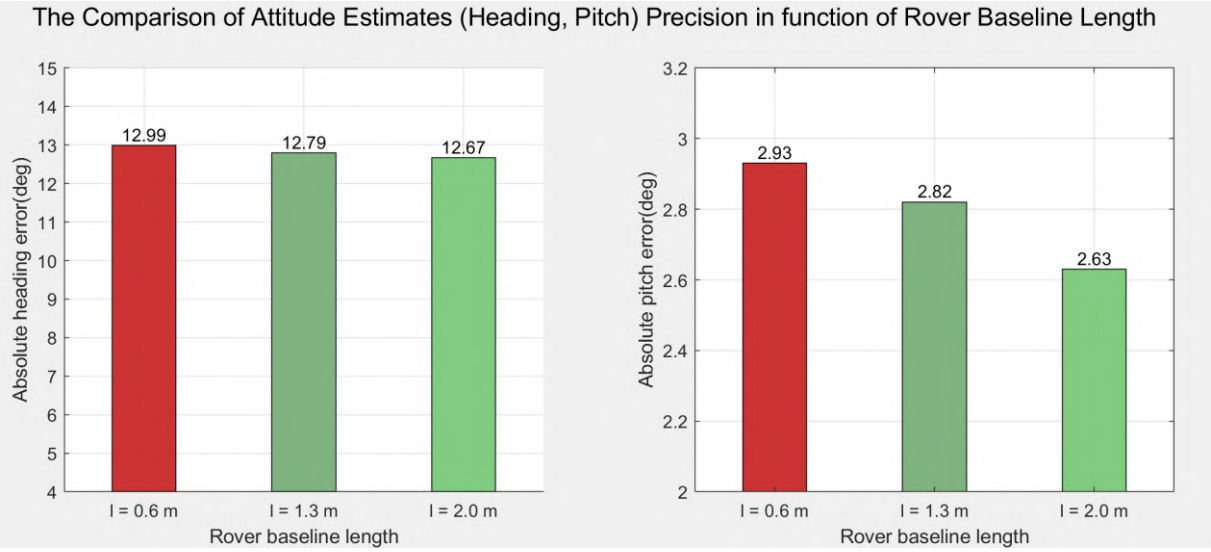

Figure 6-43 Comparisons of Attitude Estimates Precision w.r.t Rover Baseline Length (Dataset2 - GPS only)

Table 6-8 Performance comparison for different array baselines for data collection 2 – Suburban, GPS only

Variation of Dataset 2	Performance indicator	Unit	Mean	Standard deviation	50% bound	95% bound
Single receiver	Horizontal positioning error	m	1.25	1.42	0.78	2.47
	Fix success rate	%	15.72	N/A	N/A	N/A
Dual receiver $l = 0.6$ m	Horizontal positioning error	m	0.88	1.89	0.59	2.59
	Absolute heading error	deg	12.99	12.89	5.89	15.48
	Absolute pitch error	deg	2.93	3.67	2.27	5.27
	Fix success rate	%	34.72	N/A	N/A	N/A
Dual receiver $l = 1.3$ m	Horizontal positioning error	m	0.84	1.78	0.57	2.25
	Absolute heading error	deg	12.79	13.78	5.48	15.38
	Absolute pitch error	deg	2.82	3.87	2.19	5.09
	Fix success rate	%	37.43	N/A	N/A	N/A
Dual receiver $l = 2.0$ m	Horizontal positioning error	m	0.82	1.85	0.53	2.12
	Absolute heading error	deg	12.67	12.82	5.14	15.14
	Absolute pitch error	deg	2.63	3.83	1.87	4.87
	Fix success rate	%	37.65	N/A	N/A	N/A

6.3.2.3. Performance Comparison between Single and Multi-receiver system– GPS/GALILEO

In the second scenario, the GPS/ Galileo dual constellation configuration is applied in our algorithm. Thanks to the Galileo system, the total minimum number of observations has increased from 5 to 12 in such a suburban environment, significant amelioration in terms of the accuracy can be found in Table 6-9 for both the single receiver and multi-receiver systems.

Table 6-9 Performance comparison for different array baselines for data collection 2 – Suburban, GPS/GALILEO

Variation of Dataset 2	Performance indicator	Unit	Mean	Standard deviation	50% bound	95% bound
Single receiver	Horizontal positioning error	m	0.92	0.98	0.48	1.95
	Fix success rate	%	18.25	N/A	N/A	N/A
Dual receiver $l = 0.6$ m	Horizontal positioning error	m	0.78	0.68	0.59	1.64
	Absolute heading error	deg	11.58	10.69	5.38	13.54
	Absolute pitch error	deg	2.85	3.55	2.06	4.88
	Fix success rate	%	39.85	N/A	N/A	N/A
Dual receiver $l = 1.3$ m	Horizontal positioning error	m	0.65	0.58	0.47	1.58
	Absolute heading error	deg	11.19	11.08	5.11	13.94
	Absolute pitch error	deg	2.61	3.64	1.99	4.79
	Fix success rate	%	41.43	N/A	N/A	N/A
Dual receiver $l = 2.0$ m	Horizontal positioning error	m	0.61	0.49	0.37	1.53
	Absolute heading error	deg	11.04	9.82	4.95	12.54
	Absolute pitch error	deg	2.45	3.28	1.86	4.35
	Fix success rate	%	45.65	N/A	N/A	N/A

Clearly shown in Figure 6-44, consistent with the previous results, the dual-receiver system always provides better performance than the single receiver RTK solution, in terms of the fix success rate and the positioning result. At the same time, the estimation accuracy of the vehicle attitude also slightly improved, as shown in Figure 6-45.

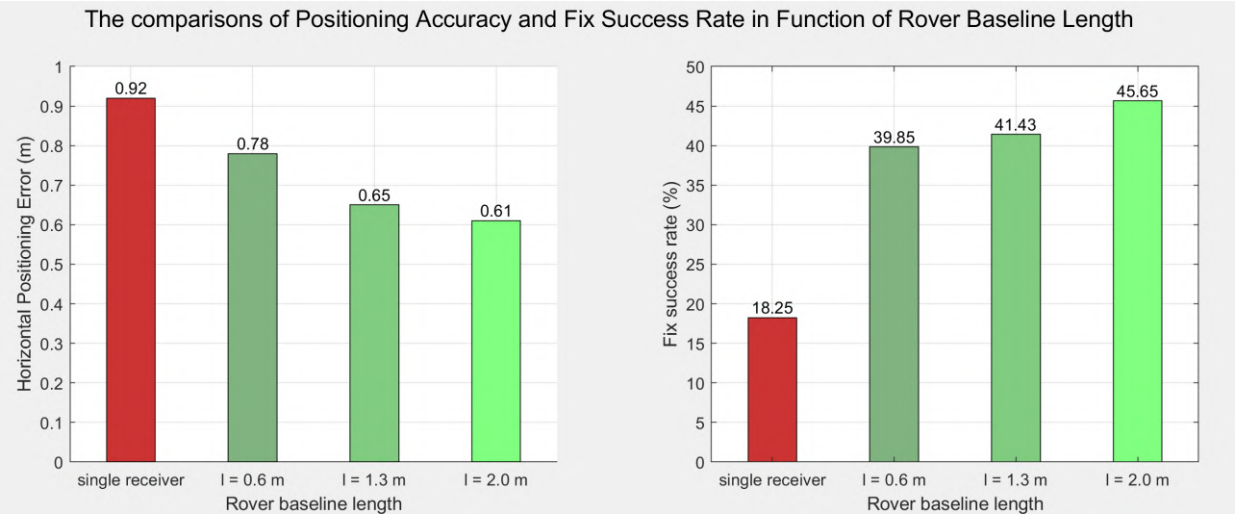

Figure 6-44 Comparisons of Positioning Accuracy and Fix Success Rate w.r.t Rover Baseline Length (Dataset2- GPS/GALILEO)

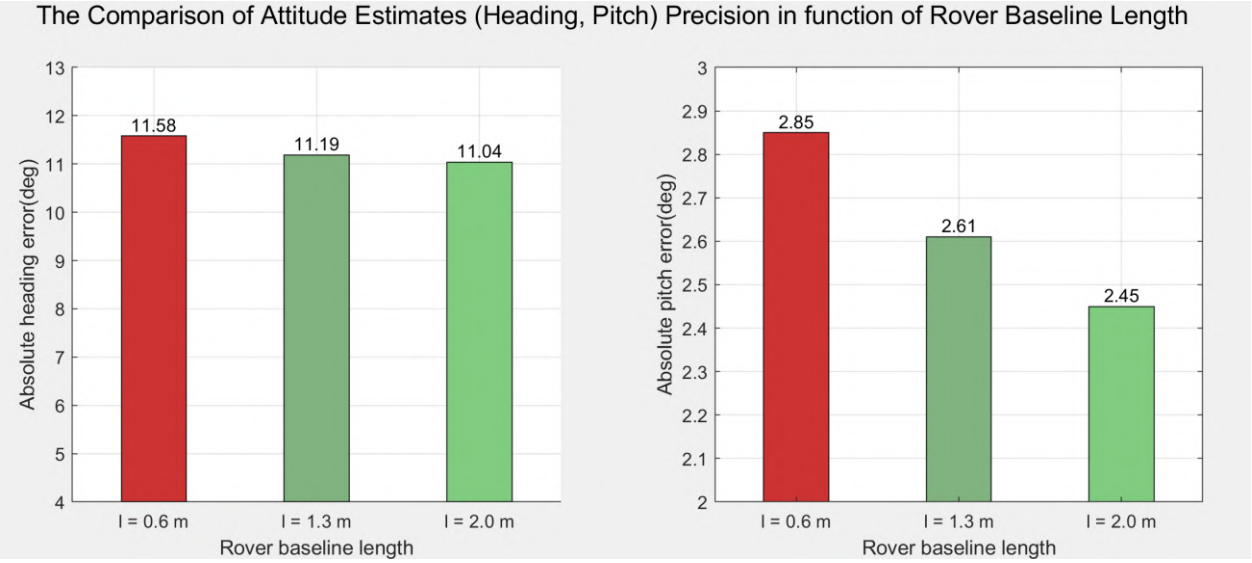

Figure 6-45 Comparisons of Attitude Estimates Precision w.r.t Rover Baseline Length (Dataset2 – GPS/GALILEO)

6.3.3. Urban environment

Finally, the algorithm has been tested against the most GNSS-challenging environment (urban environment) and high dynamic applications. As introduced in Section 6.1.4, the third measurement session was performed when the vehicle was from ENAC to the city center, the high-end GNSS receiver with IMU provided a decimeter-level trajectory accuracy in the urban scenario.

The same procedure has been conducted to project the SPAN system's reference solution to the physical center of the master rover antenna. The number of visible satellites was much lower than for the other two environments. A clear uncertainty increase in the position solution was observed in the reference result during the trajectory section where the number of satellites was fewer than six.

6.3.3.1. Typical States Estimation Results

Typical results of the state estimations (position and attitude of the vehicle) for the third data collection are given in the following figures. Figure 6-46 shows the comparison between the reference trajectory and the dual-receiver solution. In some extremely harsh situations, the number of visible satellites is not sufficient to enable a solution from our algorithm. That is why there are some data breakpoints in

the plot of the dual-receiver solution. However, this situation is still an improvement compared to the single-receiver operation. The dual-receiver system performs better than the single-receiver situation and provides better solution availability thanks to the doubled observations redundancy.

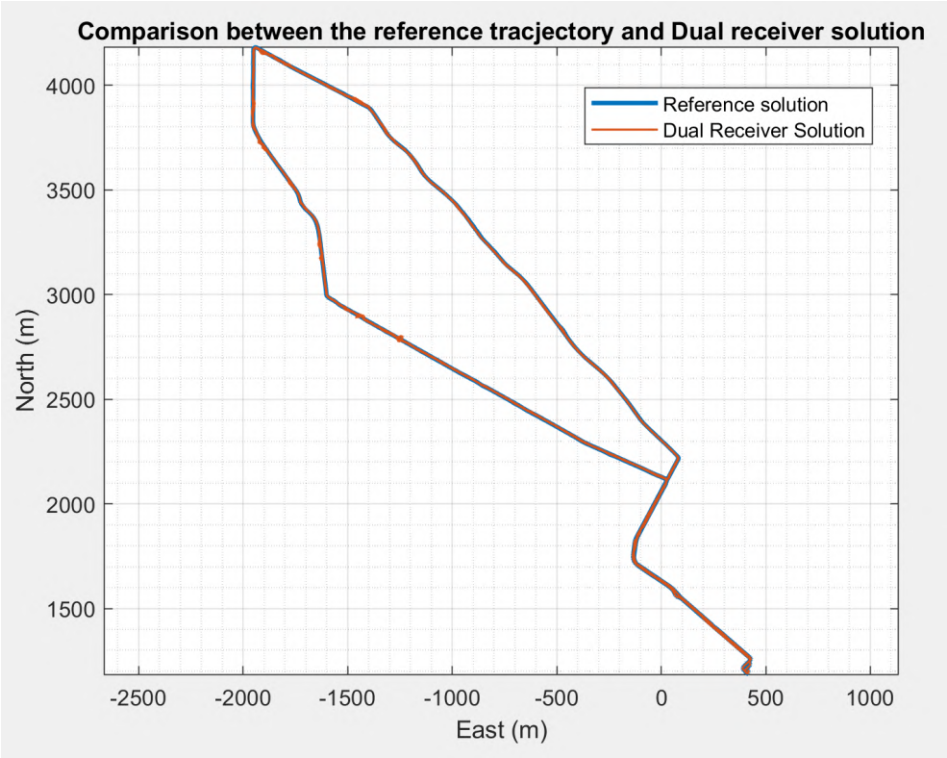

Figure 6-46 Comparison between the Reference Trajectory and the Dual-receiver Solution (Dataset 3)

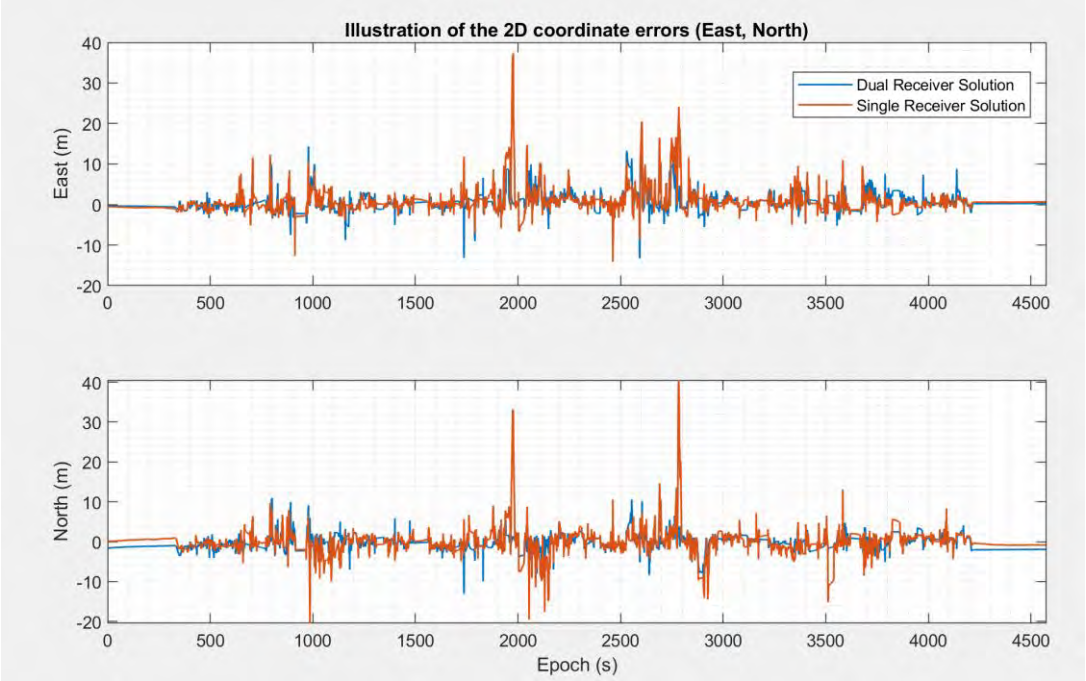

Figure 6-47 Comparison of the 2D coordinate error: Single receivers vs Dual-receiver (Dataset 3)

In Figure 6-47, the horizontal (east and north) position coordinates errors are plotted respectively with respect to the receiver's reference position. The solution of the single receiver system and the dual-receiver system are both presented.

Once again, the accuracy of the dual-receiver solution is better than the single receiver solution even in such an urban environment. However, compared with the previous datasets, it can be clearly noticed that the errors of both the two methods have greatly increased. In addition, it is evident from the figure that many outliers in the positioning results appear due to the limited number of visible satellites or bad signal quality for both algorithms. In addition, during several epochs when the first rover receiver fails to observe sufficient GNSS satellites ($N_{sat} < 3$), the single receiver system cannot provide even a solution, but the proposed multi-receiver algorithm may successfully provide a solution by the procedure of dual-receiver combination. Overall, the superiority of the dual-receiver solution is obvious, a better positioning precision and solution availability can always be obtained using the proposed multi-receiver method.

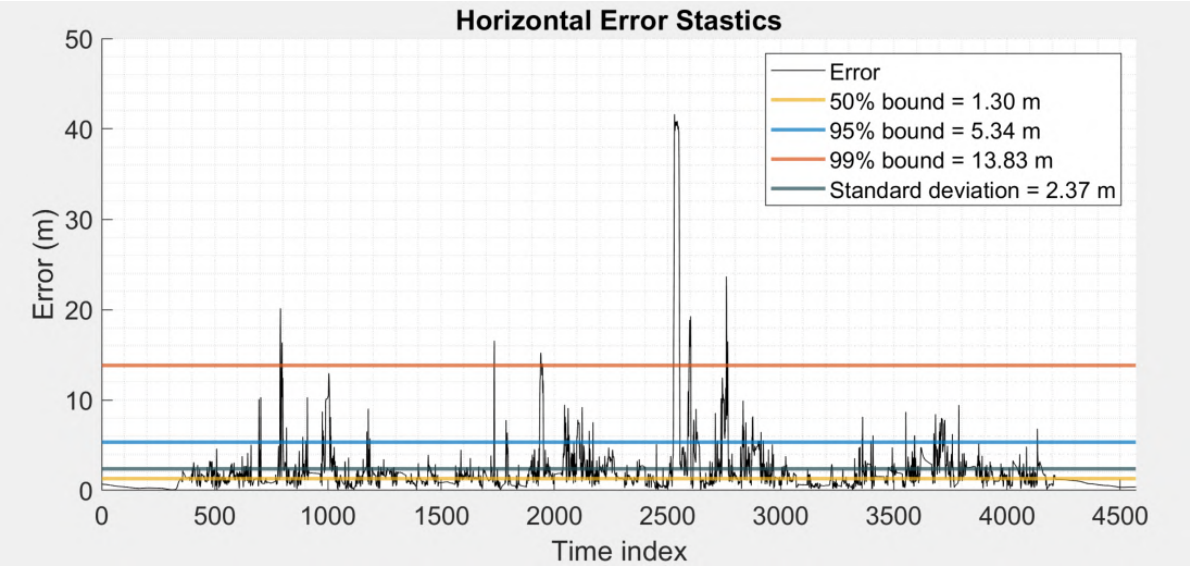

Figure 6-48 Illustration of Horizontal Positioning Error Statistics Calculation (Dataset 3)

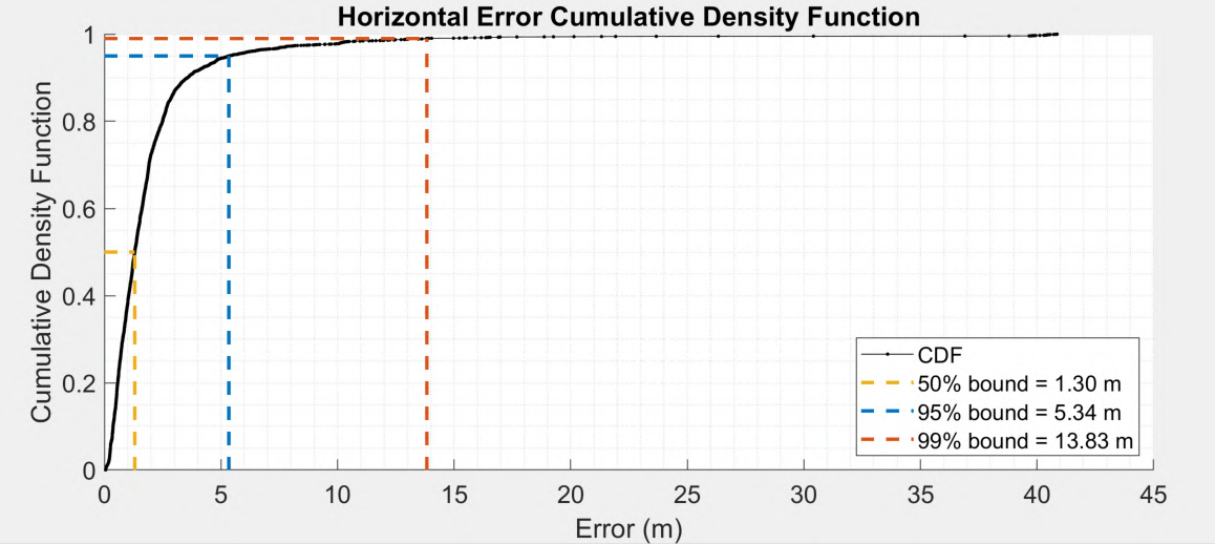

Figure 6-49 Corresponding Cumulative Density Function of the Horizontal Error (Dataset 3)

Same as previous datasets, precise statistics of the horizontal positioning error has been obtained by conducting different analysis. Figure 6-48 gives an illustration of the Horizontal positioning statistics

calculation process using the proposed multi-receiver methodology and Figure 6-49 shows the corresponding cumulative density function of the horizontal error.

The estimation of the attitude-related states (pitch and heading angles) in the urban environment is plotted in Figure 6-50. It can be seen that the error between the estimated result and the reference result is relatively large. This is mainly because the vehicle is moving fast with great movement dynamics. During certain epochs, the speed of the vehicle is very high and the phase of the multipath changes very quickly, the estimation of the heading becomes extremely erroneous. In this case, only during the period that the car is moving smoothly, the estimation of the car's attitude can be considered as a reference for the vehicle's posture.

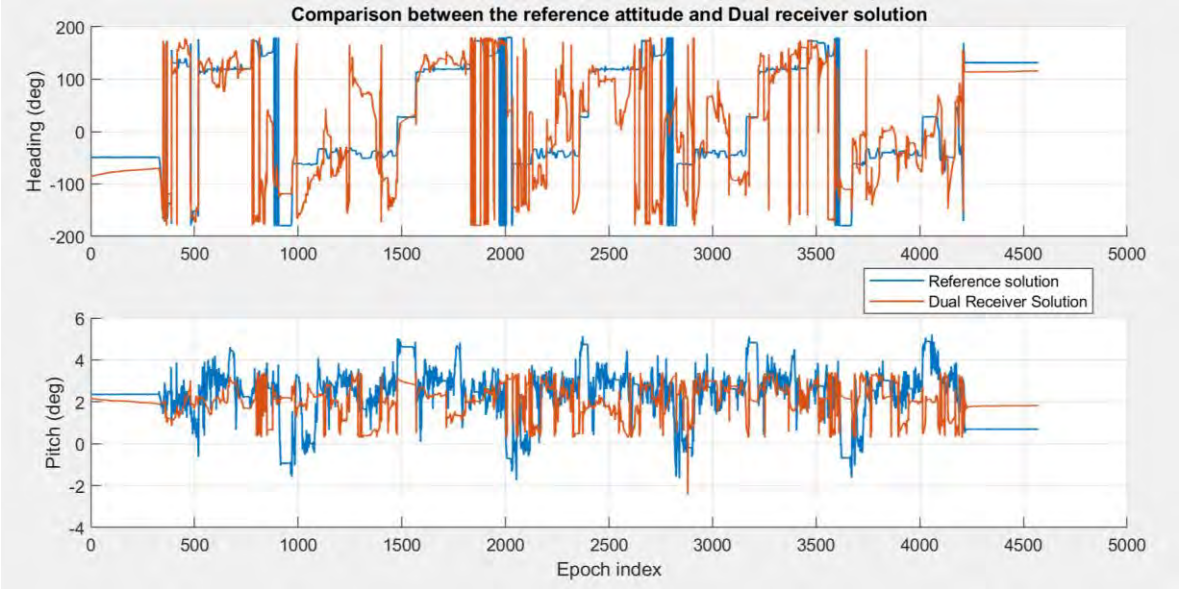

Figure 6-50 Illustration of vehicle attitude estimation (Dataset 3)

In the following sections, the detailed performance comparison results of the single and multi-receiver systems in the urban environment will be presented, as well as the result when considering the GPS/Galileo dual constellation.

6.3.3.2. Performance Comparison between Single and Multi-receiver system - GPS only

Only the GPS constellation is considered in the first scenario. Table 6-10 gives the performance comparison between the proposed dual-receiver system and the single receiver system in the urban environment with different array baseline lengths configurations. It should be noted that the solution availability is considered as a complementary metric to evaluate the performance of the algorithms in such an extremely harsh situation.

In such an environment, it is extremely difficult to successfully fix the integer ambiguities. This is reflected in the fix success rate result as shown clearly in Figure 6-51, which has dropped sharply compared to the previous situation. Especially for the case with a single receiver, there is no fixing success declared. Due to the poor environmental condition, too frequent appearances of cycle slips and multipath clearly interrupt the IAR process.

Table 6-10 Performance comparison for different array baselines for data collection 3 – Urban, GPS only

Variation of Dataset 3	Performance indicator	Unit	Mean	Standard deviation	50% bound	95% bound	Solution Availability
Single receiver	Horizontal positioning error	m	3.87	3.26	2.68	8.32	84.2%
	Fix success rate	%	0	N/A	N/A	N/A	
Dual receiver $l = 0.6$ m	Horizontal positioning error	m	2.25	2.62	1.59	5.63	93.5%
	Absolute heading error	deg	32.18	22.78	22.32	48.32	
	Absolute pitch error	deg	4.36	3.86	3.85	7.45	
	Fix success rate	%	7.48	N/A	N/A	N/A	
Dual receiver $l = 1.3$ m	Horizontal positioning error	m	2.18	2.51	1.48	5.42	93.6%
	Absolute heading error	deg	31.45	16.62	19.65	46.65	
	Absolute pitch error	deg	4.09	3.52	3.98	6.98	
	Fix success rate	%	7.75	N/A	N/A	N/A	
Dual receiver $l = 2.0$ m	Horizontal positioning error	m	2.01	2.37	1.30	5.34	93.6%
	Absolute heading error	deg	30.72	18.53	18.59	38.59	
	Absolute pitch error	deg	3.89	3.71	3.63	6.83	
	Fix success rate	%	7.93	N/A	N/A	N/A	

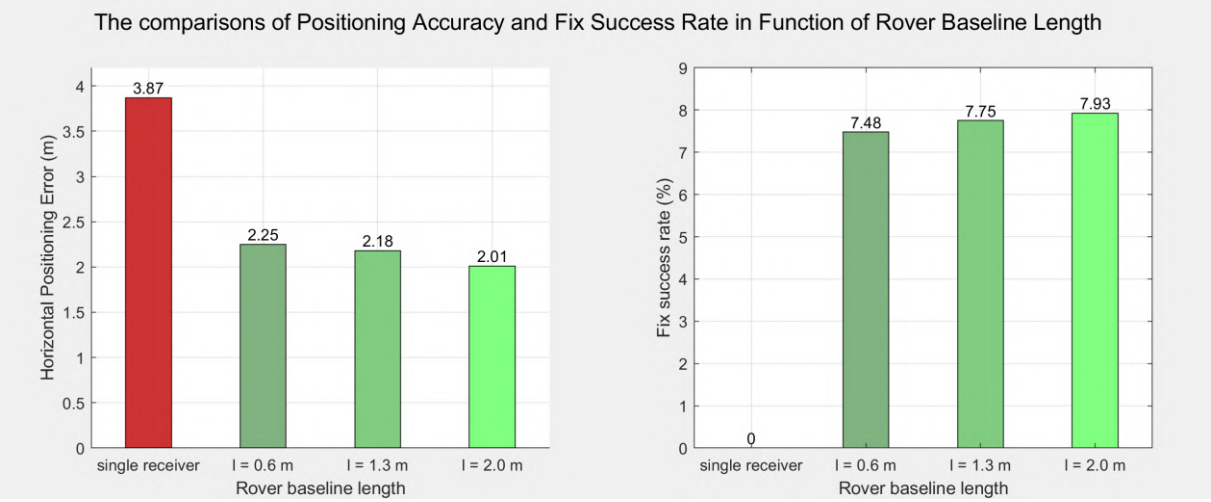

Figure 6-51 Comparisons of Positioning Accuracy and Fix Success Rate w.r.t Rover Baseline Length (Dataset3 - GPS only)

Additionally, in such a harsh environment, compared to dual-receiver, the solution availability decreased greatly for the single receiver solution and a better accuracy result is obtained in the dual-receiver situation. Moreover, there is no huge difference in the accuracy of the positioning results

between the different dual-receiver variations. Unsurprisingly, the attitude accuracy improves slightly as the array baseline length increases as plotted in Figure 6-52, although the accuracy of the estimation of the vehicle attitude is seriously degraded compared to previous datasets.

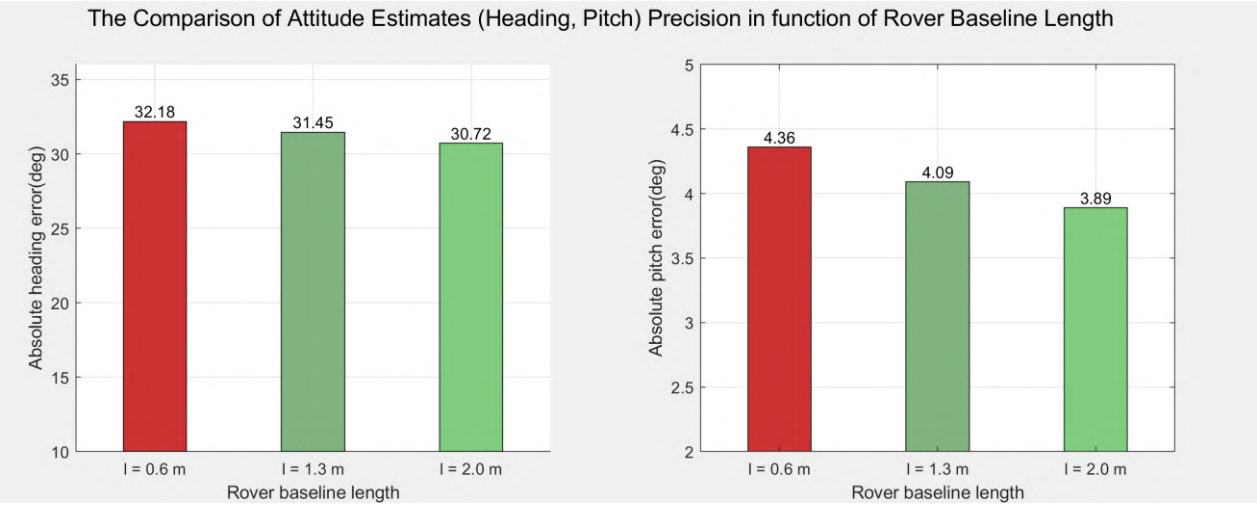

Figure 6-52 Comparisons of Attitude Estimates Precision w.r.t Rover Baseline Length (Dataset3 - GPS only)

6.3.3.3. *Performance Comparison between Single and Multi-receiver system– GPS/GALILEO*

To improve the GNSS measurement availability especially in the city center, the Galileo constellation is considered. The advantage of considering the Galileo constellation is very clear. It almost doubles the total number of available satellites at each epoch as shown in Figure 6-22.

As may be seen from Figure 6-53 and Figure 6-54, the improvement brought by the Galileo system is significant, for both the single receiver and multi-receiver systems. In fact, in such a GNSS-challenging environment where it is harder to maintain a sufficient number of tracked satellites especially when using the low-cost receivers, an additional system can greatly improve satellite visibility and thus improve positioning accuracy and solution availability.

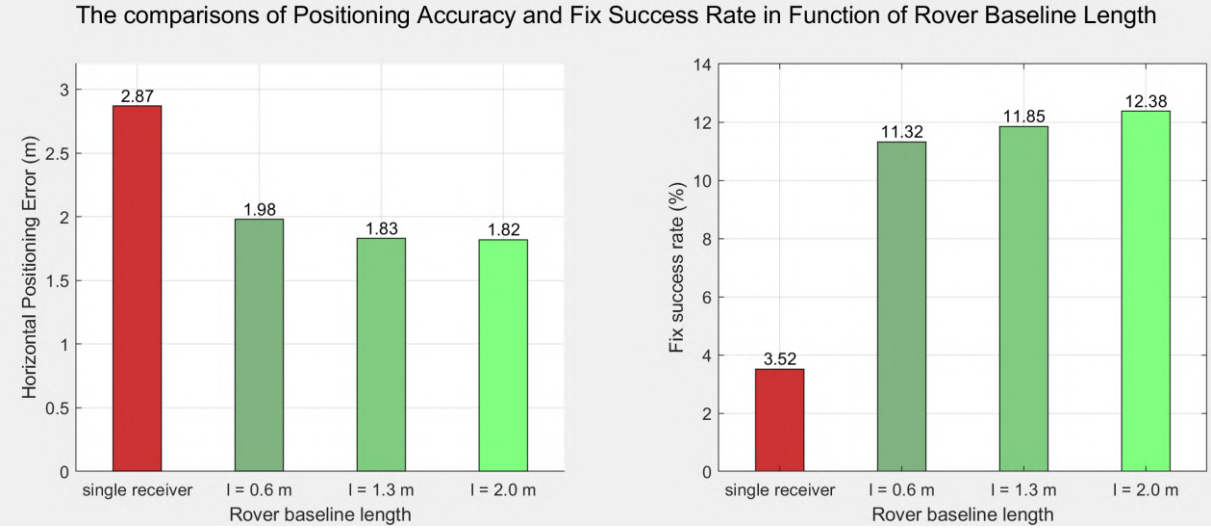

Figure 6-53 Comparisons of Positioning Accuracy and Fix Success Rate w.r.t Rover Baseline Length (Dataset3- GPS/GALILEO)

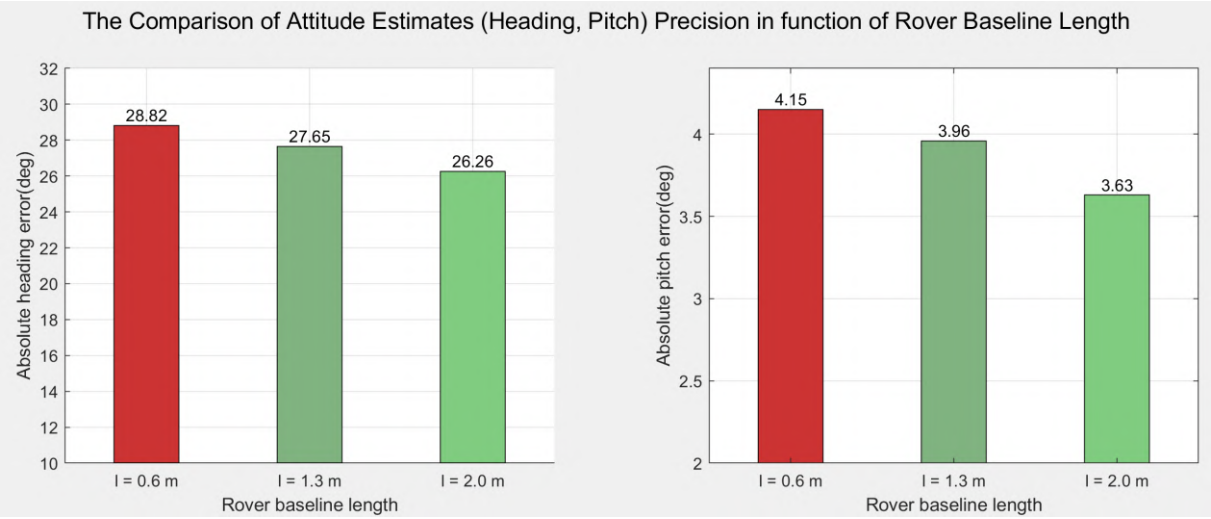

Figure 6-54 Comparisons of Attitude Estimates Precision w.r.t Rover Baseline Length (Dataset3 – GPS/GALILEO)

Besides, the comparisons in Table 6-11 reveal that the use of the receiver array improves the ambiguity fix success rate, positioning accuracy, and also solution availability for all considered array baseline length values. We can conclude that the use of an array of receivers with known geometry to improve RTK performance is feasible and effective.

Table 6-11 Performance comparison for different array baselines for data collection 3 – Urban, GPS/GALILEO

Variation of Dataset 3	Performance indicator	Unit	Mean	Standard deviation	50% bound	95% bound	Solution Availability
Single receiver	Horizontal positioning error	m	2.87	2.85	2.25	7.26	94.2%
	Fix success rate	%	3.52	N/A	N/A	N/A	
Dual receiver $l = 0.6$ m	Horizontal positioning error	m	1.98	2.35	1.27	5.34	98.5%
	Absolute heading error	deg	28.82	18.87	20.82	40.68	
	Absolute pitch error	deg	4.15	3.56	3.58	6.43	
	Fix success rate	%	11.32	N/A	N/A	N/A	
Dual receiver $l = 1.3$ m	Horizontal positioning error	m	1.83	2.43	1.25	4.93	98.7%
	Absolute heading error	deg	27.65	18.62	18.39	37.65	
	Absolute pitch error	deg	3.96	3.82	3.36	5.69	
	Fix success rate	%	11.85	N/A	N/A	N/A	
Dual receiver $l = 2.0$ m	Horizontal positioning error	m	1.82	2.28	1.08	4.88	98.6%
	Absolute heading error	deg	26.26	18.25	17.36	32.68	
	Absolute pitch error	deg	3.63	3.44	2.88	5.85	
	Fix success rate	%	12.38	N/A	N/A	N/A	

6.4. Chapter Summary

This chapter aims at validating the proposed multi-receiver architecture to actual situations by using the real measurement collected from different environments with different lengths of array antenna baselines. Firstly, the three data collections scenarios are described and analyzed, as well as the equipment and the hardware set-up embedded on the vehicle.

Secondly, to improve the signal quality by detecting and eliminating measurement outliers, the signal pre-processing steps are conducted. Then, in order to optimize our processing, the correlation of the measurement errors affecting observations taken by our array of receivers has been determined. After that, the performance of our real-time single frequency cycle-slip detection and repair algorithm has been assessed, by comparing it to the cycle slips detected by a dual-frequency algorithm performed in post-processing. These two investigations yielded important information to tune our Kalman Filter.

The algorithm was first tested on the open-sky environment to validate and give a reference demonstration of the performance of our multi-receiver system. Favorable results have been observed, the algorithm succeeded in outputting the right positioning result, with an average accuracy of about 0.01 m and a millimeter-level accuracy could be obtained when the ambiguities are successfully fixed.

The results from the analysis of the datasets from the suburban and urban test drives gave us some useful information on the robustness of the multi-receiver RTK system in harsh environments. Reliable ambiguity fixing was found to be extremely unlikely in the urban environment due to the degraded signal quality. However, thanks to the appropriate signal pre-processing procedures and the GPS/Galileo dual GNSS constellation, together with the proposed multi-receiver methodology, the horizontal position error is below 4 meters in the urban dataset 95% of the time, even with the frequent NLOS signals and high-amplitude multipath in such an environmental condition. These results are particularly satisfactory considering the type of environment encountered.

Finally, through real data processing results for all the datasets, we demonstrated that our multi-receiver RTK system is more robust to degraded satellite geometry, in terms of ambiguity fixing rate, solution availability, and get a better position accuracy under the same conditions when compared with the single receiver system. Additionally, our method achieves a relatively accurate estimation of the attitude of the vehicle which provides additional information beyond the positioning. Our experiments correlate favorably with our previous simulation results and further support the idea of using an array of receivers with known geometry to improve the RTK performance.

Due to the rich results obtained in this section, another two conference papers [147], [148], and a journal article [149] were published during the Ph.D.

Chapter 7. Conclusions and Perspectives

The current chapter firstly summarizes the main conclusions of the work conducted during this Ph.D. thesis and reminds the major contributions of this dissertation. Several recommendations for future research in this field are addressed in the second part.

7.1. Thesis Conclusions

The research work of this Ph.D. is carried out in the context of increasing demands of the GNSS-based precise positioning applications in constraint environments. The objective of this Ph.D. was then to explore the possibility of achieving GNSS precise positioning with a low-cost architecture: using multiple low-cost, single-frequency receivers with known geometry to enable the vehicle attitude determination and RTK performance amelioration, especially in GNSS signal-degraded environments like the urban environment.

As a first step, **Chapter 2** gives the state of art of the GNSS functional and stochastic model. An overview of the different GNSS systems includes the GPS, Galileo, BeiDou, and GLONASS. Their corresponding transmitted signals are presented. This is followed by a functional description of GNSS receivers which aims at showing how GNSS signals are processed by the receiver and how the receiver will respectively give the code pseudorange and the carrier phase measurements as by-products. The GNSS code and phase observations including all nominal error sources are also described since they have a pivotal influence on the GNSS precise positioning. In addition, even though there is a wide variety of GNSS systems since the Ph.D. focuses on low-cost GNSS receivers which mostly can only receive single-frequency signals, only GPS L1 C/A and Galileo E1 OS signals are presented in detail.

In **Chapter 3,** we have focused on the introduction and classification of the state of the art of GNSS-based precise positioning and attitude estimation techniques, which helps us to identify the proper techniques that are used in this Ph.D. thesis. The description of the GNSS precise positioning techniques is firstly provided, which includes the DGNSS (Differential GNSS), PPP (Precise Point Positioning), and RTK (Real-Time Kinematic), the comparison between each technique is presented. The challenges of the GNSS's precise positioning in highly constrained environments are revealed. As presented, precise positioning with a stand-alone GPS receiver or using differential corrections is known to be strongly degraded in a GNSS-challenged environment due to frequent signal masking, strong multipath effect, frequent cycle slips on carrier phase, etc. To achieve precise positioning in these GNSS signal-degraded environments, the RTK methodology has been preferred over the PPP methodology due to its fast convergence time, better precision, and easier integer ambiguity resolution process. In addition, for the low-cost GNSS receivers which provide only single-frequency GNSS measurement, the lack of accurate atmosphere correction models, as well as its long convergence time, indeed restrict the application of the PPP methodology in a constrained area. Therefore, RTK is chosen as the precise positioning algorithm for this dissertation. What is more, after having studied existing GNSS-based

attitude estimation methods and detailed their advantages and challenges, we noticed that there is still room for improvement and new methods exploring.

Based on the previous considerations, the architecture of the multi-receiver RTK precise positioning system has been proposed and presented in **Chapter 4**. The proposed multi-receiver architecture is based on an Extended Kalman Filter (EKF) which combines multi-constellation (GPS + Galileo) GNSS measurements. In the measurement model of the proposed, the position of receiver 2 is expressed in terms of the position of receiver 1 and the baseline vector between the 2 receivers of the array such that it contains the known array baseline length information and the attitude information that we want to estimate. The use of the multiple receivers' architecture is expected to improve the performance of the RTK positioning taking advantage of the known geometry and measurement redundancy, and the additional observability of attitude can also be an interesting feature for some specific applications.

Based on this architecture, the performance of the proposed method has been tested and quantified through both the experimental and real data set, and the results obtained have been presented in **Chapter 5** and **Chapter 6**, respectively. The focus is to provide practical evidence of the performance improvement obtained by applying the proposed multi-receiver RTK precise positioning and attitude determination method instead of the traditional single receiver method.

In **Chapter 5**, the proposed precise position and attitude determination algorithm has been tested and quantified through the experimental data set, to enable the conduction of several specific comparison scenarios between our multi-receiver system and the traditional single receiver system, and the results obtained have been presented. Different scenarios are conducted including varying the distance between the 2 antennas of the receiver array, the satellite geometry, the amplitude, and the correlation level of the noise measurement to validate the influence of the using of an array of receivers. The results of the simulator show that our multi-receiver RTK system is more robust to noise and degraded satellite geometry, in terms of ambiguity fixing rate, and gets a better position accuracy under the same conditions when compared with the single receiver system. Additionally, our method achieves a relatively accurate estimation of the attitude of the vehicle which provides additional information beyond the positioning. Two specific cases study (cycle slip detection, multiple rover receivers connected to the same antenna) are also presented. Both studies result in interesting findings and have further strengthened our confidence in using the multi-receiver architecture for RTK positioning and attitude determination. The positive results obtained from the simulation made us eager to use real data collections to verify and further improve our multi-receiver model.

In **Chapter 6,** the algorithm is then tested using real data. To reflect different environmental situations, 3 different GNSS raw observation data collections campaigns under various satellite visibility conditions are conducted in Toulouse, France. The environmental conditions of these 3 data collection scenarios are firstly reviewed, as well as the details about the data collection set-ups. The availability statistics of the GNSS measurements in different scenarios are also presented. The performance of the proposed multi-receiver RTK navigation solution (position estimation and attitude determination accuracy) is then assessed based on the test results using the collected real GNSS data in all the considered environmental conditions. The impact of the distance between the 2 antennas of the receiver array and the advantages brought by the GPS/Galileo dual constellation are also analyzed and presented.

The algorithm was first tested on the open-sky environment to validate and give a reference demonstration of the performance of our multi-receiver system. Favorable results have been observed, the algorithm succeeded in outputting the right positioning result, with an average accuracy of about 0.01 m and a millimeter-level accuracy could be obtained when the ambiguities are successfully fixed.

The results from the analysis of the datasets from the suburban and urban test drives gave us some useful information on the robustness of the multi-receiver RTK system in harsh environments. Reliable ambiguity fixing was found to be extremely unlikely in an urban environment due to the degraded signal quality. However, thanks to the appropriate signal pre-processing procedures and the GPS/Galileo dual GNSS constellation, together with the proposed multi-receiver methodology, the horizontal position error is below 4 meters in the urban dataset 95% of the time, even with the frequent NLOS signals and high-amplitude multipath in such an environmental condition. These results are particularly satisfactory considering the type of environment encountered.

Finally, in comparison with the traditional single receiver system, the results of all the datasets demonstrated that our multi-receiver RTK system is more robust to degraded satellite geometry and always gets a better positioning accuracy under the same conditions. Our experiments correlate favorably with our previous simulation results and further support the idea of using an array of receivers with known geometry to improve the RTK performance.

Generally, the main property investigated is the proposed method's **superior performance in terms of positioning accuracy**. Precise positioning is the primary objective of the discussed method and the Ph.D. thesis, but a number of other benefits are achieved as well, whose importance is not secondary:

- A **higher IAR success rate** is achieved: The multi-receiver method enables a much higher probability of correct ambiguity estimation: the capacity of fixing the correct set of integer carrier phase ambiguities is largely augmented. Successful ambiguity resolution is also fundamental to improve the GNSS-based attitude estimation accuracy which is up to two orders of magnitude with respect to the float solutions.

- The **better solution availability (SA)**: The SA, which is defined as the number of epochs during which positions are successfully calculated and provided over the total number of epochs, is much improved in highly constrained environments.

- **Vehicle attitude estimation support**: The proposed methodology achieves a relatively accurate estimation of the attitude of the vehicle which provides additional information beyond the positioning.

- The **improvement of the single-frequency cycle slip detection**: In our simulator presented in **Chapter 5**, by using a centralized cycle slips detection method and taking advantage of the diverse data observations from an array of receivers with known geometry, the prediction accuracy of the differential phase in time is ameliorated, thus the occurrence of CS can be detected more accurately and timely.

Overall, these findings are in accordance with the objective of this Ph.D. thesis. The proposed method also has great potential for many applications such as:

- **Aerospace applications**: guidance and navigation of aircraft, unmanned air vehicles, and satellites. Spaceborne missions may greatly benefit from the GNSS-based alternative to classical attitude sensors.
- **Maritime applications**: precise orientation estimates are required for general navigation in open waters. The attitude estimation by using the proposed method can be complementary to the other attitude estimation sensors.
- **Agriculture applications**: precise farming needs a reliable attitude estimation and RTK precise positioning system to precisely guide moving machinery.
- **Industrial applications**: applications like autonomous driving need precise positioning and attitude information to provide a better and safer solution.

7.2. Perspectives

The initial goal of this Ph.D. study was reached, as explained in the previous section. However, the topic of this PhD study is quite exploratory. Based on this proof-of-concept made in this Ph.D., several future works are possible to further improve the performance of the methodology:

More GNSS constellations, the inclusion of GLONASS and BeiDou: In this thesis, only the GPS and Galileo constellations are considered. The inclusion of other GNSS constellations like GLONASS and BeiDou would bring more reliability on PVT solutions, in particular, through their pilot signals.

Dual-frequency measurement: For this study, only the single frequency measurements are taken into account because the low-cost receivers usually did not process dual-frequency signals. Taking the distinguished developments of the GNSS receiver industry, we believe that the consideration of dual-frequency measurement would much improve the positioning accuracy, by taking advantage of a better cycle slip detection process and additional redundant GNSS measurements.

Hybridization with other sensors: Despite the use of GPS and Galileo measurements, satellite visibility was found to be low in highly constrained environments. The addition of a low-cost IMU or other sensors like lidar, radar, and video SLAM should allow keeping a reasonable level of accuracy during short signal blockages.

Better IAR techniques: In this thesis, the well-known LAMBDA method is used for the IAR process. Since the system has the geometry constraint between the array receivers**,** the constrained IAR methods (e.g., MCLAMBDA method) could be applied to improve the IAR process and may solve the integer ambiguities faster and more accurately.

Better cycle slip detection techniques: In this study, two single-frequency CS detection methods have been introduced. Other CS-DR techniques could be tested, notably those that would benefit from the improved accuracy of the receiver array solution.

Arrays with more than 2 receivers: In this thesis, we only considered the configuration with 2 rover receivers, the multi-receiver architecture with more than 2 receivers could also be assessed to further improve the measurement redundancy and estimate the third attitude angle.

Mitigation of NLOS conditions: The multipath is extremely severe in GNSS challenged environments, the interest of such an array for the mitigation of NLOS conditions permitted by the spatial diversity of the array can be further investigated.

Examine the use of the other estimation filters: The proposed solution is based on an EKF. However, this filter is not optimal in the case of non-gaussian measurement noise. The use of other estimation filters that are better adapted to measurements from a multipath environment (unscented Kalman filters, particle filters…) could be investigated.

Other types of GNSS data sources exploration: We can use raw GNSS data tracked by smartphones to test more possibilities and applications

References

[1] P. Misra and P. Enge, *Global positioning system: signals, measurements, and performance*. Lincoln, Mass.: Ganga-Jamuna Press, 2006.

[2] P. Henkel and C. Gunther, "Attitude determination with low-cost GPS/ INS," p. 9, 2013.

[3] M. Iafrancesco, "GPS/INS Tightly coupled position and attitude determination with low-cost sensors Master Thesis," p. 69, 2015.

[4] P. Henkel, P. Berthold, and J. J. Kiam, "Calibration of magnetic field sensors with two mass-market GNSS receivers," in *2014 11th Workshop on Positioning, Navigation and Communication (WPNC)*, Dresden, Germany, Mar. 2014, pp. 1–5. doi: 10.1109/WPNC.2014.6843306.

[5] G. Gabriele and J. B. Peter, "GNSS-Based Attitude Determination," *G*, Jul. 11, 2011. https://insidegnss.com/gnss-based-attitude-determination/ (accessed Jan. 22, 2021).

[6] D. Medina, A. Heselbarth, R. Buscher, R. Ziebold, and J. Garcia, "On the Kalman filtering formulation for RTK joint positioning and attitude quaternion determination," in *2018 IEEE/ION Position, Location and Navigation Symposium (PLANS)*, Monterey, CA, Apr. 2018, pp. 597–604. doi: 10.1109/PLANS.2018.8373432.

[7] F. Aghili and A. Salerno, "Attitude determination and localization of mobile robots using two RTK GPSs and IMU," in *2009 IEEE/RSJ International Conference on Intelligent Robots and Systems*, St. Louis, MO, USA, Oct. 2009, pp. 2045–2052. doi: 10.1109/IROS.2009.5354770.

[8] F. Aghili and A. Salerno, "3-D Localization of mobile robots and its observability analysis using a pair of RTK GPSs and an IMU," in *2010 IEEE/ASME International Conference on Advanced Intelligent Mechatronics*, Montreal, QC, Canada, Jul. 2010, pp. 303–310. doi: 10.1109/AIM.2010.5695718.

[9] G. Zheng and D. Gebre-Egziabher, "Enhancing Ambiguity Resolution Performance Using Attitude Determination Constraints," presented at the ION GNSS, Savannah, Georgia, Sep. 2009.

[10] N. Nadarajah, A. Khodabandeh, K. Wang, M. Choudhury, and P. Teunissen, "Multi-GNSS PPP-RTK: From Large- to Small-Scale Networks," *Sensors*, vol. 18, no. 4, p. 1078, Apr. 2018, doi: 10.3390/s18041078.

[11] A. Khodabandeh and P. J. G. Teunissen, "Single-Epoch GNSS Array Integrity: An Analytical Study," in *VIII Hotine-Marussi Symposium on Mathematical Geodesy*, vol. 142, N. Sneeuw, P. Novák, M. Crespi, and F. Sansò, Eds. Cham: Springer International Publishing, 2015, pp. 263–272. doi: 10.1007/1345_2015_64.

[12] A. Khodabandeh and P. J. G. Teunissen, "Array-based satellite phase bias sensing: theory and GPS/BeiDou/QZSS results," *Meas. Sci. Technol.*, vol. 25, no. 9, p. 095801, Sep. 2014, doi: 10.1088/0957-0233/25/9/095801.

[13] Fan, Li, Cui, and Lu, "Precise and Robust RTK-GNSS Positioning in Urban Environments with Dual-Antenna Configuration," *Sensors*, vol. 19, no. 16, p. 3586, Aug. 2019, doi: 10.3390/s19163586.

[14] ICAO, "Annex 10 - Aeronautical Telecommunications - Volume I - Radio Navigational Aids," *ICAO*, Jul. 2018.

[15] Global Positioning Systems Wing, Systems engineering and integration, "NAVSTAR GPS Space Segment/Navigation User Segment Interfaces, IS-GPS-200," May 2020.

[16] PNT IAC of the Central Research Institute of Machine Building, "GLONASS Open Service Performance Standard (OS PS), Edition 2.2," Jun. 2020.

[17] China Satellite Navigation Office, "BeiDou Navigation Satellite System Signal In Space Interface Control Document," Jun. 2020.

[18] European GNSS Agency, "Galileo Open Service Signal-In-Space Interface Control Document (OS SIS ICD), Issue 2.0," Jan. 2021.

[19] INDIAN SPACE RESEARCH ORGANIZATION, "INTERFACE CONTROL DOCUMENT (ICD) OF DISTRESS ALERT TRANSMITTER - SECOND GENERATION (DAT-SG) Ver 1.2 - February 2021," Feb. 2021.

[20] Japan Cabinet Office, “Quasi-Zenith Satellite System Interface Specification Satellite Positioning, Navigation and Timing Service (IS-QZSS-PNT-004),” Jan. 2021.
[21] Official U.S. government information about the Global Positioning System (GPS) and related topics, “GPS.gov: Space Segment.” https://www.gps.gov/systems/gps/space/ (accessed Jun. 23, 2021).
[22] INFORMATION AND ANALYSIS CENTER FOR POSITIONING, NAVIGATION AND TIMING (IAC PNT), “GLONASS Constellation status.” https://www.glonass-iac.ru/en/GLONASS/index.php (accessed Jun. 23, 2021).
[23] GPS, “Navstar GPS user equipment introduction,” 1996.
[24] “An Introduction to GNSS: GPS, GLONASS, Galileo and Other Global Navigation Satellite Systems,” *calameo.com*. https://www.calameo.com/read/00191579602f9b13b088e (accessed Mar. 08, 2021).
[25] E. Kaplan and C. Hegarty, *Understanding GPS: principles and applications*. Artech house, 2005.
[26] J. A. A. Rodriguez, “On generalized signal waveforms for satellite navigation,” PhD Thesis, Universitätsbibliothek der Universität der Bundeswehr München, 2008.
[27] ICGNSS, “Current and Planned Global and Regional Navigation Satellite Systems and Satellite-based Augmentations Systems,” *Int. Comm. Glob. Navig. Satell. Syst. Provid. Forum U. N. Off. Outer Space Aff.*, 2010.
[28] “GPS.gov: New Civil Signals.” https://www.gps.gov/systems/gps/modernization/civilsignals/ (accessed Jun. 15, 2021).
[29] J. J. Spilker Jr, P. Axelrad, B. W. Parkinson, and P. Enge, *Global positioning system: theory and applications, volume I*. American Institute of Aeronautics and Astronautics, 1996.
[30] RE Philip Kwan, “NAVST AR GPS Space Segment/User Segment L1C Interfaces, IS-GPS-800,” May 2019.
[31] J. Betz and M. Blanco, “Enhancing the Future of Civil Gps Overview of the L1c Signal,” Apr. 2007.
[32] T. Stansell and G. P. S. Wing, *Update on GPS L1C signal modernization*.
[33] P. Enge, “GPS Modernization: Capabilities of the New Civil Signals,” *Australian international aerospace congress, Brisbane*, p. 22, Jul. 2003.
[34] “ED-259 - Minimum Operational Performance Standards for Galileo - Global Positioning System - Satellite-Based Augmentation System Airborne Equipment,” *EUROCAE*, Feb. 2019.
[35] RISDE, “Global navigation satellite system GLONASS, Interface control document, Navigation radiosignal in bands L1, L2, Edition 5.1,” *Russian Institute of Space device Engineering*, 2008.
[36] P. Groves, *Principles of GNSS, Inertial, and Multisensor Integrated Navigation Systems, Second Edition*. 2013.
[37] M. Petovello, “GLONASS inter-frequency biases and ambiguity resolution,” *GNSS*, pp. 24–28, 2009.
[38] China Satellite Navigation Office, “BeiDou Navigation Satellite System official website - system.” http://en.beidou.gov.cn/SYSTEMS/System/ (accessed Jun. 26, 2021).
[39] “China completes BeiDou-3 worldwide navigation constellation,” *GPS World*, Jun. 23, 2020. https://www.gpsworld.com/china-completes-beidou-3-worldwide-navigation-constellation/ (accessed Jun. 27, 2021).
[40] Aerospace-technology, “BeiDou-3 Navigation Satellite System, China.” https://www.aerospace-technology.com/projects/beidou-3-navigation-satellite-system/ (accessed Jun. 27, 2021).
[41] European GNSS Agency, *PPP-RTK market and technology report*. 2019.
[42] Y. Wang, “Localization Precise in Urban Area,” PhD Thesis, INPT, 2019. Accessed: Jun. 20, 2021. [Online]. Available: https://tel.archives-ouvertes.fr/tel-02917137
[43] NovAtel lnc., *An Introduction to GNSS: GPS, GLONASS, BeiDou, Galileo and other Global Navigation Satellite Systems, Second Edition*. Accessed: Mar. 08, 2021. [Online]. Available: https://novatel.com/an-introduction-to-gnss
[44] E. D. Kaplan and C. Hegarty, *Understanding GPS: principles and applications*. Boston: Artech House, 2006.
[45] P. Teunissen and O. Montenbruck, *Springer Handbook of Global Navigation Satellite Systems*. Springer, 2017.

[46] B. Hofmann-Wellenhof, H. Lichtenegger, and E. Wasle, *GNSS – Global Navigation Satellite Systems: GPS, GLONASS, Galileo, and more*. Springer Science & Business Media, 2007.
[47] C. Pendão, A. Ferreira, A. Moreira, and H. Silva, *Challenges in Characterization of GNSS Precise Positioning Systems for Automotive*. 2020.
[48] S. Carcanague, "Low-cost GPS/GLONASS precise positioning algorithm in constrained environment," PhD Thesis, Institut National Polytechnique de Toulouse-INPT, 2013.
[49] J. M. Dow, R. E. Neilan, and C. Rizos, "The international GNSS service in a changing landscape of global navigation satellite systems," *J. Geod.*, vol. 83, no. 3–4, pp. 191–198, 2009.
[50] L. Wanninger, "Carrier-phase inter-frequency biases of GLONASS receivers," *J. Geod.*, vol. 86, no. 2, pp. 139–148, 2012.
[51] "GPS for Land Surveyors, Fourth Edition," p. 350.
[52] Trimble lnc., "Trimble - GPS Tutorial." https://www.trimble.com/gps_tutorial/dgps-how.aspx (accessed Mar. 07, 2021).
[53] R. Ong, "Reliability of combined GPS/GLONASS ambiguity resolution," in *Masters Abstracts International*, 2010, vol. 49, no. 03.
[54] C. Macabiau, "Analysis of the feasibility of using GPS carrier phase ambiguity resolution techniques for precision approaches," PhD Thesis, INPT, 1997.
[55] P. Teunissen, "Towards a unified theory of GNSS ambiguity resolution," *J. Glob. Position. Syst.*, vol. 2, no. 1, pp. 1–12, 2003.
[56] P. J. G. Teunissen, "The GPS integer least-squares statistics," *Phys. Chem. Earth Part Solid Earth Geod.*, vol. 25, no. 9–11, pp. 673–677, 2000.
[57] P. J. G. Teunissen, "The least-squares ambiguity decorrelation adjustment: a method for fast GPS integer ambiguity estimation," *J. Geod.*, vol. 70, no. 1–2, pp. 65–82, Nov. 1995, doi: 10.1007/BF00863419.
[58] B. J. Clark and D. M. Bevly, "GPS/INS integration with fault detection and exclusion in shadowed environments," in *2008 IEEE/ION Position, Location and Navigation Symposium*, 2008, pp. 1–8.
[59] O. Julien, G. Lachapelle, and M. E. Cannon, "Galileo L1 Civil Receiver Tracking Loops' Architecture," in *2007 IEEE International Symposium on Circuits and Systems*, New Orleans, LA, USA, May 2007, pp. 1737–1741. doi: 10.1109/ISCAS.2007.377930.
[60] Z. Dai, "MATLAB software for GPS cycle-slip processing," *GPS Solut.*, vol. 16, pp. 267–272, Apr. 2012, doi: 10.1007/s10291-011-0249-1.
[61] H.-K. Lee, J. Wang, and C. Rizos, "Effective Cycle Slip Detection and Identification for High Precision GPS/INS Integrated Systems," *J. Navig.*, vol. 56, no. 3, pp. 475–486, Sep. 2003, doi: 10.1017/S0373463303002443.
[62] G. Giorgi, *GNSS Carrier Phase-Based Attitude Determination Estimation and Applications*, PhD Thesis. 2011.
[63] M. D. Shuster, "A survey of attitude representations," *Navigation*, vol. 8, no. 9, pp. 439–517, 1993.
[64] E. Olguín Díaz, *3D Motion of Rigid Bodies: A Foundation for Robot Dynamics Analysis*, vol. 191. Cham: Springer International Publishing, 2019. doi: 10.1007/978-3-030-04275-2.
[65] "PlanetPhysics/Direction Cosine Matrix - Wikiversity." https://en.wikiversity.org/wiki/PlanetPhysics/Direction_Cosine_Matrix (accessed Jun. 28, 2021).
[66] "Axis–angle representation," *Wikipedia*. May 13, 2021. Accessed: Jun. 28, 2021. [Online]. Available: https://en.wikipedia.org/w/index.php?title=Axis%E2%80%93angle_representation&oldid=1022906751
[67] H. Parwana and M. Kothari, "Quaternions and Attitude Representation," *ArXiv170808680 Cs*, Aug. 2017, Accessed: Mar. 22, 2021. [Online]. Available: http://arxiv.org/abs/1708.08680
[68] S. W. Shepperd, "Quaternion from Rotation Matrix," *J. Guid. Control*, vol. 1, no. 3, pp. 223–224, May 1978, doi: 10.2514/3.55767b.
[69] J. Diebel, "Representing Attitude: Euler Angles, Unit Quaternions, and Rotation Vectors," p. 35.
[70] C. E. Cohen, "Attitude determination," *Glob. Position. Syst. Theory Appl.*, vol. 2, pp. 519–538, 1996.

[71] G. Lu, *Development of a GPS multi-antenna system for attitude determination.* University of Calgary Calgary, Canada, 1995.
[72] P. Xu, Y. Shu, X. Niu, J. Liu, W. Yao, and Q. Chen, "High-rate multi-GNSS attitude determination: experiments, comparisons with inertial measurement units and applications of GNSS rotational seismology to the 2011 Tohoku Mw9.0 earthquake," *Meas. Sci. Technol.*, vol. 30, no. 2, p. 024003, Feb. 2019, doi: 10.1088/1361-6501/aaf987.
[73] M. S. Grewal, L. R. Weill, and A. P. Andrews, *Global positioning systems, inertial navigation, and integration*. John Wiley & Sons, 2007.
[74] M. Iafrancesco, "GPS/INS Tightly coupled position and attitude determination with low-cost sensors," *MSc Thesis*, 2015.
[75] P. Machado, "InerTouchHand," 2012. doi: 10.13140/2.1.4959.3601.
[76] A. Noureldin, T. B. Karamat, and J. Georgy, "Fundamentals of inertial navigation, satellite-based positioning and their integration," 2013.
[77] X. Zhu, W. Tian, G. Li, and J. Yu, *Research on Localization Vehicle Based on Multiple Sensors Fusion System*, vol. 2. 2017, p. 494. doi: 10.1109/ICCNEA.2017.75.
[78] G. Giorgi and P. Teunissen, "GNSS Carrier Phase-Based Attitude Determination," 2012. doi: 10.5772/38381.
[79] G. Giorgi and P. Teunissen, *Carrier phase GNSS attitude determination with the Multivariate Constrained LAMBDA method*. 2010, p. 12. doi: 10.1109/AERO.2010.5446910.
[80] C. E. Cohen, "Attitude determination using GPS: Development of an all solid state guidance, navigation, and control sensor for air and space vehicles based on the global positioning system," PhD Thesis, Stanford University, 1993.
[81] J. K. baxsalary, "A study of the equivalence between a Gauss-Markoff model and its augmentation by nuisance parameters," *Stat. J. Theor. Appl. Stat.*, vol. 15, no. 1, pp. 3–35, 1984.
[82] X.-W. Chang, X. Yang, and T. Zhou, "MLAMBDA: a modified LAMBDA method for integer least-squares estimation," *J. Geod.*, vol. 79, pp. 552–565, Jan. 2005, doi: 10.1007/s00190-005-0004-x.
[83] P. Xu, C. Shi, and J. Liu, "Integer estimation methods for GPS ambiguity resolution: an applications oriented review and improvement," *Surv. Rev.*, vol. 44, no. 324, pp. 59–71, 2012.
[84] B. Wang, L. Miao, S. Wang, and J. Shen, "A constrained LAMBDA method for GPS attitude determination," *GPS Solut.*, vol. 13, no. 2, pp. 97–107, 2009.
[85] P. J. G. Teunissen, "The affine constrained GNSS attitude model and its multivariate integer least-squares solution," *J. Geod.*, vol. 86, no. 7, pp. 547–563, 2012.
[86] J. F. Ellis and G. A. Creswell, "Interferometric attitude determination with the Global Positioning System," *J. Guid. Control*, vol. 2, no. 6, pp. 522–527, 1979.
[87] A. G. Evans, "Roll, pitch, and yaw determination using a global positioning system receiver and an antenna periodically moving in a plane," *Mar. Geod.*, vol. 10, no. 1, pp. 43–52, 1986.
[88] F. Van Graas and M. Braasch, "GPS interferometric attitude and heading determination: Initial flight test results," *Navigation*, vol. 38, no. 4, pp. 297–316, 1991.
[89] G. Lachapelle, M. E. Cannon, G. Lu, and B. Loncarevic, "Shipborne GPS attitude determination during MMST-93," *IEEE J. Ocean. Eng.*, vol. 21, no. 1, pp. 100–104, 1996.
[90] F. C. Park, J. Kim, and C. Kee, "Geometric descent algorithms for attitude determination using the global positioning system," *J. Guid. Control Dyn.*, vol. 23, no. 1, pp. 26–33, 2000.
[91] A. A. Ardalan and M.-H. Rezvani, "An iterative method for attitude determination based on misaligned GNSS baselines," *IEEE Trans. Aerosp. Electron. Syst.*, vol. 51, no. 1, pp. 97–107, 2015.
[92] P. Axelrad and L. M. Ward, "On-Orbit GPS Based Attitude & Antenna Baseline Estimation," in *Proceedings of the 1994 National Technical Meeting of The Institute of Navigation*, 1994, pp. 441–450.
[93] I. Y. Bar-Itzhack, P. Y. Montgomery, and J. C. Garrick, "Algorithms for attitude determination using the global positioning system," *J. Guid. Control Dyn.*, vol. 21, no. 6, pp. 846–852, 1998.
[94] J. L. Crassidis and F. L. Markley, "New algorithm for attitude determination using Global Positioning System signals," *J. Guid. Control Dyn.*, vol. 20, no. 5, pp. 891–896, 1997.

[95] L. Dai, G. R. Hu, K. V. Ling, and N. Nagarajan, "Real-time attitude determination for microsatellite by LAMBDA method combined with Kalman filtering," in *22nd AIAA International Communications Satellite Systems Conference & Exhibit 2004 (ICSSC)*, 2004, p. 3118.

[96] H.-J. Euler and C. Hill, "Attltude Determination: Exploiting all Information for Optimal Ambiguity Resolution," in *Proceedings of the 8th International Technical Meeting of the Satellite Division of The Institute of Navigation (ION GPS 1995)*, 1995, pp. 1751–1757.

[97] G. Giorgi and P. J. Buist, "Single-epoch, single-frequency, standalone full attitude determination: experimental results," in *Proceedings of the 4th ESA Workshop on Satellite Navigation User Equipment Technologies, NAVITEC*, 2008, p. 8.

[98] A. Hauschild and O. Montenbruck, "GPS-based attitude determination for microsatellites," in *Proceedings of the 20th International Technical Meeting of the Satellite Division of the Institute of Navigation (ION GNSS 2007)*, 2007, pp. 2424–2434.

[99] D. Kim and R. B. Langley, "GPS ambiguity resolution and validation: methodologies, trends and issues," in *Proceedings of the 7th GNSS Workshop–International Symposium on GPS/GNSS, Seoul, Korea*, 2000, vol. 30, no. 2.12.

[100] L. V. Kuylen, F. Boon, and A. Simsky, "Attitude determination methods used in the polarx2@ multi-antenna gps receiver," in *Proceedings of the 18th International Technical Meeting of the Satellite Division of The Institute of Navigation (ION GNSS 2005)*, 2005, pp. 125–135.

[101] J. Madsen and E. G. Lightsey, "Robust spacecraft attitude determination using global positioning system receivers," *J. Spacecr. Rockets*, vol. 41, no. 4, pp. 635–644, 2004.

[102] Y. Li, K. Zhang, C. Roberts, and M. Murata, "On-the-fly GPS-based attitude determination using single- and double-differenced carrier phase measurements," *GPS Solut.*, vol. 8, pp. 93–102, Jul. 2004, doi: 10.1007/s10291-004-0089-3.

[103] M. L. Psiaki, "Batch algorithm for global-positioning-system attitude determination and integer ambiguity resolution," *J. Guid. Control Dyn.*, vol. 29, no. 5, pp. 1070–1079, 2006.

[104] P. S. Henkel, "Tightly coupled precise point positioning and attitude determination," *IEEE Trans. Aerosp. Electron. Syst.*, vol. 51, no. 4, pp. 3182–3197, 2015.

[105] C. E. Cohen, E. G. Lightsey, B. W. Parkinson, and W. A. Feess, "Space flight tests of attitude determination using GPS," *Int. J. Satell. Commun.*, vol. 12, no. 5, pp. 427–433, Sep. 1994, doi: 10.1002/sat.4600120504.

[106] D. S. De Lorenzo, S. Alban, J. Gautier, and P. Enge, "GPS attitude determination for a JPALS testbed: Integer initialization and testing," in *PLANS 2004. Position Location and Navigation Symposium (IEEE Cat. No.04CH37556)*, Monterey, CA, USA, 2004, pp. 762–770. doi: 10.1109/PLANS.2004.1309071.

[107] A. Morales-Reyes, N. Haridas, A. T. Erdogan, and T. Arslan, "Fault Tolerant and Adaptive GPS Attitude Determination System," in *2009 IEEE Aerospace conference*, Big Sky, MT, USA, Mar. 2009, pp. 1–8. doi: 10.1109/AERO.2009.4839532.

[108] M. Unwin, P. Purivigraipong, A. da Silva Curiel, and M. Sweeting, "Stand-alone spacecraft attitude determination using real flight GPS data from UOSAT-12," *Acta Astronaut.*, vol. 51, no. 1–9, pp. 261–268, Jul. 2002, doi: 10.1016/S0094-5765(02)00038-3.

[109] A. Raskaliyev, S. Patel, T. Sobh, and A. Ibrayev, "GNSS-Based Attitude Determination Techniques—A Comprehensive Literature Survey," *IEEE Access*, vol. PP, pp. 1–1, Jan. 2020, doi: 10.1109/ACCESS.2020.2970083.

[110] I. GNSS, "GNSS Filtering Options," *Inside GNSS - Global Navigation Satellite Systems Engineering, Policy, and Design*, Mar. 09, 2013. https://insidegnss.com/gnss-filtering-options/ (accessed Jun. 16, 2021).

[111] D. Kubrak, "Hybridisation of a GPS Receiver with Low-Cost Sensors for Personal Positioning in Urban Environment.," PhD Thesis, Télécom ParisTech, 2007.

[112] Christophe MACABIAU and Paul THEVENON, "Filtre de Kalman," IENAC L 3ème année lecture note.

[113] R. E. Kalman, "A New Approach to Linear Filtering and Prediction Problems," *J. Basic Eng.*, vol. 82, no. 1, pp. 35–45, Mar. 1960, doi: 10.1115/1.3662552.

[114]G. Welch and G. Bishop, “An Introduction to the Kalman Filter,” p. 16, 2006.
[115]A. B. Afia, “Development of GNSS/INS/SLAM Algorithms for Navigation in Constrained Environments,” PhD Thesis, INPT, 2017.
[116]E. A. Wan and R. Van Der Merwe, “The unscented Kalman filter for nonlinear estimation,” in *Proceedings of the IEEE 2000 Adaptive Systems for Signal Processing, Communications, and Control Symposium (Cat. No.00EX373)*, Lake Louise, Alta., Canada, 2000, pp. 153–158. doi: 10.1109/ASSPCC.2000.882463.
[117]S. J. Julier and J. K. Uhlmann, “New extension of the Kalman filter to nonlinear systems,” in *Signal processing, sensor fusion, and target recognition VI*, 1997, vol. 3068, pp. 182–193.
[118]F. Gustafsson *et al.*, “Particle filters for positioning, navigation, and tracking,” *IEEE Trans. Signal Process.*, vol. 50, no. 2, pp. 425–437, Feb. 2002, doi: 10.1109/78.978396.
[119]C. Hide, T. Moore, and C. Hill, “A Multi-Sensor Navigation Filter for High Accuracy Positioning in all Environments,” *J. Navig.*, vol. 60, no. 3, pp. 409–425, Sep. 2007, doi: 10.1017/S0373463307004328.
[120]T. Takasu, “RTKLIB version. 2.4.2 Manual,” Apr. 2013.
[121]H. Kuusniemi, “User-level reliability and quality monitoring in satellite-based personal navigation,” Tampere University of Technology, Tampere, 2005.
[122]Richard B. Langley, “GPS Receiver System Noise,” *GPS WORLD, Innovation*, Jun. 1997.
[123]S. Bisnath and R. Langley, “Pseudorange Multipath Mitigation By Means of Multipath Monitoring and De-Weighting,” Jan. 2001.
[124]H. Kuusniemi and G. Lachapelle, “GNSS Signal Reliability Testing in Urban and Indoor Environments,” vol. 2004, Jan. 2004.
[125]Y. Wang and O. Julien, “Cycle-slip Detection and Repair Using a Low Cost Single Frequency Receiver with Inertial-aiding,” p. 23.
[126]G. D. MacGougan, “Real-Time Kinematic Surveying using Tightly-Coupled GPS and Ultra-Wideband Ranging,” *PHD Thesis*, p. 221, Aug. 2009.
[127]N. ZHU, “GNSS Propagation Channel Modeling in Constrained Environments: Contribution to the Improvement of the Geolocation Service Quality/,” Theses, Université de Lille, 2018. Accessed: Jun. 20, 2021. [Online]. Available: https://hal.archives-ouvertes.fr/tel-01959797
[128]G. Xu and Y. Xu, *GPS: theory, algorithms and applications*. Springer, 2016.
[129]S. Carcanague, “Real-time geometry-based cycle slip resolution technique for single-frequency PPP and RTK,” 2012.
[130]P. Buist, “The Baseline Constrained LAMBDA Method for Single Epoch, Single Frequency Attitude Determination Applications,” presented at the ION GNSS, Fort Worth, Texas, Sep. 2007.
[131]S. Verhagen, B. Li, and P. J. G. Teunissen, “Ps-LAMBDA: Ambiguity success rate evaluation software for interferometric applications,” *Comput. Geosci.*, vol. 54, pp. 361–376, Apr. 2013, doi: 10.1016/j.cageo.2013.01.014.
[132]B. Li, S. Verhagen, and P. Teunissen, “GNSS integer ambiguity estimation and evaluation: LAMBDA and Ps-LAMBDA,” *Lect. Notes Electr. Eng.*, vol. 244, pp. 291–301, Jan. 2013, doi: 10.1007/978-3-642-37404-3-26.
[133]S. Verhagen, “On the Reliability of Integer Ambiguity Resolution,” *Navigation*, vol. 52, pp. 99–110, Jun. 2005, doi: 10.1002/j.2161-4296.2005.tb01736.x.
[134]S. Verhagen and P. J. G. Teunissen, “GNSS ambiguity resolution: which subset to fix?,” p. 15.
[135]L. Baroni and H. K. Kuga, “Analysis of Attitude Determination Methods Using GPS Carrier Phase Measurements,” *Math. Probl. Eng.*, vol. 2012, pp. 1–10, 2012, doi: 10.1155/2012/596396.
[136]P. Teunissen and S. Verhagen, “On the Foundation of the Popular Ratio Test for GNSS Ambiguity Resolution,” presented at the ION GNSS, Long Beach, California, Sep. 2004.
[137]P. Teunissen, *A New Method for Fast Carrier Phase Ambiguity Estimation*. 1994, p. 573. doi: 10.1109/PLANS.1994.303362.
[138]P. Teunissen, “Least-Squares Estimation of the Integer GPS Ambiguities,” Jan. 1993.
[139]P. D. Jonge and C. Tiberius, “The LAMBDA method for integer ambiguity estimation: implementation aspects,” *Delft Geod. Comput. Cent. Lgr Ser.*, vol. 12, 1996.

[140]X. Hu, P. Thevenon, and C. Macabiau, “Improvement of RTK performances using an array of receivers with known geometry,” *ION ITM 2020 Conf. San Diego Calif. U. S. 2020*, pp. 440–453.

[141]X. Hu, P. Thevenon, and C. Macabiau, “Cycle Slip Detection and Repair Using an Array of Receivers with Known Geometry for RTK Positioning,” PLANS 2020 IEEE/ION Position, Location and Navigation Symposium, Apr. 2020, pp. 1123-1134 / ISBN: 978-1-7281-9446–2. doi: 10.1109/PLANS46316.2020.9109871.

[142]X. Hu, P. Thevenon, and C. Mababiau, “Improving reliability and efficiency of RTK ambiguity resolution using multiple rover receivers connected to the same antenna,” in *2020 European Navigation Conference (ENC)*, Nov. 2020, pp. 1–10. doi: 10.23919/ENC48637.2020.9317367.

[143]T. Takasu and A. Yasuda, “Development of the low-cost RTK-GPS receiver with an open source program package RTKLIB,” *Int. Symp. GPSGNSS*, Jan. 2009.

[144]E. Realini, “goGPS free and constrained relative kinematic positioning with low cost receivers,” Apr. 2009.

[145]S. B. Bisnath, “Efficient, Automated Cycle-Slip Correction Of Dual-Frequency Kinematic GPS Data,” Sep. 2000, pp. 145–154. Accessed: Jun. 21, 2021. [Online]. Available: http://www.ion.org/publications/abstract.cfm?jp=p&articleID=1398

[146]N. ZHU, J. MARAIS, D. Betaille, and M. Berbineau, “GNSS Position Integrity in Urban Environments: A Review of Literature,” *IEEE Trans. Intell. Transp. Syst.*, p. 17p, Jan. 2018, doi: 10.1109/TITS.2017.2766768.

[147]X. Hu, P. Thevenon, and C. Macabiau, “Attitude Determination and RTK Performances Amelioration Using Multiple Low-Cost Receivers with Known Geometry,” ION ITM 2021, International Technical Meeting, Jan. 2021, pp. 439–453. doi: 10.33012/2021.17841.

[148]A. Banuelos, B Jan, X. HU, P. Thevenon *et al.*, “Centralized Processing of Multiple Smartphone Raw Measurements with Fixed and Known Position Onboard a Vehicle,” ION GNSS+ 2021, St.Louis, United States, Sep. 2021. Available: https://www.ion.org/gnss/abstracts.cfm?paperID=10473

[149]X. Hu, P. Thevenon, and C. Macabiau, “Attitude Determination and RTK Positioning Using Multiple Low-Cost Receivers with Known Geometry,” *GPS World*, vol. 32, no. 5, p. 35, May 2021.